Development of a Transparent Peptide Functionalized Bacterial Derived Cellulose Wound Dressing

A Dissertation
Submitted to the Faculty of
WORCESTER POLYTECHNIC INSTITUTE
In partial fulfillment of the requirements for the
Degree of Doctor of Philosophy in
Biomedical Engineering
July 21st, 2023
By

Elizabeth (Elzani) Margaretha van Zyl

Approved by:

Jeannine M. Coburn, Ph.D.
Associate Professor, Advisor
Biomedical Engineering
Worcester Polytechnic Institute

George D. Pins, Ph.D.
Professor, Chair
Biomedical Engineering
Worcester Polytechnic Institute

Marsha W. Rolle, Ph.D.
Affiliate Professor
Biomedical Engineering
Worcester Polytechnic Institute

Eric M. Young, Ph.D.
Assistant Professor
Chemical Engineering
Worcester Polytechnic Institute

Katie A. Bush, Ph.D.
Senior Vice President
Scientific & Medical Affairs
AVITA Medical

Acknowledgments

Ubuntu. I am because we are.

In true South African fashion, I acknowledge that I have made it to this point because of the people around.

First and foremost, I would like to thank my advisor, Jeannine M. Coburn Ph.D., for her support through both my masters and PhD degrees. Without her home kombucha culture this project would never have been started. (That was supposed to be a kombucha starter joke.) I extend my heartfelt appreciation to the members of my doctoral committee, George Pins Ph.D., Marsha Rolle Ph.D., Eric Young Ph.D., and Katie Bush Ph.D. for their invaluable insights, constructive criticism, and thoughtful suggestions. Their expertise and scholarly contributions have significantly enriched my work and broadened my understanding of the subject matter.

I would like to express my deepest appreciation to my family for their unwavering love, encouragement, and understanding. Their belief in my abilities and their constant support have been a driving force behind my perseverance. I would also like to thank them for their understanding over the years as many weekly calls were made from the lab. Ek het julle almal baie lief en dankie dat julle almal sam met my gestap het duur die proses.

My sincere gratitude goes to my lab mates, friends, and peers. Your camaraderie, friendships and overall ridiculous shenanigans have made the sad science days tolerable. I would like to specifically thank my lab mate and friend Kate Mistretta, who has been through all the highs and lows with me. Words can never truly capture how much of an impact you have had on my life. I would also like to specifically thank Sabine Hahn for all her physical, emotional, and mental support over the years. My deepest appreciation goes to my roommate and friend Athenia Jones for agreeing to live with me for the past couple of years, for always being willing to listen and provide support, and for understanding and joining me in my gremlin ways.

Words cannot adequately express the depth of my gratitude and appreciation to my lovely one Ari Athair. My lovely one Ari. For all the late night phone calls and peptalks, and for being sunshine on the rainy days. I am truly so thankful for the entire Athair family for all their love and support over the few years.

I would like to thank all the short legged long torso pupperonies, Seneca, Wadi, and Grumpy who have offered emotional support over the past 6 years.

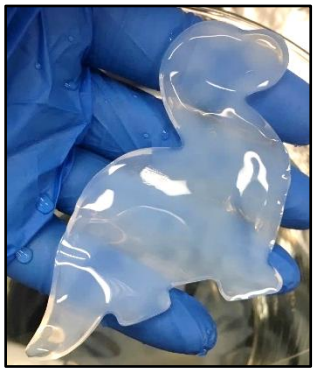

Finally, I must acknowledge the cellulose dinosaur who has joined me on all my poster presentations, podium talks, patent applications, and my dissertation defense.

Table of Contents

Table of Figures

Table of Tables

Abbreviations

AMP: Antimicrobial Peptides
ANOVA: analysis of variance
ATCC: American Type Culture Collection
BC: bacterial-derived cellulose
Bcs: bacterial cellulose synthase
CBDs: Cellulose Binding Domains
CBPs: Cellulose Binding Peptides
CP-MAS: Cross-Polarization Magic Angle Spinning
EGF: epidermal growth factor
FBS: Fetal bovine serum
FGF: fibroblast growth factor
HS: Hestrin Schramm
HSD: honest significance test
K.: Komagataeibacter
μ_{max}: maximum growth rate
NHDF: normal human dermal fibroblast
NMR: nuclear magnetic resonance spectroscopy
PEG: poly(ethylene glycol)
PHEMA: poly(2-hydroxyethyl methacrylate)
PMMA: poly(methyl methacrylate)
PPP: pentose phosphate pathway
SAXS: Small-angle X-ray scattering
SD: standard deviation
SEM: Scanning electron microscopy
TCP: Tissue culture plastic
WAXS: wide-angle X-ray scattering

Previous Publications

van Zyl, E. M., & Coburn, J. M. (2019). Hierarchical structure of bacterial-derived cellulose and its impact on biomedical applications. *Current Opinion in Chemical Engineering*, *24*, 122-130.

van Zyl, E. M., Kennedy, M. A., Nason, W., Fenlon, S. J., Young, E. M., Smith, L. J., ... & Coburn, J. M. (2023). Structural properties of optically clear bacterial cellulose produced by Komagataeibacter hansenii using arabitol. *Biomaterials Advances*, *148*, 213345.

Abstract

By 2030, one in six people worldwide will be over the age of 60. With this aging population and the increased prevalence of antibiotic-resistant bacteria, the prevalence of chronic wounds is of great concern. Chronic wounds, or those that fail to complete the normal wound healing process within three months, affect 2.4 to 4.5 million people annually in the United States alone. Chronic wounds house senescent cell populations with impaired proliferative and secretory capacities, making them unresponsive to conventional wound healing signals. In at least 90% of chronic wounds, this lack of wound healing activity allows invading pathogens to access the wound site and flourish in the moist, nutrient-rich wound bed. Bacterial cellulose (BC), synthesized by *Acetobacter* species, is a pure biopolymer with a nanofibrous network architecture comparable to human extracellular matrix. BC has been proposed as a wound dressing due to its biocompatibility, ability to provide a moist environment, high liquid absorption capabilities, and oxygen diffusion properties. Additionally, BC's native fibrillar structure and extensive hydrogen bonding is believed to effectively scavenge reactive oxygen species from the wound bed, resulting in increased wound healing and reepithelization. However, its lack of wound visualization capabilities and antibacterial surface functionality limits its clinical effectivity.

In this thesis, we aimed to address these identified limitations. To address the lack of material transparency, we developed a novel method for producing BC by investigating alternative culture supplements. Increasing ratios of D-arabitol/D-glucose in culture showed increased material transparency, irrespective of cellulose yield and thickness. Increased optical transparency values of the synthesized BC were observed compared to commercially available transparent hydrogel wound dressings. The fibrillar and overarching hierarchical BC structures were investigated to elucidate the mechanism behind this induced transparency. We identified no differences in crystallinity between BC samples but did observe decreased microfiber width. Liquid absorption capabilities were assessed to determine the effects of increased transparency and altered microstructure on the material functionality. Though decreased liquid absorption capabilities of BC with higher transparency were observed, all BC samples had higher absorption values than commercially available foam-based and hydrogel-based dressings. Overall, the increased transparency increases BC's potential use application without compromising the effectiveness of BC's inherent wound healing capabilities. To address BC's lack of antibacterial surface functionality, we designed bifunctional chimeric peptides to functionalize the BC surface by combining cellulose binding peptides (CBPs) with antimicrobial peptides (AMPs), specifically KR-12. By linking the two functional peptides, the peptide solutions exhibited decreased antibacterial activity but increased cellulose binding capabilities compared to the individual unlinked AMP and CBP peptides. The functionalized BC material exhibited active surface antibacterial activity while maintaining biocompatibility *in vitro*.

In summary, we developed a method for producing bacterial derived cellulose materials with tunable transparency while maintaining the inherent wound healing capabilities associated with native BC. Further, we designed and evaluated chimeric peptide sequences for retained surface antibacterial activity once tethered to the BC surface. The primary scientific contribution of this work is the development of transparent native BC materials for use in a broader range of applications that are not limited to chronic wound care. Additionally, the investigation of novel chimeric peptide design provides insights into more advanced means of antibacterial treatment without the use of antibiotic agents.

1. Chapter 1: Overview

1.1. Introduction

Increasing concern lies in the danger of chronic wounds due to an aging population and the widespread rise of antibiotic resistance [1]. In the US, chronic wounds affect 2.4-4.5 million people, resulting in a yearly direct Medicare cost of over $13.5 billion [1, 2]. Chronic wounds fail to progress through the normal healing process within three months. They are classified into four categories based on location, depth, and appearance (arterial ulcers, diabetic ulcers, pressure ulcers, and venous ulcers). However, all chronic wounds share standard features, including excessive levels of proinflammatory cytokines, persistent infection, and senescent cell populations [3].

Due to the open nature and impaired wound healing capabilities of chronic wounds, moist wound dressings that provide a protective barrier are required. Chronic wounds are traditionally treated with hydrocolloid and non-adherent foam-based dressings, while more advanced approaches include polysaccharide-based wound dressings such as chitosan, chitin, alginate, and hyaluronic acid [4]. These cutaneous wound treatments generally lack effective antibacterial properties, become adhered to the wound, or require multiple dressing changes to ensure adequate absorption of excess exudate, often resulting in maceration of the wound site [5-10]. Wound infection, the leading cause of wound-related morbidity, is routinely diagnosed through changes in the appearance of the wound [11]. Therefore, improved transparency and visualization with the primary wound dressings in place facilitates early infection detection while reducing the number of wound dressing changes required. Wound infection control is currently addressed with wound debridement and application of antiseptics or antibiotics, though these are toxic to mammalian cells and promote the development of antibiotic resistant bacteria [12].

Bacterial-derived cellulose (BC) has been studied for wound dressing applications due to its biocompatibility, water holding capacity, liquid/gas permeability, and handleability properties [3, 4, 13]. Although BC has been studied as a dressing material for cutaneous wounds, to date, antibacterial properties and transparency have yet to be effectively incorporated as a property of cellulose material [14]. BC,

predominantly produced by *Acetobacter* species, is formed at the air-liquid interface of static culture [15]. Evidence exists that the production of pure transparent BC is possible by altering the cellulose fibrillar morphology and hierarchical structure through altered medium and culture conditions, warranting further investigation [16-19].

Cationic antimicrobial peptides (AMPs), such as LL-37 and its analog KR-12, offer a promising alternative to the growing concern of antibiotic resistance [20]. Though the narrow therapeutic ratio of AMPs in solution hinders their clinical use, AMP immobilization has been shown to decrease mammalian cell cytotoxicity and increase *in vitro* stability without compromising the AMP's antimicrobial activity [21-23]. Cellulose binding peptides (CBPs, also called cellulose binding domains/modules) interact with and bind to the cellulose surface to bring the hydrolytic region of enzymes such as cellulase into proximity with the cellulose surface [24]. CBPs provide a mechanism for immobilizing AMPs to the surface of BC, overcoming the limitation attributed to mammalian cytotoxicity and aiding in the prevention of wound infection [11, 25-27].

1.2. Overall objective

The overall objective of this work was to develop a method for making transparent bacterial-derived cellulose (BC), modify BC with chimeric AMPs, and assess the bioactivity.

This dissertation was separated into two specific aims to achieve this objective and develop a more clinically relevant cellulose-based wound dressing. We evaluated the effects of altered in culture carbon sources on overall material transparency in **Specific Aim 1**. Ultimately using varying concentrations of arabitol/glucose to produce BC with tunable transparency and evaluated the fibrillar/hierarchical structure and morphology of the resultant altered material properties. In **Specific Aim 2**, we designed and evaluated chimeric CBP-AMP peptides and investigated their bioactivity after non-covalently tethered to the BC surface. Additionally, we evaluated the mammalian cellular response to the peptide functionalized BC. The expected outcome of this dissertation was a novel method for the formation of transparent cellulose and to

design and determine the therapeutic effectivity of CBP-AMP surface functionalized BC through antimicrobial and cytotoxicity assessments.

1.3. Specific Aim 1: Develop and characterize optically clear cellulose.

The objective of this aim was to develop optically clear BC materials utilizing arabitol as a carbon source and characterize the resulting changes to structural and physical properties. In **Aim 1.1**, we sought to form transparency BC by using arabitol as a primary carbon source and harnessing an alternative metabolic pathway. Bacterial growth, cellulose yield, and material transparency were assessed for culture conditions containing different concentrations of glucose/arabitol. In **Aim 1.2**, we sought to elucidate the mechanism of increased transparency by assessing the fibrillar morphology and hierarchical structure of the altered cellulose. In **Aim 1.3**, the effectivity of transparent BC as a wound dressing was assessed through biocompatibility assays and the comparison of liquid retention capabilities compared to commercially available wound dressing materials. The outcome of this aim was the development of a BC material with optical clarity comparable to transparent commercially available wound dressings and determine the overall structure of the material.

1.4. Specific Aim 2: Characterize CBP-AMP bioactivity on the BC surface.

The objective of this aim was to determine the structure and activity of chimeric CBP-AMP peptides and then assess the bioactivity of BC functionalized with the chimeric peptide. In **Aim 2.1**, the peptide secondary and amphiphilic structure was characterized using both modeling and experimental techniques. In **Aim 2.2**, the bioactivity of the chimeric peptides' CBP and AMP regions was assessed via cellulose binding, mammalian cell biocompatibility, anti-bacterial, and endotoxin binding assays of the chimeric peptide sequences in solution. Aim 2.3 assessed the bioactivity of the chimeric peptide sequences tethered to BC for biocompatibility and antibacterial activity. The outcome of this aim was that critical structural components and known bioactivity of the cationic AMP and CBP are retained in the chimeric CBP-AMP peptide sequence, both in solution and tethered to BC.

Overall, this work capitalized on BC's existing favorable wound dressing properties while incorporating visualization capabilities and effective antibacterial activity to develop an ideal BC-based chronic wound dressing.

1.5. References

[1] R.G. Frykberg, J. Banks, Challenges in the treatment of chronic wounds, Advances in wound care 4(9) (2015) 560-582.
[2] S.R. Nussbaum, M.J. Carter, C.E. Fife, J. DaVanzo, R. Haught, M. Nusgart, D. Cartwright, An economic evaluation of the impact, cost, and medicare policy implications of chronic nonhealing wounds, Value in Health 21(1) (2018) 27-32.
[3] R. Zeng, C. Lin, Z. Lin, H. Chen, W. Lu, C. Lin, H. Li, Approaches to cutaneous wound healing: basics and future directions, Cell and tissue research 374(2) (2018) 217-232.
[4] A. Khalid, R. Khan, M. Ul-Islam, T. Khan, F. Wahid, Bacterial cellulose-zinc oxide nanocomposites as a novel dressing system for burn wounds, Carbohyd. Polym. 164 (2017) 214-221.
[5] A.L.R. Pires, Â.M. Moraes, Improvement of the mechanical properties of chitosan-alginate wound dressings containing silver through the addition of a biocompatible silicone rubber, Journal of Applied Polymer Science 132(12) (2015).
[6] C. Longinotti, The use of hyaluronic acid based dressings to treat burns: A review, Burns & trauma 2(4) (2014) 162-168.
[7] J. Voigt, V.R. Driver, Hyaluronic acid derivatives and their healing effect on burns, epithelial surgical wounds, and chronic wounds: A systematic review and meta-analysis of randomized controlled trials, Wound repair and regeneration 20(3) (2012) 317-331.
[8] J. Hilton, D. Williams, B. Beuker, D. Miller, K. Harding, Wound dressings in diabetic foot disease, Clinical infectious diseases 39(Supplement_2) (2004) S100-S103.
[9] G. Dabiri, E. Damstetter, T. Phillips, Choosing a wound dressing based on common wound characteristics, Advances in wound care 5(1) (2016) 32-41.
[10] H.W. Lim, S.A. Collins, J.S. Resneck Jr, J.L. Bolognia, J.A. Hodge, T.A. Rohrer, M.J. Van Beek, D.J. Margolis, A.J. Sober, M.A. Weinstock, The burden of skin disease in the United States, Journal of the American Academy of Dermatology 76(5) (2017) 958-972. e2.
[11] L.D. Lozeau, J. Grosha, D. Kole, F. Prifti, T. Dominko, T.A. Camesano, M.W. Rolle, Collagen tethering of synthetic human antimicrobial peptides cathelicidin LL37 and its effects on antimicrobial activity and cytotoxicity, Acta biomaterialia 52 (2017) 9-20.
[12] H. Ullah, H.A. Santos, T. Khan, Applications of bacterial cellulose in food, cosmetics and drug delivery, Cellulose 23(4) (2016) 2291-2314.
[13] P. Muangman, S. Opasanon, S. Suwanchot, O. Thangthed, Efficiency of microbial cellulose dressing in partial-thickness burn wounds, The Journal of the American College of Certified Wound Specialists 3(1) (2011) 16-19.
[14] E.M. van Zyl, J.M. Coburn, Hierarchical structure of bacterial-derived cellulose and its impact on biomedical applications, Curr. Opin. Chem. Eng. 24 (2019) 122-130.
[15] S.S. de Souza, F.V. Berti, K.P. de Oliveira, C.Q. Pittella, J.V. de Castro, C. Pelissari, C.R. Rambo, L.M. Porto, Nanocellulose biosynthesis by Komagataeibacter hansenii in a defined minimal culture medium, Cellulose 26(3) (2019) 1641-1655.
[16] S. Wang, T. Li, C. Chen, W. Kong, S. Zhu, J. Dai, A.J. Diaz, E. Hitz, S.D. Solares, T. Li, Transparent, anisotropic biofilm with aligned bacterial cellulose nanofibers, Adv. Funct. Mater. 28(24) (2018) 1707491.
[17] N. Yin, M.D. Stilwell, T.M. Santos, H. Wang, D.B. Weibel, Agarose particle-templated porous bacterial cellulose and its application in cartilage growth in vitro, Acta biomaterialia 12 (2015) 129-138.

[18] M. Rezazadeh, V. Babaeipour, E. Motamedian, Reconstruction, verification and in-silico analysis of a genome-scale metabolic model of bacterial cellulose producing Komagataeibacter xylinus, Bioprocess and Biosystems Engineering (2020) 1-10.
[19] B. Jacob, I.S. Park, J.K. Bang, S.Y. Shin, Short KR-12 analogs designed from human cathelicidin LL-37 possessing both antimicrobial and antiendotoxic activities without mammalian cell toxicity, Journal of Peptide Science 19(11) (2013) 700-707.
[20] R.E. Hancock, H.-G. Sahl, Antimicrobial and host-defense peptides as new anti-infective therapeutic strategies, Nature biotechnology 24(12) (2006) 1551-1557.
[21] L.D. Lozeau, J. Grosha, I.M. Smith, E.J. Stewart, T.A. Camesano, M.W. Rolle, Alginate Affects Bioactivity of Chimeric Collagen Binding LL37 Antimicrobial Peptides Adsorbed to Collagen-Alginate Wound Dressings, ACS Biomater. Sci. Eng. (2020).
[22] J. Kang, M.J. Dietz, B. Li, Antimicrobial peptide LL-37 is bactericidal against Staphylococcus aureus biofilms, PLoS One 14(6) (2019).
[23] E.J. Jervis, C.A. Haynes, D.G. Kilburn, Surface diffusion of cellulases and their isolated binding domains on cellulose, Journal of Biological Chemistry 272(38) (1997) 24016-24023.
[24] R. Weishaupt, J.N. Zünd, L. Heuberger, F. Zuber, G. Faccio, F. Robotti, A. Ferrari, G. Fortunato, Q. Ren, K. Maniura-Weber, Antibacterial, Cytocompatible, Sustainably Sourced: Cellulose Membranes with Bifunctional Peptides for Advanced Wound Dressings, Advanced Healthcare Materials (2020) 1901850.
[25] N. Khazanov, T. Iline-Vul, E. Noy, G. Goobes, H. Senderowitz, Design of compact biomimetic cellulose binding peptides as carriers for cellulose catalytic degradation, The Journal of Physical Chemistry B 120(2) (2016) 309-319.
[26] E.Y. Kim, G. Rajasekaran, S.Y. Shin, LL-37-derived short antimicrobial peptide KR-12-a5 and its d-amino acid substituted analogs with cell selectivity, anti-biofilm activity, synergistic effect with conventional antibiotics, and anti-inflammatory activity, European journal of medicinal chemistry 136 (2017) 428-441.
[27] M. Gullo, S. La China, P.M. Falcone, P. Giudici, Biotechnological production of cellulose by acetic acid bacteria: current state and perspectives, Appl. Microbiol. Biot. 102 (2018) 6885-6898.

2. Chapter 2: Background

Excerpts from the following chapter appear in van Zyl, E. M., and Coburn, J. M. "Hierarchical structure of bacterial-derived cellulose and its impact on biomedical applications." *Current Opinion in Chemical Engineering* 24 (2019): 122-130 and is reproduced here with permission from Elsevier. These sections are denoted by an asterisk (*).

2.1. Prevalence of Chronic Wounds

By 2030, one in six people worldwide will be over the age of 60 [1]. The worldwide aging population, high prevalence of lifestyle-related diseases known for impairing wound healing, such as obesity and diabetes, along with the ever-emerging occurrence of intrinsic and acquired antibiotic resistance makes the prevalence of chronic wounds of great concern [2, 3]. Each year, approximately 14 million Americans are diagnosed with skin and soft tissue infections, and cutaneous infections have been determined to be the root cause of 31% of skin disease-related deaths [4-6]. Chronic wounds pose a significant burden to both the healthcare system and patient, as it is estimated that treatment of a single chronic ulcer costs upwards of $50,000 [7]. In at least 90% of chronic wounds, impaired wound healing activity allows invading pathogens to access the wound site and flourish in the moist, nutrient-rich wound bed [8]. Upwards of two hundred different species can flourish in a single chronic wound, including species known for biofilm production and inherent or acquired antibiotic resistance [9].

2.1.1. Anatomy and Physiology of Skin

From a physiological standpoint, the skin performs vital functions such as protection against physical, chemical, and biological assailants, thermoregulation, and prevention of excess water loss [10]. Cutaneous skin is a continuous lining of the body's surface and can be divided into the epidermis, dermis, and subcutaneous tissue [11, 12].

The epidermis can be divided further into four layers according to the keratinocyte morphology and position: the stratum basal cell layer (stratum germinativum), the squamous cell layer (stratum spinosum), the granular cell layer (stratum granulosum), and the cornified horny cell layer (stratum

corneum) [13]. This layer provides mechanical protection of the lower epidermis and prevents water loss and invasion of foreign pathogens [10]. Protein-rich cells are surrounded by a continuous extracellular lipid matrix that provides waterproofing and barrier functions [14]. Additionally, the epidermis houses melanocytes for DNA protection from ultraviolet light, Merkel cells for detection of tactile sensation, and Langerhans cells for immunoprotection [10].

The semi-permeable barrier between the dermis and epidermis, labeled the dermal-epidermal junction, structurally supports the epidermis while establishing cell polarity and growth direction [14]. The dermis consists of amorphous connective tissue that is vascularized, innervated, and contains epidermally derived appendages, fibroblasts, macrophages and mast cells [10]. The dermis, comprised of collagen and elastin, protects the body from mechanical injury, thermal changes, and includes receptors of sensory stimuli [14]. Dermal vasculature plays a key role in thermal regulation [15]. In disease states, such as obesity and diabetes, impaired and delayed cutaneous vasculature response has been observed [16]. In obese patients ineffective collagen deposition has also been noted along with impaired barrier functions [17].

2.1.2. Wound Healing Mechanism and Chronic Wounds

The normal skin wound healing mechanism is a linear process comprised of 4 main stages: hemostasis, inflammation, proliferation, and remodeling (**Figure 2.1**) [18, 19]. Hemostasis starts immediately after the wound is incurred. Vasculature is constricted, a fibrin clot is formed, and pro-inflammatory cytokines and growth factors are released [19]. Chemotaxis of inflammatory cells occur once the bleeding is controlled, and the wound healing process moves into the inflammatory phase. The inflammation phase is characterized by the infiltration and function of neutrophils, macrophages, and lymphocytes [20-22]. Neutrophils clear the wound area of cellular debris and invading microbes, while macrophages help to clear apoptotic cells, release cytokines, and promote the transition to the proliferative phase [23, 24]. The proliferation phase overlaps with the end of the inflammation phase, as fibroblasts start to promote collagen and granulation tissue formation for extra-cellular matrix (ECM) synthesis [20, 22]. Wound healing then progresses into the remodeling phase, where ECM is degraded, reorganized,

resynthesized, and granulation tissue is remodeled to achieve maximum tensile strength through scar tissue formation [18, 19].

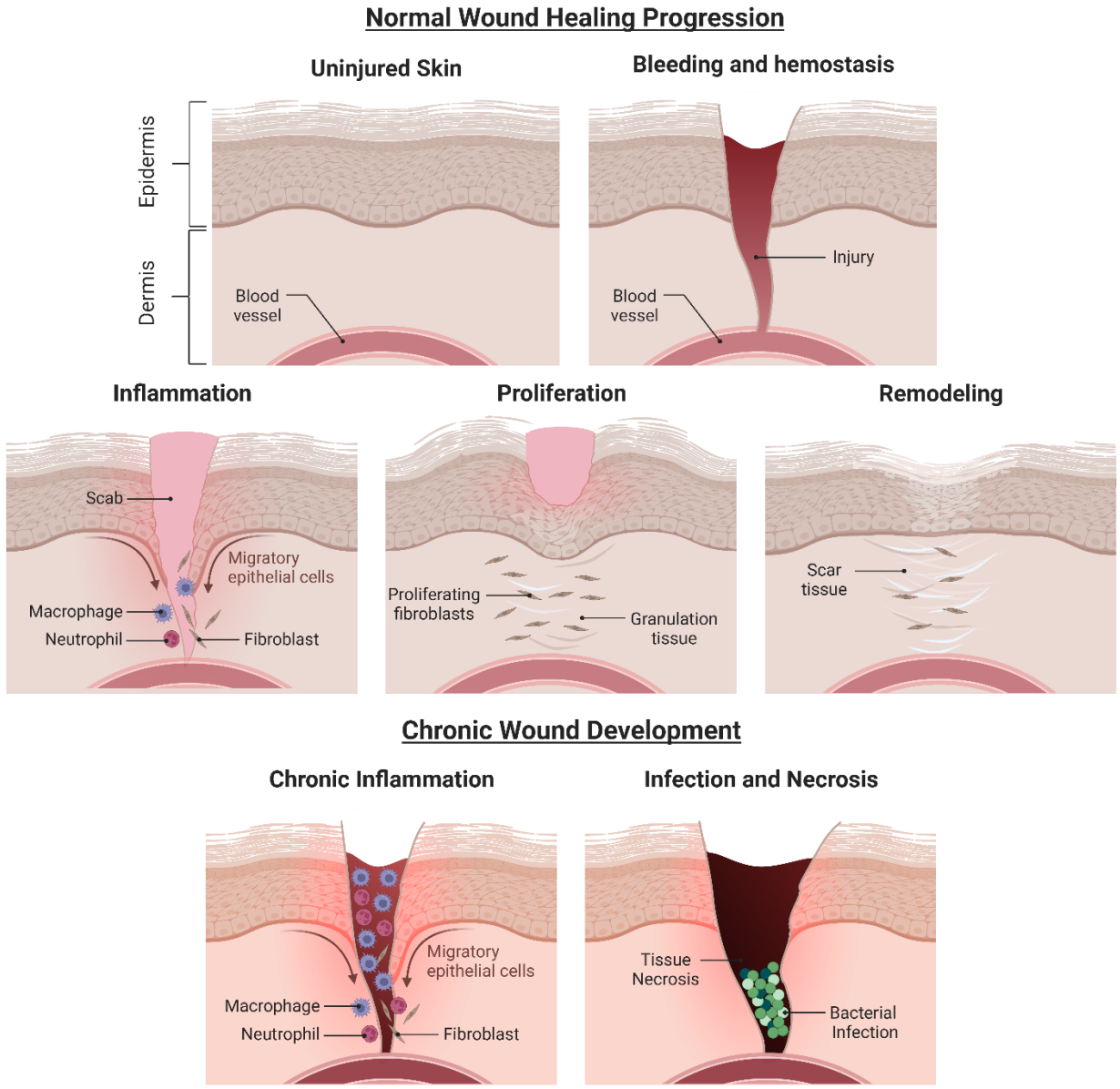

Figure 2.1. Normal and chronic wound healing progression.
Made using biorender.com

Chronic wound development is typically driven by systemic factors such as age, disease state (diabetes, keloids, hereditary healing disorders), medications, and overall nutrition [19, 25]. These systemic conditions affect local wound site factors such as oxygenation, infection, and venous sufficiency which are known to impair wound healing. Chronic wounds are marked as wounds that do not heal within 3 months

[26-29]. Though chronic wounds are diagnosed through long term inability to progress through normal wound healing pathways, impaired wound healing capabilities can be identified on a molecular level as early as 6 hours post injury [30]. Chronic wounds are marked by increased oxidative stress, elevated H_2O_2 producing enzymes, lack of antioxidant pathways, and subsequent high levels of reactive oxygen species (ROS), shortly after injury [30, 31]. High levels of ROS in the wound bed result in further tissue damage and elevated production of pro-inflammatory cytokines, preventing healing progression out of the inflammation phase [32]. Along with chronic inflammation, the combined presence and activity of cell types typically present in more distinct phases of wound healing is indicative of the dysregulated activity in the wound bed [30]. Neutrophils are typically only present during early stages of normal wound healing, however in chronic wounds the stay present and secrete myeloperoxidase that converts ROS such as H_2O_2 into various types of hypohalous acids causing further damage to an already fragile wound bed [33]. Simultaneously, growth factor degradation occurs in the wound site as prolonged inflammation leads to higher levels of ECM degrading matrix metalloproteases (MMPs) and decreases in protease inhibitors [34, 35]. ECM analysis of chronic wounds also identified fibrin cuffs around wound bed vasculature and an overall increase in degraded ECM and its contributing components [36]. Various factors are secreted that prevent the proliferation and migration of keratinocytes and fibroblasts, inducing senescent cell populations in the wound bed, effectively stopping any active attempts at wound closure [37]. Further, tissue necrosis is commonly observed due to insufficient vascular and chronic hypoxia in the wound bed [38]. This lack of wound closure and wound healing activity allows for invading pathogens to access the wound site and flourish in the moist nutrient rich wound bed [39]. *Staphylococcus aureus* (*S. aureus*) is the main microbe found to cause early stage wound infections. As infection continues, additional bacteria such as *Escherichia coli* (*E. coli*) and *Pseudomonas aeruginosa* (*P. aeruginosa*) infiltrate the wound site [40].

2.1.3. Chronic Wound Treatment, Limitations, and Alternative Approaches

Traditional means of treating chronic wounds consist of surgical debridement and non-adherent foam-based dressings that absorb excess exudate from the wound [2]. Non-adherent foam-based dressings

require frequent dressing changes, and are not transparent, allowing for increased exposure time to infectious pathogens [39, 41, 42]. Over the last two decades, the parameters of an ideal wound dressing have shifted towards dressings that promote moist environments. An ideal wound dressing is described as one that is biocompatible, provides a moist environment, non-adhesive, antibacterial, transparent, allows for oxygen diffusion, removes excess exudate, and has facile painless removal capabilities [25, 43-45]. These parameters have been identified to allow for increased wound healing, while transparency allows medical professionals to clinically assess the wound site for size, redness, margins, maceration, inflammation, cellulitis, or purulent exudate [46]. Additionally, wound site infections are predominantly diagnosed in response to visual changes of the wound site. Further motivating the need for transparent wound dressing materials that allow for wound visualization without disrupting the fragile wound bed [46].

Hydrocolloid dressings, predominantly comprised of carboxymethyl cellulose, have become prominent in wound dressing applications due to their cost effectiveness, their semi-permeability to liquid/gases, and because they facilitate autolytic debridement [25, 47]. Wounds treated with hydrocolloid dressings have shown a statistically significant increase in wound healing compared to treatment with sterile gauze [48]. Hydrocolloid dressings, however, require frequent dressing changes for exudative wounds, resulting in exposure to invading microbes, and are known to cause contact dermatitis [25, 47]. More advanced dressing materials have been developed and can be broken up by synthetic and natural derived materials [25]. Synthetic materials include poly(lactide-co-glycolide) (PLGA), polyurethane, polyethylene glycol (PEG), and polycaprolactone [49]. As a whole, synthetic materials are reproducible and easily manufactured, but many times their properties fail to match the structure of native ECM and they can become adherent to the wound [49]. Additionally, synthetic materials can trigger a foreign body response and have been associated with the stimulation of chronic inflammation, toxicity, and immunological reactions in the wound site [50]. Natural materials such as chitosan, chitin, alginate, collagen, hyaluronic acid and cellulose based wound dressings have been highly researched in recent years [25, 49]. These materials are biocompatible and their natural structure mimics that of native ECM [49, 50]. Chitosan and

chitin wound dressings have been shown to have antibacterial properties and aid in hemostatic effectivity, but they are mechanically weak and have poor handleability properties [25, 51]. Derived from algae, alginate is effective in dressing highly exudating wounds but has also been found to cause adverse effects such as dehydration of the wound bed, upregulation of pro-inflammatory cytokine secretion, and cytotoxicity towards NK cells [52-54]. Collagen wound dressings have been shown to promote tissue granulation and angiogenesis in the wound bed, although in some studies wound healing was not accelerated compared to conventional dressing materials [55]. Additionally, collagen has been shown to increase the production of inflammatory cytokines at levels similar to when cells are exposed to LPS [54]. Hyaluronic acid (HA) dressings promote mesenchymal and epithelial cell migration which in turn improves collagen deposition in the wound site [56]. However, HA dressings are molecular weight sensitive where low molecular weight is pro-inflammatory and high molecular weight inhibits nutrient supply to the wound site [57, 58]. Bacterial derived cellulose (BC), a natural biopolymer, provides a promising material for wound dressing applications. BC is a readily available biopolymer with several intrinsic properties that make it a promising material for wound dressing applications. Most notably BC is biocompatible, is able to retain moisture, absorb excess wound exudate, and scavenge ROS resulting in increased granulation tissue formation [59, 60].

2.2. Bacterial Derived Cellulose as a Biomaterial

2.2.1. Bacterial Cellulose Introduction

* Cellulose is produced by plants, bacteria (*acetobacter*, *acanthamoeba*, and *achromobacter spp*.), algae (*valonia*, *chaetamorpha spp.*) and fungi [61-63]. In plants, cellulose is the structural component of plant cell walls and the fibers of cotton [64]. Due to its relative abundance and inexpensive nature, cellulose has become a prominent material for biomaterial research applications. Plant cellulose, however, is synthesized in a matrix of contaminant molecules, namely hemicelluloses, lignin, and pectin [65]. The percentage of cellulose found in plant materials ranges from 50% to 90%, necessitating purification through time consuming and costly chemical processing that results in low cellulose yields [64]. The additional cost

and production steps required to purify plant-based cellulose limits its utilization in biomedical applications [65]. Alternatively, bacterial-derived cellulose (BC) has been identified as a high-quality pure cellulose, synthesized and organized as twisted ribbons of micro-fibril bundles, requiring minimal purification processing [66]. BC was first identified in 1886 by A.J. Brown who observed "a jelly-like translucent mass on the surface of the culture fluid; this growth rapidly increases until the whole surface of the liquid is covered with a gelatinous membrane" [67]. After performing composition analysis, Brown described the membrane as cellulose that was synthesized by a strain of bacteria that he named *Bacterium xylinum* [67]. A rod-shaped aerobic Gram-negative bacteria, *Bacterium xylinum* was later renamed *Acetobacter xylinum*, then *Gluconacetobacter xylinus*, and is currently classified as *Komagataeibacter xylinus* [68, 69]. Since Brown's discovery, BC has been extensively studied due to its ease of fabrication, biocompatibility, high yield strength, and water retention properties [70]. Realizing that there are other cellulose-producing microbes, this review will focus primarily on BC from *Komagataeibacter ssp.* as they are the predominantly studied strains for biomedical applications due to their high BC yield, purity, and crystallinity [71].

2.2.2. Bacterial-Derived Cellulose Synthesis

* The culture medium for cellulose-producing microbial strains consists of a nitrogen and a carbon source [72]. The carbon source is typically glucose but may also be other carbon sources, such as sucrose, fructose, mannitol, molasses, and fruit juice [73-75]. The glucose is metabolized through the pentose-phosphate pathway (PPP) or the Krebs cycle, depending on the physiological state of the culture [76]. Cellulose production is regulated by oxygen supply and is independent of carbon source concentration [77]. There are four key enzymatic steps in the synthesis of BC as outlined in **Figure 2.2A** [76].

* First, the glucose is phosphorylated by glucokinase forming glucose-6-phosphate (Glc-6-P). Glc-6-P is isomerized to glucose-1-phosphate (Glc-1-P) by phosphoglucomutase. Then uridine diphodphoglucose (UDP-Glc) is synthesized by UDP-Glc-phyrophosphorylate (UGPase), which can be utilized by cellulose synthase for cellulose synthesis [78-80]. The cellulose synthase enzymatic reaction occurs via a protein complex composed of two main bacterial-derived cellulose synthase (Bcs) subunits:

BcsA, an inner membrane protein that is the first gene in the operon encoded by bcsA; BcsB, a periplasmic protein that is anchored to the inner wall and is the binding protein for c-di-GMP during cellulose synthase activation [81]. The PPP is believed to play a role in increased production of c-di-GMP, the known activator of the cellulose synthase reaction **(Figure 2.3**) [81-83]. BcsB is required for the catalytic activity of BcsA. These two enzymes form a complex that is essential for cellulose synthesis [81, 84, 85]. Two other subunits exist: BcsC, believed to be a transmembrane pore that allows for microfibril formation by transporting glucan chains outside of the bacterium, and BcsD, a soluble protein present in the periplasmic space that plays a role in the crystallization of cellulose [85-88]. Purified BcsA and BcsB proteins are sufficient to catalyze cellulose synthesis; however, mutations in BcsC and BcsD have been shown to greatly decrease the yield of synthesized cellulose [89]. Recently, the cellulose synthesis and membrane translocation has been visualized by *in crystallo* methods providing significant understanding of the entire process that may be utilized in the future for novel polysaccharide synthesis by bacterium [82].

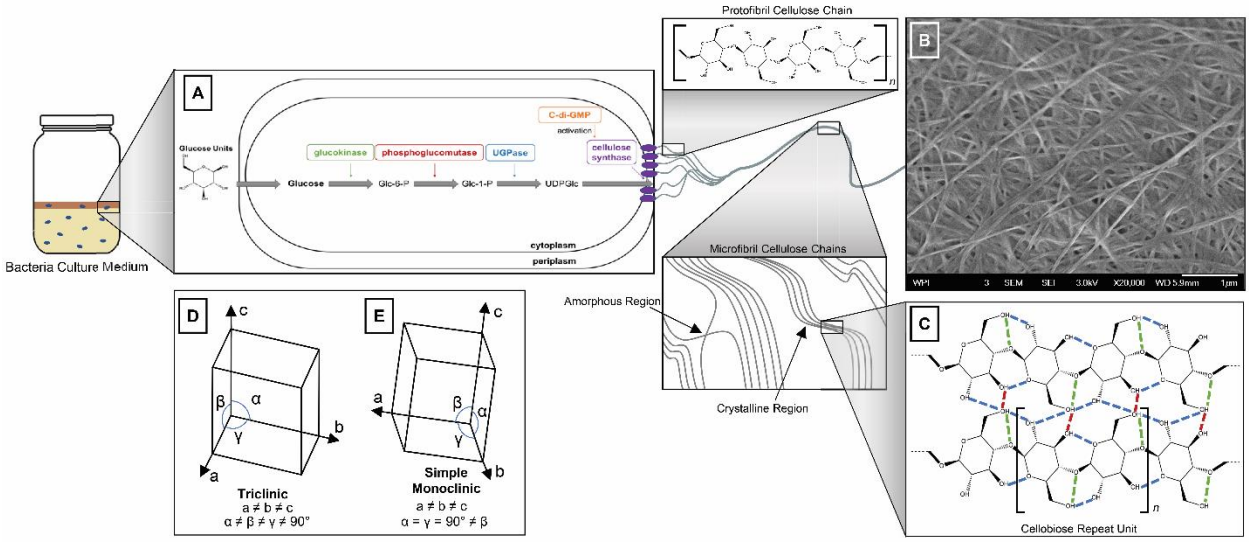

Figure 2.2. Bacterial Cellulose Synthesis and Structure

(A) Four key enzymatic steps that allow for cellulose production adapted from [80, 90], (B) scanning electron microscopy (SEM) of BC membrane showing the nanofibrous structure, (C) differences in inter and intra molecular bonds in cellulose Iα (red bonds), cellulose Iβ (green bonds), and the bonds that are in both amorphs (blue bonds) adapted from [91, 92], (D) triclinic crystal structure of cellulose Iα, (E) monoclinic crystal structure of cellulose Iβ.

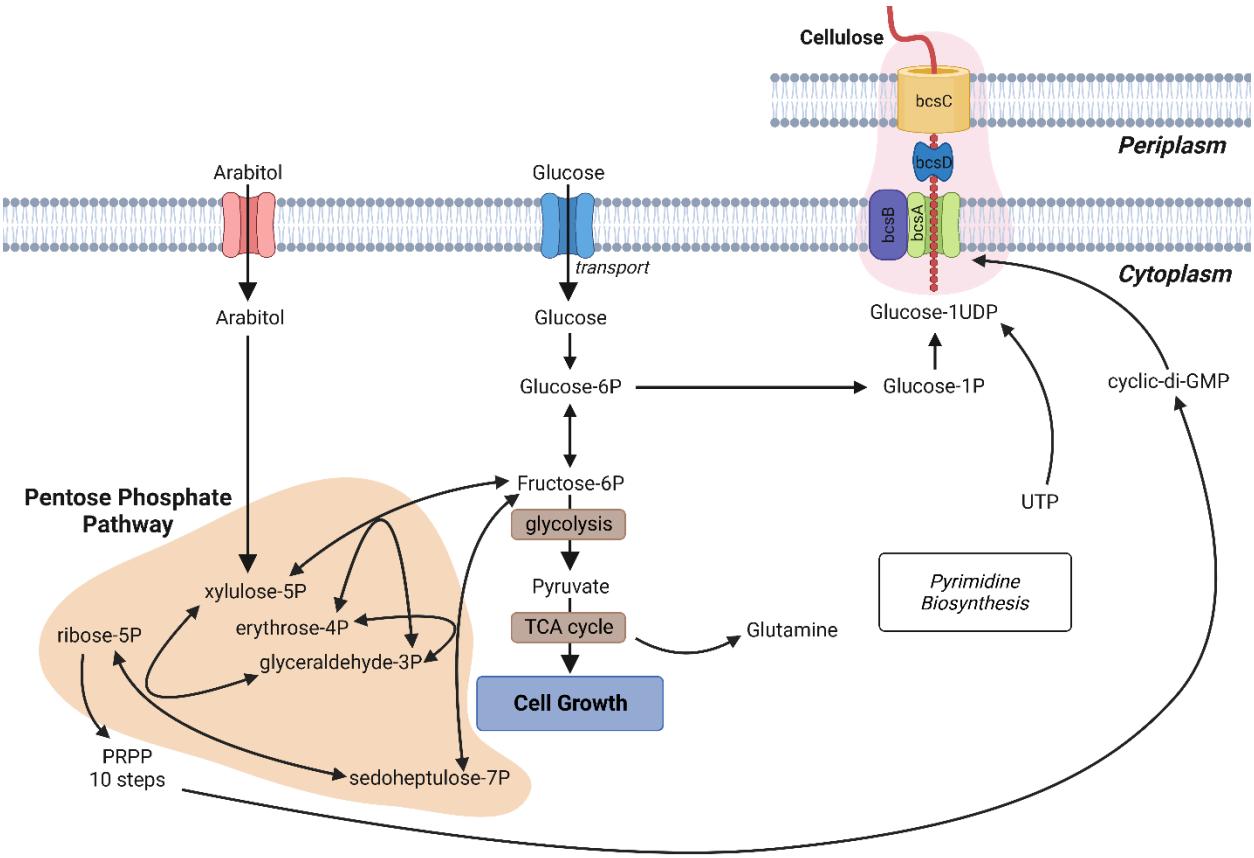

Figure 2.3. Carbon source metabolism and cellulose synthesis within the bacterium. Metabolic pathway provided by Eric M. Young. Cellulose synthase complex adapted from [93]. Made using Biorender.com

2.2.3. Bacterial-Derived Polymers and Membrane Structure

* Cellulose is a polysaccharide composed of β(1→4) linked D-glucose monomer units present as pyranose rings, a cyclic isomer that has five carbons and one oxygen in a ring of six atoms (**Figure 2.2C**). Cellulose synthesis occurs inside the bacterium and is extruded as ribbon-like microfibers between the outer and cytoplasmic membranes at a rate of 2 μm/min [94, 95]. These 1.5 nm wide microfibers have the correct conformation that allows for bacterium-directed self-assembly into bundles of microfibrils that range between 30-50 nm in diameter as shown in **Figure 2.2B** [95, 96]. The presence of several hydroxyl groups with similar reactivity and significant hydrogen bonding allows for the formation of insoluble cellulose polysaccharide chains [89, 97]. Inter- and intra-chain hydrogen bonds allow for the formation of stiffened polysaccharide chains held together by weak van der Waals forces and form layered sheets of cellulose

[91]. These cellulose sheets are reinforced by dispersion forces between the stacked heterocyclic monomers rings [76].

* Bacteria can produce both the cellulose I and cellulose II structure, or parallel and anti-parallel cellulose chains, respectively; though cellulose I is predominantly formed [98]. The cellulose II structure is primarily observed when cellulose I is mercerized, or alkali treated to break bundled fibers down into microfibrils, then reassembled which produces a more thermodynamically stable structure [76, 99, 100]. Cellulose I is further broken down into two different amorph structures: cellulose Iα and cellulose Iβ. Cellulose Iα is a meta-stable phase of cellulose I with a triclinic unit cell (**Figure 2.2D**), while cellulose Iβ is a stable phase of cellulose with a two chain monoclinic unit cell (**Figure 2.2E**) [101]. When cellulose fibers are extruded from the bacterium they orient randomly so the overall cellulose structure swaps and alternates between the different amorph phases of cellulose [91]. Cellulose Iα exhibits intra-molecular hydrogen bonding between O_3–H→O_5' and inter-molecular hydrogen bonding between O_6–H→O_3', while cellulose Iβ exhibits intra- and inter-molecular hydrogen bonding between O_6'→H–O_2' as shown in **Figure 2.2C** [91]. Using high resolution solid-state carbon-13 nuclear magnetic resonance (^{13}C NMR) to study the structure of cellulose Iα and cellulose Iβ, Vanderhart et al. showed that cellulose Iα has singlets, or paired electrons, at the C-1 and C-6, and a closely spaced doublet, or an unpaired electron, at C-4 while cellulose Iβ has doublets at C-1, C-4, and C-6 [102, 103]. These NMR observations, along with the findings that cellulose Iβ is formed irreversibly from cellulose Iα, which requires energy input into the system, indicates that cellulose Iβ is more thermodynamically stable than cellulose Iα [91, 104]. BC has the highest concentration of cellulose Iα polymorph at 70%. Because cellulose Iα is meta-stable, BC is less thermodynamically stable than other types of cellulose that have an increased percentage of cellulose Iβ [105, 106].

2.2.4. Culture Conditions and Cellulose Structure

* *Komagataeibacter xylinus* may be cultured under static or dynamic culturing conditions that result in the formation of a variety of material structures. Under static culturing, flat cellulose pellicles form

at the air-liquid interface of the culture system as shown in **Figure 2.4A**. Since the cellulose forms at the air-liquid interface under static conditions, a variety of form factors can be fabricated based on oxygen exposure including hollow tubes and transparent soft cellulose [107, 108]. Alternatively, in agitated culturing aggregated cellulose shapes form as shown in **Figure 2.4B**; the shape of the cellulose material formed varies depending on the bacteria strain [109, 110]. Toyosaki et al. determined that some strains of *Acetobacter* were more suited for agitated culture and consistently produced more stable cellulose than other strains [109]. The increased shear stress in agitated culture increases the solid material dispersion in the culture and has been seen to increase both bacteria growth and cellulose synthesis rates [109, 111]. However, mutations can occur in some strains that leads to non-cellulose producing cultures [109]. Inoculum volume, or the volume of microbe suspension used to propagate into a larger volume culture, also impacts the cellulose spheres formed. Hu et al. showed that with increased inoculum volume there is decreased space between individual bacterium, decreasing the number of cellulose spheres formed as adjacent bacteria synthesis aggregates fuse together [112].

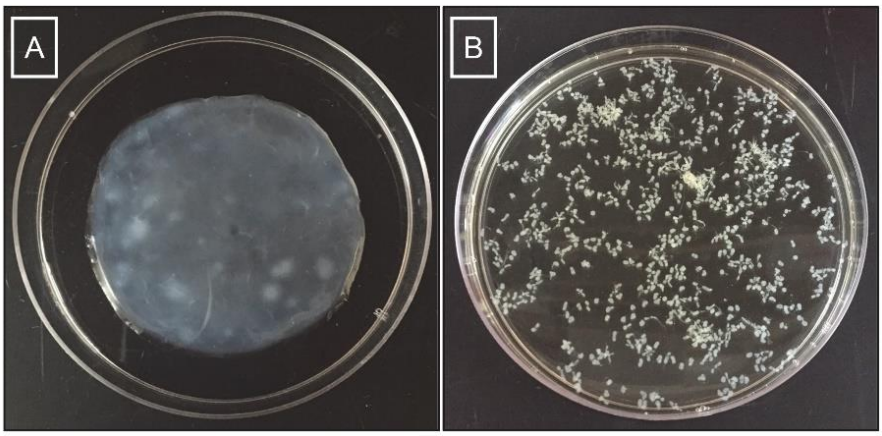

Figure 2.4. (A) cellulose membrane or pellicle, (B) cellulose aggregates.

* Tanskul et al. isolated a strain of cellulose-producing bacteria, *Rhodococcus sp.* MI 2, from ripe fruit and vegetables [113]. The bacteria were either cultured under static conditions, in a rotating shaker at 180 rpm, or with a magnetic stirrer all at 25°C. Under static conditions the cellulose produced was three-dimensional interconnected net-like structured pellicles. While under rotating conditions the cellulose produced was tapioca-pearls/irregular aggregate shapes. Under stirring conditions, the cellulose produced

was feather like shapes and aggregates [113]. The altered culturing conditions not only affected the macro-structure of the cellulose materials, it also changed the inter- and intra- molecular structure of BC. Using SEM, Watanabe et al. showed that both static and agitated culture produce cellulose that have similar fibrous structures [114]. However, X-ray diffractometry (XRD) showed that agitated culture resulted in cellulose with smaller crystal sizes, and a lower degree of polymerization, crystallinity, and cellulose Iα percentage [114]. A correlation between crystal size and percent of cellulose Iα formed was identified that suggests agitated culture interferes with the crystallization process of BC, resulting in smaller crystallite formation and thus preferentially inducing the formation of cellulose Iβ [110, 114, 115]. This indicates that under agitated culture conditions more thermodynamically stable cellulose is produced. In static culture under low culture temperatures, between 10°C and 36°C, increased cellulose Iα content has been observed [116]. In both static and agitated conditions, structural variations of BC pellicles have been observed with different cellulose producing *Komagataeibacter xylinus* strains [110]. Singhsa et al. performed XRD analysis on cellulose pellicles, produced by five different strains, harvested after seven days of culture. Three of the five strains produced cellulose with a 20% higher degree of crystallinity and an average of 1 nm larger crystallites than the other two strains. The difference in crystallite size indicates that the three strains produced less thermodynamically stable cellulose due to their increased cellulose Iα content [110].

* Changes in BC yield and marginal changes in structure have also been observed when using alternative carbon sources in the culture medium [117]. The cellulose yield, when produced using glycerol as a carbon source, was found to be 1.5 times higher than with glucose as the carbon source [117]. Using XRD, the cellulose produced with glycerol as a carbon source had a crystallinity index of 78% versus 88% with glucose as a carbon source [117]. Another study found that glucose, mannitol, and fructose resulted in a higher cellulose yield in the first 48 hours of culture as compared to glycerol and sucrose, but that glycerol and sucrose resulted in a higher cellulose yield after 96 hours of culture [118]. ^{13}C-NMR showed no difference in crystallinity, cellulose Iα, or cellulose Iβ, for cellulose produced on different carbon sources and for different incubation times. However, SEM images showed that pellicles formed with glycerol and

fructose carbon sources had a microfibril directionality not seen in the pellicles grown with other carbon sources [118]. Additionally, mannitol was found to support high cellulose yields. TGA of the samples showed that mannitol had a higher maximum decomposition temperature when compared to sucrose and thus an increased thermal stability. Increased crystallinity of cellulose produced with mannitol as a carbon source is believed to explain the thermal degradation behavior that was observed [119]. These studies are further summarized in **Table 2.1**. Additionally, Fang and Catchmark found that the use of galactose as a carbon source allows for the incorporation of non-cellulosic polysaccharides in the cellulosic network which decreased the crystallinity and crystal size of the cellulose produced [120]. This incorporation is believed to be through surface coating or self-aggregation [120]. The production of non-cellulosic polysaccharides as well as the altered structure of cellulose produced with alternative sugars as a carbon source suggests that natural molecular incorporation and hybrid cellulose formation is possible.

Table 2.1. Structural differences in BC due to altered carbon sources

Bacteria Strain	Carbon Source	Yield	Cellulose Iα (%)	Crystallinity (%)
G. xylinus (ATCC 10245) [117] * Yield calculated in comparison to 1% glucose	Glucose	100%*	-	88%
	Fructose	95%	-	86%
	Inositol	85%	-	75%
	Glycerol	155%	-	78%
G. xylinus (ATCC 53524) [118]	Fructose	1.78 g/L	61%	85%
	Glucose	1.89 g/L	62%	80%
	Glycerol	0.82 g/L	60%	80%
	Mannitol	2.04 g/L	65%	90%
G. xylinus (PTCC 1734) [119]	Mannitol	~ 5.7%	-	65.5%
	Food-grade Sucrose	1.3%	-	-
	Sucrose	2.4%	-	63.2%
	Date Syrup	4.7%	-	-
	Glucose	3.4%	-	-

* Hybrid cellulose formation is further supported by the observation that *N*-acetylglucosamine (GlcNAc) can be incorporation in the bacterial-synthesized polymer forming lysozyme-susceptible pellicles [121, 122]. Yadav et al. further indicated that GlcNAc uptake and incorporation is possible through not only innate mechanisms, as indicated by previous studies, but also by genetically engineering the bacteria.

When isolating the gene required for metabolisms of GlcNAc, molecular incorporation of GlcNAc was observed by wild type *G. xylinus* [123]. Genetically engineered *G. xylinus* expressing an operon from *Candida albicans* that allows for the production of cytoplasmic UDP-GlcNAc monomers results in the production of hybrid cellulose comprised of both glucose and GlcNAc. XRD determined that the hybrid cellulose was comprised of both cellulose Iα and cellulose II, a less crystalline cellulose amorph. Complete degradation with lysozymes further supported that GlcNAc was incorporated [124]. Having genetic control of BC production allows for not only the creation of degradable cellulose but also genetically engineering functionalized cellulose.

2.2.5. Additives and Alternative Nitrogen Sources

* As with alternative carbon sources, the nitrogen source and additives in the culture medium can also influence the structure of the cellulose formed. Shi et al. studied the effects of medium formulations on the DP of the cellulose formed by *Gluconacetobacter intermedius* BC-41. The DP of cellulose produced in A9 medium (glucose, yeast, peptone, $Na_2HPO_412H_2O$, corn syrup, acetic acid, alcohol) was 22.9% higher than that produced in Schenk and Hildebrandt (SH) medium (glucose, peptone, yeast, $Na_2HPO_412H_2O$, citric acid) [125]. The addition of 2,6-dichlorobenzonitrile, a cellulose synthesis inhibitor, promoted the production of cellulose II instead of the more commonly produced cellulose I [98]. Additionally, the most common carbon source for BC production is glucose. However, Zhong et al. determined that only 19.05% of initial cultured glucose was incorporated into cellulose while 40.03% was converted into gluconic acid byproduct [126]. This increase in gluconic acid negatively impacts cellulose production due to the decreased pH of the culture [127]. The addition of lignosulfonate inhibits gluconic acid formation in the culture allowing for increased cellulose production with increased crystallinity and decreased amorphous regions [128]. A variety of alternative additives have been tested in microbial culture to promote cellulose yield while retaining the material's unique properties. Agar, carboxymethylcellulose (CMC), microcrystalline cellulose, and sodium alginate were all individually tested to promote cellulose production

[129]. The addition of CMC resulted the production of a more thermodynamically stable cellulose amorph as well as the highest cellulose yield [129]. These studies are further summarized in **Table 2.2**.

Table 2.2. Structural differences in BC due to altered additives and nitrogen sources

Bacteria Strain	Additive/Nitrogen Source	Yield	Cellulose Iα (%)	Crystallinity Index /%	DP
G. intermedius BC-41 [125]	Schenk Hildebrant (SH) Medium	-	-	-	1613.3
	A9 Medium	-	-	-	2301.7
G. xylinus (ATCC 10245, IFO 13693, IFO 13772, IFO 13773, IFO 14815, IFO 15237) [117]	HS Medium	0.114 – 0.3036 g/30mL	43-44	3.02-3.95	-
	HS Medium + lignosulfonate	0.2178 – 0.4896 g/30mL	42-44	3.53-4.0	-
A. xylinum (ATCC 700178) [129]	Corn steep liquor with fructose (Control medium)	~ 1.25g/L	-	85%	-
	0.5% Avicel	~ 4.5g/L	-	-	-
	0.5% CMC	~ 7.25g/L	-	83.3%	-
	0.5% Sodium Alginate	~ 1g/L	-	-	-
	0.2% Agar	4.5g/L	-	-	-

2.2.6. Bacterial Derived Cellulose Applications

* BC's bacterial origin has led to biocompatibility and immunogenic concerns. However, sterilized BC has been found to be biocompatible in both *in vivo* and *in vitro* testing [130, 131]. For detailed information on the biocompatibility analysis of BC , readers may consult references [92, 132-134]. The unique structure and biocompatibility of BC opens the doors to a wide variety of biomedical applications. The close-fitting microstructure of BC supports entrapment of *E. coli* while allowing for the permeability of analyte molecules. This encapsulated system allowed for the development of a cell-based living sensor system that, as a proof of concept, expressed a dual-color riboswitch causing the *E. coli* to fluoresce either green or red in the presence of a target analyte [135]. Bacterial-derived cellulose has also been researched as a vehicle for directed cell delivery [136]. Bacterial cellulose/acrylic acid hydrogels have been

investigated as a wound dressing and cell carrier for partial-thickness burn wounds [136]. The hydrogels allowed for the rapid attachment of cells but also allowed the cells to migrate from the hydrogel into the wound site [136]. Another study modified the material's chemical composition by crosslinking dextran to cellulose. This modification promoted and enhanced cell proliferation more than unmodified cellulose and may be a promising hydrogel based wound dressing [137]. Cellulose based wound dressings have been found to provide immediate pain relief, reduced treatment time, improve development of granulation tissue, and accelerated re-epithelialization [138, 139]. The analgesic and increased healing affects observed when using bacteria derived cellulose (BC) wound dressings are not fully understood but could be connected to the capture of ions and ROS by loose hydrogen bonds or the network structure of BC mimicking that of the extracellular matrix of human skin [140-142]. Additionally, BC is readily available and has a lower cost than other natural based wound dressings [25, 49]. Several BC composite materials have also been investigated. Hybrid composite wound dressings comprised of BC and copolymer of 3-hydroxybutyric and 4-hydroxybutyric acids [P(3HB/4HB)] have been shown to be an effective vehicle for drug delivery in would dressing applications [143]. Despite this, BC's lack of transparent and antibacterial properties greatly limits its clinical application.

2.2.7. Previous Methods for Achieving Transparency in Bacterial Derived Cellulose

To produce transparent BC methods such as incorporation of composite materials with optical clarity as well as altering the BC culture conditions have been employed. Composite materials that enhance optical clarity such as PEG, cyclodextrin, PVA, poly(methyl methacrylate) (PMMA), and poly(2-hydroxyethyl methacrylate) (PHEMA) have been used to induce transparency in BC [44, 144-147]. Commonly used in soft contact lenses, in its pure form PHEMA has a 95% light transmittance [44]. BC/PHEMA composite materials, increases the transmittance of native BC by roughly 10% [44]. Similarly, Kono et al. increased the overall transparency of BC fibers by increasing the concentration of PMMA as a composite material [148]. BC/PMMA composites showed light transmittance values between 74-81% at a wavelength of 700 nm [149]. Han et al. determined that by making BC/PVA composites light transmittance

values up to 96% in the visible light region were achieved [150]. These methods, however, generally reduce the inherent wound healing capabilities of native BC as the fibrillar structure and loose hydrogen bonds known for scavenging reactive oxygen species are altered during the composite manufacturing process. Additionally, the incorporation of composite materials increases the overall cost and manufacturing time of the material [44, 140-142, 144-147].

Few studies have shown the development of pure transparent cellulose; of the literature available, the transparency of the material is rarely fully characterized or the primary focus of the research. Utilizing defined minimal culture medium, Souza et al. was able to produce pure transparent BC from a *Komagataeibacter hansenii* [151]. It was noted that the transparent material had a lower fiber density compared to cellulose formed in full culture medium. This low fiber density was attributed to nutrient restriction caused by the defined minimal medium. By wet stretching BC pellicle, Wang et al. observed alignment of cellulose nanofibers, resulting in a highly transparent films [152]. BC pellicles stretched to 40% strain exhibited increased light transmittance properties when compared to unstretched pellicles [153]. Though understudied, these findings suggest that altered morphology and hierarchical structure may alter the optical properties of bacterial cellulose. These findings further point to media formulation, specifically nutrient restriction in defined medium, as a possible way to control morphology and structure of BC.

2.2.8. Methods for Incorporating Antibacterial Activity into Bacterial Derived Cellulose

Various approaches to incorporate antimicrobial agents into BC wound dressings have been studied such as the addition of copper, silver, lignin, chitosan, antibiotics, peptides, and other cationic antimicrobial agents [44, 144, 146, 154-158]. These approaches have resulted in favorable antimicrobial activity, however there are significant drawbacks. Antiseptics, such as chlorhexidine and iodine, inhibit fibroblast proliferation and migration, impeding normal wound healing progression [159]. Additionally, chlorohexidine resistance in specific bacterial strains has been found to be synonymous with increased antibiotic resistance [160, 161]. Alternative methods for incorporating antibacterial activity, such as copper and silver ions/nanoparticles remain a debated topic as to their biocompatibility in large quantities. Silver

has been shown to upregulate pro-MMP-9 in stimulated cells, elevated levels of which are already known to be present in chronic wounds. This is believed to be responsible for preventing wound healing through growth factor degradation and degradation of provisional ECM matrix laid down during early wound healing steps [21, 159]. Alternative antibacterial agents comprised mainly of biopolymer materials have burst release concerns and antibiotic grafting promotes antibiotic resistance, is toxic to mammalian cells and hinders healing [162]. Overall, these antimicrobial approaches are associated with hindered cellular proliferation, leading to a need for an antimicrobial agent that overcomes antibiotic resistance and promotes healing [162].

2.3. Antimicrobial Peptides (AMPs)

2.3.1. Cationic AMPs

Antimicrobial peptides (AMPs) are small molecular weight proteins that have broad spectrum antimicrobial activity against invading bacteria, viruses, and fungi [163]. AMPs are part of the host's natural immune system and are generally positively charged and have both hydrophobic and hydrophilic sides to enable aqueous solubility and lipid membrane penetration capability [163]. The antimicrobial activity of AMPs is mainly through non-receptor mediated damage to the bacterial membrane. This non-specific physical disruption of the microbial cell wall is driven by the electrostatic interaction between the positively charged AMP and negatively charged bacterial membrane [164]. This interaction increases membrane permeability and eventually leads to cell lysis [165]. Four main hypotheticals models of membrane-cavity formation exist for cationic AMPs: barrel-stave, toroidal-pore, non-pore carpet, and detergent-like carpet models (**Figure 2.5**) [165]. In the barrel-stave model, peptide binding to the membrane occurs causing membrane thinning as local phospholipid head groups shift [166]. As the AMP penetrates the membrane, hydrophobic peptide regions interact with the hydrophobic regions of the membrane, while hydrophilic peptide regions turn inward to form a pore in the membrane [165, 166]. The toroidal-pore model's mechanism is very similar, however the AMPs induce bending of bound lipid molecules, forming toroidal pore complexes with lipid head groups embedded inside the lipid hydrophobic center [166]. In the non-

pore carpet model, also known as the aggregate model, the AMPs form channels in the membrane by binding to the cytoplasmic membrane to form peptide-lipid complex micelles, which allow for continuous intracellular leakage and eventual cell death [167]. The detergent-like carpet model utilizes the electrostatic effects of AMPs to rupture the cell wall in a surfactant like manner, forming micelles around the ruptured membrane clusters. This method causes almost complete cell membrane lysis [168]. These models and their proposed effectivity are highly dependent on the peptide to lipid ratio. All methods require a minimum threshold of peptide-lipid ratio. At high peptide-lipid ratios, the AMPs are believed to be vertically oriented and insert themselves into the hydrophobic center, in accordance with the barrel-stave model, but at low peptide-lipid ratios, the AMPs are parallel on the surface of the membrane in accordance with the non-pore carpet model [169-171].

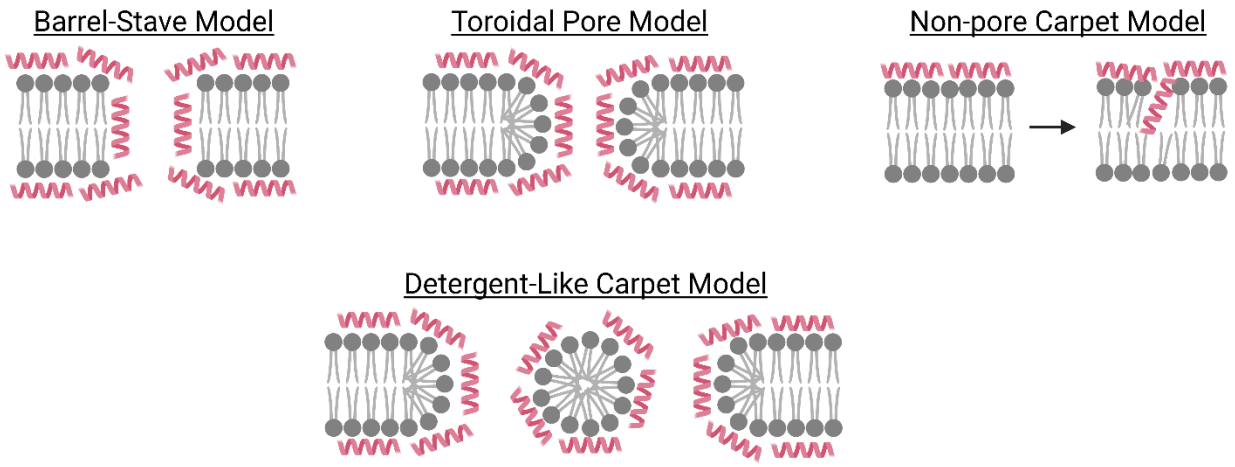

Figure 2.5. Proposed mechanism of action by cationic AMPs.
Where the phospholipids are denoted in grey, and the antimicrobial peptides are denoted in pink. Made using biorender.com

2.3.2. Cathelicidin AMPs

Cathelicidins, a subclass of AMPs, are synthesized as preproproteins with highly conserved N-terminal domain usually consisting of 94-114 amino acids [172]. Most cathelicidins are linear peptides folded into amphipathic α-helices. Generally the degree of α-helix structure conformation directly correlates to the antibacterial activity of the peptide [173]. Cathelicidins, stored in a nonfunctional form in neutrophils and macrophage secretory granules, are released upon leukocyte activation and processed by extracellular

cleaved to active peptide forms and play a key role in the innate immune system [174]. Over 113 mature cathelicidin peptides have been found and characterized from a range of sources in the animal kingdom [175]. These peptides are known to perform key functions other than exerting antibacterial activity, specifically immune modulating activity. To date, only one active cathelicidin peptide has been found in the human body, LL-37, and is arguable one of the most widely studied AMPs [172].

2.3.3. Human Cathelicidin LL-37

CAP-18, the only known human cathelicidin, is expressed by monocytes, neutrophils, mast cells, stem cells, NK cells, B cells, and T cells, and is thus widely found in human saliva, skin, gastrointestinal tissue, the urinary tract, and respiratory airways [172]. The 37 amino acid long active domain, LL37, plays a role in wound healing, apoptosis regulation, chemotactic activity, and exhibits antibacterial, antiviral, antifungal, and antiparasitic activity [176]. Additionally, the down regulation of LL-37 is associated with chronic ulcers and increased susceptibility to wound infection [177]. This multi-action capability and key role in wound healing makes LL-37 a promising AMP for incorporated antibacterial activity of wound dressing materials. LL-37, however, has a very narrow therapeutic window where marginally higher concentrations kill not only invading pathogens but are detrimental to host cells. It has been determined that in certain tissues the concentration of LL-37 is below the minimum inhibitory concentration (MIC) required to kill invading pathogens [178]. In solution, LL-37 exhibits cytotoxicity at concentrations higher than 10 μM and has limited *in vivo* stability [162, 173, 179-181]. Though immobilization of LL-37 has been shown to decrease mammalian cell cytotoxicity and increase *in vivo* stability without compromising the AMPs antimicrobial activity, its long peptide chain makes it susceptible to proteolytic degradation [162, 179, 180, 182]. Additionally *S. aureus* has been observed to develop into small colony variants that develop resistance mechanisms to LL-37, such as transmembrane potential reduction, unsaturation of lipids, and metabolic alteration [164, 183]. To overcome these limitations, LL-37 antimicrobial domain, specifically KR-12 and analogues thereof, have been developed by isolating the active antibacterial region of LL-37

[182]. This domain and the analogues have strong antibacterial characteristics, decreased likelihood of inducing bacterial resistance, prolonged proteolytic resistance, and antiendotoxic activity [182].

2.3.4. Engineering AMPs (KR-12)

KR-12, the smallest LL-37 derived antibacterial peptide, corresponds to residues 18-29 of the LL-37 sequence [184]. Wang et al. determined the TC_{50} value of KR-12 is greater than 63.5 μM, while LL-37's TC_{50} was only 18.4 μM [185]. Jacob et al. found that KR-12 has a 17.6 fold improvement in therapeutic index compared to LL-37 [182]. Though still a newer AMP, KR-12's enhanced biocompatibility and comparable antibacterial activity has made it an increasingly popular option for use as an antibacterial agent. Preliminary studies of KR-12 therapy in four different mouse models of colitis showed reduction in ulcer severity scoring and decreased overall bacterial count. KR-12 was also found to attenuate intestinal inflammation in these semi-chronic induced models [186]. Additionally, KR-12 is known to directly bind to LPS and mediate the pro-inflammatory and subsequent proptosis of LPS stimulated macrophages [187]. Lipopolysaccharides (LPS) are an important outer membrane component of gram-negative bacteria. LPS is a highly potent toxin, endotoxin, towards mammalian cells when released from the bacterial membrane during infection [188]. LPS is generally comprised of a hydrophobic domain (lipid A), covalently linked to a hydrophilic polysaccharide chain [189, 190]. Lipid A, known to be a pathogen-associated molecular patterns (PAMP), the only region of LPS recognized by the innate immune system, and is capable of stimulating a highly sensitive and robust immune response [191]. Recognition and stimulation is largely driven by the toll-like receptor 4 (TLR4)-MD2-CD14 complex found in cell types such as macrophages and dendrites [191-193]. This KR-12 driven inflammatory mediation process is believed to be orchestrated by the electrostatic interaction of AMP and the negatively charged lipid A component of LPS. This interaction structurally changes the structure of LPS from cubic lamellar to multilamellar, preventing LPS from stimulating the TLR-4 receptors on host cells and initiating inflammation pathways [194, 195].

For controlled release and designated surface antibacterial activity increasing interest involving peptide immobilization methods and subsequent bioactivity assessments have been investigated. Diosa et

al. studies the antimicrobial activity and proteolytic stability of KR-12 adsorbed to chitosan-silica hybrid material. Adsorbed peptide exhibited decreased antibacterial activity due to steric hindrance, but increased protection from proteolytic activity due to selective interactions with the solid surface [196]. Liu et al, conjugated KR-12 onto eggshell membranes and reported less than 3% bacterial survival of *E. coli*, *S. aureus*, and methicillin-resistant *Staphylococcus aureus* (MRSA). Further, the HaCaT cells, a keratinocyte cell line, cultured on KR-12 functionalized eggshell membranes increased proliferation levels compared to unfunctionalized eggshell membranes [197]. In 2016, Nie et al. covalently immobilized KR-12 onto a titanium surface for orthopedic implant applications. Nie et al. found that KR-12 not only retained its antibacterial activity but also played a role in promoting early adhesion and proliferation of bone mesenchymal stem cells [198]. In 2017, this same research group determined that KR-12 antibacterial activity when covalently immobilized on the titanium surface is improved by 7% with the addition of a PEG spacer. Additionally, the incorporation of a PEG spacer significantly decreased proinflammatory cytokine secretion (TNF-α and IL-1β) in cell culture supernatant [199]. In this case the flexibility of the PEG spacer allowed for decrease steric hinderance of KR-12. This steric hinderance and disruption in secondary structure further explains why in some cases physisorption and covalent immobilization methods resulted in partial and full deactivation of KR-12's activity [200]. Though KR-12 provided an excellent means of providing antibacterial activity without the concern of antibiotic resistance, more effective immobilization methods are required to maintain peptide functionality.

2.4. Cellulose Binding Modules and Proteins

2.4.1. Cellulose Binding Modules (CBMs)

Carbohydrate/Cellulose binding modules (CBM) are defined as a continuous amino acid sequence within a carbohydrate-active enzyme with a discrete fold that allows for carbohydrate binding [201]. It should be noted that carbohydrate binding modules and cellulose binding domains (CBDs) are used interchangeably in literature as naming conventions have changed over time. The main functions of CBMs in nature are to target cellulose, bind and bring hydrolases into proximity, while simultaneously disrupting

the crystalline structure of cellulose [202]. Based on structural and functional similarities CBMs have been grouped into three main types: Type A, Type B, and Type C. Type A CBMs have a hydrophobic planar conformation comprised of aromatic residues, allowing for crystalline surface binding [203]. While Type B and C display a cleft arrangement characterized by steric restrictions which limit their binding capabilities to amorphous cellulose only [203]. BC's high degree of crystallinity (80-89%) thus limits the CBM binding capacity to Type A CBMs [204]. The planar aromatic residuals, tryptophan, or tyrosine, located on the hydrophobic region of Type A CBMs form stacking π-bond interactions with the sugar rings in cellulose. This interaction forms strong van der Waals interactions which are further stabilized by hydrogen bonds that form between polar amino acid side chains and the cellulose substrate [202, 203, 205]. Additionally, CBM-cellulose interactions have been characterized as a dynamic process where CBMs are still mobile on the surface of the crystalline cellulose [201].

The high cellulose binding affinity of CBMs make them an attractive option for non-covalent functionalization of the relatively inert surface of cellulose materials. For biomedical applications, CBMs have been found to effectively immobilize Arg-Gly-Asp (RGD) sequences to cellulose surfaces for increased fibroblast adhesion [206]. The CBM-RGD functionalized surface allowed for increased cell adhesion at as little as 1 hour post cell seeding [134, 207]. Alternatively, Petrile et al. linked Ile-Lys-Val-Ala-Val (IKVAV) to cellulose and observed 100% improvement of N1E-115 rat neuroblast cell (PC12) adhesion [208]. Florea at al. functionalized cellulose pellicles by engineering expression vectors that allow for fusion of proteins to short cellulose-binding domains (CBDs) that non-covalently bind to cellulose fibers. Binding of CBD superfolder green fluorescent protein (CBD-sfGFP) extracted from *E. coli*, produced a five-fold increase in cellulose binding than green fluorescent protein (GFP) alone [209]. These studies suggest that CBMs can be effectively used to non-covalently tether bioactive structures to a highly crystalline surface.

2.4.2. Cellulose Binding Proteins (CBPs)

Shorter amino acid cellulose binding peptides (CBPs) have been engineered, while maintaining equal or increased cellulose binding affinity. Khazanov et al. digitally designed compact CBPs by reducing CBM1's size from a 36 mer CBM to an 18 mer CBP while maintaining its original 3D conformation. Cellulose binding was assessed both computationally and experimentally, finding that overall these engineered mutations resulted in a CBP with a higher cellulose binding affinity ($1.45 \pm 0.30 \times 10^6$ M^{-1}) and increased maximal surface coverage (6.77 ± 0.10 μmol/gr) compared to the complete CBM ($0.94 \pm 0.15 \times 10^6$ M^{-1} and 5.07 ± 0.05 μmol/gr) [210]. Khazanov et al. determined that through their iterative process of computational modeling and experimental assessments they were able to design more fine-tuned CBP sequences. Guo et al. engineered a seven residue long peptide that exhibited a four order of magnitude increase in binding affinity [211]. Within in the realm of CBPs, this heptapeptide sequence has been described as a minimal consensus amino acid sequence [211, 212]. The cellulose binding mechanism of the short sequence is believed to be through CH/π stacking interactions, and hydrogen bonds between peptide sidechains and cellulose [211]. Weishaupt et al. used this shorter sequence to non-covalently tether RGD and an antimicrobial ligand tet009 to the surface of BC. A 2.2 fold increase in cell proliferation and cell spreading was observed with BC functionalized with RDG compared to unfunctionalized controls. Weishaupt et al. also established methods for the successful tethering and quantifying of CBP-tet009 to cellulose, and observed effective bacterial mediation with the engineered antimicrobial ligand [212]. However, tet009 does not contain any additional activity, aside from antimicrobial properties, and would not increase wound healing capabilities [212]. Further, significantly increased bioactivity of tet009 was observed when tethered to electrospun cellulose: polyurethane membranes compared to pure BC materials [212].

2.5. Conclusions

Wound healing is a highly structured process with clearly defined indicators of progression through the main stages of healing. Unfortunately, factors such as oxygenation and venous insufficiency increase oxidative stress and high levels of ROS in the wound bed resulting in impaired wound healing capabilities.

Healing is further marred by the high prevalence of infection and ineffective treatment options that both increased wound healing function and mitigate invading pathogen activity. Bacterial derived cellulose inherently exhibits ideal properties for use as a wound dressing material that have been tested and confirmed *in vivo* and clinically. Despite these positive findings, the lack of wound visualization and surface antibacterial properties hinders BC's effectivity in a clinical setting. By altering the culture conditions of BC, the development of pure transparent cellulose has been observed. This observation currently lacks full investigation and understanding behind the mechanism of induced transparency. The lack of antibacterial activity may be addressed using engineered AMPs with broad range antibacterial activity, such as KR-12, and CBPs as a mode for non-covalent tethering that still allows for full motion and functionality of the AMP. Addressing these two main limitations of BC's use is critical for the development of functionally active biomaterials with enhanced wound healing and wound care capabilities.

2.6. References

[1] W.H. Organization, UN Decade of Healthy Ageing 2021-2030 (Nd).
[2] G. Han, R. Ceilley, Chronic wound healing: a review of current management and treatments, Advances in therapy 34(3) (2017) 599-610.
[3] J. Grip, R.E. Engstad, I. Skjæveland, N. Škalko-Basnet, J. Isaksson, P. Basnet, A.M. Holsæter, Beta-glucan-loaded nanofiber dressing improves wound healing in diabetic mice, European Journal of Pharmaceutical Sciences 121 (2018) 269-280.
[4] A.L. Hersh, H.F. Chambers, J.H. Maselli, R. Gonzales, National trends in ambulatory visits and antibiotic prescribing for skin and soft-tissue infections, Archives of internal medicine 168(14) (2008) 1585-1591.
[5] D. Simões, S.P. Miguel, M.P. Ribeiro, P. Coutinho, A.G. Mendonça, I.J. Correia, Recent advances on antimicrobial wound dressing: A review, European journal of pharmaceutics and biopharmaceutics 127 (2018) 130-141.
[6] H.W. Lim, S.A. Collins, J.S. Resneck Jr, J.L. Bolognia, J.A. Hodge, T.A. Rohrer, M.J. Van Beek, D.J. Margolis, A.J. Sober, M.A. Weinstock, The burden of skin disease in the United States, Journal of the American Academy of Dermatology 76(5) (2017) 958-972. e2.
[7] D. Paquette, V. Falanga, Leg ulcers, Clinics in geriatric medicine 18(1) (2002) 77-88.
[8] C. Attinger, R. Wolcott, Clinically addressing biofilm in chronic wounds, Advances in wound care 1(3) (2012) 127-132.
[9] S.E. Dowd, Y. Sun, P.R. Secor, D.D. Rhoads, B.M. Wolcott, G.A. James, R.D. Wolcott, Survey of bacterial diversity in chronic wounds using pyrosequencing, DGGE, and full ribosome shotgun sequencing, BMC microbiology 8 (2008) 1-15.
[10] P.A. Kolarsick, M.A. Kolarsick, C. Goodwin, Anatomy and physiology of the skin, Journal of the Dermatology Nurses' Association 3(4) (2011) 203-213.
[11] E. McLafferty, C. Hendry, A. Farley, The integumentary system: anatomy, physiology and function of skin, Nursing Standard (through 2013) 27(3) (2012) 35.
[12] A. Pfalzgraff, K. Brandenburg, G. Weindl, Antimicrobial peptides and their therapeutic potential for bacterial skin infections and wounds, Frontiers in pharmacology 9 (2018) 281.
[13] W.D. James, D. Elston, T. Berger, Andrew's Diseases of the Skin E-Book: Clinical Dermatology, Elsevier Health Sciences2011.
[14] D. Chu, Overview of biology, development, and structure of skin. K. Wolff, LA Goldsmith, SI Katz, BA Gilchrest, AS Paller, & DJ Leffell, New York: McGraw-Hill, 2008.
[15] M. Venus, J. Waterman, I. McNab, Basic physiology of the skin, Surgery (Oxford) 28(10) (2010) 469-472.
[16] L.A. Sokolnicki, N.A. Strom, S.K. Roberts, S.A. Kingsley-Berg, A. Basu, N. Charkoudian, Skin blood flow and nitric oxide during body heating in type 2 diabetes mellitus, Journal of Applied Physiology 106(2) (2009) 566-570.
[17] G. Yosipovitch, A. DeVore, A. Dawn, Obesity and the skin: skin physiology and skin manifestations of obesity, Journal of the American Academy of Dermatology 56(6) (2007) 901-916.
[18] A.C.d.O. Gonzalez, T.F. Costa, Z.d.A. Andrade, A.R.A.P. Medrado, Wound healing-A literature review, Anais brasileiros de dermatologia 91(5) (2016) 614-620.
[19] S.a. Guo, L.A. DiPietro, Factors affecting wound healing, Journal of dental research 89(3) (2010) 219-229.

[20] A. Gosain, L.A. DiPietro, Aging and wound healing, World journal of surgery 28(3) (2004) 321-326.
[21] I. George Broughton, J.E. Janis, C.E. Attinger, The basic science of wound healing, Plastic and reconstructive surgery 117(7S) (2006) 12S-34S.
[22] A.C. Campos, A.K. Groth, A.B. Branco, Assessment and nutritional aspects of wound healing, Current Opinion in Clinical Nutrition & Metabolic Care 11(3) (2008) 281-288.
[23] A.J. Meszaros, J.S. Reichner, J.E. Albina, Macrophage-induced neutrophil apoptosis, The Journal of Immunology 165(1) (2000) 435-441.
[24] D.M. Mosser, J.P. Edwards, Exploring the full spectrum of macrophage activation, Nature reviews immunology 8(12) (2008) 958-969.
[25] R. Zeng, C. Lin, Z. Lin, H. Chen, W. Lu, C. Lin, H. Li, Approaches to cutaneous wound healing: basics and future directions, Cell and tissue research 374(2) (2018) 217-232.
[26] M. Walker, D. Metcalf, D. Parsons, P. Bowler, A real-life clinical evaluation of a next-generation antimicrobial dressing on acute and chronic wounds, Journal of wound care 24(1) (2015) 11-22.
[27] S.W. Jere, H. Abrahamse, N.N. Houreld, The JAK/STAT signaling pathway and photobiomodulation in chronic wound healing, Cytokine & growth factor reviews 38 (2017) 73-79.
[28] A.A. Tandara, T.A. Mustoe, Oxygen in wound healing—more than a nutrient, World journal of surgery 28(3) (2004) 294-300.
[29] P.G. Rodriguez, F.N. Felix, D.T. Woodley, E.K. Shim, The role of oxygen in wound healing: a review of the literature, Dermatologic surgery 34(9) (2008) 1159-1169.
[30] P. Basu, J.H. Kim, S. Saeed, M. Martins-Green, Using systems biology approaches to identify signalling pathways activated during chronic wound initiation, Wound Repair and Regeneration 29(6) (2021) 881-898.
[31] S. Dhall, D. Do, M. Garcia, D.S. Wijesinghe, A. Brandon, J. Kim, A. Sanchez, J. Lyubovitsky, S. Gallagher, E.A. Nothnagel, A novel model of chronic wounds: importance of redox imbalance and biofilm-forming bacteria for establishment of chronicity, PLoS One 9(10) (2014) e109848.
[32] P. Basu, M. Martins-Green, Signaling pathways associated with chronic wound progression: A systems biology approach, Antioxidants 11(8) (2022) 1506.
[33] Z. Prokopowicz, J. Marcinkiewicz, D.R. Katz, B.M. Chain, Neutrophil myeloperoxidase: soldier and statesman, Archivum immunologiae et therapiae experimentalis 60 (2012) 43-54.
[34] R. Edwards, K.G. Harding, Bacteria and wound healing, Current opinion in infectious diseases 17(2) (2004) 91-96.
[35] N.B. Menke, K.R. Ward, T.M. Witten, D.G. Bonchev, R.F. Diegelmann, Impaired wound healing, Clinics in dermatology 25(1) (2007) 19-25.
[36] G.S. Schultz, G. Ladwig, A. Wysocki, Extracellular matrix: review of its roles in acute and chronic wounds, World wide wounds 2005 (2005) 1-18.
[37] H. Al Sadoun, M. Burgess, K.E. Hentges, K.A. Mace, Enforced expression of Hoxa3 inhibits classical and promotes alternative activation of macrophages in vitro and in vivo, The Journal of Immunology 197(3) (2016) 872-884.
[38] R. Zhao, H. Liang, E. Clarke, C. Jackson, M. Xue, Inflammation in chronic wounds, International journal of molecular sciences 17(12) (2016) 2085.
[39] R.G. Frykberg, J. Banks, Challenges in the treatment of chronic wounds, Advances in wound care 4(9) (2015) 560-582.

[40] A.F. Cardona, S.E. Wilson, Skin and soft-tissue infections: a critical review and the role of telavancin in their treatment, Clinical Infectious Diseases 61(suppl_2) (2015) S69-S78.
[41] J.S. Boateng, K.H. Matthews, H.N. Stevens, G.M. Eccleston, Wound healing dressings and drug delivery systems: a review, Journal of pharmaceutical sciences 97(8) (2008) 2892-2923.
[42] A. Khalid, R. Khan, M. Ul-Islam, T. Khan, F. Wahid, Bacterial cellulose-zinc oxide nanocomposites as a novel dressing system for burn wounds, Carbohyd. Polym. 164 (2017) 214-221.
[43] M. Mulder, The selection of wound care products for wound bed preparation: wound care, Professional Nursing Today 15(6) (2011) 30-36.
[44] Z. Di, Z. Shi, M.W. Ullah, S. Li, G. Yang, A transparent wound dressing based on bacterial cellulose whisker and poly (2-hydroxyethyl methacrylate), Int. J. Biol. Macromol. 105 (2017) 638-644.
[45] M.A. Fonder, G.S. Lazarus, D.A. Cowan, B. Aronson-Cook, A.R. Kohli, A.J. Mamelak, Treating the chronic wound: A practical approach to the care of nonhealing wounds and wound care dressings, Journal of the American Academy of Dermatology 58(2) (2008) 185-206.
[46] S. Dogra, R. Sarangal, Summary of recommendations for leg ulcers, Indian dermatology online journal 5(3) (2014) 400.
[47] A. Grada, Z. Obagi, T. Phillips, Management of chronic wounds in patients with pemphigus, Chronic Wound Care Management and Research 6 (2019) 89.
[48] J.G. Powers, C. Higham, K. Broussard, T.J. Phillips, Wound healing and treating wounds: Chronic wound care and management, Journal of the American Academy of Dermatology 74(4) (2016) 607-625.
[49] E. Gianino, C. Miller, J. Gilmore, Smart wound dressings for diabetic chronic wounds, Bioengineering 5(3) (2018) 51.
[50] J. Mano, G. Silva, H.S. Azevedo, P. Malafaya, R. Sousa, S.S. Silva, L. Boesel, J.M. Oliveira, T. Santos, A. Marques, Natural origin biodegradable systems in tissue engineering and regenerative medicine: present status and some moving trends, Journal of the Royal Society Interface 4(17) (2007) 999-1030.
[51] A.-H. Stricker-Krongrad, Z. Alikhassy, N. Matsangos, R. Sebastian, G. Marti, F. Lay, J.W. Harmon, Efficacy of chitosan-based dressing for control of bleeding in excisional wounds, Eplasty 18 (2018).
[52] Y. Qin, The gel swelling properties of alginate fibers and their applications in wound management, Polymers for Advanced Technologies 19(1) (2008) 6-14.
[53] S. Barnett, S. Varley, The effects of calcium alginate on wound healing, Annals of the Royal College of Surgeons of England 69(4) (1987) 153.
[54] C.W. Shields IV, L.L.W. Wang, M.A. Evans, S. Mitragotri, Materials for immunotherapy, Advanced Materials 32(13) (2020) 1901633.
[55] O. Singh, S.S. Gupta, M. Soni, S. Moses, S. Shukla, R.K. Mathur, Collagen dressing versus conventional dressings in burn and chronic wounds: a retrospective study, Journal of cutaneous and aesthetic surgery 4(1) (2011) 12.
[56] Z. Hussain, H.E. Thu, A.N. Shuid, H. Katas, F. Hussain, Recent advances in polymer-based wound dressings for the treatment of diabetic foot ulcer: an overview of state-of-the-art, Current drug targets 19(5) (2018) 527-550.
[57] G.M. Campo, A. Avenoso, S. Campo, A. D'Ascola, G. Nastasi, A. Calatroni, Molecular size hyaluronan differently modulates toll-like receptor-4 in LPS-induced inflammation in mouse chondrocytes, Biochimie 92(2) (2010) 204-215.

[58] K. Ghazi, U. Deng-Pichon, J.-M. Warnet, P. Rat, Hyaluronan fragments improve wound healing on in vitro cutaneous model through P2X7 purinoreceptor basal activation: role of molecular weight, PLoS One 7(11) (2012).
[59] Y. Li, H. Jiang, W. Zheng, N. Gong, L. Chen, X. Jiang, G. Yang, Bacterial cellulose–hyaluronan nanocomposite biomaterials as wound dressings for severe skin injury repair, Journal of Materials Chemistry B 3(17) (2015) 3498-3507.
[60] A. Khalid, H. Ullah, M. Ul-Islam, R. Khan, S. Khan, F. Ahmad, T. Khan, F. Wahid, Bacterial cellulose–TiO 2 nanocomposites promote healing and tissue regeneration in burn mice model, RSC advances 7(75) (2017) 47662-47668.
[61] M.H. Deinema, L. Zevenhuizen, Formation of cellulose fibrils by gram-negative bacteria and their role in bacterial flocculation, Arch. Mikrobiol. 78(1) (1971) 42-57.
[62] A. Matthysse, Role of bacterial cellulose fibrils in Agrobacterium tumefaciens infection, J. Bacteriol. 154(2) (1983) 906-915.
[63] R. Jonas, L.F. Farah, Production and application of microbial cellulose, Polym. Degrad. Stabil. 59(1-3) (1998) 101-106.
[64] T. Richmond, Higher plant cellulose synthases, Genome Biol. 1(4) (2000) reviews3001. 1.
[65] L.R. Lynd, P.J. Weimer, W.H. Van Zyl, I.S. Pretorius, Microbial cellulose utilization: fundamentals and biotechnology, Microbiol. Mol. Biol. R. 66(3) (2002) 506-577.
[66] R.M. Brown Jr, Emerging technologies and future prospects for industrialization of microbially derived cellulose, Conf. P. ACS (1992) 76-79.
[67] A.J. Brown, XLIII.—On an acetic ferment which forms cellulose, J. Chem. Soc., Trans. 49 (1886) 432-439.
[68] R. Buchanan, N. Gibbns, Family VI. Acetobacteraceae, Bergey's Man. Syst. Bacteriol. 1 (1984) 267-78.
[69] Y. Yamada, P. Yukphan, H.T.L. Vu, Y. Muramatsu, D. Ochaikul, Y. Nakagawa, Subdivision of the genus Gluconacetobacter Yamada, Hoshino and Ishikawa 1998: the proposal of Komagatabacter gen. nov., for strains accommodated to the Gluconacetobacter xylinus group in the α-Proteobacteria, Ann. Microbiol. 62(2) (2012) 849-859.
[70] F. Esa, S.M. Tasirin, N.A. Rahman, Overview of bacterial cellulose production and application, Agric. Acric. Sci. Proc. 2 (2014) 113-119.
[71] D.R. Ruka, G.P. Simon, K.M. Dean, Altering the growth conditions of Gluconacetobacter xylinus to maximize the yield of bacterial cellulose, Carbohyd. Polym. 89(2) (2012) 613-622.
[72] K. Ramana, A. Tomar, L. Singh, Effect of various carbon and nitrogen sources on cellulose synthesis by Acetobacter xylinum, World J. Microbiol. Bactechnol. 16(3) (2000) 245-248.
[73] C. Molina-Ramírez, M. Castro, M. Osorio, M. Torres-Taborda, B. Gómez, R. Zuluaga, C. Gómez, P. Gañán, O.J. Rojas, C. Castro, Effect of different carbon sources on bacterial nanocellulose production and structure using the low pH resistant strain Komagataeibacter medellinensis, Materials 10(6) (2017) 639.
[74] N. Tyagi, S. Suresh, Production of cellulose from sugarcane molasses using Gluconacetobacter intermedius SNT-1: optimization & characterization, J. Clean. Prod. 112 (2016) 71-80.
[75] S.-P. Lin, Y.-H. Huang, K.-D. Hsu, Y.-J. Lai, Y.-K. Chen, K.-C. Cheng, Isolation and identification of cellulose-producing strain Komagataeibacter intermedius from fermented fruit juice, Carbohyd. Polym. 151 (2016) 827-833.
[76] P. Ross, R. Mayer, M. Benziman, Cellulose biosynthesis and function in bacteria, Microbiol. Rev. 55(1) (1991) 35-58.

[77] A. Budhiono, B. Rosidi, H. Taher, M. Iguchi, Kinetic aspects of bacterial cellulose formation in nata-de-coco culture system, Carbohyd. Polym. 40(2) (1999) 137-143.
[78] M. Benziman, B. Rivetz, Factors affecting hexose phosphorylation in Acetobacter xylinum, J. Bacteriol. 111(2) (1972) 325-333.
[79] M. Swissa, Y. Aloni, H. Weinhouse, M. Benizman, Intermediatry steps in Acetobacter xylinum cellulose synthesis: studies with whole cells and cell-free preparations of the wild type and a celluloseless mutant, J. Bacteriol. 143(3) (1980) 1142-50.
[80] K.Y. Lee, G. Buldum, A. Mantalaris, A. Bismarck, More than meets the eye in bacterial cellulose: biosynthesis, bioprocessing, and applications in advanced fiber composites, Macromol. Biosci. 14(1) (2014) 10-32.
[81] J.L. Morgan, J. Strumillo, J. Zimmer, Crystallographic snapshot of cellulose synthesis and membrane translocation, Nature 493(7431) (2013) 181.
[82] J.L. Morgan, J.T. McNamara, M. Fischer, J. Rich, H.-M. Chen, S.G. Withers, J. Zimmer, Observing cellulose biosynthesis and membrane translocation in crystallo, Nature 531(7594) (2016) 329.
[83] M. Rezazadeh, V. Babaeipour, E. Motamedian, Reconstruction, verification and in-silico analysis of a genome-scale metabolic model of bacterial cellulose producing Komagataeibacter xylinus, Bioprocess and Biosystems Engineering (2020) 1-10.
[84] O. Omadjela, A. Narahari, J. Strumillo, H. Mélida, O. Mazur, V. Bulone, J. Zimmer, BcsA and BcsB form the catalytically active core of bacterial cellulose synthase sufficient for in vitro cellulose synthesis, P. Natl. Acad. Sci. USA (2013) 201314063.
[85] M. Liu, L. Liu, S. Jia, S. Li, Y. Zou, C. Zhong, Complete genome analysis of Gluconacetobacter xylinus CGMCC 2955 for elucidating bacterial cellulose biosynthesis and metabolic regulation, Sci. Rep. 8(1) (2018) 6266.
[86] R. Standal, T.-G. Iversen, D.H. Coucheron, E. Fjaervik, J.M. Blatny, S. Valla, A new gene required for cellulose production and a gene encoding cellulolytic activity in Acetobacter xylinum are colocalized with the bcs operon, J. Bacteriol. 176(3) (1994) 665-672.
[87] I.M. Saxena, K. Kudlicka, K. Okuda, R. Brown, Characterization of genes in the cellulose-synthesizing operon (acs operon) of Acetobacter xylinum: implications for cellulose crystallization, J. Bacteriol. 176(18) (1994) 5735-5752.
[88] J. Du, V. Vepachedu, S.H. Cho, M. Kumar, B.T. Nixon, Structure of the cellulose synthase complex of Gluconacetobacter hansenii at 23.4 Å resolution, PLoS One 11(5) (2016) e0155886.
[89] J.B. McManus, Y. Deng, N. Nagachar, T.-h. Kao, M. Tien, AcsA–AcsB: The core of the cellulose synthase complex from Gluconacetobacter hansenii ATCC23769, Enzyme Microb. Tech. 82 (2016) 58-65.
[90] M. Gao, J. Li, Z. Bao, M. Hu, R. Nian, D. Feng, D. An, X. Li, M. Xian, H. Zhang, A natural in situ fabrication method of functional bacterial cellulose using a microorganism, Nat. Commun. 10(1) (2019) 437.
[91] J.D. Fontana, H.S. Koop, M. Tiboni, A. Grzybowski, A. Pereira, C.D. Kruger, M.G. da Silva, L.P. Wielewski, New insights on bacterial cellulose, Food Biosynthesis, Elsevier2017, pp. 213-249.
[92] G.F. Picheth, C.L. Pirich, M.R. Sierakowski, M.A. Woehl, C.N. Sakakibara, C.F. de Souza, A.A. Martin, R. da Silva, R.A. de Freitas, Bacterial cellulose in biomedical applications: A review, Int. J. Biol. Macromol. 104 (2017) 97-106.

[93] M. Gullo, S. La China, P.M. Falcone, P. Giudici, Biotechnological production of cellulose by acetic acid bacteria: current state and perspectives, Appl. Microbiol. Biot. 102 (2018) 6885-6898.
[94] R.M. Brown, J. Willison, C.L. Richardson, Cellulose biosynthesis in Acetobacter xylinum: visualization of the site of synthesis and direct measurement of the in vivo process, P. Natl. Acad. Sci. USA 73(12) (1976) 4565-4569.
[95] C. Tokoh, K. Takabe, M. Fujita, H. Saiki, Cellulose synthesized by Acetobacter xylinum in the presence of acetyl glucomannan, Cellulose 5(4) (1998) 249-261.
[96] C.H. Haigler, R.M. Brown, M. Benziman, Calcofluor white ST alters the in vivo assembly of cellulose microfibrils, Science 210(4472) (1980) 903-906.
[97] S. Kobayashi, J. Sakamoto, S. Kimura, In vitro synthesis of cellulose and related polysaccharides, Prog. Polym. Sci. 26(9) (2001) 1525-1560.
[98] X. Yu, R.H. Atalla, Production of cellulose II by Acetobacter xylinum in the presence of 2, 6-dichlorobenzonitrile, Int. J. Biol. Macromol. 19(2) (1996) 145-146.
[99] M. Wada, M. Ike, K. Tokuyasu, Enzymatic hydrolysis of cellulose I is greatly accelerated via its conversion to the cellulose II hydrate form, Polym. Degrad. Stabil. 95(4) (2010) 543-548.
[100] S. Hokkanen, A. Bhatnagar, E. Repo, S. Lou, M. Sillanpää, Calcium hydroxyapatite microfibrillated cellulose composite as a potential adsorbent for the removal of Cr (VI) from aqueous solution, Chem. Eng. J. 283 (2016) 445-452.
[101] J. Sugiyama, J. Persson, H. Chanzy, Combined infrared and electron diffraction study of the polymorphism of native celluloses, Macromolecules 24(9) (1991) 2461-2466.
[102] R.H. Atalla, D.L. Vanderhart, Native cellulose: a composite of two distinct crystalline forms, Science 223(4633) (1984) 283-285.
[103] D.L. VanderHart, R. Atalla, Studies of microstructure in native celluloses using solid-state carbon-13 NMR, Macromolecules 17(8) (1984) 1465-1472.
[104] F. Horii, A. Hirai, H. Yamamoto, Microstructural analysis of microfibrils of bacterial cellulose, Macromolecular Symposia, Wiley Online Library, 1997, pp. 197-205.
[105] H. Yamamoto, F. Horii, CPMAS carbon-13 NMR analysis of the crystal transformation induced for Valonia cellulose by annealing at high temperatures, Macromolecules 26(6) (1993) 1313-1317.
[106] H. Yamamoto, F. Horii, A. Hirai, Structural studies of bacterial cellulose through the solid-phase nitration and acetylation by CP/MAS 13 C NMR spectroscopy, Cellulose 13(3) (2006) 327.
[107] N. Isobe, T. Komamiya, S. Kimura, U.-J. Kim, M. Wada, Cellulose hydrogel with tunable shape and mechanical properties: From rigid cylinder to soft scaffold, Int. J. Biol. Macromol. 117 (2018) 625-631.
[108] K.V. Ramana, H.V. Batra, Occurrence of cellulose-producing Gluconacetobacter spp. in fruit samples and kombucha tea, and production of the biopolymer, Appl. Biochem. Biotech. 176(4) (2015) 1162-1173.
[109] H. Toyosaki, T. Naritomi, A. Seto, M. Matsuoka, T. Tsuchida, F. Yoshinaga, Screening of bacterial cellulose-producing Acetobacter strains suitable for agitated culture, Biosci. Biotechnol. Biochem. 59(8) (1995) 1498-1502.
[110] P. Singhsa, R. Narain, H. Manuspiya, Physical structure variations of bacterial cellulose produced by different Komagataeibacter xylinus strains and carbon sources in static and agitated conditions, Cellulose 25(3) (2018) 1571-1581.

[111] W. Dudman, Cellulose production by Acetobacter strains in submerged culture, Microbiology 22(1) (1960) 25-39.
[112] Y. Hu, J.M. Catchmark, E.A. Vogler, Factors impacting the formation of sphere-like bacterial cellulose particles and their biocompatibility for human osteoblast growth, Biomacromolecules 14(10) (2013) 3444-3452.
[113] S. Tanskul, K. Amornthatree, N. Jaturonlak, A new cellulose-producing bacterium, Rhodococcus sp. MI 2: Screening and optimization of culture conditions, Carbohyd. Polym. 92(1) (2013) 421-428.
[114] K. Watanabe, M. Tabuchi, Y. Morinaga, F. Yoshinaga, Structural features and properties of bacterial cellulose produced in agitated culture, Cellulose 5(3) (1998) 187-200.
[115] W. Czaja, D. Romanovicz, R. Malcolm Brown, Structural investigations of microbial cellulose produced in stationary and agitated culture, Cellulose 11(3-4) (2004) 403-411.
[116] H. Yamamoto, F. Horn, In Situ crystallization of bacterial cellulose I. Influences of polymeric additives, stirring and temperature on the formation celluloses I α and I β as revealed by cross polarization/magic angle spinning (CP/MAS) 13 C NMR spectroscopy, Cellulose 1(1) (1994) 57-66.
[117] S.M. Keshk, K. Sameshima, Evaluation of different carbon sources for bacterial cellulose production, Afr. J. Biotechnol. 4(6) (2005) 478-482.
[118] D. Mikkelsen, B.M. Flanagan, G. Dykes, M. Gidley, Influence of different carbon sources on bacterial cellulose production by Gluconacetobacter xylinus strain ATCC 53524, J. Appl. Microbiol. 107(2) (2009) 576-583.
[119] F. Mohammadkazemi, M. Azin, A. Ashori, Production of bacterial cellulose using different carbon sources and culture media, Carbohyd. Polym. 117 (2015) 518-523.
[120] L. Fang, J.M. Catchmark, Characterization of cellulose and other exopolysaccharides produced from Gluconacetobacter strains, Carbohyd. Polym. 115 (2015) 663-669.
[121] A. Shirai, M. Takahashi, H. Kaneko, S.-I. Nishimura, M. Ogawa, N. Nishi, S. Tokura, Biosynthesis of a novel polysaccharide by Acetobacter xylinum, Int. J. Biol. Macromol. 16(6) (1994) 297-300.
[122] R. Ogawa, Y. Miura, S. Tokura, T. Koriyama, Susceptibilities of bacterial cellulose containing N-acetylglucosamine residues for cellulolytic and chitinolytic enzymes, Int. J. Biol. Macromol. 14(6) (1992) 343-347.
[123] V. Yadav, B. Panilaitis, H. Shi, K. Numuta, K. Lee, D.L. Kaplan, N-acetylglucosamine 6-phosphate deacetylase (nagA) is required for N-acetyl glucosamine assimilation in Gluconacetobacter xylinus, PLoS One 6(6) (2011) e18099.
[124] V. Yadav, B.J. Paniliatis, H. Shi, K. Lee, P. Cebe, D.L. Kaplan, Novel in vivo-degradable cellulose-chitin copolymer from metabolically engineered Gluconacetobacter xylinus, Appl. Environ. Microb. 76(18) (2010) 6257-6265.
[125] Q.-S. Shi, J. Feng, W.-R. Li, G. Zhou, A.-M. Chen, Y.-S. Ouyang, Y.-B. Chen, Effect of different conditions on the average degree of polymerization of bacterial cellulose produced by Gluconacetobacter intermedius BC-41, Cell. Chem. Technol 47 (2013) 503-508.
[126] C. Zhong, G.-C. Zhang, M. Liu, X.-T. Zheng, P.-P. Han, S.-R. Jia, Metabolic flux analysis of Gluconacetobacter xylinus for bacterial cellulose production, Appl. Microbiol. Biot. 97(14) (2013) 6189-6199.
[127] K. Toda, T. Asakura, M. Fukaya, E. Entani, Y. Kawamura, Cellulose production by acetic acid-resistant Acetobacter xylinum, J. Ferment. Bioeng. 84(3) (1997) 228-231.

[128] S. Keshk, K. Sameshima, Influence of lignosulfonate on crystal structure and productivity of bacterial cellulose in a static culture, Enzyme Microb. Tech. 40(1) (2006) 4-8.
[129] K.-C. Cheng, J.M. Catchmark, A. Demirci, Effect of different additives on bacterial cellulose production by Acetobacter xylinum and analysis of material property, Cellulose 16(6) (2009) 1033.
[130] Y. Hou, X. Wang, J. Yang, R. Zhu, Z. Zhang, Y. Li, Development and biocompatibility evaluation of biodegradable bacterial cellulose as a novel peripheral nerve scaffold, J. Biomed. Mater. Res. A 106(5) (2018) 1288-1298.
[131] J. Piasecka-Zelga, P. Zelga, J. Szulc, J. Wietecha, D. Ciechańska, An in vivo biocompatibility study of surgical meshes made from bacterial cellulose modified with chitosan, Int. J. Biol. Macromol. 116 (2018) 1119-1127.
[132] M. Roman, A.P. Haring, T.J. Bertucio, The Growing Merits and Dwindling Limitations of Bacterial Cellulose-Based Tissue Engineering Scaffolds, Curr. Opin. Chem. Eng. (2019).
[133] G. Helenius, H. Bäckdahl, A. Bodin, U. Nannmark, P. Gatenholm, B. Risberg, In vivo biocompatibility of bacterial cellulose, J Biomed. Mater. Res. A 76(2) (2006) 431-438.
[134] F.K. Andrade, N. Alexandre, I. Amorim, F. Gartner, A.C. Maurício, A.L. Luís, M. Gama, Studies on the biocompatibility of bacterial cellulose, J. Bioact. Compat. Polym. 28(1) (2013) 97-112.
[135] I. Drachuk, S. Harbaugh, R. Geryak, D.L. Kaplan, V.V. Tsukruk, N. Kelley-Loughnane, Immobilization of recombinant E. coli cells in a bacterial cellulose–silk composite matrix to preserve biological function, ACS Biomater. Sci. Eng. 3(10) (2017) 2278-2292.
[136] E.Y.X. Loh, N. Mohamad, M.B. Fauzi, M.H. Ng, S.F. Ng, M.C.I.M. Amin, Development of a bacterial cellulose-based hydrogel cell carrier containing keratinocytes and fibroblasts for full-thickness wound healing, Sci. Rep. 8(1) (2018) 2875.
[137] S.-P. Lin, H.-N. Kung, Y.-S. Tsai, T.-N. Tseng, K.-D. Hsu, K.-C. Cheng, Novel dextran modified bacterial cellulose hydrogel accelerating cutaneous wound healing, Cellulose 24(11) (2017) 4927-4937.
[138] J. Fontana, A. De Souza, C. Fontana, I. Torriani, J. Moreschi, B. Gallotti, S. De Souza, G. Narcisco, J. Bichara, L. Farah, Acetobacter cellulose pellicle as a temporary skin substitute, Appl. Biochem. Biotech. 24(1) (1990) 253-264.
[139] W. Czaja, A. Krystynowicz, S. Bielecki, R.M. Brown Jr, Microbial cellulose—the natural power to heal wounds, Biomaterials 27(2) (2006) 145-151.
[140] W.K. Czaja, D.J. Young, M. Kawecki, R.M. Brown, The future prospects of microbial cellulose in biomedical applications, Biomacromolecules 8(1) (2007) 1-12.
[141] H.G. de Oliveira Barud, R.R. da Silva, H. da Silva Barud, A. Tercjak, J. Gutierrez, W.R. Lustri, O.B. de Oliveira Junior, S.J. Ribeiro, A multipurpose natural and renewable polymer in medical applications: Bacterial cellulose, Carbohyd. Polym. 153 (2016) 406-420.
[142] H.L.d. Almeida Jr, L. Monteiro, N.M. Rocha, H. Scheffer, Scanning electron microscopy of a blister roof in dystrophic epidermolysis bullosa, Anais brasileiros de dermatologia 88(6) (2013) 966-968.
[143] T. Volova, A. Shumilova, E. Nikolaeva, A. Kirichenko, E. Shishatskaya, Biotechnological wound dressings based on bacterial cellulose and degradable copolymer P (3HB/4HB), Int. J. Biol. Macromol. (2019).
[144] M.J. Tabaii, G. Emtiazi, Transparent nontoxic antibacterial wound dressing based on silver nano particle/bacterial cellulose nano composite synthesized in the presence of tripolyphosphate, Journal of Drug Delivery Science and Technology 44 (2018) 244-253.

[145] A. Gupta, D. Keddie, V. Kannappan, H. Gibson, I. Khalil, M. Kowalczuk, C. Martin, X. Shuai, I. Radecka, Production and characterisation of bacterial cellulose hydrogels loaded with curcumin encapsulated in cyclodextrins as wound dressings, European Polymer Journal 118 (2019) 437-450.
[146] A. Gupta, S.M. Briffa, S. Swingler, H. Gibson, V. Kannappan, G. Adamus, M. Kowalczuk, C. Martin, I. Radecka, Synthesis of Silver Nanoparticles Using Curcumin-Cyclodextrins Loaded into Bacterial Cellulose-Based Hydrogels for Wound Dressing Applications, Biomacromolecules (2020).
[147] Y. Wang, C. Wang, Y. Xie, Y. Yang, Y. Zheng, H. Meng, W. He, K. Qiao, Highly transparent, highly flexible composite membrane with multiple antimicrobial effects used for promoting wound healing, Carbohyd. Polym. 222 (2019) 114985.
[148] H. Kono, H. Tsujisaki, K. Tajima, Reinforcing Poly (methyl methacrylate) with Bacterial Cellulose Nanofibers Chemically Modified with Methacryolyl Groups, Nanomaterials 12(3) (2022) 537.
[149] A. Santmarti, J.W. Teh, K.-Y. Lee, Transparent poly (methyl methacrylate) composites based on bacterial cellulose nanofiber networks with improved fracture resistance and impact strength, Acs Omega 4(6) (2019) 9896-9903.
[150] Y. Han, C. Li, Q. Cai, X. Bao, L. Tang, H. Ao, J. Liu, M. Jin, Y. Zhou, Y. Wan, Studies on bacterial cellulose/poly (vinyl alcohol) hydrogel composites as tissue-engineered corneal stroma, Biomedical Materials 15(3) (2020) 035022.
[151] S.S. de Souza, F.V. Berti, K.P. de Oliveira, C.Q. Pittella, J.V. de Castro, C. Pelissari, C.R. Rambo, L.M. Porto, Nanocellulose biosynthesis by Komagataeibacter hansenii in a defined minimal culture medium, Cellulose 26(3) (2019) 1641-1655.
[152] S. Wang, T. Li, C. Chen, W. Kong, S. Zhu, J. Dai, A.J. Diaz, E. Hitz, S.D. Solares, T. Li, Transparent, anisotropic biofilm with aligned bacterial cellulose nanofibers, Adv. Funct. Mater. 28(24) (2018) 1707491.
[153] N. Yin, M.D. Stilwell, T.M. Santos, H. Wang, D.B. Weibel, Agarose particle-templated porous bacterial cellulose and its application in cartilage growth in vitro, Acta biomaterialia 12 (2015) 129-138.
[154] S. Wichai, P. Chuysinuan, S. Chaiarwut, P. Ekabutr, P. Supaphol, Development of bacterial cellulose/alginate/chitosan composites incorporating copper (II) sulfate as an antibacterial wound dressing, Journal of Drug Delivery Science and Technology 51 (2019) 662-671.
[155] D. Zmejkoski, D. Spasojević, I. Orlovska, N. Kozyrovska, M. Soković, J. Glamočlija, S. Dmitrović, B. Matović, N. Tasić, V. Maksimović, Bacterial cellulose-lignin composite hydrogel as a promising agent in chronic wound healing, Int. J. Biol. Macromol. 118 (2018) 494-503.
[156] S. Ye, L. Jiang, J. Wu, C. Su, C. Huang, X. Liu, W. Shao, Flexible amoxicillin-grafted bacterial cellulose sponges for wound dressing: in vitro and in vivo evaluation, ACS applied materials & interfaces 10(6) (2018) 5862-5870.
[157] P. Basmaji, G.M. de Olyveira, M.L. dos Santos, A.C. Guastaldi, Novel antimicrobial peptides bacterial cellulose obtained by symbioses culture between polyhexanide biguanide (PHMB) and green tea, Journal of Biomaterials and Tissue Engineering 4(1) (2014) 59-64.
[158] R. Portela, C.R. Leal, P.L. Almeida, R.G. Sobral, Bacterial cellulose: a versatile biopolymer for wound dressing applications, Microbial biotechnology 12(4) (2019) 586-610.

[159] G.W. Thomas, L.T. Rael, R. Bar-Or, R. Shimonkevitz, C.W. Mains, D.S. Slone, M.L. Craun, D. Bar-Or, Mechanisms of delayed wound healing by commonly used antiseptics, Journal of Trauma and Acute Care Surgery 66(1) (2009) 82-91.
[160] S.E. Brooks, M.A. Walczak, R. Hameed, P. Coonan, Chlorhexidine resistance in antibiotic-resistant bacteria isolated from the surfaces of dispensers of soap containing chlorhexidine, Infection Control & Hospital Epidemiology 23(11) (2002) 692-695.
[161] S. Koljalg, P. Naaber, M. Mikelsaar, Antibiotic resistance as an indicator of bacterial chlorhexidine susceptibility, Journal of Hospital Infection 51(2) (2002) 106-113.
[162] L.D. Lozeau, J. Grosha, I.M. Smith, E.J. Stewart, T.A. Camesano, M.W. Rolle, Alginate Affects Bioactivity of Chimeric Collagen Binding LL37 Antimicrobial Peptides Adsorbed to Collagen-Alginate Wound Dressings, ACS Biomater. Sci. Eng. (2020).
[163] A. Izadpanah, R.L. Gallo, Antimicrobial peptides, Journal of the American Academy of Dermatology 52(3) (2005) 381-390.
[164] D. Ciumac, H. Gong, X. Hu, J.R. Lu, Membrane targeting cationic antimicrobial peptides, Journal of colloid and interface science 537 (2019) 163-185.
[165] Q.-Y. Zhang, Z.-B. Yan, Y.-M. Meng, X.-Y. Hong, G. Shao, J.-J. Ma, X.-R. Cheng, J. Liu, J. Kang, C.-Y. Fu, Antimicrobial peptides: mechanism of action, activity and clinical potential, Military Medical Research 8 (2021) 1-25.
[166] P. Kumar, J.N. Kizhakkedathu, S.K. Straus, Antimicrobial peptides: diversity, mechanism of action and strategies to improve the activity and biocompatibility in vivo, Biomolecules 8(1) (2018) 4.
[167] J.D. Hale, R.E. Hancock, Alternative mechanisms of action of cationic antimicrobial peptides on bacteria, Expert review of anti-infective therapy 5(6) (2007) 951-959.
[168] T.-H. Lee, K. N Hall, M.-I. Aguilar, Antimicrobial peptide structure and mechanism of action: a focus on the role of membrane structure, Current topics in medicinal chemistry 16(1) (2016) 25-39.
[169] F. Abrunhosa, S. Faria, P. Gomes, I. Tomaz, J.C. Pessoa, D. Andreu, M. Bastos, Interaction and lipid-induced conformation of two cecropin− melittin hybrid peptides depend on peptide and membrane composition, The Journal of Physical Chemistry B 109(36) (2005) 17311-17319.
[170] E. Strandberg, P. Wadhwani, P. Tremouilhac, U.H. Dürr, A.S. Ulrich, Solid-state NMR analysis of the PGLa peptide orientation in DMPC bilayers: structural fidelity of 2H-labels versus high sensitivity of 19F-NMR, Biophysical journal 90(5) (2006) 1676-1686.
[171] J.P. Silva, R. Appelberg, F.M. Gama, Antimicrobial peptides as novel anti-tuberculosis therapeutics, Biotechnology advances 34(5) (2016) 924-940.
[172] G. Wang, J.L. Narayana, B. Mishra, Y. Zhang, F. Wang, C. Wang, D. Zarena, T. Lushnikova, X. Wang, Design of antimicrobial peptides: progress made with human cathelicidin LL-37, Antimicrobial Peptides: Basics for Clinical Application (2019) 215-240.
[173] L.D. Lozeau, J. Grosha, D. Kole, F. Prifti, T. Dominko, T.A. Camesano, M.W. Rolle, Collagen tethering of synthetic human antimicrobial peptides cathelicidin LL37 and its effects on antimicrobial activity and cytotoxicity, Acta biomaterialia 52 (2017) 9-20.
[174] J. Ageitos, A. Sánchez-Pérez, P. Calo-Mata, T. Villa, Antimicrobial peptides (AMPs): Ancient compounds that represent novel weapons in the fight against bacteria, Biochemical pharmacology 133 (2017) 117-138.
[175] G. Wang, X. Li, Z. Wang, APD3: the antimicrobial peptide database as a tool for research and education, Nucleic acids research 44(D1) (2016) D1087-D1093.

[176] G. Wang, Human antimicrobial peptides and proteins, Pharmaceuticals 7(5) (2014) 545-594.
[177] R. Ramos, J.P. Silva, A.C. Rodrigues, R. Costa, L. Guardão, F. Schmitt, R. Soares, M. Vilanova, L. Domingues, M. Gama, Wound healing activity of the human antimicrobial peptide LL37, Peptides 32(7) (2011) 1469-1476.
[178] M.G. Scott, D.J. Davidson, M.R. Gold, D. Bowdish, R.E. Hancock, The human antimicrobial peptide LL-37 is a multifunctional modulator of innate immune responses, The journal of immunology 169(7) (2002) 3883-3891.
[179] R.E. Hancock, H.-G. Sahl, Antimicrobial and host-defense peptides as new anti-infective therapeutic strategies, Nature biotechnology 24(12) (2006) 1551-1557.
[180] J. Kang, M.J. Dietz, B. Li, Antimicrobial peptide LL-37 is bactericidal against Staphylococcus aureus biofilms, PLoS One 14(6) (2019).
[181] L.D. Lozeau, S. Youssefian, N. Rahbar, T.A. Camesano, M.W. Rolle, Concentration-Dependent, Membrane-Selective Activity of Human LL37 Peptides Modified with Collagen Binding Domain Sequences, Biomacromolecules 19(12) (2018) 4513-4523.
[182] B. Jacob, I.S. Park, J.K. Bang, S.Y. Shin, Short KR-12 analogs designed from human cathelicidin LL-37 possessing both antimicrobial and antiendotoxic activities without mammalian cell toxicity, Journal of Peptide Science 19(11) (2013) 700-707.
[183] Ø. Samuelsen, H.H. Haukland, B.C. Kahl, C. von Eiff, R.A. Proctor, H. Ulvatne, K. Sandvik, L.H. Vorland, Staphylococcus aureus small colony variants are resistant to the antimicrobial peptide lactoferricin B, Journal of Antimicrobial Chemotherapy 56(6) (2005) 1126-1129.
[184] G. Wang, Structures of human host defense cathelicidin LL-37 and its smallest antimicrobial peptide KR-12 in lipid micelles, Journal of Biological Chemistry 283(47) (2008) 32637-32643.
[185] G. Wang, K.M. Watson, R.W. Buckheit Jr, Anti-human immunodeficiency virus type 1 activities of antimicrobial peptides derived from human and bovine cathelicidins, Antimicrobial agents and chemotherapy 52(9) (2008) 3438-3440.
[186] N. Fabisiak, A. Fabisiak, A. Chmielowiec-Korzeniowska, L. Tymczyna, W. Kamysz, R. Kordek, M. Bauer, E. Kamysz, J. Fichna, Anti-inflammatory and antibacterial effects of human cathelicidin active fragment KR-12 in the mouse models of colitis: a novel potential therapy of inflammatory bowel diseases, Pharmacological Reports 73 (2021) 163-171.
[187] Z. Hu, T. Murakami, K. Suzuki, H. Tamura, K. Kuwahara-Arai, T. Iba, I. Nagaoka, Antimicrobial cathelicidin peptide LL-37 inhibits the LPS/ATP-induced pyroptosis of macrophages by dual mechanism, PLoS One 9(1) (2014) e85765.
[188] P.G. Adams, L. Lamoureux, K.L. Swingle, H. Mukundan, G.A. Montaño, Lipopolysaccharide-induced dynamic lipid membrane reorganization: tubules, perforations, and stacks, Biophysical journal 106(11) (2014) 2395-2407.
[189] C.R. Raetz, Bacterial endotoxins: extraordinary lipids that activate eucaryotic signal transduction, J. Bacteriol. 175(18) (1993) 5745-5753.
[190] E.T. Rietschel, T. Kirikae, F.U. Schade, U. Mamat, G. Schmidt, H. Loppnow, A.J. Ulmer, U. Zähringer, U. Seydel, F. Di Padova, Bacterial endotoxin: molecular relationships of structure to activity and function, The FASEB Journal 8(2) (1994) 217-225.
[191] S.I. Miller, R.K. Ernst, M.W. Bader, LPS, TLR4 and infectious disease diversity, Nature Reviews Microbiology 3(1) (2005) 36-46.

[192] S. Akira, S. Uematsu, O. Takeuchi, Pathogen recognition and innate immunity, Cell 124(4) (2006) 783-801.
[193] C.A. Janeway Jr, R. Medzhitov, Innate immune recognition, Annual review of immunology 20(1) (2002) 197-216.
[194] S. Bhattacharjya, De novo designed lipopolysaccharide binding peptides: structure based development of antiendotoxic and antimicrobial drugs, Current medicinal chemistry 17(27) (2010) 3080-3093.
[195] Y. Rosenfeld, N. Papo, Y. Shai, Endotoxin (lipopolysaccharide) neutralization by innate immunity host-defense peptides: peptide properties and plausible modes of action, Journal of Biological Chemistry 281(3) (2006) 1636-1643.
[196] J. Diosa, F. Guzman, C. Bernal, M. Mesa, Formation mechanisms of chitosan-silica hybrid materials and its performance as solid support for KR-12 peptide adsorption: Impact on KR-12 antimicrobial activity and proteolytic stability, Journal of Materials Research and Technology 9(1) (2020) 890-901.
[197] M. Liu, T. Liu, X. Zhang, Z. Jian, H. Xia, J. Yang, X. Hu, M. Xing, G. Luo, J. Wu, Fabrication of KR-12 peptide-containing hyaluronic acid immobilized fibrous eggshell membrane effectively kills multi-drug-resistant bacteria, promotes angiogenesis and accelerates re-epithelialization, International journal of nanomedicine 14 (2019) 3345.
[198] H. Ao, C. Chen, K. Xie, J. Zhou, T. Long, T. Tang, B. Yue, Covalent immobilization of KR-12 peptide onto a titanium surface for decreasing infection and promoting osteogenic differentiation, Rsc Advances 6(52) (2016) 46733-46743.
[199] T. Long, H. Li, X. Wang, B. Yue, A comparative analysis of antibacterial properties and inflammatory responses for the KR-12 peptide on titanium and PEGylated titanium surfaces, RSC advances 7(55) (2017) 34321-34330.
[200] K. Chanci, J. Diosa, M.A. Giraldo, M. Mesa, Physical behavior of KR-12 peptide on solid surfaces and Langmuir-Blodgett lipid films: Complementary approaches to its antimicrobial mode against S. aureus, Biochimica et Biophysica Acta (BBA)-Biomembranes 1864(1) (2022) 183779.
[201] O. Shoseyov, Z. Shani, I. Levy, Carbohydrate binding modules: biochemical properties and novel applications, Microbiol. Mol. Biol. Rev. 70(2) (2006) 283-295.
[202] A.B. Boraston, D.N. Bolam, H.J. Gilbert, G.J. Davies, Carbohydrate-binding modules: fine-tuning polysaccharide recognition, Biochemical journal 382(3) (2004) 769-781.
[203] D. Guillén, S. Sánchez, R. Rodríguez-Sanoja, Carbohydrate-binding domains: multiplicity of biological roles, Appl. Microbiol. Biot. 85(5) (2010) 1241-1249.
[204] E.M. van Zyl, J.M. Coburn, Hierarchical structure of bacterial-derived cellulose and its impact on biomedical applications, Curr. Opin. Chem. Eng. 24 (2019) 122-130.
[205] A. Bernardes, V. Pellegrini, F. Curtolo, C. Camilo, B. Mello, M. Johns, J. Scott, F. Guimaraes, I. Polikarpov, Carbohydrate binding modules enhance cellulose enzymatic hydrolysis by increasing access of cellulases to the substrate, Carbohyd. Polym. 211 (2019) 57-68.
[206] F.K. Andrade, S.M.G. Moreira, L. Domingues, F. Gama, Improving the affinity of fibroblasts for bacterial cellulose using carbohydrate-binding modules fused to RGD, J Biomed. Mater. Res. A 92(1) (2010) 9-17.
[207] F.K. Andrade, R. Costa, L. Domingues, R. Soares, M. Gama, Improving bacterial cellulose for blood vessel replacement: Functionalization with a chimeric protein containing a cellulose-binding module and an adhesion peptide, Acta Biomaterialia 6(10) (2010) 4034-4041.

[208] R. Pértile, S. Moreira, F. Andrade, L. Domingues, M. Gama, Bacterial cellulose modified using recombinant proteins to improve neuronal and mesenchymal cell adhesion, Biotechnology progress 28(2) (2012) 526-532.
[209] M. Florea, H. Hagemann, G. Santosa, J. Abbott, C.N. Micklem, X. Spencer-Milnes, L. de Arroyo Garcia, D. Paschou, C. Lazenbatt, D. Kong, Engineering control of bacterial cellulose production using a genetic toolkit and a new cellulose-producing strain, P. Natl. Acad. Sci. USA (2016) 201522985.
[210] N. Khazanov, T. Iline-Vul, E. Noy, G. Goobes, H. Senderowitz, Design of compact biomimetic cellulose binding peptides as carriers for cellulose catalytic degradation, The Journal of Physical Chemistry B 120(2) (2016) 309-319.
[211] J. Guo, J.M. Catchmark, M.N.A. Mohamed, A.J. Benesi, M. Tien, T.-h. Kao, H.D. Watts, J.D. Kubicki, Identification and characterization of a cellulose binding heptapeptide revealed by phage display, Biomacromolecules 14(6) (2013) 1795-1805.
[212] R. Weishaupt, J.N. Zünd, L. Heuberger, F. Zuber, G. Faccio, F. Robotti, A. Ferrari, G. Fortunato, Q. Ren, K. Maniura-Weber, Antibacterial, Cytocompatible, Sustainably Sourced: Cellulose Membranes with Bifunctional Peptides for Advanced Wound Dressings, Advanced Healthcare Materials (2020) 1901850.

3. Chapter 3: Development of Optically Clear Bacterial Cellulose

Structural properties of optically clear bacterial cellulose produced by *Komagataeibacter hansenii* using arabitol

Elizabeth M. van Zyl[a], Mitchell A. Kennedy[b], Wendy Nason[c], Sawyer J. Fenlon[a], Eric M. Young[d], Luis J. Smith[c], Surita R Bhatia[b], Jeannine M. Coburn[a]

[a] Department of Biomedical Engineering, Worcester Polytechnic Institute, Worcester, MA 01609
[b] Department of Chemistry, Stony Brook University, Stony Brook, NY 11794
[c] Carlson School of Chemistry and Biochemistry, Clark University, Worcester, MA 01610
[d] Department of Chemical Engineering, Worcester Polytechnic Institute, Worcester, MA 01609

The following chapter appears in van Zyl, E. M., Kennedy, M. A., Nason, W., Fenlon, S. J., Young, E. M., Smith, L. J., Bhatia, S. R., and Coburn, J. M., "Structural properties of optically clear bacterial cellulose produced by *Komagataeibacter hansenii* using arabitol." *Biomaterials Advances* 148 (2023): 213345 and is reproduced here with permission from Elsevier. Sections involving serum absorption capabilities are a new addition. Supporting information from the manuscript has been brought into the body of this chapter.

3.1. Abstract and Graphical Abstract

Bacterial cellulose (BC) exhibits beneficial properties for use in biomedical applications but is limited by its lack of tunable transparency capabilities. To overcome this deficiency, a novel method to synthesize transparent BC materials using an alternative carbon source, namely arabitol, was developed. Characterization of the BC pellicles was performed for yield, transparency, surface morphology, and molecular assembly. Transparent BC was produced using mixtures of glucose and arabitol. Zero percent arabitol pellicles exhibited 25% light transmittance, which increased with increasing arabitol concentration through to 75% light transmittance. While transparency increased, overall BC yield was maintained indicating that the altered transparency may be induced on a micro-scale rather than a macro-scale. Significant differences in fiber diameter and the presence of aromatic signatures were observed. Overall, this research outlines methods for producing BC with tunable optical transparency, while also bringing new insight to insoluble components of exopolymers produced by *Komagataeibacter hansenii*.

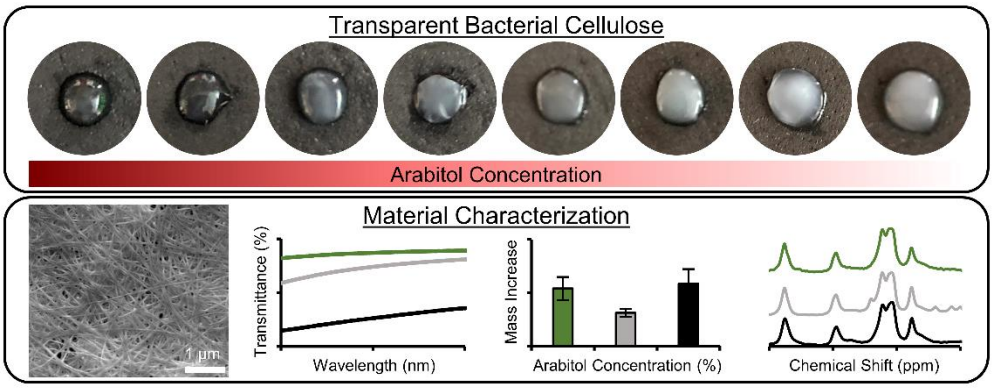
Transparent Bacterial Cellulose
Arabitol Concentration
Material Characterization
1 µm
Transmittance (%)
Wavelength (nm)
Mass Increase
Arabitol Concentration (%)
Chemical Shift (ppm)

3.2. Introduction

Transparent materials are needed in biomedical applications like wound dressing, to monitor healing, and in biosensing, to interface with optical devices. Predominantly produced by *Komagataeibacter* ssp., BC is synthesized and extruded as ribbon-like microfibers that further self-assemble into network-structured pellicles at the air-liquid interface of static liquid cultures [1]. This network structure and BC's composition of $\beta(1 \rightarrow 4)$ linked D-glucose monomer units produces cellulose with inherent biocompatibility, water holding capacity, liquid/gas permeability, and handleability properties [2-4]. However, only a few reports have qualitatively described methods for transparent BC production [2-6].

The predominant method to induce transparency in BC is through the incorporation of composite materials such as poly(2-hydroxyethyl methacrylate) (PHEMA), poly(methyl methacrylate) (PMMA), (poly(ethylene glycol) (PEG), and cyclodextrin [2-7]. PHEMA, commonly used in soft contact lenses, exhibits around 95% light transmittance in its pure form [6]. Di et al. found that, by making a BC/PHEMA composite, the transmittance of native BC can be increased by roughly 10% [6]. Similarly, Kono et al. increased the overall transparency of BC fibers by increasing the concentration of PMMA as a composite material [7]. Though beneficial for increasing transparency, the incorporation of composite materials increases cost and manufacturing time. Furthermore, synthesis of pure transparent BC would allow for increased use in biomedical applications such as for wound care and biosensing [8].

Utilizing defined minimal culture medium, Souza et al. was able to produce pure transparent BC from a *Komagataeibacter hansenii* [9]. It was noted that the transparent material had a lower fiber density compared to cellulose formed in full culture medium. This low fiber density was attributed to nutrient restriction caused by the defined minimal medium. Wang et al. observed similar changes in transparency when creating anisotropic biofilms with aligned BC nanofibers [10]. BC pellicles stretched to 40% strain exhibited increased light transmittance properties when compared to unstretched pellicles [11]. These three findings suggest that altering the morphology and hierarchical structure of the cellulose fibers may alter the

optical properties of the material. These findings further point to media formulation, specifically nutrient restriction in defined medium, as a possible way to control morphology and structure of BC.

Several studies have investigated the media formulation for its impact on BC production and yield. These focus largely on different carbon sources and associated concentrations. Specifically, pure hexose and hexose-derived polyol sugars, such as glucose, fructose, and mannitol, allow for higher cellulose production, while pentose and pentose-derived polyol sugars, such as xylose, xylitol, and arabitol, result in decreased cellulose production [12, 13]. Additionally, BC has been effectively produced using complex media like waste fruit juice, orange peels, molasses, cheese whey, and other industrial/food waste sources [14-16]. These waste resources are generally rich in mixtures of hexose sugars such as glucose and fructose, and typically result in high cellulose production [17].

Besides changes in overall cellulose production, differences in cellulose hierarchical structure, notably the crystallinity, have been observed when comparing hexose and pentose carbon sources [18, 19]. Keshk and Sameshima determined that the use of glucose produced cellulose with 88% crystallinity, while pentose and pentose-derived sugars such as arabitol and xylose produced cellulose with a degree of crystallinity as low as 75% [18, 19]. While altered transparency was not reported in these studies, it is generally understood that polymer matrices become more opaque with increasing crystallinity [20].

The mechanism by which this altered crystallinity occurs is not fully understood but it is believed to be due to differences in the metabolic pathways of specific hexose and pentose sugars [19, 21, 22]. Since BC is made from uridine diphosphate-glucose monomers, it is thought that hexose and hexose-derived sugars like glucose, fructose, and mannitol can readily be converted to BC monomers [23]. This would explain the high BC production on these sugars [24]. However, pentose and pentose-derived sugars, such as arabitol and xylose, are metabolized through the pentose phosphate pathway (PPP), which means that bacteria cultured with pentose sugars as a carbon source must instead use the gluconeogenesis pathway to

synthesize BC monomers [19, 23]. This increased energetic cost likely results in the observed low BC production from pentose sugars.

Based on the likely connection between carbon source metabolism, BC structure, and transparency, we investigated and characterized BC pellicles produced using different ratios of hexose and pentose sugar mixtures. We chose, the pentose sugar, arabitol, because of its impact on the PPP under certain conditions, as shown by Oikawa et al. [19]. Blends of arabitol and glucose with a constant total carbon source molarity were investigated. The objective was to determine the relationship between cellulose transparency and molecular level properties to gain an understanding of the transparency. The bacterial growth rates, BC yield, transparency, morphology, and hierarchical chemical structure of BC formed were evaluated.

3.3. Materials and Methods

3.3.1. Materials

Komagataeibacter hansenii NQ5 (*K. hansenii* ATCC 53582) was purchased from the American Type Culture Collection (ATCC), Manassas, VA, USA. Bacto™ peptone and Difco™ yeast extract was purchased from Becton, Dickenson and Company, Franklin Lakes, NJ, USA, while agar was sourced from Sunrise Science Products, San Diego, CA, USA. D-arabitol (>99% purity), and sodium chloride (ACS reagent, ≥99% purity) were purchased from Alfa Aesar Co., Inc, China. D-glucose (BioReagent, ≥99.5% purity), citric acid (99% purity), sodium phosphate dibasic (BioReagent, ≥99.5% purity), sodium hydroxide (ACS reagent, ≥97.0% purity), calcium chloride (≥93% purity), and cellulase from *Trichoderma reesei* (aqueous solution, ≥700 units/g) were sourced from Sigma-Aldrich, Burlington, MA, USA. Human male heat inactivated AB plasma-derived serum was sourced from Access Biologicals LLC, Vista, CA, USA. Iscove's modified Dulbecco's medium was purchased from Lonza Biologics, Walkersville, MD, USA, while fetal bovine serum (FBS), 0.25% trypsin-EDTA, penicillin streptomycin, and 200mM L-glutamine were sourced from Life Technologies, Waltham, MA, USA. Animal-free recombinant human epidermal

growth factor (EGF) and fibroblast growth factor (FGF) were purchased from PeproTech, Waltham, MA, USA. Tris buffered saline (TBS) was sourced from VWR Life Sciences, Bridgeport, NJ, USA. All well plates were sourced from Greiner Bio-One, Monroe, NC, USA, and Falcon™ round-bottom test tubes were sourced from Corning, Inc, Corning, NY, USA.

3.3.2. BC pellicle production and purification

The cellulose-producing bacterial strain, *Komagataeibacter hansenii NQ5* was streaked onto a Hestrin Schramm (HS) agar plate (20 mg/mL glucose, 5 mg/mL peptone, 5 mg/mL yeast extract, 1.15 mg/mL citric acid, 2.7 mg/mL disodium phosphate, 15 mg/mL agar) and allowed to grow at 30°C for 4 d. Single colonies from the HS plate were used to inoculate 5 mL of HS liquid medium (20 mg/mL glucose, 5 mg/mL peptone, 5 mg/mL yeast extract, 1.15 mg/mL citric acid, 2.7 mg/mL disodium phosphate) in a 14 mL Falcon™ round bottom culture tube and allowed to grow on a rotating drum for 4 d at 30°C. The culture was then expanded in static cultures using 10% (v/v) inoculum in fresh HS medium. Fresh HS medium without a carbon source was then inoculated with 0.1% (v/v) static cultured bacteria and supplemented to 1 mM of total carbon source. To allow for pellicle formation, 2 mL of inoculated HS media, was cultured in 12-well tissue culture plates under static conditions at 30°C for 7 d. To purify the BC pellicles, they were removed, washed in 0.1 M NaOH at 60°C for 4 h, and then rinsed with DI H_2O until the fluid reached a neutral pH (**Figure 3.1**).

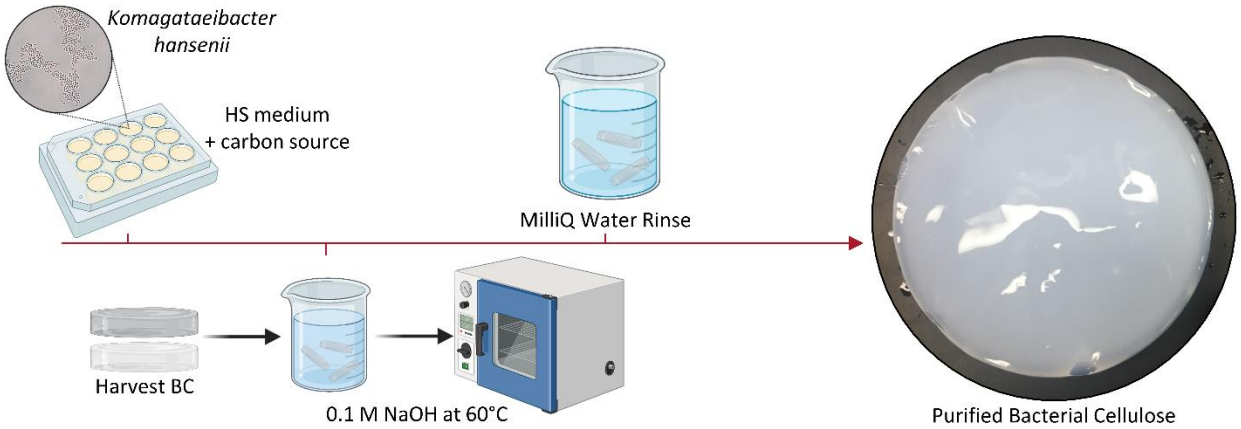

Figure 3.1. BC synthesis and purification method
Made using Biorender.com

3.3.3. Cellulose yield

To determine the effects of varying concentrations of glucose and arabitol as a carbon source, fresh HS medium without a carbon source was inoculated with 0.1% (v/v) static cultured bacteria. The media was supplemented to 1 mM of total carbon source with mixtures of D-arabitol and D-glucose (**Table 3.1)**. From here on, the arabitol/glucose combination will be reported as per the given label and referred to as the "arabitol concentration."

Table 3.1. Arabitol and glucose concentrations used for bacteria growth and BC production

Label	Arabitol Concentration (mM)	Glucose Concentration (mM)
100% Arabitol	1.00	0.00
95% Arabitol	0.95	0.05
90% Arabitol	0.90	0.10
85% Arabitol	0.85	0.15
80% Arabitol	0.80	0.20
75% Arabitol	0.75	0.25
50% Arabitol	0.50	0.50
25% Arabitol	0.25	0.75
0% Arabitol	0.00	1.00

Pellicles were allowed to form and were purified using the methods described above. Purified pellicles were weighed while hydrated and then lyophilized using a shelf lyophilizer (Labconco, Kansas City, MO) for 48 h at a temperature of -25°C and an absolute vacuum pressure of 0.210 Torr. Estimated BC pellicle thickness was calculated using the hydrated weight and Equation 1:

$$volume = \frac{mass}{density} \qquad \textit{Equation 1}$$

where mass refers to the hydrated BC pellicle weight and density refers to the reported hydrated cellulose density of 1.25 g cm^{-3} [25]. In this case, the volume refers to that of a cylinder, $\pi r^2 h$, where r is the radius of a well in a 12-well plate, and h refers to pellicle thickness. Estimated BC pellicle thickness was determined by solving for h. Sideview images were also taken to qualitatively compare the thickness of the

pellicles. After lyophilized pellicles were weighed, the bacterial cellulose yield was calculated using **Equation 2**.

$$\%\ yield = \frac{cellulose\ dry\ weight}{total\ carbon\ source\ weight} \times 100 \qquad Equation\ 2$$

The total carbon source mass was calculated using the molar concentrations, the molecular masses, and the total volumes of all carbon sources in culture.

3.3.4. Bacterial growth kinetics

Growth kinetic studies were performed to identify the effects of arabitol concentration on the growth rate of *K. hansenii*. In a 96-well plate, inoculated HS media was supplemented with 0.4% (v/v) cellulase from *Trichoderma reesei*. The media was supplemented with carbon sources (**Table 3.1**). Absorbance measurements at 600 nm were taken every 30 m for 7 d under shaken conditions at 30°C (Biotek Synergy H1, Winooski, VT). The maximum growth rate (μ_{max}) was identified from the slope of the linear region of the kinetic curves (**Figure 3.2**).

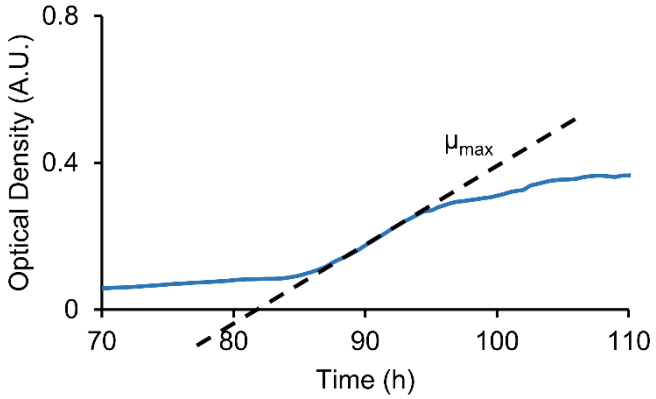

Figure 3.2. Representative bacterial growth kinetic curve.
Dashed line indicating how μ_{max} was identified from the linear region of the curve.

3.3.5. Light transmission analysis

The light transmission of freshly produced BC pellicles was measured in the visible light region using a UV-Vis spectrophotometer (Thermo Scientific Evolution 300 UV-Visible Spectrophotometer, Waltham, MA). All transmissions readings were performed inside the enclosed UV-Vis spectrophotometer

chamber, to prevent light reflection from outside sources. Transmission spectral readings were performed between wavelengths of 300-800 nm with a step size of 2 nm. Average visible light transmission (400 – 700 nm range) was compared between test groups. Using this method, light transmission measurements of a commercially available transparent hydrogel wound dressing (Covidien^{TM} Kendall^{TM}, Mansfield, MA) were also performed.

3.3.6. Liquid absorption

The liquid absorption capabilities of BC pellicles were assessed in both human serum and a salt solution containing 142 mM sodium chloride and 3.3. mM calcium chloride in de-ionized water. Both the human serum and salt solution was prewarmed to 37°C. Lyophilized BC pellicles were weighed and placed in either the serum or salt solution weighing a minimum of 40-times that of the lyophilized BC pellicles and incubated at 37°C. Pellicles were weighed at 1 h and 24 h after initial submersion in each respective liquid (. Liquid absorbance was then calculated relative to the dry material weight. Using this method, the liquid absorption properties in both serum and the salt solution were also determined for a commercially available foam based wound dressing and transparent hydrogel based wound dressing (Covidien^{TM} Kendall^{TM}, Mansfield, MA).

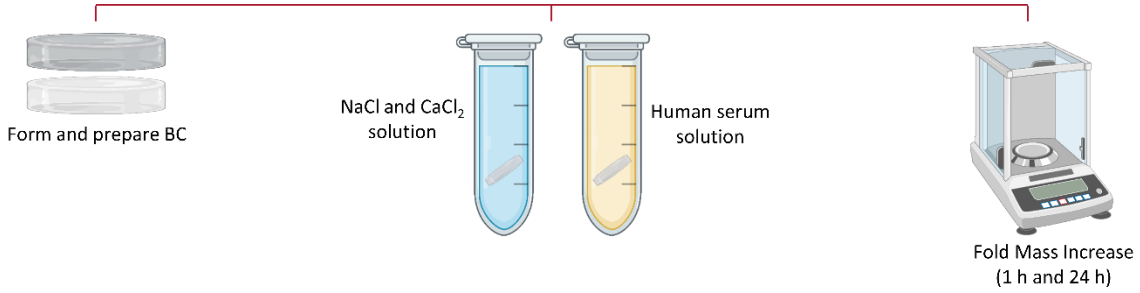

Figure 3.3. Salt based and serum based liquid absorption assessment method
Made using Biorender.com

3.3.7. Cytotoxicity Analysis

Cytotoxicity studies were performed to determine if the BC pellicles produced using different carbon source mixtures impact overall material biocompatibility. BC pellicles produced using 85% and 0% arabitol was used to compare cytotoxicity. BC pellicles were formed in 96-well plates and purified as

described above, then autoclaved in 1x tris-buffered saline (TBS; 25 mM tris, 140 mM NaCl, 3 mM KCl, pH 7.2). Normal Human Dermal Fibroblasts (NHDF; American Type Culture Collection CRL-2565) were cultured in growth medium (Iscove's modified Dulbecco's medium, 10% FBS, 100 U/mL penicillin, 100 µg/mL streptomycin, 2 mM L-glutamine, 0.01 µg/mL EGF, 0.005 µg/mL FGF) at 37°C and 5% CO_2. Cells were passaged serially using 0.25% trypsin-EDTA. For cytotoxicity studies, wells in 48-well plates were seeded with 3,000 NHDF and the cells allowed to attach for 24 h. BC pellicles were then placed in cell seeded wells. Three days after adding BC pellicles, a resazurin metabolic assay was performed to quantify cell metabolism. Fluorescent signal of the resazurin solution after incubation were read at an excitation wavelength of 544 nm and emission wavelength of 590 nm using a SpectraMax M2 plate reader (Molecular Devices Inc., San Jose, CA). Cells were also cultured on tissue culture plastic (TCP) with no BC pellicles added as an untreated control, and resazurin solution was added to wells with no cells as a background control. Results were normalized to the untreated control measurements. Brightfield imaging of wells were performed in bright field an upright microscope (Nikon Eclipse E600, Tokyo, Japan) with a digital camera (Spot Insight CMOS 5.1, Sterling Heights, MI).

3.3.8. Scanning electron microscopy (SEM) and image analysis

The morphology of BC pellicles produced using 100%, 85%, 50%, and 0% arabitol concentration was evaluated to identify difference in cellulose fiber diameter. Pellicles were dried overnight, sputter coated with two coats of 4 nm of gold (Sputter Coater Cressinton 208hr, Watford, England) and imaged with a field emission scanning electron microscope using an 8-10 kV electron beam (Quanta 200 FEG MK11, FEI Inc., Hillsboro, Oregon). Images were taken at 30,000X and fiber diameter was analyzed manually using ImageJ, where a minimum of 200 fibers were analyzed per image.

3.3.9. Small-angle X-ray scattering (SAXS) and wide-angle X-ray scattering (WAXS)

Pellicles for small-angle scattering (SAXS) and wide-angle X-ray scattering (WAXS) were loaded into 1.0-mm glass thin-walled capillaries (Charles Supper, Westborough, MA). SAXS and WAXS measurements were conducted at the Complex Materials Scattering (CMS, 11-BM) beamline of the

National Synchrotron Light Source II (NSLS-II) at Brookhaven National Laboratory. The scattered data were collected using a beam energy of 13.5 keV and beam size of 200 X 200 μm with a Pilatus 2M area detector (Dectris, Switzerland). For SAXS studies, the detector, consisting of 0.172 mm square pixels in a 1475 × 1679 array, was placed five meters downstream from the sample position. The collected 2D scattering patterns were reduced to 1D scattering intensity, $I(q)$, by circular average, where q is the magnitude of the scattering vector, $q = (4\pi/\lambda)\sin(\theta)$, where λ is the wavelength of the incident X-ray beam, 0.9184 Å, and 2θ is the scattering angle. For SAXS studies, the q range measured was 0.0034 -0.185 A^{-1}. A blank of glass and air was subtracted from the original data for further analysis. Crystallite sizes were estimated qualitatively with the Scherrer equation, by evaluating the peak width at half maximum.

3.3.10. Solid-state nuclear magnetic resonance spectroscopy (NMR) analysis

Solid state NMR spectra were collected using a Varian Unity INOVA spectrometer. Cross-Polarization Magic Angle Spinning (CP-MAS) ^{13}C – (^{1}H) experiments were performed at a field strength of 9.4 T using a resonance frequency of 100.529 MHz for ^{13}C and 399.760 MHz for ^{1}H with a 4.0 mm Chemagnetics T3 probe and a spinning rate of 10 kHz. A Hahn echo was appended to the CP-MAS sequence with an echo delay of one rotor period. The ^{13}C 180° pulse of 5 μs was used for the echo. A ^{1}H 90° pulse of 3.3 μs and a constant amplitude spin lock pulse was used with a contact time of 2.0 ms, a ^{13}C radio frequency strength of 85 kHz and a ^{1}H radio frequency strength of 95 kHz. ^{1}H TPPM decoupling with a radio frequency strength of 100 kHz was used. All spectra were processed using the program RMN, version 2.01 (PhySy, Ltd., http://www.physyapps.com). The spectra were fit using a mixed gaussian/Lorentzian line shape in the DMFIT software suite [26]. All ^{13}C spectra were referenced to tetramethylsilane (0 ppm).

3.3.11. Statistical Analysis

All statistical analysis was performed using GraphPad Prism 7. Normality of fiber diameter data was evaluated through Shapiro-Wilk test. Statistical analysis of the cellulose yield, liquid absorption capabilities, and fiber diameter was conducted using an analysis of variance (ANOVA) followed by a Tukey

post-hoc test. Statistical analysis of cell viability was conducted using Welch's t-test. All data are presented as mean ± standard deviation (SD) unless otherwise indicated.

3.4. Results and Discussion

3.4.1. BC yield and light transmittance

Commonly, *K. hansenii* is cultured using glucose as a carbon source. In this work, we tested BC production using different mixtures of progressively increased arabitol and decreased glucose content (**Table 3.1**). Pellicles from the 100% arabitol group exhibited a significantly decreased BC yield of 0.6% (**Figure 3.4A**), with concomitant increased pellicle transparency (**Figure 3.4B, C**). Increased BC yield with incremental increases in glucose concentration were observed starting with the 95% arabitol group and peaking with the 75% arabitol group, with a maximum BC yield of 5.4%. This indicates that the addition of glucose and its subsequent metabolism directly aided in increased BC production. However, for the 50% to 0% arabitol groups a decrease in BC yield is observed. Though outside of the scope of the current work, the changes in yield may be due to altered metabolic processes. For instance, the low yield for the 100% arabitol group may be due to additional metabolic steps for arabitol utilization and the increased energetic cost associated with metabolism through the PPP. The decreased BC yield at the higher glucose concentrations may be due to gluconic acid production during glucose metabolism. An increase in gluconic acid production would decrease the pH of the culture, preventing effective BC formation [27, 28].

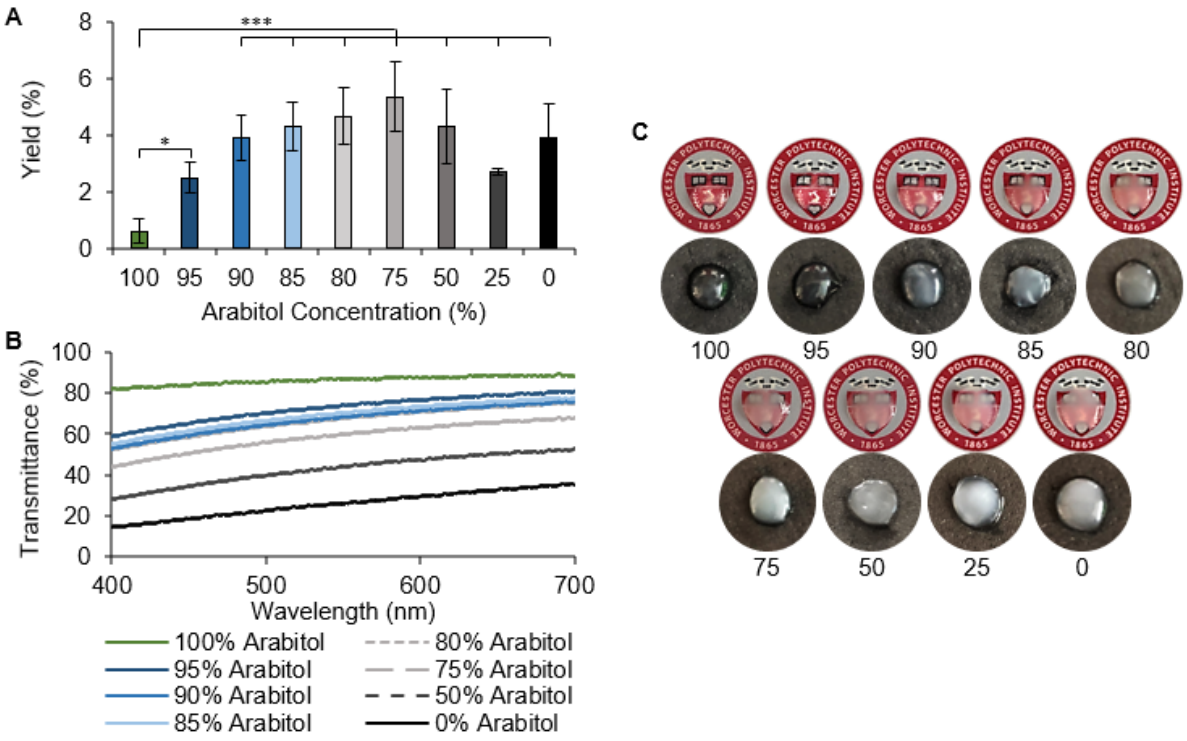

Figure 3.4. Yield and light transmittance of BC with varying arabitol concentrations.
(A) BC yield from bacteria cultured with decreased arabitol concentrations. Data are presented as mean ± SD from three independent experiments (n= 3 per experiment). Statistical differences determined by an ANOVA followed by the Tukey's HSD test (* $p < 0.01$, *** $p < 0.001$). **(B)** Increased transparency with increased arabitol concentrations shown through light transmission **(C)** and imaging.

When looking at transparency, pellicles from the 0% arabitol group exhibited an average light transmission of 25 ± 2%, while the pellicles from the 100% arabitol group exhibited light transmission of 89 ± 7% (**Figure 3.4B, C, Figure 3.5A, B**). For the mixed carbon source groups, a stepwise increase in light transmittance was observed between 0% and 80% arabitol (**Figure 3.4B**). This trend plateaus for pellicles in the 75%, 80%, 85%, 90%, and 95% arabitol groups at 58-73% light transmittance as indicated by the statistical significance compared to the transmittance for 0% arabitol at 26 ± 3%. When the arabitol concentration was increased from 95% to 100%, the light transmission increased from 73 ± 6% to 89 ± 7%, likely due to the significant decrease in BC yield.

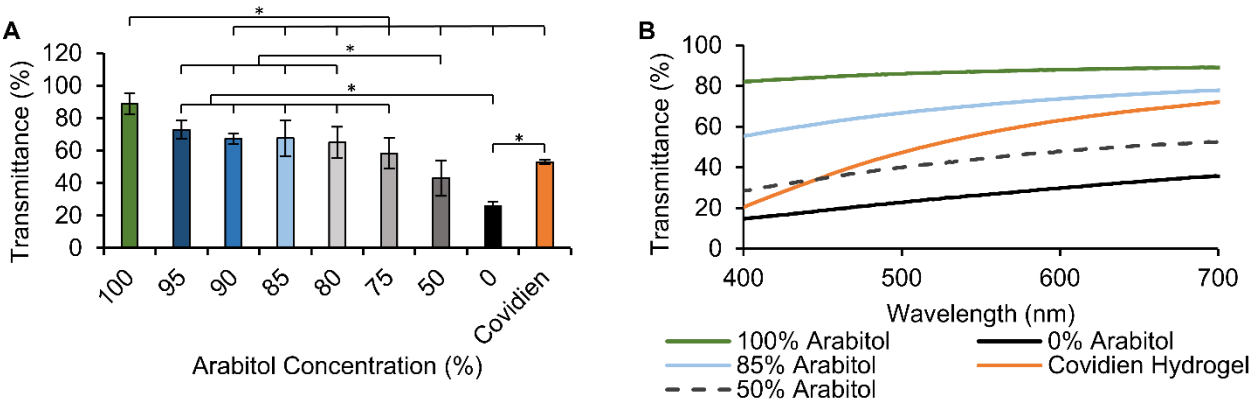

Figure 3.5. Average light transmittance of the BC pellicles and a commercial dressing (Covidien). (A) Average light transmittance across the visible light spectrum for BC pellicles and a commercially available hydrogel wound dressing. Data are presented as mean ± SD from three independent experiments (n = 3 per experiment). Statistical differences determined by an ANOVA followed by the Tukey's HSD test (* $p < 0.05$). (B) Increased transparency of BC using increased arabitol concentrations compared to spectral transparency readings of commercially available hydrogel wound dressing. Data averaged from three individual experiments (n = 3 per experiment).

The images in **Figure 3.4C** further emphasize the optical clarity of pellicles formed using 80% arabitol or higher. The increase in yield associated with consistently higher transmittance values for 80% - 90% arabitol groups indicated that the transparency was not a result of lower cellulose production. To ensure that differences in thickness and hydration did not affect light transmittance through the pellicles, side-view images and estimated thickness calculations were compared for each group (**Figure 3.6A, B**). Thickness was estimated using the wet mass of the BC pellicles and the relationship between volume, mass, and density. Where the material thickness was determined by using the reported hydrated cellulose density of 1.25 g cm^{-3} and solving for the height in the volume equation; $\pi r^2 h$ [25]. The estimated pellicle thickness was consistent with the low BC yield observed with 100% arabitol group. For the other groups (95% through 0% arabitol) a correlation between decreasing transparency and increasing BC thickness was not observed. In addition to pellicle thickness, a qualitative assessment of pellicle handleability was performed (**Figure 3.7**), where the top and bottom panels show different angles of the BC pellicle. For all groups other than 100% arabitol, no qualitative difference in handleability was observed (**Video S1-S5**).

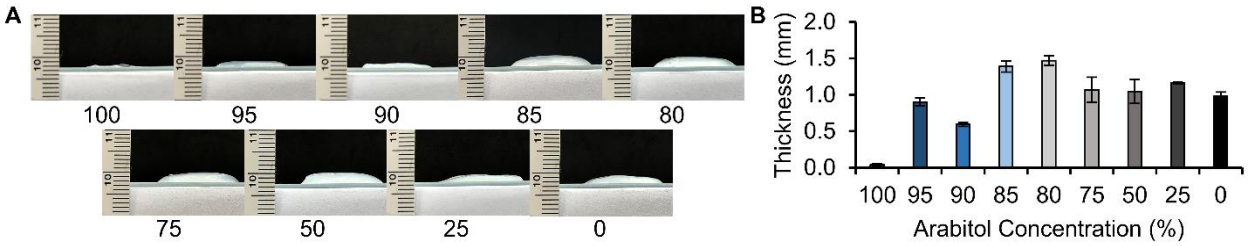

Figure 3.6 . BC pellicles hydration and thickness comparison.
(A) Qualitative sideview images of hydrated BC pellicles. (B) Estimated BC pellicles thickness values calculated using wet weight measurements.

Compared to commercially available wound dressing, BC pellicles produced using arabitol exhibited transmission values between that of film based wound dressings, and hydrogel-based dressings. Polyurethane derived film wound dressings such as 3M Medical's Tegaderm™ and Johnson and Johnson's Bioclusive™ have light transmission values of 74.4% and 89.4%, respectively [29]. Though these wound dressings exhibit higher transmission values than the BC produced using 80-95% arabitol, these dressings are only indicated for use as protective coverings of low exudating wounds. The Covidien™ Kendall™ PEG/propylene glycol derived hydrogel wound dressing exhibited a light transmission lower than the BC produced using 80-95% arabitol, with a transmission value of 53 ± 1% (**Figure 3.5A**, **B**). This hydrogel wound dressing is marketed as extremely absorbent while its transparency allows for wound visualization. Overall, these results indicate that BC pellicles produced using 80-95% arabitol exhibit transmittance values within the range of commercially available transparent wound dressings.

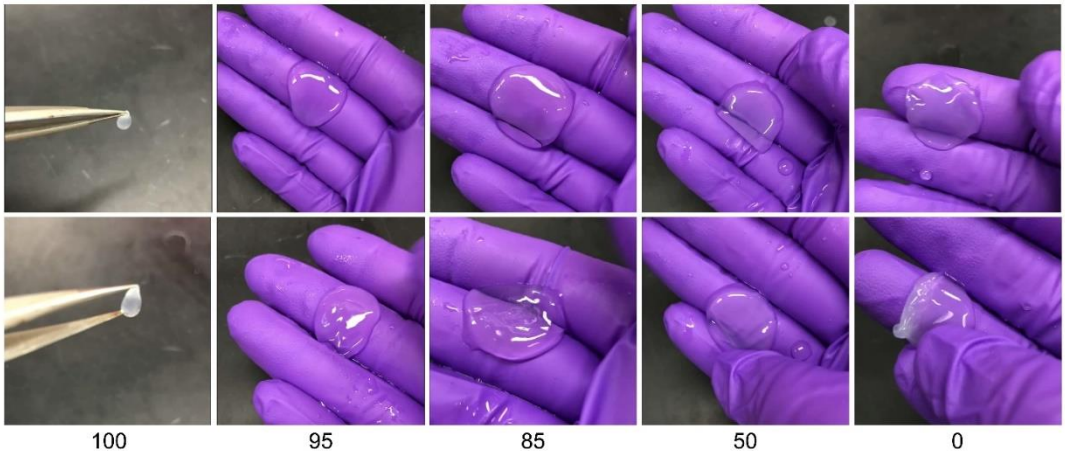

Figure 3.7. Qualitative still images isolated from videos of BC.
Showing the BC formed from different arabitol groups and their relative handleability.

3.4.2. Bacterial growth kinetics

Growth kinetic experiments were performed to compare how each arabitol concentration group affected the growth rate of *K. hansenii*. From the growth kinetic curves (**Figure 3.8A**), there was a delay in the onset of the exponential growth phase with increasing arabitol concentration. Using the slope of the linear region of the growth kinetic curves, maximum growth rate (μ_{max}) values were calculated (**Figure 3.8B**). All arabitol groups tested resulted in comparable μ_{max} values ranging between 0.0050 and 0.0069 h^{-1}. No statistical significance was observed, indicating the arabitol concentration has little impact on the maximum growth rate of *K. hansenii*.

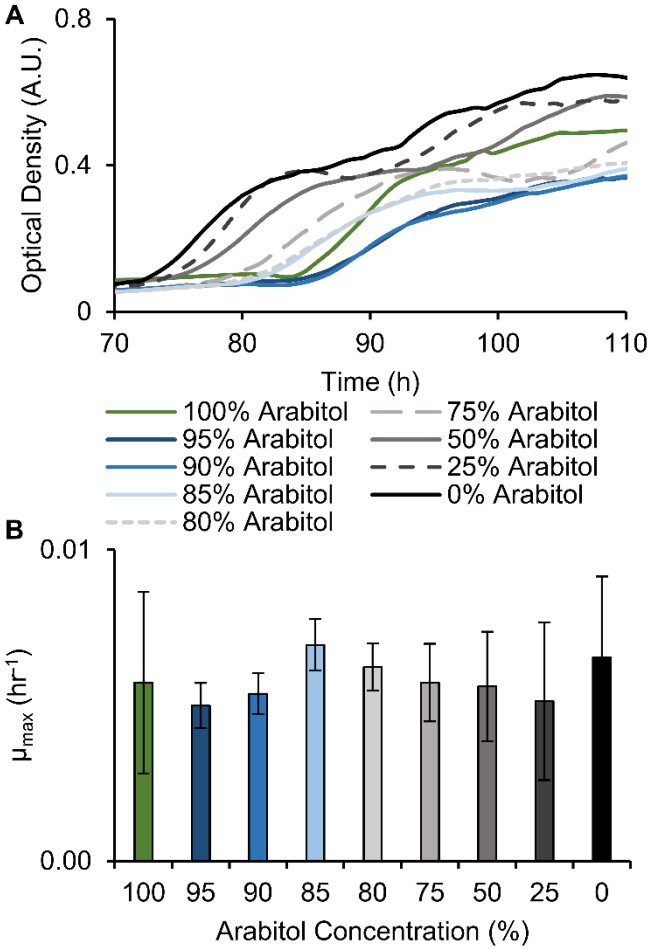

Figure 3.8. K. hansenii bacterial growth using reduced amounts of arabitol.
(A) Bacterial growth kinetics curves. **(B)** Maximum growth rate (μmax) identified from the linear region of the growth kinetic curves. Data are presented as mean ± SD from three independent experiments (n = 3 per arabitol concentration and experiment).

3.4.3. BC liquid absorption

To assess the effect of the culture condition on the intrinsic properties of the BC produced, liquid absorption analysis was performed. The liquid absorption capacity of freeze-dried BC pellicles 1 h (**Figure 3.9A**) and 24 h (**Figure 3.9B**) after initial submersion was assessed. No significant difference in liquid absorption was observed between 1 h and 24 h, indicating that pellicles had maximized liquid absorption by 1 h. At 1 h, a significant difference in liquid absorption was observed between the 0% arabitol control group and 95%, 90%, 85%, 80%, and 75% arabitol groups; where the 0% arabitol group had an average of 128-fold increase in mass, while 95%, 90%, 85%, 80%, and 75% arabitol groups had averages of 71, 58, 62, 52, and 50-fold mass increases, respectively. The region between 75% and 95% arabitol correlated to the transparency plateau identified in **Figure 3.4B**. Similarly, at 24 h the 0% arabitol group had an average of 148-fold mass increase, while 95%, 90%, 85%, 80%, and 75% arabitol groups had an average of 69, 54, 65, 53, and 51-fold increase in mass, respectively (**Figure 3.9B**). At both the 1 h and 24 h time points 100% arabitol BC pellicles absorbed more liquid, 108-fold and 111-fold increase in mass respectively, than pellicles produced using 75% - 95% arabitol. The increase in liquid absorption capability of BC pellicles produced using 100% arabitol indicated that liquid absorption does not directly correlate with increased transparency. The increased liquid absorption capabilities of BC were observed when comparing all BC pellicles with the liquid absorption capabilities of a commercially available hydrogel and foam based dressing. At 1 h the hydrogel and foam based wound dressings exhibited a 2.3-fold and 12.1-fold mass increase, respectively. At 24 h slightly more liquid was absorbed, and the mass fold increased to 2.8 and 13.5 mass fold increase, respectively. Previous research has reported a 37.3-fold mass increase for dry BC films [30]. However, a different *Komagataeibacter* strain was used to produce the pellicles, potentially leading to altered liquid absorption capabilities. Overall, the network structure of BC allowed the pellicles to trap and retain liquid within the material, resulting in removal of excess wound exudate from the wound bed. This is essential for wound healing as it prevents maceration of the wound edges [31]. Additionally the hydrogel-like nature and liquid absorption capacity of BC prevents wound bed dehydration [31].

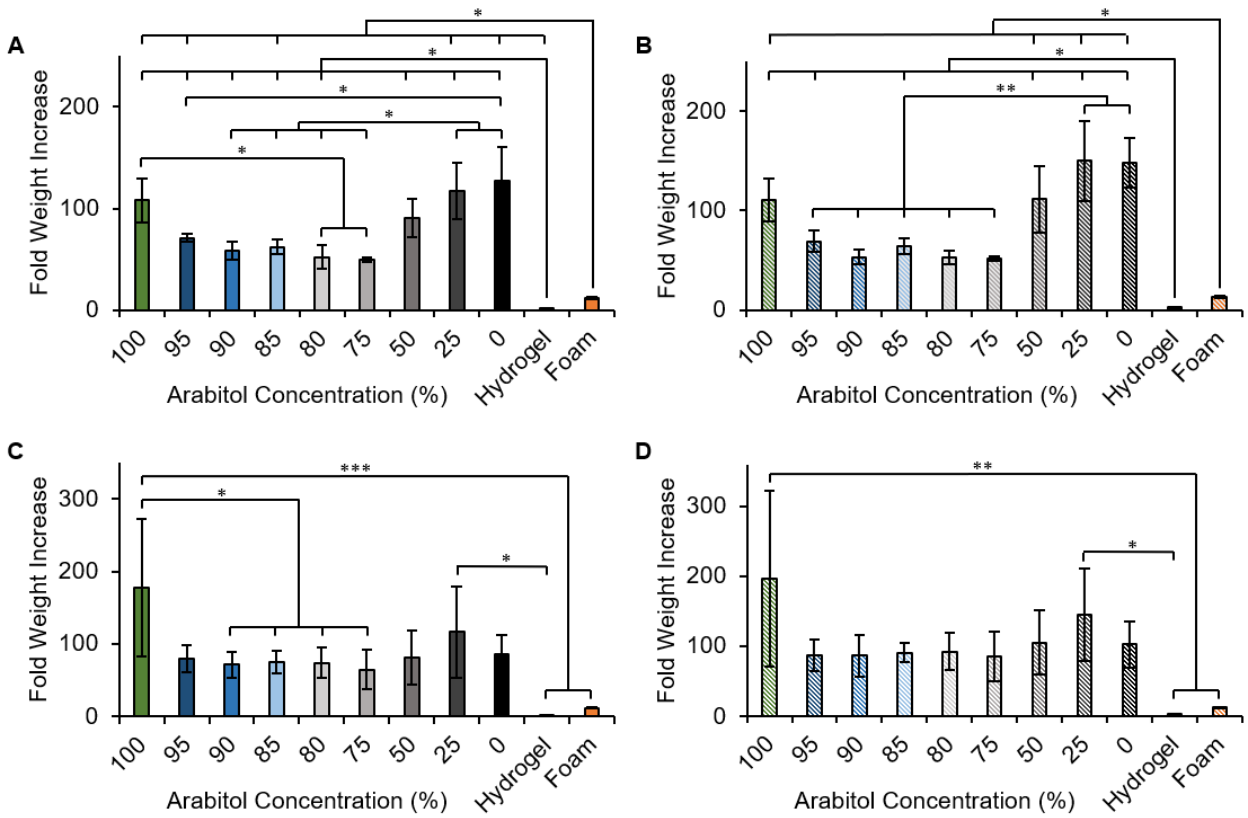

Figure 3.9. BC pellicle liquid absorption presented as fold mass increase.
BC pellicle and commercially available hydrogel and foam based wound dressings fold mass increase after **(A)** 1h and **(B)** 24 h of submersion in a salt solution and **(C)** 1 h and **(D)** 24 h of submersion in human serum. Data are presented as mean ± SD from three independent experiments (n = 3 per experiment). Statistical differences determined by an ANOVA followed by the Tukey's HSD test (* $p < 0.05$, ** $p < 0.005$).

This study was repeated using 100% human serum to better understand the wound exudate absorption capabilities with fluid containing small molecules and additional proteins (**Figure 3.9C, D**). Consistent with the salt liquid absorption experiment, no significant difference was observed between 1 h (**Figure 3.9C**) and 24 h (**Figure 3.9D**). Also consistent with the salt liquid absorption experiment, 100% arabitol had higher liquid absorption capability than 90-75% BC samples with a fold mass increase of 177, compared to 71, 75, 74, and 65 fold mass increase of 90%, 85%, 75% and 70% BC respectively. Pellicles submerged in serum resulted in increased variability in fold mass increase compared to samples submerged in the salt solution. With the understanding that BC pellicles do not contain cylindrical pores but instead micro-channels of varying sizes, the variability can be attributed to the random probability that larger molecules in serum, such as albumin (3.8 nm diameter, 15 nm long), are able to diffuse through larger

channels in the material [32, 33]. This increase in variability is not observed in either of the commercially available wound dressing materials as pore size can be more constrained and controlled in the manufacturing process.

To ensure that transparency was maintained after submersion in serum, images were taken of the samples (**Figure 3.10**). The serum fluid itself was fully opaque (**Figure 3.10A**), and the submerged sample was not detectable in the tube. Pre-hydrated 85% BC (**Figure 3.10B**) and lyophilized 85% BC (**Figure 3.10C**) were tested and both samples maintained transparency 24 h after submersion.

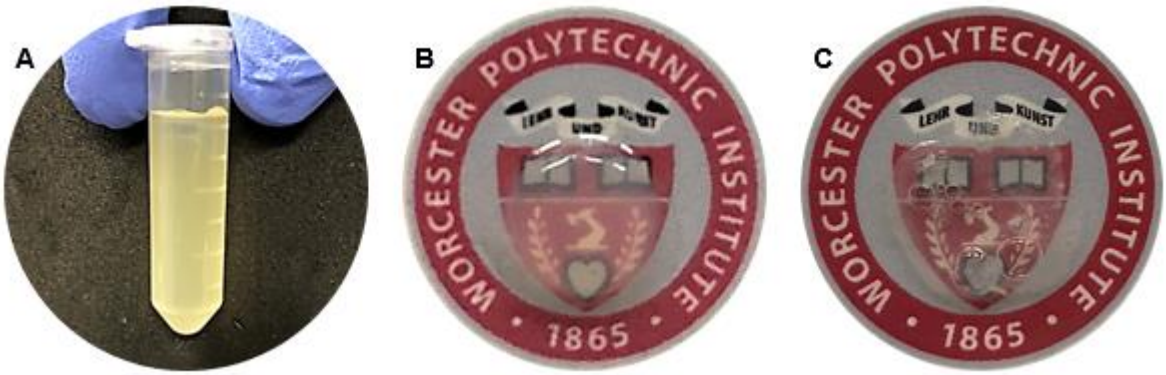

Figure 3.10. 85% BC submerged in 100% human serum.
(A) Opacity of the serum solution used, (B) observed transparency of pre-hydrated BC submerged for 24 h, **(C)** observed transparency of lyophilized BC submerged for 24 h.

3.4.4. BC cytotoxicity

Viability of NHDF cells exposed to BC pellicles formed using 85% and 0% arabitol were assessed using a resazurin metabolic based colorimetric assay. The ISO standard for *in vitro* material cytotoxicity, states that if a materials results in cell viability at or above 70% compared to untreated cells the material is not cytotoxic (denoted by the grey dashed line in **Figure 3.11A**) [34, 35]. Normalized to the untreated control, cell viability after exposure to BC formed using 85% and 0% arabitol was 71.4 ± 7.4% and 82.6 ± 14.1%, respectively (**Figure 3.11A**). This is above the ISO standard for cytotoxic materials. No statistical difference in viability was observed, nor any changes to overall cell morphology (**Figure 3.11B**). Additionally, the decrease in viability observed for both the 80% and 0% arabitol groups can be attributed to the nature of this experimental setup. In this set up, the BC materials sunk to the bottom of the culture

well which may have prevented adequate nutrient transport to the cells directly underneath the pellicle as well as resulted in cellular abrasion. This resulted in cell death underneath the pellicle, however, the cells surrounding the material, were unaffected and were seen to grow up to the edge of the BC material (**Figure 3.11C**). As the assay was dependent on metabolic activity, the overall decrease in cells present in the wells due to abrasion issues resulted in a decrease in cell viability compared to the untreated control wells. Overall, however, the BC formed using either 0% or 85% arabitol did not elicit a cytotoxic response *in vitro*.

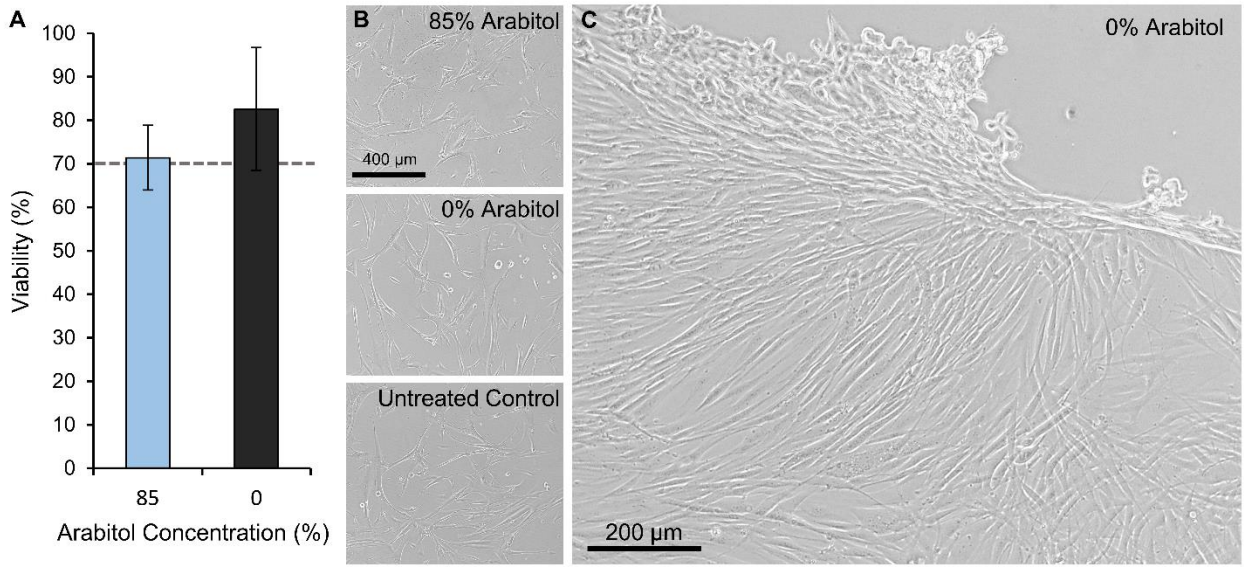

Figure 3.11. Viability assessment of NHDF cultures with 0% and 85% arabitol BC. (A) Viability of cells on Day 3 after exposure to BC pellicles formed with 85% and 0% arabitol normalized to untreated controls. Dashed grey line indicates 70% viability. (B) Representative images of NHDF cells on Day 3 after being cultured with and without BC pellicles. (C) Representative image of NHDF on Day 5 after being cultured with 0% arabitol BC showing cellular growth up to the end of the BC material.

3.4.5. BC fiber diameter

Since BC is produced as a semicrystalline nanofibrous network, it is possible that the fiber diameter may change due to altered carbon sources. To investigate if using glucose and arabitol as the carbon sources alter BC fiber diameter, SEM imaging and image analysis was performed. BC pellicles from the most transparent group (100% arabitol), the transparency plateau region (85% arabitol group), below the transparency plateau region (50% arabitol group), and the control (0% arabitol group) were evaluated (**Figure 3.12**). Fiber diameter analysis indicated that the 100% arabitol group had an average median fiber

diameter that was significantly larger than all other groups (52 nm versus 32 - 41 nm). Conversely, the 85% arabitol group had the smallest average median fiber diameter (32 nm), while 50% and 0% arabitol produced pellicles with average median fiber diameters of 41 nm and 39 nm, respectively. Though it may seem counter intuitive that 100% arabitol and 85% arabitol would produce pellicles with the largest and smallest fiber widths, respectively, an additional observation regarding fiber density was observed; the 85% arabitol group produced BC pellicles with a more dense (larger number of fibers) network structure as observed by SEM imaging (**Figure 3.12A)**. Lower fiber density has been attributed to nutrient restriction in the media culture [9]; however, this reasoning does not apply in this case. The 100% arabitol group arguably provides a more nutrient restrictive media condition than 85% arabitol group given the lack of glucose present, and differences in fiber density were not observed between 100% arabitol and 0% arabitol. An alternative explanation may be attributed to how the bacterium produces cellulose. Cellulose fibers are extruded from the bacterium as 1.5 nm-wide nanofibers that self-assemble in microfibril bundles [36, 37]. SEM imaging allows for the diameter measurement of the microfibril bundle and not the individual extruded nanofibers. The occurrence of more fibers with lower fiber diameter, as in the case for the 85% arabitol group, may indicate that the conformation or crystallization of the initial extruded nanofiber may be altered in a way that prevents extensive self-assembly of the fibers post-extrusion.

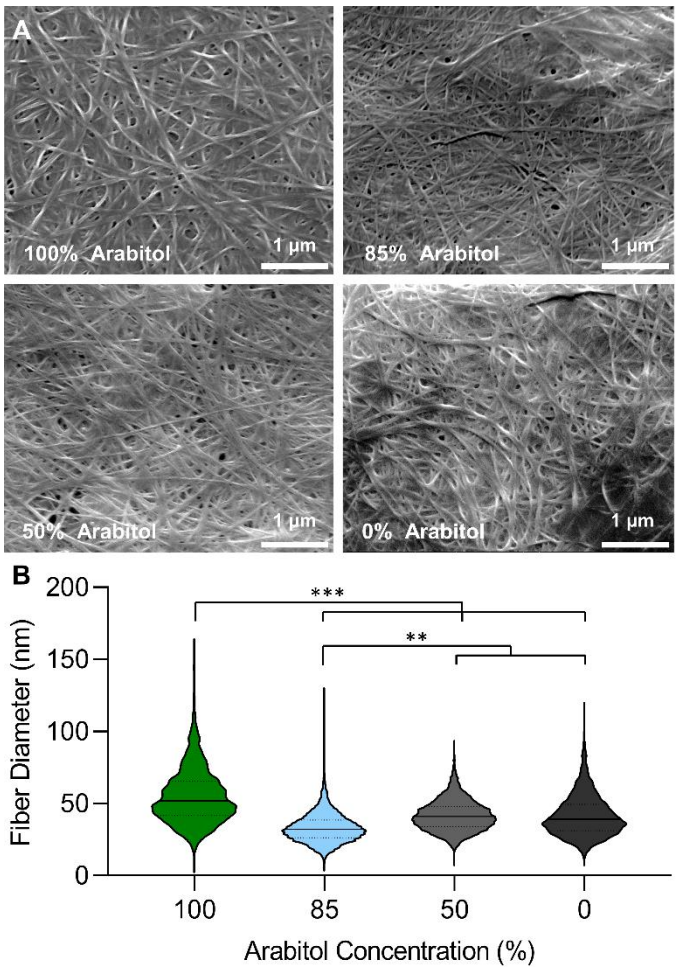

Figure 3.12. BC fiber diameter comparison between different carbon source mixture groups. **(A)** SEM images at 30000X of the microstructure and fiber morphology of BC pellicles. **(B)** BC nanofibril diameter values. Data are presented as median ± SD from three in dependent experiments (n = 6 images per pellicle). Statistical differences determined by an ANOVA followed by the Tukey's HSD test (** $p < 0.005$, *** $p < 0.0005$).

3.4.6. SAXS analysis

Further characterization of the morphology was performed through analysis of SAXS spectra. As the percentage of arabitol used for BC production increased, the overall shape of the SAXS spectra and the features corresponding to large-scale structures were retained and no shoulder-like scattering was observed (**Figure 3.13A**). A small feature was observed in the range q = 0.025-0.1 A^{-1} (**Figure 3.13B**). This feature manifests as two small peaks, corresponding to length scales of about 9.7 nm and 11.7 nm; the characteristic length scale is estimated at 2π over q. As the concentration of arabitol increased, these peaks gradually became broader and less prominent until they were nearly indistinguishable for the pellicle produced using

100% arabitol. Additionally, there appeared to be a slight variation in the slope of the decay of the scattered intensity at low *q*. This feature appeared to be minimal and retained across the groups, so further analysis would be needed to determine whether it corresponds to a subtle change in the structure.

Differences in the relative intensities likely do not occur due to a difference in scattering power (electron density) but in the relative pellicle densities in the X-ray path. The scattered intensity generally followed a power-law decay with an α exponent of 2 at very low *q*, then 2.6 at higher *q*. Though there was a slight deviation in the region where the features exist, these α exponent values are consistent with literature values of hydrated cellulose. Where low *q* regions (< 0.05 $Å^{-1}$) corresponds to the inner structure of water swollen BC bundles while high *q* regions (> 0.07 $Å^{-1}$) correspond to the surface of the BC pellicle plus a constant background [38-40]. BC pellicles are comprised of highly crystalline and amorphous regions that cannot be distinguished though SAXS analysis. Further crystallite dimension and crystalline fraction analysis was determined using WAXS and solid-state NMR.

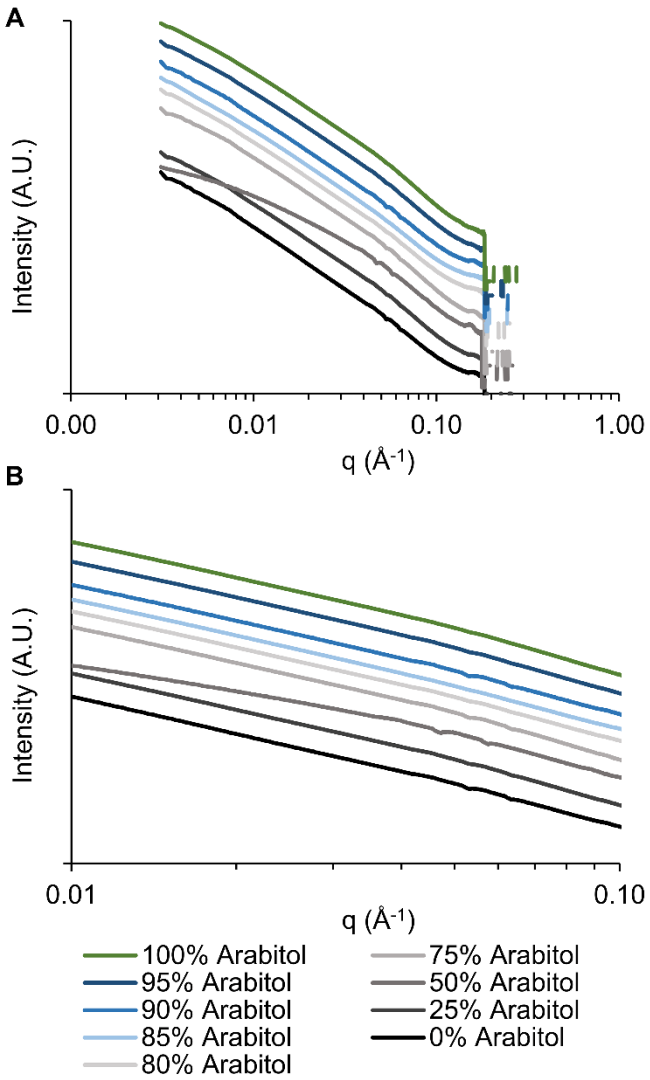

Figure 3.13. SAXS intensities from BC pellicles produced using mixtures of glucose and arabitol. **(A)** Full spectral reading of each pellicle and **(B)** zoomed in identified region of interest.

3.4.7. WAXS and solid-state NMR analysis

Further characterization of the morphology and molecular structural differences between BC pellicles was performed via WAXS and solid-state NMR. When analyzing the pellicles via WAXS, the peak width at a 2θ value of 13.4 was fairly maintained across all groups, indicating that the crystallite size remained the same (**Figure 3.14**). Though the peak width at a 2θ value of 13.4 was maintained, the peak intensity varied with changing arabitol concentration, even when adjusted to the scale of the scattering intensity. When comparing the ratio of the peak intensities with the total intensity of the spectra, there was a steady increase observed between 25% and 75% arabitol groups. Peak intensity was lost for the 80%

arabitol group, and then slowly increases again between 85% arabitol and 95% arabitol groups and reached a maximum peak intensity for the 100% arabitol group. The loss in peak intensity for pellicles produced using 80% to 95% arabitol corresponds with the previously identified plateaued transparency and liquid absorption findings. The change in peak intensity could be attributed to a change in crystallinity. However, the broad peak between a 2θ value of 15 and 20, which is likely due to water or possibly amorphous regions of the cellulose, prevents accurate crystallinity calculation [41]. Overall WAXS analysis showed that peak positions and the number of peaks were well-maintained across all groups, indicating the crystal phase was not affected.

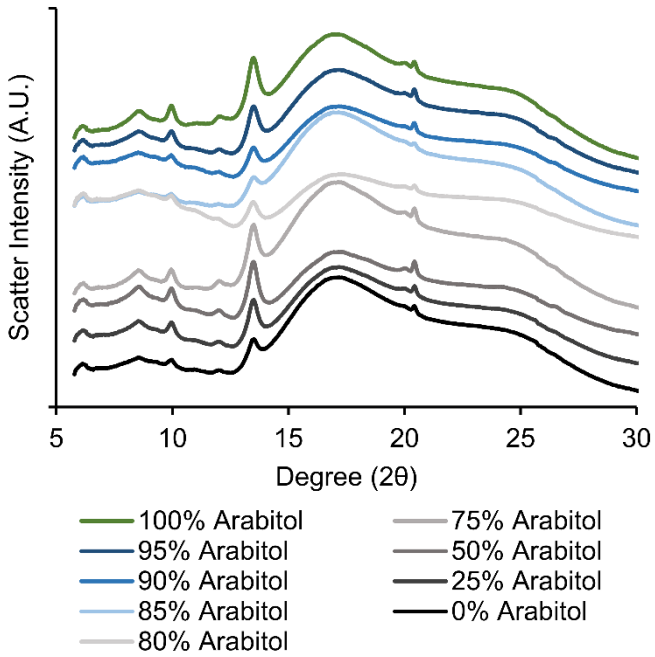

Figure 3.14. WAXS intensities from BC pellicles produced using mixtures of glucose and arabitol.

To further analyze the crystallinity of the pellicles produced, solid state CP-MAS NMR analysis was performed (**Figure 3.15)**. To properly compare spectra between groups of interest, CP-MAS NMR was performed on a group selected based the transparency data: (1) group above the transparent plateau region (100% arabitol), (2 and 3) groups within and directly below the plateau region (85% arabitol and 75% arabitol), (4) well below the plateau region (50% arabitol and 25% arabitol), and (5) the control group (0% arabitol). Full spectra between 0 and 250 ppm were collected (**Figure 3.15A**), and the region corresponding

to cellulose structure was isolated between 50 and 110 ppm (**Figure 3.15B**). To quantify the relative crystallinity of the pellicles, the crystalline and amorphous regions of the resonances at the C-4 carbon in the BC pellicles were fit primarily with one gaussian peak each. This was done by fitting a gaussian peak for the crystalline region centered around 88 ppm and a gaussian peak for the amorphous region centered around 84 ppm. A small additional gaussian peak was included where necessary to better replicate the line shape; in most cases this line belonged in the amorphous region of the signal. Additional gaussian fits were used to build out the other regions of the ^{13}C NMR signal to allow for a proper fit of the region of interest using least-squares difference minimization. To determine the areas of the crystalline and amorphous regions of the C-4 signal, two approaches were utilized: 1) areas of the fitted peak shapes and 2) integrated areas of the two regions sans fitting. For both calculation methods, the same trends were observed, and no appreciable crystallinity differences were observed between arabitol concentration groups (**Table 3.2**). The crystallinity observed in this study is lower than some of the values previously reported [42-44]. However, culture conditions such as temperature, specific strain, and media pH are known to alter crystallinity so direct comparisons are not always accurate [36].

Table 3.2. Cellulose Crystallinity Relative to Arabitol Concentration

Arabitol Concentration (%)	Crystallinity (% by peak fit method)	Crystallinity (% by integration method)
100	70	66
85	69	65
75	65	67
50	68	65
25	66	65
0	70	61

When the overall spectrum for the pellicles was considered (**Figure 3.15A**), a difference was observed in the total amount of cellulose in the pellicle. In all groups, a signal for a carboxylic acid group (-COOH) at around 172 ppm was observed (**Figure 3.15C**). The intensity of this peak varied slightly from group to group. A second set of signals were observed in the 110 to 160 ppm region that was associated

with aromatic carbons. These signals also manifested spinning side bands at the expected multiples of the magic angle spinning rate, 10 kHz, indicative of the order and crystallinity of these carbon atoms. Using the integrated region of the C-1 carbon signal of cellulose at 105 ppm and the integrated regions of the aromatic carbons, an estimate of the percentage of aromatic carbons was calculated. In the case of aromatic carbons, the overall integral was summed from the primary chemical shift region along with the side band regions. The overall integral for the aromatic carbons was divided by six for the purpose of population estimation. The overall aromatic carbon content was found to vary across the groups. Both cellulose and aromatic carbon structures were observed in the 0% arabitol group. The aromatic carbon content decreased in the 25% arabitol group as compared to the 0% arabitol group. The 50% and 75% arabitol group exhibited no aromatic carbons potentially due to the strong signal contributed by the C1 – C6 carbons. The cross-polarization conditions used across samples were the same and the observed level of crystallinity in the cellulose component was constant, so the efficiency of the CP-MAS NMR is expected to be the same for each experiment. The difference in observed signal intensities would then be governed essentially by carbon content. As the 50% arabitol and 75% arabitol groups resulted in pellicles with higher yields, it is possible that the aromatic signatures are present but undetectable due to their relative abundance in the sample. Subsequently, the aromatic carbons appeared in the 85% and 100% arabitol group. For the 100% arabitol group, the aromatic carbons made up most of the carbon fraction by an approximate factor of four. Though the presence of aromatic carbons in BC has not been reported previously, it is known that the polymers produced by these bacterium can be influenced by culture conditions [45].

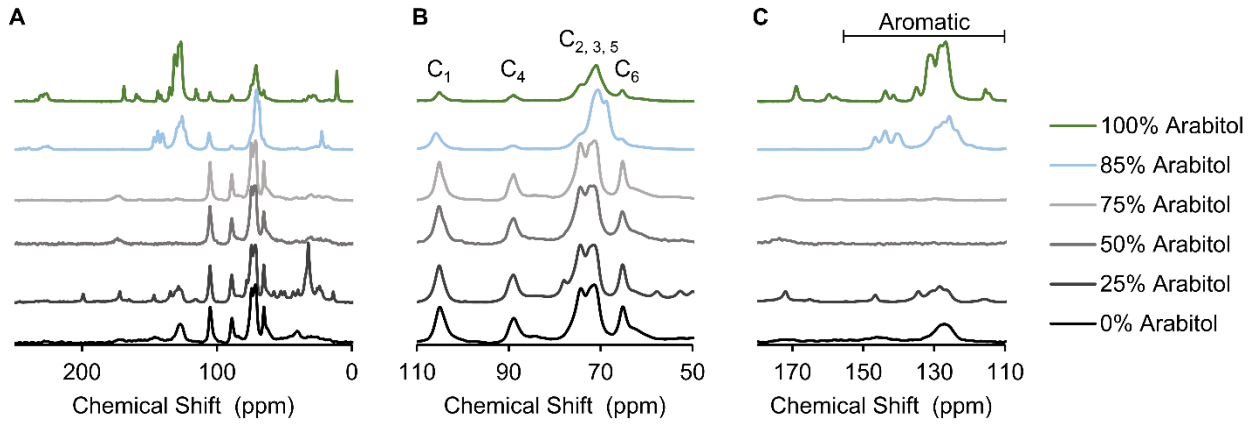

Figure 3.15. CP-MAS spectra of BC produced using various carbon source mixtures. **(A)** Variation in full NMR spectra of BC pellicles, **(B)** spectra associated with the cellulose molecular region (the peaks for the C_{1-6} carbons are identified), and **(C)** isolated region attributed to aromatic carbons in the pellicles.

Though the predominant insoluble exopolysaccharide produced by this class of microbes is cellulose, other exopolysaccharides have been reported when grown on alternative carbon sources [46-49]. The bacterial cellulose synthases of *Acetobacter* species have previously been shown to be promiscuous – Yadav *et al.* showed that UDP-GlcNAc could be incorporated into the BC polymer chain [49]. Additionally, other exopolysaccharides have been reported when grown on alternative carbon sources [46-49]. It is plausible that other UDP-sugars are formed under the conditions reported here and incorporated into the exopolysaccharide giving rise to the differences observed in the cellulose molecular region of the NMR.

The aromatic signature is most likely from proteinaceous extracellular material, which is often found in naturally derived biopolymers. Further evidence for this is that the aromatic signature is anticorrelated with BC yield – essentially, protein may make up a higher fraction of the pellicle when BC yield is lower. Williams et al. showed that aromatic amino acids, such as phenylalanine, tryptophane, and tyrosine exhibit ^{13}C signal between 100 and 160 ppm [50]. These aromatic amino acids are formed in both the PPP and glycolysis [51]. The surprising observation of these proteinaceous aromatic signatures in both the 0% and 100% arabitol groups could be attributed to underrepresentation of BC ^{13}C NMR signal ranges than 100 ppm, alternative allocation of increased signal in the 100-160 ppm range, and differences in bacterial strains researched. ^{13}C NMR signal for BC is predominantly truncated to show signal only within

the 50-110 ppm range, resulting in underreporting of regions outside of the cellulose range [52, 53]. Alternatively, Yamazawa et al., attributed signal in the aromatic region to the presence of spinning sidebands [54]. Further, the reclassification of *K. hansenii* as the proposed representative type strain for a new genus (*Novacetimonas*) based on phylogenetic analysis of the cellulose biosynthesis genes, indicated that there are distinct genetic differences from other *Komagataeibacter* strains [55], which may produce distinctly different exopolymers and concentration of proteinaceous extracellular material. The exact chemical composition of the exopolymers present within the pellicles using blends of glucose and arabitol as the carbon source is subject of continued investigation.

3.5. Conclusions

In this study, a method was developed to produce novel tunable transparent bacterial-derived cellulose. It was determined that modulation of the ratio of glucose and arabitol as the carbon source in static culture aided in the production of transparent BC by *K. hansenii*. Similar trends in data convergence for higher arabitol concentration groups (80%-95%), were observed for transparency, liquid absorption capabilities, and WAXS spectra analysis. A significantly smaller fiber diameter was also observed in the 85% arabitol group. Overall, these observations indicate that the use of arabitol concentrations between 80% and 95%, while holding mass of carbon-containing species constant, results in changes to both the microstructures and molecular structures of the BC produced. BC produced using higher arabitol concentrations (between 75%-95%) exhibited average transmittance values greater than 60%, while 100% arabitol group pellicles allowed for over 80% transmittance. Overall, the 85% arabitol group produced optimal pellicles based on the balance between cellulose yield and material transparency. Though the mechanism for this increased transparency was determined to not be due to decreased crystallinity, NMR spectra revealed a shift in sugar carbon signals and an aromatic signature that is strongest in the 100% arabitol group. This result indicates that *K. hansenii* NQ5 may not solely produce pure BC when supplemented with arabitol. This work is the first to show that BC composition and transparency can be manipulated by carbon source alone. This establishes that new exopolymers of varying monomer

composition may be accessible simply through the feeding of *Komagataeibacter* species with different carbon sources.

3.6. Acknowledgements

This research used resources of the Electron Microscopy Core Facility at UMass Chan Medical School supported by Award Number S10RR021043 from the National Institutes of Health National Center for Research Resources. This research used beamline 11-BM of the National Synchrotron Light Source II, U.S. Department of Energy (DOE) Office of Science User Facilities operated for the DOE Office of Science by Brookhaven National Laboratory under Contract No. DE-SC0012704. We thank Dr. Ruipeng Li, Brookhaven National Laboratory, for the SAXS/WAXS measurements.

3.7. References

[1] S.-P. Lin, H.-N. Kung, Y.-S. Tsai, T.-N. Tseng, K.-D. Hsu, K.-C. Cheng, Novel dextran modified bacterial cellulose hydrogel accelerating cutaneous wound healing, Cellulose 24(11) (2017) 4927-4937.
[2] M.J. Tabaii, G. Emtiazi, Transparent nontoxic antibacterial wound dressing based on silver nano particle/bacterial cellulose nano composite synthesized in the presence of tripolyphosphate, Journal of Drug Delivery Science and Technology 44 (2018) 244-253.
[3] A. Gupta, D. Keddie, V. Kannappan, H. Gibson, I. Khalil, M. Kowalczuk, C. Martin, X. Shuai, I. Radecka, Production and characterisation of bacterial cellulose hydrogels loaded with curcumin encapsulated in cyclodextrins as wound dressings, European Polymer Journal 118 (2019) 437-450.
[4] A. Gupta, S.M. Briffa, S. Swingler, H. Gibson, V. Kannappan, G. Adamus, M. Kowalczuk, C. Martin, I. Radecka, Synthesis of Silver Nanoparticles Using Curcumin-Cyclodextrins Loaded into Bacterial Cellulose-Based Hydrogels for Wound Dressing Applications, Biomacromolecules (2020).
[5] Y. Wang, C. Wang, Y. Xie, Y. Yang, Y. Zheng, H. Meng, W. He, K. Qiao, Highly transparent, highly flexible composite membrane with multiple antimicrobial effects used for promoting wound healing, Carbohyd. Polym. 222 (2019) 114985.
[6] Z. Di, Z. Shi, M.W. Ullah, S. Li, G. Yang, A transparent wound dressing based on bacterial cellulose whisker and poly (2-hydroxyethyl methacrylate), Int. J. Biol. Macromol. 105 (2017) 638-644.
[7] H. Kono, H. Tsujisaki, K. Tajima, Reinforcing Poly (methyl methacrylate) with Bacterial Cellulose Nanofibers Chemically Modified with Methacryolyl Groups, Nanomaterials 12(3) (2022) 537.
[8] F.G. Torres, O.P. Troncoso, K.N. Gonzales, R.M. Sari, S. Gea, Bacterial cellulose-based biosensors, Medical Devices & Sensors 3(5) (2020) e10102.
[9] S.S. de Souza, F.V. Berti, K.P. de Oliveira, C.Q. Pittella, J.V. de Castro, C. Pelissari, C.R. Rambo, L.M. Porto, Nanocellulose biosynthesis by Komagataeibacter hansenii in a defined minimal culture medium, Cellulose 26(3) (2019) 1641-1655.
[10] S. Wang, T. Li, C. Chen, W. Kong, S. Zhu, J. Dai, A.J. Diaz, E. Hitz, S.D. Solares, T. Li, Transparent, anisotropic biofilm with aligned bacterial cellulose nanofibers, Adv. Funct. Mater. 28(24) (2018) 1707491.
[11] N. Yin, M.D. Stilwell, T.M. Santos, H. Wang, D.B. Weibel, Agarose particle-templated porous bacterial cellulose and its application in cartilage growth in vitro, Acta biomaterialia 12 (2015) 129-138.
[12] K.V.S. Hodel, L.M.d.S. Fonseca, I.M.d.S. Santos, J.C. Cerqueira, R.E.d. Santos-Júnior, S.B. Nunes, J.D.V. Barbosa, B.A.S. Machado, Evaluation of Different Methods for Cultivating Gluconacetobacter hansenii for Bacterial Cellulose and Montmorillonite Biocomposite Production: Wound-Dressing Applications, Polym. 12(2) (2020) 267.
[13] P. Zikmanis, S. Kolesovs, M. Ruklisha, P. Semjonovs, Production of bacterial cellulose from glycerol: the current state and perspectives, Bioresources and Bioprocessing 8(1) (2021) 1-14.
[14] S. Bandyopadhyay, N. Saha, P. Sáha, Characterization of bacterial cellulose produced using media containing waste apple juice, Applied Biochemistry and Microbiology 54(6) (2018) 649-657.

[15] M. Salari, M.S. Khiabani, R.R. Mokarram, B. Ghanbarzadeh, H.S. Kafil, Preparation and characterization of cellulose nanocrystals from bacterial cellulose produced in sugar beet molasses and cheese whey media, Int. J. Biol. Macromol. 122 (2019) 280-288.
[16] Z. Hussain, W. Sajjad, T. Khan, F. Wahid, Production of bacterial cellulose from industrial wastes: a review, Cellulose 26(5) (2019) 2895-2911.
[17] R.T. Machado, A.B. Meneguin, R.M. Sabio, D.F. Franco, S.G. Antonio, J. Gutierrez, A. Tercjak, A.A. Berretta, S.J. Ribeiro, S.C. Lazarini, Komagataeibacter rhaeticus grown in sugarcane molasses-supplemented culture medium as a strategy for enhancing bacterial cellulose production, Industrial Crops and Products 122 (2018) 637-646.
[18] S.M. Keshk, K. Sameshima, Evaluation of different carbon sources for bacterial cellulose production, Afr. J. Biotechnol. 4(6) (2005) 478-482.
[19] T. Oikawa, T. Morino, M. Ameyama, Production of cellulose from D-arabitol by Acetobacter xylinum KU-1, Biosci. Biotechnol. Biochem. 59(8) (1995) 1564-1565.
[20] A. Riley, Basics of polymer chemistry for packaging materials, Packaging Technology, Elsevier2012, pp. 262-286.
[21] T. Oikawa, J. Nakai, Y. Tsukagawa, K. Soda, A novel type of D-mannitol dehydrogenase from Acetobacter xylinum: occurrence, purification, and basic properties, Biosci. Biotechnol. Biochem. 61(10) (1997) 1778-1782.
[22] M. Rezazadeh, V. Babaeipour, E. Motamedian, Reconstruction, verification and in-silico analysis of a genome-scale metabolic model of bacterial cellulose producing Komagataeibacter xylinus, Bioprocess and Biosystems Engineering (2020) 1-10.
[23] S.S.d. Souza, J.d.V. Castro, L.M. Porto, Modeling the core metabolism of Komagataeibacter hansenii ATCC 23769 to evaluate nanocellulose biosynthesis, Brazilian Journal of Chemical Engineering 35 (2018) 869-886.
[24] M. Gullo, S. La China, G. Petroni, S. Di Gregorio, P. Giudici, Exploring K2G30 genome: a high bacterial cellulose producing strain in glucose and mannitol based media, Frontiers in microbiology 10 (2019) 58.
[25] K.-Y. Lee, J.J. Blaker, A. Bismarck, Surface functionalisation of bacterial cellulose as the route to produce green polylactide nanocomposites with improved properties, Composites Science and Technology 69(15-16) (2009) 2724-2733.
[26] D. Massiot, F. Fayon, M. Capron, I. King, S. Le Calvé, B. Alonso, J.O. Durand, B. Bujoli, Z. Gan, G. Hoatson, Modelling one-and two-dimensional solid-state NMR spectra, Magnetic resonance in chemistry 40(1) (2002) 70-76.
[27] C. Zhong, G.-C. Zhang, M. Liu, X.-T. Zheng, P.-P. Han, S.-R. Jia, Metabolic flux analysis of Gluconacetobacter xylinus for bacterial cellulose production, Appl. Microbiol. Biot. 97(14) (2013) 6189-6199.
[28] K. Toda, T. Asakura, M. Fukaya, E. Entani, Y. Kawamura, Cellulose production by acetic acid-resistant Acetobacter xylinum, J. Ferment. Bioeng. 84(3) (1997) 228-231.
[29] C. Chen, D.G. Diven, S. Lockhart, B. Bell, Laser transmission through transparent membranes used in cutaneous laser treatment, Journal of the American Academy of Dermatology 45(6) (2001) 919-923.
[30] B. Wei, G. Yang, F. Hong, Preparation and evaluation of a kind of bacterial cellulose dry films with antibacterial properties, Carbohyd. Polym. 84(1) (2011) 533-538.
[31] H. Li, J. Yang, X. Hu, J. Liang, Y. Fan, X. Zhang, Superabsorbent polysaccharide hydrogels based on pullulan derivate as antibacterial release wound dressing, J. Biomed. Mater. Res. A 98(1) (2011) 31-39.

[32] A.M. Sokolnicki, R.J. Fisher, T.P. Harrah, D.L. Kaplan, Permeability of bacterial cellulose membranes, Journal of membrane science 272(1-2) (2006) 15-27.
[33] A. Tojo, S. Kinugasa, Mechanisms of glomerular albumin filtration and tubular reabsorption, International journal of nephrology 2012 (2012).
[34] S. Prasadh, M. Gupta, R. Wong, In vitro cytotoxicity and osteogenic potential of quaternary Mg-2Zn-1Ca/X-Mn alloys for craniofacial reconstruction, Sci. Rep. 12(1) (2022) 8259.
[35] I. Iso, 10993–5: 2009 Biological evaluation of medical devices—part 5: tests for in vitro cytotoxicity, International Organization for Standardization, Geneva (2009) 34.
[36] E.M. van Zyl, J.M. Coburn, Hierarchical structure of bacterial-derived cellulose and its impact on biomedical applications, Curr. Opin. Chem. Eng. 24 (2019) 122-130.
[37] R.M. Brown Jr, J. Willison, C.L. Richardson, Cellulose biosynthesis in Acetobacter xylinum: visualization of the site of synthesis and direct measurement of the in vivo process, P. Natl. Acad. Sci. USA 73(12) (1976) 4565-4569.
[38] P.W. Schmidt, Small-angle scattering studies of disordered, porous and fractal systems, Journal of Applied Crystallography 24(5) (1991) 414-435.
[39] P.A. Penttilä, T. Imai, J. Sugiyama, Fibrillar assembly of bacterial cellulose in the presence of wood-based hemicelluloses, Int. J. Biol. Macromol. 102 (2017) 111-118.
[40] P.A. Penttilä, T. Imai, M. Capron, M. Mizuno, Y. Amano, R. Schweins, J. Sugiyama, Multimethod approach to understand the assembly of cellulose fibrils in the biosynthesis of bacterial cellulose, Cellulose 25(5) (2018) 2771-2783.
[41] A. Kamdem Tamo, I. Doench, L. Walter, A. Montembault, G. Sudre, L. David, A. Morales-Helguera, M. Selig, B. Rolauffs, A. Bernstein, Development of Bioinspired Functional Chitosan/Cellulose Nanofiber 3D Hydrogel Constructs by 3D Printing for Application in the Engineering of Mechanically Demanding Tissues, Polym. 13(10) (2021) 1663.
[42] P. Singhsa, R. Narain, H. Manuspiya, Physical structure variations of bacterial cellulose produced by different Komagataeibacter xylinus strains and carbon sources in static and agitated conditions, Cellulose 25(3) (2018) 1571-1581.
[43] W. Czaja, D. Romanovicz, R. Malcolm Brown, Structural investigations of microbial cellulose produced in stationary and agitated culture, Cellulose 11(3-4) (2004) 403-411.
[44] S. Sheykhnazari, T. Tabarsa, A. Ashori, A. Shakeri, M. Golalipour, Bacterial synthesized cellulose nanofibers; Effects of growth times and culture mediums on the structural characteristics, Carbohyd. Polym. 86(3) (2011) 1187-1191.
[45] J. Trček, I. Dogsa, T. Accetto, D. Stopar, Acetan and acetan-like polysaccharides: genetics, biosynthesis, structure, and viscoelasticity, Polym. 13(5) (2021) 815.
[46] L. Fang, J.M. Catchmark, Characterization of cellulose and other exopolysaccharides produced from Gluconacetobacter strains, Carbohyd. Polym. 115 (2015) 663-669.
[47] V. Yadav, L. Sun, B. Panilaitis, D.L. Kaplan, In vitro chondrogenesis with lysozyme susceptible bacterial cellulose as a scaffold, J. Tissue Eng. Regen. M. 9(12) (2015) E276-E288.
[48] V. Yadav, B. Panilaitis, H. Shi, K. Numuta, K. Lee, D.L. Kaplan, N-acetylglucosamine 6-phosphate deacetylase (nagA) is required for N-acetyl glucosamine assimilation in Gluconacetobacter xylinus, PLoS One 6(6) (2011) e18099.
[49] V. Yadav, B.J. Paniliatis, H. Shi, K. Lee, P. Cebe, D.L. Kaplan, Novel in vivo-degradable cellulose-chitin copolymer from metabolically engineered Gluconacetobacter xylinus, Appl. Environ. Microb. 76(18) (2010) 6257-6265.

[50] J.K. Williams, K. Schmidt-Rohr, M. Hong, Aromatic spectral editing techniques for magic-angle-spinning solid-state NMR spectroscopy of uniformly 13C-labeled proteins, Solid state nuclear magnetic resonance 72 (2015) 118-126.
[51] K. Shimizu, Bacterial Cellular Metabolic Systems: Metabolic Regulation of a Cell System with 13C-metabolic Flux Analysis, Elsevier2013.
[52] A. Idström, S. Schantz, J. Sundberg, B.F. Chmelka, P. Gatenholm, L. Nordstierna, 13C NMR assignments of regenerated cellulose from solid-state 2D NMR spectroscopy, Carbohyd. Polym. 151 (2016) 480-487.
[53] J.-S. Jeong, J.-Y. Park, Water absorption and maintenance of nanofiber cellulose production by Gluconacetobacter rhaeticus TL-2C, Afr. J. Biotechnol. 11(40) (2012) 9630-9632.
[54] A. Yamazawa, T. Iikura, A. Shino, Y. Date, J. Kikuchi, Solid-, solution-, and gas-state NMR monitoring of 13C-cellulose degradation in an anaerobic microbial ecosystem, Molecules 18(8) (2013) 9021-9033.
[55] P.R. Brandão, M.T. Crespo, F.X. Nascimento, Phylogenomic and comparative analyses support the reclassification of several Komagataeibacter species as novel members of the Novacetimonas gen. nov. and bring new insights into the evolution of cellulose synthase genes, International Journal of Systematic and Evolutionary Microbiology 72(2) (2022) 005252.

4. Chapter 4: Characterization of CBP-AMP peptide bioactivity

Elizabeth M. van Zyl[a], Jeannine M. Coburn[a,*]

[a] Department of Biomedical Engineering, Worcester Polytechnic Institute, Worcester, MA 01609

4.1. Introduction

Increasing concern lies in the danger of chronic wounds due to an aging population and the widespread rise of antibiotic resistance [1]. In the US, chronic wounds affect 2.4-4.5 million people, resulting in a yearly direct Medicare cost of over $13.5 billion [1, 2]. Chronic wounds, wounds that fail to progress through normal healing processes within 3 months, generally develop due to systemic factors such as age, disease state (diabetes, keloids, hereditary healing disorders), medications, and overall nutrition [3, 4].These wounds are marked by senescent fibroblast and keratinocyte cell populations due to increased oxidative stress, elevated H_2O_2 producing enzymes, lack of antioxidant pathways, and subsequent high levels of reactive oxygen species (ROS) shortly after injury [5-10]. Further lack of wound closure and wound healing activity allows for invading pathogens to access the wound site and flourish in the moist nutrient rich wound bed [1]. Wound infection control is currently addressed with wound debridement and application of antiseptics or antibiotics, though these are toxic to mammalian cells and promote the development of antibiotic resistant bacteria [11]. Antiseptics, such as chlorhexidine and iodine, inhibit fibroblast proliferation and migration, impeding normal wound healing progression [12]. Additionally, chlorohexidine resistance in specific bacterial strains has been found to be synonymous with increased antibiotic resistance [13, 14]. Alternative methods for addressing wound infections include the use of silver based gels or materials. Silver has been shown to upregulate pro-MMP-9 in stimulated cells, elevated levels of which are already known to be present in chronic wounds. This is believed to be responsible for preventing wound healing through growth factor degradation and degradation of provisional ECM matrix laid down during early wound healing steps [12, 15]. Overall, these antimicrobial approaches are associated

with hindered cellular proliferation, leading to a need for an antimicrobial agent that overcomes antibiotic resistance and promotes healing [16].

Cationic antimicrobial peptides (AMPs), such as human cathelicidin LL-37 offers a promising alternative to the growing concern of antibiotic resistance [17]. Though effective as an antibacterial agent, LL-37 exhibits cytotoxicity at concentrations higher than 10 μM and has limited *in vivo* stability [16-20]. Additionally, its long peptide chain makes it susceptible to proteolytic degradation and in some cases *S. aureus* has been observed to develop small colony variants that develop resistance mechanisms to LL-37, such as transmembrane potential reduction, unsaturation of lipids, and metabolic alteration [16-18, 21-23]. The shortest antimicrobial motif of LL-37, KR-12, overcomes these limitations [23]. KR-12 exhibits various bioactive properties such as board antibacterial activity against both gram-negative and gram-positive bacteria, neutralization of lipopolysaccharides (LPS), modulation of inflammatory response, and the possible promotion of wound closure through epithelialization functions such as epithelial cell migration, proliferation, and differentiation [23-28]. Though the narrow therapeutic ratio and susceptibility to proteolysis of AMPs in solution hinders their clinical use, AMP immobilization has been shown to decrease mammalian cell cytotoxicity and increase *in vitro* stability without compromising the AMP's antimicrobial activity [16, 18, 29].

Bacterial-derived cellulose (BC) has been studied for wound dressing applications due to its biocompatibility, water holding capacity, liquid/gas permeability, and handleability properties [4, 30, 31]. With BC's extensive exploration for use as a wound dressing and more recent incorporation of wound visualization capabilities, the lack of antibacterial surface properties remains to be addressed [32, 33]. Cellulose binding peptides (CBPs, also called cellulose binding domains/modules) interact with and bind to the cellulose surface to bring the hydrolytic region of cellulase enzymes into proximity with the cellulose surface [34]. CBPs provide a mechanism for immobilizing AMPs to the surface of BC, overcoming the limitation attributed to mammalian cytotoxicity and aiding in the prevention of wound infection [19, 35-38]. Recent advancements in this field include Weishaupt et al.'s use of a short CBP sequence to non-

covalently functionalize cellulose with the antimicrobial ligand tet009, and Barbosa et al.'s use of a full CBD to tether the antimicrobial hexapeptide MP196 to cellulose based materials [34, 39].

To further develop bifunctional chimeric peptide sequences for the non-covalent functionalization of BC, we evaluated two different CBP sequences. The first CBP evaluated (Long CBP) was engineered by Khazanov et al. by modifying the sequence and structure of cellulose binding domains (CBDs) from *Trichoderma reesei* cellobiohydrolase I [35]. Specifically, the Long CBP is comprised of residues 4-8, 25-36 from the complete CBD, with the following engineered mutations: H4G, Y5W, Y31W, C35T, insT35a, and L36P. Khazanov et al. determined these engineered mutations resulted in a CBP with a higher cellulose binding affinity ($1.45 \pm 0.30 \times 10^6$ M^{-1}) and increased maximal surface coverage (6.77±0.10 μmol/gr) compared to the complete CBD ($0.94 \pm 0.15 \times 10^6$ M^{-1} and 5.07 ± 0.05 μmol/gr) [35]. The second CBP evaluated in this work (Short CBP) was initially identified and characterized by Guo et al. using phage display [40]. The Short CBP was found to have a binding affinity to crystalline cellulose of ~10^5 M^{-1}, span approximately five glucose rings in length, and exhibit cellulose binding through CH/π stacking interactions and hydrogen bonds between peptide sidechains and cellulose [40]. Within in the realm of CBDs, this heptapeptide sequence has been described as a minimal consensus amino acid sequence [34, 40].

Though this is the first reported use of CBPs to tether KR-12 to a material surface, alternative covalent and electrostatic based methods have been explored with varying success. Diosa et al. studied the antimicrobial activity and proteolytic stability of KR-12 adsorbed to chitosan-silica hybrid material. Adsorbed peptide exhibited decreased antibacterial activity due to steric hindrance, but increased protection from proteolytic activity due to selective interactions with the solid surface [41]. Liu et al, conjugated KR-12 onto eggshell membranes and reported less than 3% bacterial survival of *E. coli*, *S. aureus*, and methicillin-resistant *Staphylococcus aureus* (MRSA). Further, HaCaT cells, a keratinocyte cell line, cultured on KR-12 functionalized eggshell membranes exhibited increased proliferation levels compared to unfunctionalized eggshell membranes [42]. Though KR-12 provided an excellent means of providing

antibacterial activity without the concern of antibiotic resistance, more effective immobilization methods are required to maintain peptide functionality.

In this work we non-covalently tethered an antimicrobial peptide (KR-12) to the surface of BC by harnessing the cellulose binding affinity of CBP sequences. The peptide structure, mammalian cytotoxicity, antibacterial capabilities, endotoxin binding, and cellulose binding properties of soluble chimeric peptides (Long-CBP-KR12 and Short-CBP-KR12) were assessed. Immobilized peptide bioactivity was further assessed through functionalized BC cytotoxicity and antibacterial properties. All for the eventual development of functionalized BC materials for use in chronic wound treatment.

4.2. Materials and Methods

4.2.1. Materials

Komagataeibacter hansenii NQ5 (*K. hansenii* ATCC 53582), Normal Human Dermal Fibroblasts (NHDF; American Type Culture Collection: CRL-2565), *Staphylococcus aureus* (S. aureus, ATCC 43866, strain designation: LRA 44.01.83), *Escherichia coli* (E. coli, ATCC 33694, strain designation: HB101) and *Pseudomonas aeruginosa* (ATCC 29260, strain designation: PA-103) were purchased from the American Type Culture Collection (ATCC), Manassas, VA, USA, while Human Endothelial Keratinocyte Cells (HaCaT, catalog number: T0020001) were purchased from AddexBio, San Diego, CA, USA. Bacto™ peptone and Difco™ yeast extract was purchased from Becton, Dickenson and Company, Franklin Lakes, NJ, USA, while agar was sourced from Sunrise Science Products, San Diego, CA, USA. D-arabitol (>99% purity), was purchased from Alfa Aesar Co., Inc, China. D-glucose (BioReagent, ≥99.5% purity), citric acid (99% purity), sodium phosphate dibasic (BioReagent, ≥99.5% purity), lipopolysaccharides (LPS) from Escherichia coli, 2,2,2-Trifluoroethanol (TFE), resazurin sodium salt (BioReagent), Mueller Hinton Broth (MHB), and sodium hydroxide (ACS reagent, ≥97.0% purity), were sourced from Sigma-Aldrich, Burlington, MA, USA. Iscove's modified Dulbecco's medium was purchased from Lonza Biologics, Walkersville, MD, USA, HyClone Dulbecco's Modified Eagle Medium (DMEM) with high glucose from

Cytiva Marlborough, MA, USA, while fetal bovine serum (FBS), 0.25% trypsin-EDTA, penicillin streptomycin, and 200mM L-glutamine were sourced from Life Technologies, Waltham, MA, USA. Animal-free recombinant human epidermal growth factor (EGF) and fibroblast growth factor (FGF) were purchased from PeproTech, Waltham, MA, USA. Tris buffered saline (TBS) was sourced from VWR Life Sciences, Bridgeport, NJ, USA. All well plates were sourced from Greiner Bio-One, Monroe, NC, USA, while Falcon™ round-bottom test tubes, and endotoxin free dimethyl sulfoxide (DMSO) were sourced from Corning, Inc, Corning, NY, USA. Pierce™ Chromogenic Endotoxin Quant Kit was purchased from Thermo Scientific. Waltham, MA, USA, and glacial acetic acid was sourced from J.T. Baker, Radnor Township, PA, USA.

4.2.2. Peptide design

The following synthetic AMP and CBP peptides sequences were purchased from Biomatik Corporation (Canada) at > 95% purity with an amidated C-terminus: KR-12 (KRIVQRIKDFLR), Short-CBP (WHWTYYW), and Long-CBP (**C**QVLNPWYSQTTPGWGQ**C**) with a disulfide bond between the cysteine residues [35, 40]. Two different chimeric peptides were designed with the KR-12 peptide linked to either the Short-CBP or Long-CBP peptide via an inert flexible linker (GSGSGGS) (**Table 4.1**). A Gly and Ser-rich linker was chosen to allow the two active domains to maintain rotational freedom, enhance the solubility of the hydrophobic peptides, and offer some resistance to proteolysis compared to other linker sequences [43, 44]. The custom designed chimeric peptides were purchased from CASLO ApS (Denmark). Amide group insertion at the C-terminal end of all peptide sequences occurred to provide proteolytic protection [45, 46]. For spectrophotometric detection and quantification, all peptide sequences were also purchased with a fluorescein (5,6-FAM) label attached via a miniPEG linker. To ensure solubility, peptides were first reconstituted in dimethyl sulfoxide (DMSO), then further diluted in 1X tris-buffered saline (TBS; 25 mM tris, 140 mM NaCl, 3 mM KCl, pH 7.2)., unless specified otherwise.

Table 4.1: Peptide Labels and Sequence Designation

Peptide Label	Peptide Sequence
Short CBP	WHWTYYW-NH2
Long-CBP	CQVLNPWYSQTTPGWGQC-NH2
KR-12	KRIVQRIKDFLR-NH2
Short-CBP-KR12	KRIVQRIKDFLR-GSGSGGS-WHWTYYW-NH2
Long-CBP-KR12	KRIVQRIKDFLR-GSGSGGS-CQVLNPWYSQTTPGWGQC-NH2
Short CBP-FAM	WHWTYYW-(AEEAc)-K(5-FAM)-NH2
Long-CBP-FAM	CQVLNPWYSQTTPGWGQC-(AEEAc)-K(5-FAM)-NH2
KR-12-FAM	KRIVQRIKDFLR-(AEEAc)-K(5-FAM)-NH2-NH2
Short-CBP-KR12-FAM	KRIVQRIKDFLR-GSGSGGS-WHWTYYW-NH2
Long-CBP-KR12-FAM	KRIVQRIKDFLR-GSGSGGS-CQVLNPWYSQTTPGWGQC-(AEEAc)-K(5-FAM)-NH2

4.2.3. Peptide modeling and helix wheel

Iterative Threading ASSEmbly Refinement (I-TASSER) server was used as an *in silico* method for predicting protein structure and function to qualitatively predict the secondary structure of each chimeric peptide sequence and its individual components [47-49]. Helix-wheel analysis was performed using the HELIQUEST software to calculate the hydrophobic moment, amino acid location, and amphiphilicity of the peptides [50].

4.2.4. Circular dichroism (CD) spectroscopy

Circular Dichroism spectroscopy (CD spec; JASCO J-1500, Jasco Inc., Oklahoma) was used with modification from a previously published method [16]. Briefly, Spectra analysis of 100 μM long-CBP, short-CBP, KR-12, Long-CBP-KR12, and Short-CBP-KR12 were obtained for wavelengths between 190 and 260 nm at 50 nm/min in a 10 mm path length cuvette at room temperature in 10 mM phosphate buffer, or buffer containing 0.1% LPS (representative environment) or 50% trifluoroethanol (TFE) solutions (positive control helix inducing solution). Thirty scans were recorded for each replicate (N = 3). The data were further analyzed for adopted secondary structure using the CDSSTR empirical model and reference set 7 in DichroWeb [51-55].

4.2.5. Mammalian cell culture maintenance

Normal Human Dermal Fibroblasts (NHDF) were maintained in Iscove's modified Dulbecco's medium supplemented with 10% FBS, 100 U/mL penicillin, 100 µg/mL streptomycin, 2 mM L-glutamine, 0.01 µg/mL EGF, and 0.005 µg/mL FGF). The HaCaT cell line, spontaneously transformed aneuploid immortal keratinocyte cell line, were maintained in Dulbecco's Modified Eagle Media (DMEM) supplemented with 10% FBS, 100 U/mL penicillin, 100 µg/mL streptomycin, and 0.4 mM L-glutamine. All cells were maintained at 5% CO_2 and 37°C in a humidified environment. NHDF were passaged using 0.25% trypsin-EDTA when 70-80% confluent, while HaCaT cells were passaged using both 0.25% trypsin-EDTA and cell scraping when 70-80% confluent.

4.2.6. Free peptide cytotoxicity

In a 96-well plate, 1,000 NHDF cells were seeded per well and allowed to attach for 24 h. Medium was then replaced with fresh medium supplemented with each peptide in solution at 80, 40, 20, 10, 5, and 2.5 µM concentrations. On days 1, 3, 5, and 7 post-peptide treatment a resazurin metabolic assay was performed to quantify cell metabolism. Fluorescent signal of the resazurin solution after incubation were read (excitation and emission at 544 nm and 590 nm) on a SpectraMax M2 plate reader (Molecular Devices, city, state, USA). Since the peptide was not expected to change the metabolic activity of the cells, fluorescent signal of resazurin directly correlated to the number of metabolically active cells in culture. For all time points no-peptide treated cells were cultured on as a positive control. Resazurin solution was also added to wells with no cells as a negative control (**Figure 4.1**). For qualitative comparison, brightfield imaging of wells were performed on an upright microscope (Nikon Eclipse E600, Tokyo, Japan) with a digital camera (Spot Insight CMOS 5.1, Sterling Heights, MI).

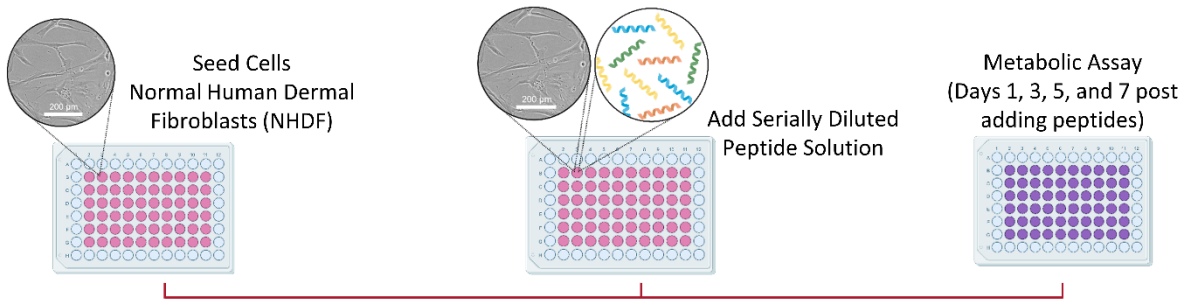

Figure 4.1. Peptide in solution cytotoxicity assessment method
Made using Biorender.com

4.2.7. Peptide minimum inhibitory concentration (MIC)

Staphylococcus aureus (*S. aureus*), *Escherichia coli* (*E. coli*) and *Pseudomonas aeruginosa* (*P. aeruginosa*) bacterial strains were cultured in Mueller Hinton broth (MHB) and then maintained on Mueller Hinton agar plates (MHA). Using a 0.5 McFarland Standard, cell turbidity was corrected to $1X10^8$ colony forming units per mL (CFU/mL) [56]. Cultures were diluted 100-fold in MHB to $1X10^6$ CFU/mL bacterial cultures. Diluted fresh cultures were used to determine the minimum inhibitory concentration (MIC) of Long-CBP, Short-CBP, KR-12, Long-CBP-KR12, and Short-CBP-KR12 in solution using a 96-well polypropylene plate based on standards set by the Clinical and Laboratory Standards Institute [19]. Briefly, serial diluted peptides starting at 80 µM concentrations along with a no peptide control wells were inoculated with $1x10^6$ CFU/mL fresh inoculum for each bacterial cell type. Negative control wells with no inoculum were also evaluated. Plates were incubated on a shaker and absorbance readings at 590 nm (OD590) were recorded using the Biotek Synergy H1 plate reader (BioTek Instruments Inc., Winooski, VT,

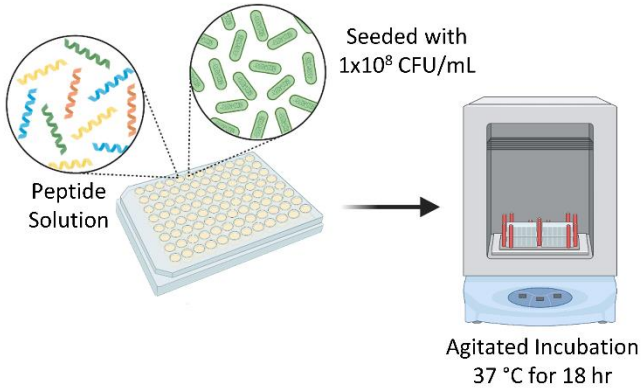

Figure 4.2. Minimum inhibitory concentration assessment method
Made using Biorender.com

USA) for 18 h after initial inoculation (**Figure 4.2**). The MIC was determined as the minimum peptide concentration that resulted in OD590 values not statistically different from sterile control values.

4.2.8. Endotoxin binding

The endotoxin binding ability of the chimeric peptides was determined and compared to KR-12 using an end-point chromogenic limulus amebocyte lysate (LAL) Quantification kit. method adapted from Wang et al. [57]. Peptide sequences were hydrated, diluted to 20 µM using endotoxin-free water and 25 µL were plated into a round bottom polypropylene 96-well plates. An equal volume of 3 endotoxin units (EU)/mL LPS solution was mixed in each well and plates were incubated for 30 min at 37 °C to allow for peptide-LPS binding. Amebocyte lysate reagent was added, and the plates were further incubated for 10 min. The chromogenic substrate was added and incubated for 6 min and the reaction stopped using 25% acetic acid. The plates were spectrophotometrically analyzed at 405 nm using a SpectraMax M2 plate reader (**Figure 4.3**). Absorbance reduction as a function of peptide concentration is directly proportional to the neutralization of LPS in solution [23].

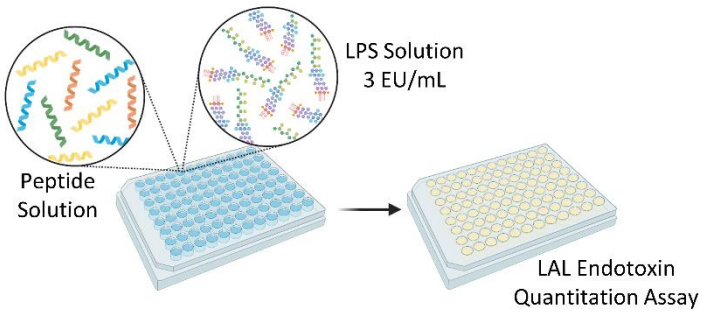

Figure 4.3. Endotoxin binding capacity assessment method
Made using biorender.com

4.2.9. Cellulose production and binding capacity

Bacterial-derived (BC) cellulose pellicles were produced as previously described [33]. Briefly, *Komagataeibacter hansenii* NQ5 static bacterium stock was established in Hestrin Schramm (HS) medium (20 mg/mL glucose, 5 mg/mL peptone, 5 mg/mL yeast extract, 1.15 mg/mL citric acid, 2.7 mg/mL disodium phosphate). Fresh HS medium without a carbon source was then inoculated with 0.1% (v/v) static cultured bacteria and supplemented to either 1 mM glucose (opaque BC) or 0.15 mM glucose and 0.85 mM arabitol

(transparent BC) as outlined in Chapter 3. To allow for pellicle formation, 200 µL of inoculated HS medium was cultured in 96-well tissue plates under static conditions at 30°C for 7 d. To purify the BC pellicles, they were removed, washed in 0.1 M NaOH at 60°C for 4 h, rinsed with DI H_2O until the fluid reached a neutral pH, and liquid autoclaved in 1X TBS.

Working solutions of fluorescently tagged peptides Long-CBP-FAM, Short-CBP-FAM, Long-CBP-KR12-FAM, short-CBP-KR12-FAM, and KR-12-FAM peptide sequences were prepared in sterile 1X TBS to achieve a concentration of 20 µM. Individual opaque and transparent BC pellicles were placed in polypropylene 96-well plates with 200 µL of peptide solution. Plates were incubated on an orbital shaker at 37°C for 48 h to allow for CBP binding to the cellulose surface. Post incubation BC samples were removed, washed with 1X TBS and used for further surface functionalization testing (**Figure 4.4**). Peptide binding was quantified through fluorescence analysis of the incubation supernatant (ex: 495 nm; em: 525 nm) (SpectraMax M2 plate reader). Reduction in supernatant fluorescence compared to peptide control wells (with no BC added) correlates directly to peptide binding to BC. Peptide binding was compared between peptide sequences and between opaque and transparent BC samples.

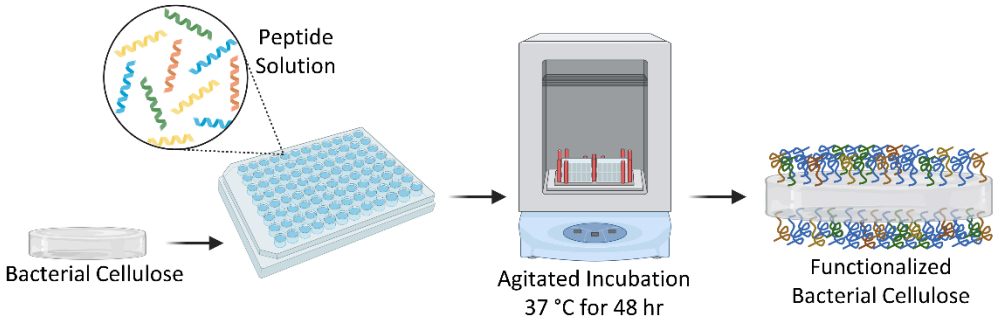

Figure 4.4. Peptide cellulose binding capacity assessment method
Made using Biorender.com

4.2.10. Surface functionalized BC cytotoxicity

Opaque and transparent BC samples were produced and functionalized in 96-well plates as described in Section 4.2.9. Wells in 48-well plates were seeded with 3,000 NHDF cells or 6,000 HaCaT cells and allowed to incubate for 24 h. Functionalized and unfunctionalized BC were then placed in cell

seeded wells. On days 1, 3, 5, and 7 after adding BC samples, a resazurin metabolic assay was performed to quantify cell metabolism (**Figure 4.5**). Fluorescent signal of the resazurin solution after incubation were read (excitation and emission at 544 nm and 590 nm) on a SpectraMax M2 (Molecular Devices, USA) plate reader. For all time points, cells were also cultured on TCP with no BC added as a positive control, and resazurin solution will be added to wells with no cells as a background control.

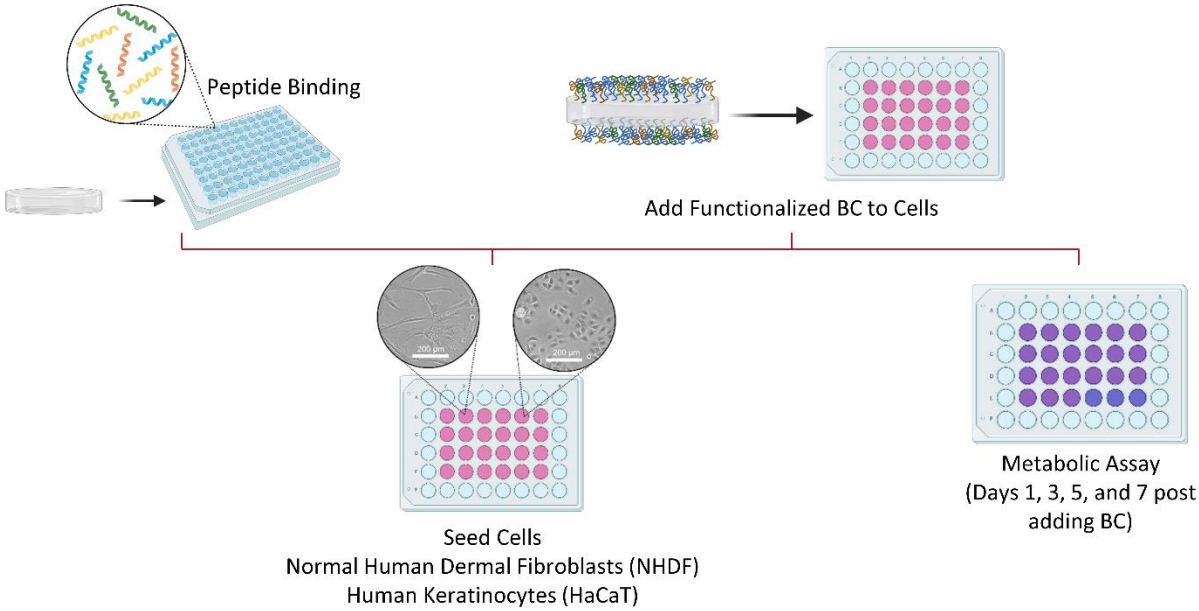

Figure 4.5. Functionalized BC mammalian cytotoxicity assessment method
Made using Biorender.com

4.2.11. Surface functionalized BC bacterial regrowth

Surface antibacterial activity was assessed against *E. coli* and *P. aeruginosa*. Functionalized and unfunctionalized transparent and opaque BC were synthesized and prepared as described in section 4.2.9. BC pellicles were incubated in 200 µL of each bacterial strain at $1X10^8$ CFU/mL for 1 h in Mueller Hinton broth (MHB). Samples were rinsed in sterile MHB to remove unattached bacteria and incubated with 200 µL fresh MHB at 37 ºC for 12 h. Bacterial regrowth was determined through comparing relative turbidity (absorbance at OD600 nm) readings on media incubated with functionalized and unfunctionalized BC (**Figure 4.6**). This procedure was also repeated on a commercially available hydrogel based wound dressing material with no known antibacterial activity.

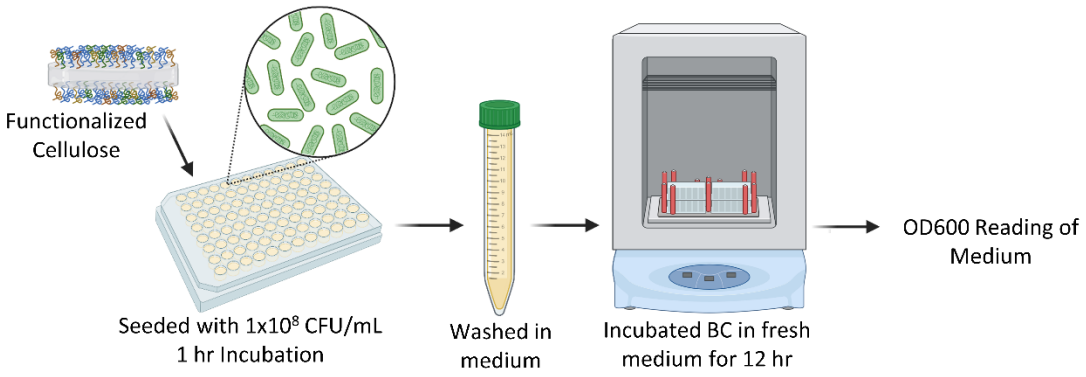

Figure 4.6. Functionalized BC antibacterial activity assessment method
Made using Biorender.com

4.2.12. Statistical analysis

All statistical analysis was performed using GraphPad Prism 7. Statistical analysis of the adopted secondary structure, effects on metabolic activity, minimum inhibitory concentration, LPS binding, cellulose binding, and effects on turbidity were conducted using an analysis of variance (ANOVA) followed by either a Tukey or Dunnett's post hoc test, as specified in the figure caption. All data are presented as mean ± standard deviation (SD) unless otherwise indicated.

4.3. Results and Discussion

4.3.1. Peptide structure and helix analysis

Three dimensional models of each chimeric peptide sequence and their individual peptide components were generated with the understanding that the main bioactivity observed from cationic AMPs are due to the peptide's α-helix structure and amphiphilicity. The I-TASSER server was used as an *in silico* method for predicting the secondary structure of the peptide sequences (**Table 4.2, Figure 4.7A**). In **Figure 4.7A**, the highest ranked model for each peptide submitted for analysis is shown. In each model the red end correlates to the C-terminal, and the blue end correlates to the N-terminal of the sequence. Due to the server's minimum amino acid sequence requirements, the Short CBP sequence was submitted including the flexible linker sequence; the same was done for the Long CBP for consistency. For the Short CBP a secondary structure of beta strands and random coils was predicted, however the Long CBP, without the AMP linked, has a small region predicted to be an α-helical structure. The predicted α-helical structure is

likely due to the proline residues found in the sequence that are known to be an effective inducer of helical hairpin turns [58, 59]. In agreement with other studies that have used the I-TASSER server to predict secondary structure, KR-12 was predicted to have an α-helix structural conformation [60]. This helical prediction was conserved in both the Long-CBP-KR12 and Short-CBP-KR12 sequences. Interestingly, the region of the Long-CBP predicted to have an inherent helical structure increases in length when linked to KR-12. Proline residues, though effective helical hairpin inducers, depend on a minimal amino acid length requirement. Previous studies have found that proline is most effective at inducing helical conformation when found in the middle of a 40 amino acid long sequence [59]. The Long-CBP-KR12 is a 37 amino acid long peptide where proline is found at position 25. The I-TASSER server reports and produces up to five models of the predicted peptide structure, based on the generation of large ensembles of structural conformations and subsequent pair-wise analysis for structural similarities.

Table 4.2. Secondary structural predication by I-TASSER server based on peptide sequence.

Peptide Label	Sequence / Predicted Secondary Structure
Long CBP	GSGSGGSCQVLNPWYSQTTPGWGQC CCCCCCCCSSSCCHHCCCCCCCCCC
Short-CBP	GSGSGGSWHWTYYW CCCCCCCSSSSSSC
KR-12	KRIVQRIKDFLR CHHHHHHHHHHC
Long-CBP-KR12	KRIVQRIKDFLRGSGSGGSCQVLNPWYSQTTPGWGQC CHHHHHHHHHHCCCCCCCCCSSCCHHHHCCCCCCCCC
Short-CBP-KR12	KRIVQRIKDFLRGSGSGGSWHWTYYW CHHHHHHHHHHCCCCCCCCSSSSSSC
	H:Helix; S:Strand; C:Coil

To further investigate the relationship between the α-helicity, net charge, hydrophobic moment, amino acid location, and amphiphilicity of the peptides HeliQuest was used to generate helical wheel diagrams (**Figure 4.7B**). KR-12's antibacterial activity is primarily driven by the amino acid location and resulting amphiphilicity of the helical structure [23]. When evaluating sequences with little to no helicity, e.g., the Long CBP and Short CBP sequences, through the HeliQuest software there were no clear observation divide between the locations of polar and non-polar residues. KR-12, a sequence known to be

amphiphilic, produced a helix chart that clearly portrayed the delineation between polar and non-polar residues. The helix chart generated for the Long-CBP-KR12 and Short-CBP-KR12 indicated that this delineation is maintained in our chimeric peptide sequences. The hydrophobic moment (μH), a quantifiable measure of amphiphilicity using the vector sum of all hydrophobic indices divided by the number of residues, is only meaningful for peptides with helical conformations and has been shown to be more important for antibacterial activity than the degree of helicity [61, 62]. KR-12 has a hydrophobic moment of 0.782, this is significantly higher that LL-37's hydrophobic moment of 0.440 [25]. The Long-CBP-KR12 and Short-CBP-KR12 have hydrophobic moments of 0.387 and 0.346, respectively, indicating that the CBP and linker have significant effects on the amphiphilicity of the peptide sequences. Though this indicates the potential for decreased antibacterial activity, from the design of these chimeric peptides and the structural models (**Figure 4.7A**) it is known that a portion of the sequence is not helical and is not designed to interact with bacterial membranes. Reducing the concern over decreased antibacterial activity solely due to a reduction in hydrophobic moment. The positive charge of cationic AMPs is essential for the initial electrostatic interactions between the peptide and the bacterial membrane [63]. The charge of the CBPs on their own were seen to be neutral at pH 7, while both chimeric sequences adopted the +4 charge exhibited by KR-12.

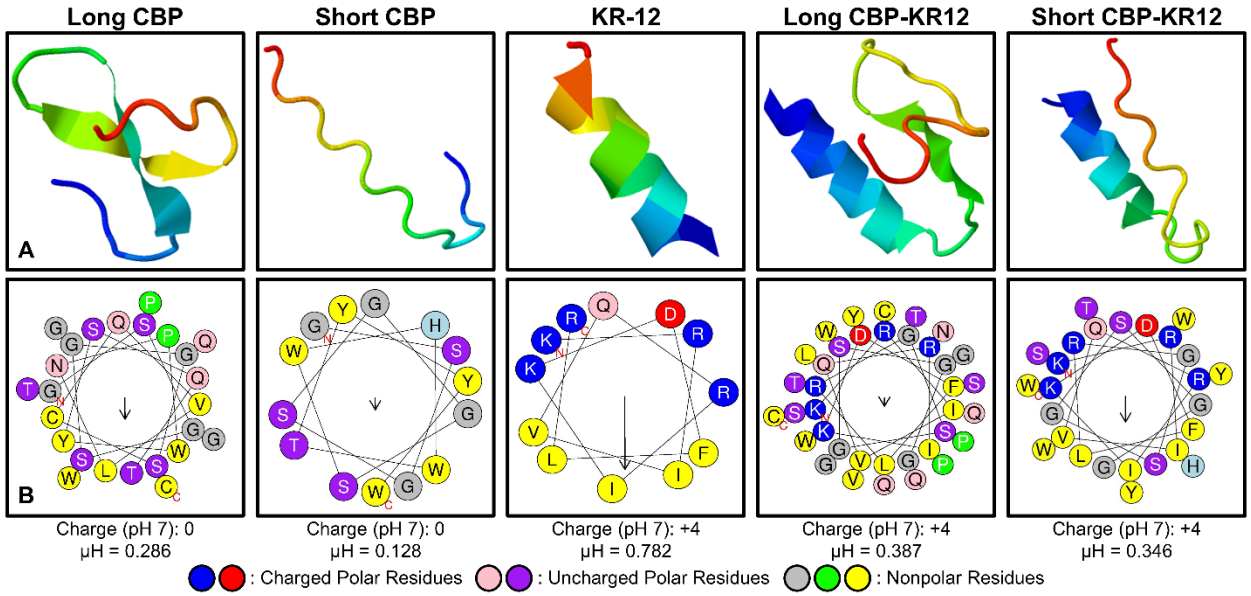

Figure 4.7. Predicted peptide structure and helix polarity delineation.
(A) Peptide structural prediction in silico using the free online I-TASSER server. (B) Helical wheel diagrams generated using HeliQuest. Arrows represent the helical hydrophobic moment of each peptide.

To further assess the secondary structure of each peptide experimentally, circular dichroism (CD) spectroscopy was performed using 10 mM phosphate buffer (standard aqueous environment), buffer containing 0.1% LPS (representative aqueous environment at the bacterial membrane interface), and buffer containing 50% TFE (positive control to induce α-helix conformation) (**Figure 4.8**). The characteristics of α-helical secondary structure in CD spectra are two minima values at 208 nm and 222 nm, and a positive band near 192 nm [23]. As increasing amounts of random coil/unordered structure is adopted the minimum at 222 nm becomes shallower and the minimum at 208 nm shifts towards lower wavelengths. Most AMPs assume a highly structured secondary structure upon interacting with the bacterial membrane [64]. KR-12's parent AMP, LL-37, however, can adopt helical secondary structures in the presence of chlorine, phosphate, sulfate, and bicarbonate ions at millimolar concentrations. This process is described as the ability of the ions to "salt out" the non-polar residues of the peptide and induce secondary structural conformation [65]. Though not as widely reported, it is not surprising nor a new observation that the CD spectra of KR-12 in phosphate buffer and phosphate buffer containing LPS look very similar (**Figure 4.8**). In both solutions KR-12 was seen to produce spectra with a small minimum around the 222 nm range and a larger minimum closer to 206 nm. In comparison, the spectra for KR-12 in phosphate buffer containing TFE had more

pronounced minima at both the 222 nm and 206 nm wavelengths. CD spectra outputs were run through DichroWeb software to determine the adopted secondary structure of each peptide sequence (**Figure 4.8**). For KR-12, a significant difference in adopted percentage of helical structure was observed between KR-12 in phosphate buffer containing LPS or TFE with 49% ± 7% and 56% ± 6% helicity, respectively. It should be noted that the percentage α-helicity observed in phosphate buffer containing TFE does not represent the true secondary structure of the peptide, but rather the relative tendency of the peptide to form a helical structure [61].

The Long CBP in phosphate buffer containing or not containing LPS adopted a more random coil, or unordered, conformation with a minimum in the 195 nm region. The Long CBP in phosphate buffer containing TFE indicated a helical structure with a minimum returning around the 222 nm range. This structural change was confirmed as the adopted structure indicated a ~10% drop in unordered structure and a corresponding ~10 - 15% increase in adopted helical structure. The Short CBP was predominantly comprised of random coil/unordered and strand conformations in all solutions tested, consistent with the computationally predicted structure (**Table 4.2**). Similar findings were reported by Guo et al., where the peptide's short amino acid sequence prevented higher order structures from forming [40].

Both Long-CBP-KR12 and Short-CBP-KR12 indicated high helicity in all solutions. When comparing the percent helicity using phosphate buffer, the Long-CBP-KR12 adopted a higher helical conformation of 69% ± 2% compared to both KR-12 and Short-CBP-KR12 with 56% ± 5% and 53% ± 0% respectively. Interestingly, the spectra for Long-CBP-KR12 in phosphate buffer with or without LPS had shallow minimum values at 222 nm, characteristic of a more random coil/unordered structure, however the minimum was not shifted to lower wavelengths as seen in the KR-12 spectra. For this reason, we observed the adopted helicity percentage between Long-CBP-KR12 in all three buffered solutions was unchanged despite seemingly different appearing spectra. Similarly for Short-CBP-KR12 we observed a larger minimum at the 222 nm range for peptide in buffer and buffer with LPS but not for peptide in buffer with TFE, and no shift in location of the minimum at 208 nm. Overall, the experimental determination of peptide

conformation and secondary structure matched the qualitative modeling, and the potential of helical conformation was retained in both chimeric peptide sequences.

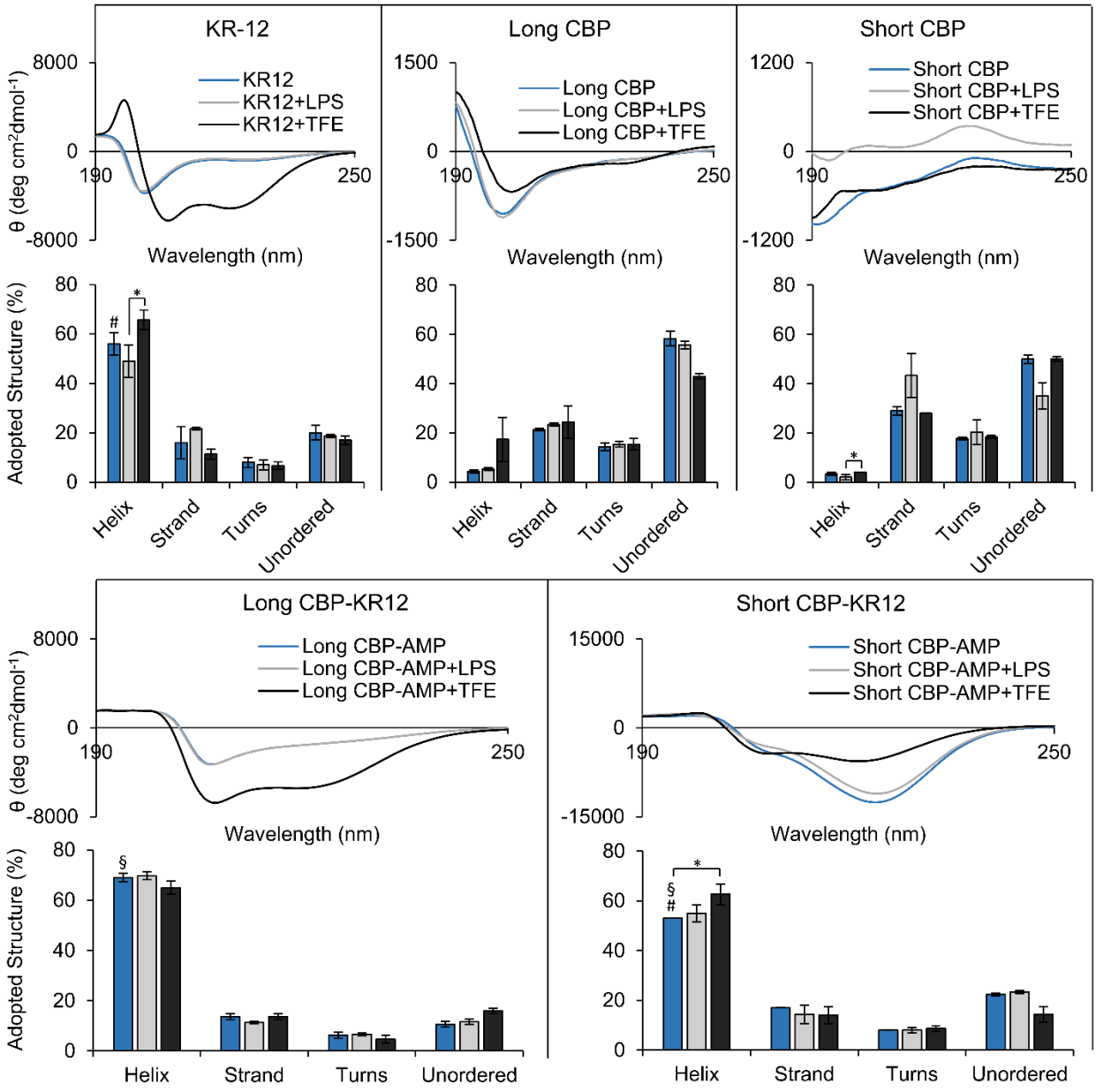

Figure 4.8. Experimental assessment of peptide secondary structure.

CD spectra of each peptide in Phosphate buffer (blue), buffer with 0.2% LPS (grey), and buffer with 50% TFE (black). Data are presented as the mean spectra from three independent readings (N = 3). Adopted structure were obtained from each independent reading. Statistical differences determined by an ANOVA followed by the Tukey's HSD test (* $p < 0.05$, § and ## $p < 0.005$). Data with the same number of pound sign symbols indicate comparison and increased number of symbols does not correlate to increased statistical significance.

With the understanding that bioactivity of AMPs, such as KR-12, is complex and relates to many factors including helicity and hydrophobic moment, **Table 4.3** contains a summary of the physiochemical properties for each peptide sequence studied in this chapter. For consistency with the modeling data, all CBP sequences were assessed with the flexible linker attached. Generally, AMPs have molecular weights less than 10 kDa, isoelectric points (pI) greater than or equal to 10, positive net charges, and an instability index less than 40 [66]. All peptides containing KR-12 fell within the ideal molecular weight and instability index range and had positive net charges. The isoelectric point, or pH where the peptide carries no net charge, was above 10 for KR-12 and the Short-CBP-KR12 at 11.72 and 10.43 respectively. The Long-CBP-KR-12's isoelectric point however was just slightly below 10 at 9.84, however this was still well above the 7.15-8.9 pH range reported for chronic wounds [67].

Table 4.3. Physiochemical properties of CBPs, AMPs, and chimeric peptide sequences

Peptide Label	Mw (Da)[a]	pI[a]	q[b]	AI[a]	H (%)[c]	μH[b]	H[b]	II[a]
Long CBP	2557.75	5.51	0	27.2	4.3	0.286	0.480	24.72
Short-CBP	1630.70	6.74	0	0	3.3	0.128	0.639	23.63
KR-12	1571.93	11.72	+4	121.67	56.0	0.782	0.193	31.95
Long-CBP-KR12	4111.67	9.84	+4	57.84	69.0	0.387	0.387	25.04
Short-CBP-KR12	3184.61	10.43	+4	56.15	53.0	0.346	0.435	24.59

Abbreviations: Mw, molecular weight; pI, isoelectric point; q, charge; AI, aliphatic index; H, helicity; μH, hydrophobic moment; H, hydrophobicity; II, instability index. [a] calculated with EXpasy Protparam **[68]**. [b] calculated with HeliQuest **[50]**. [c] calculated with DichroWeb from CD spectra **[51, 53]**.

4.3.2. Free peptide cytotoxicity

As the main proliferative cell type in the wound bed, Normal Human Dermal Fibroblasts (NHDF) are the common engineering standard for *in vitro* cytotoxicity assessment according to ISO 10993-5 [69]. The metabolic effects of chimeric peptides and their individual component peptides in solution were assessed using NHDF **(Figure 4.9**). Representative images were also compared to qualitatively assess cell morphology (**Figure 4.10**). Overall metabolic activity can be assumed to be proportional to cell count, thus increases in metabolic activity compared to untreated controls can be perceived as increases in cell

proliferation. The data are normalized to the untreated control where 100% normalized metabolic activity indicates no change compared to the control (as indicated by the grey dashed line). At high peptide concentration on day 3, KR-12 resulted in increased metabolic activity at 40 μM (121% ± 20%) and 80 μM (125% ± 10%) compared to 5 μM (86% ± 18%). Though this tread of increased proliferation in response to increased KR-12 concentration was also observed at day 5, increased variability in the data resulted in no statistical significance. Knowing that KR-12 plays an active role in key wound health pathways beyond antibacterial activity, the increased cell proliferation at higher concentrations agrees with findings from literature [25]. Song et al. noted similar findings, where NHDF exposed to higher levels of KR-12 exhibited increased metabolic activity and DNA content [26]. Further studies have indicated that no cytotoxicity towards human cells have been observed for concentrations greater than 63.5 μM [70]. Gunasekera et al. found that KR-12 showed weak cytotoxic activity towards a human lymphoma cell line resulting in a 13% loss in viability at 80 μM concentration [71]. It should be noted that human lymphoma is not a cell line that KR-12 is known to act upon, explaining the cytotoxic effects rather than increased proliferative effects observed in this and previous work.

The Long-CBP exhibited no effects on metabolic activity at all concentration across the 7 day period. As this CBP was originally designed by Khazanov et al. for use as a novel carrier for cellulose catalytic degradation, this is the first reported assessment of cytotoxicity of the free peptide *in vitro* [35]. The Short-CBP exhibited no effect on fibroblast metabolic activity up until day 5. At day 7, decreased metabolic activity was observed across all Short-CBP concentrations with 5-40 μM resulting in a tight range of 67-70% normalized metabolic activity while 80 μM resulted in 90% metabolic activity. It should be noted that similar trends were not observed for KR-12 or Long-CBP treated cells. Indicating there may be some cytotoxicity observed for Short-CBP with prolonged exposure. No definitive conclusions could be drawn as increased cellular confluence and media depletion at later timepoints resulted in increased variability.

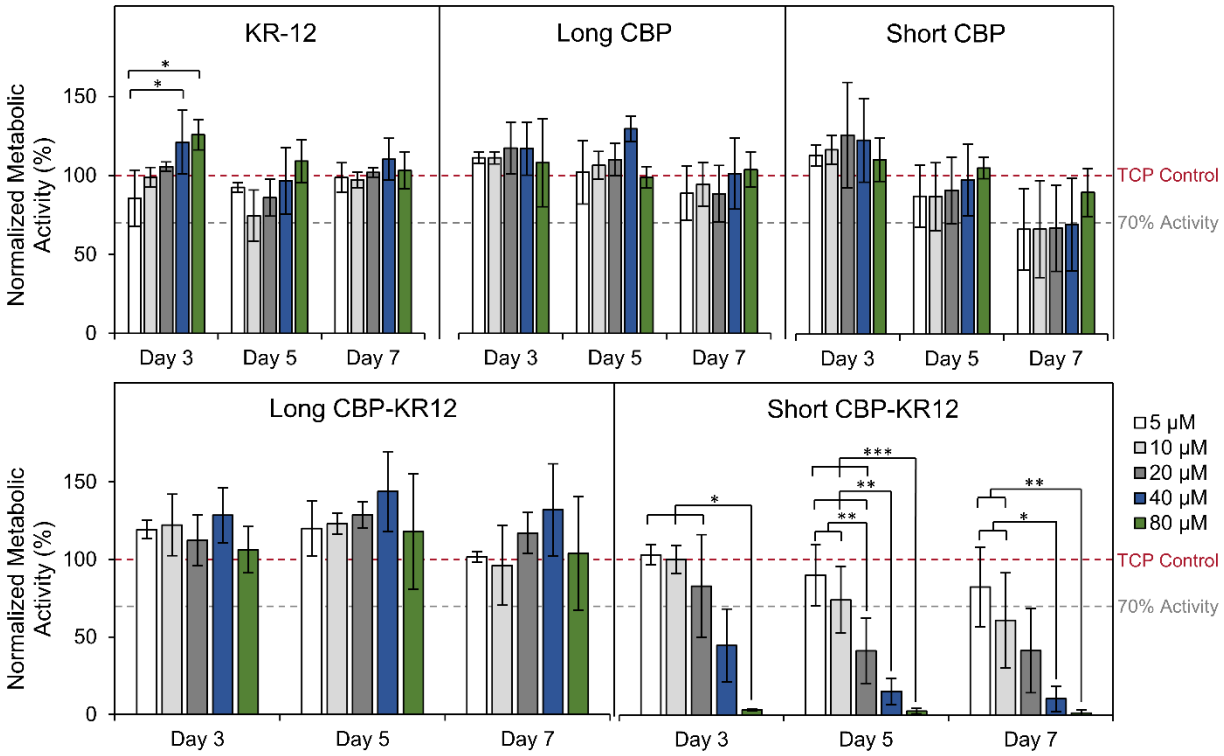

Figure 4.9. Free peptide effect on viability assessed through metabolic activity.
Effects of increasing peptide concentration on the metabolic activity of NHDF. All data are normalized to the metabolic activity of untreated control wells indicated by the red dashed line, and 70% activity is indicated by the grey dashed line. Data are presented as the mean and standard deviation from three independent experiments (n = 3 per experiment). Statistical differences determined by an ANOVA followed by the Tukey's HSD test (* $p < 0.05$, ** $p < 0.01$, *** $p < 0.005$).

The Long-CBP-KR12, like its individual components, exhibited no effects on metabolic activity across all concentrations. The Short-CBP-KR12 peptide, however, exhibited increased cytotoxicity with concentration at and above 20 µM. On day 3, 5 µM and 10 µM exhibit no significant effect on metabolic activity with 104% ± 6% and 101% ± 8%, respectively. Increasing peptide concentration to 20 µM resulted in a decrease in metabolic activity with extremely high variability of 84% ± 44%. Increasing the peptide concentration above 20 µM resulted in statistically significant decreases in metabolic activity where 40 µM resulted in metabolic activity of 45% ± 24% and 80 µM resulted in essentially what can be characterized as near complete cell death with a quantifiable metabolic activity of only 3% ± 1%. This trend was consistent for all time points. The increase in cytotoxic activity of short-CBP-KR12 despite clear evidence of biocompatibility of its individual CBP and AMP components could be attributed to the low solubility of

the peptide. Although Short-CBP-KR12 can initially solubilize in media the peptide crashes out of solution over the course of the initial 3 days, resulting in aggregation and increased cytotoxicity at higher concentration and prolonged exposure. Solubility issues is a known issue with AMPs in solution, and further experiments were designed with the understanding that free Short-CBP-KR12 above 20 μM may result in adverse cellular response [34]. This cytotoxic concentration is still higher than the reported cytotoxic threshold of soluble LL-37 at 13 μM [72]. According to ISO 10993-5, cytotoxicity is defined as any concentration that reduces the cellular metabolic activity by more than 30% compared to untreated control groups grown on tissue culture plastic (TCP) [34, 73]. All peptide sequences except higher concentrations of Short-CBP-KR12 and later timepoints of Short-CBP fell well above the 70% relative metabolic activity cutoff.

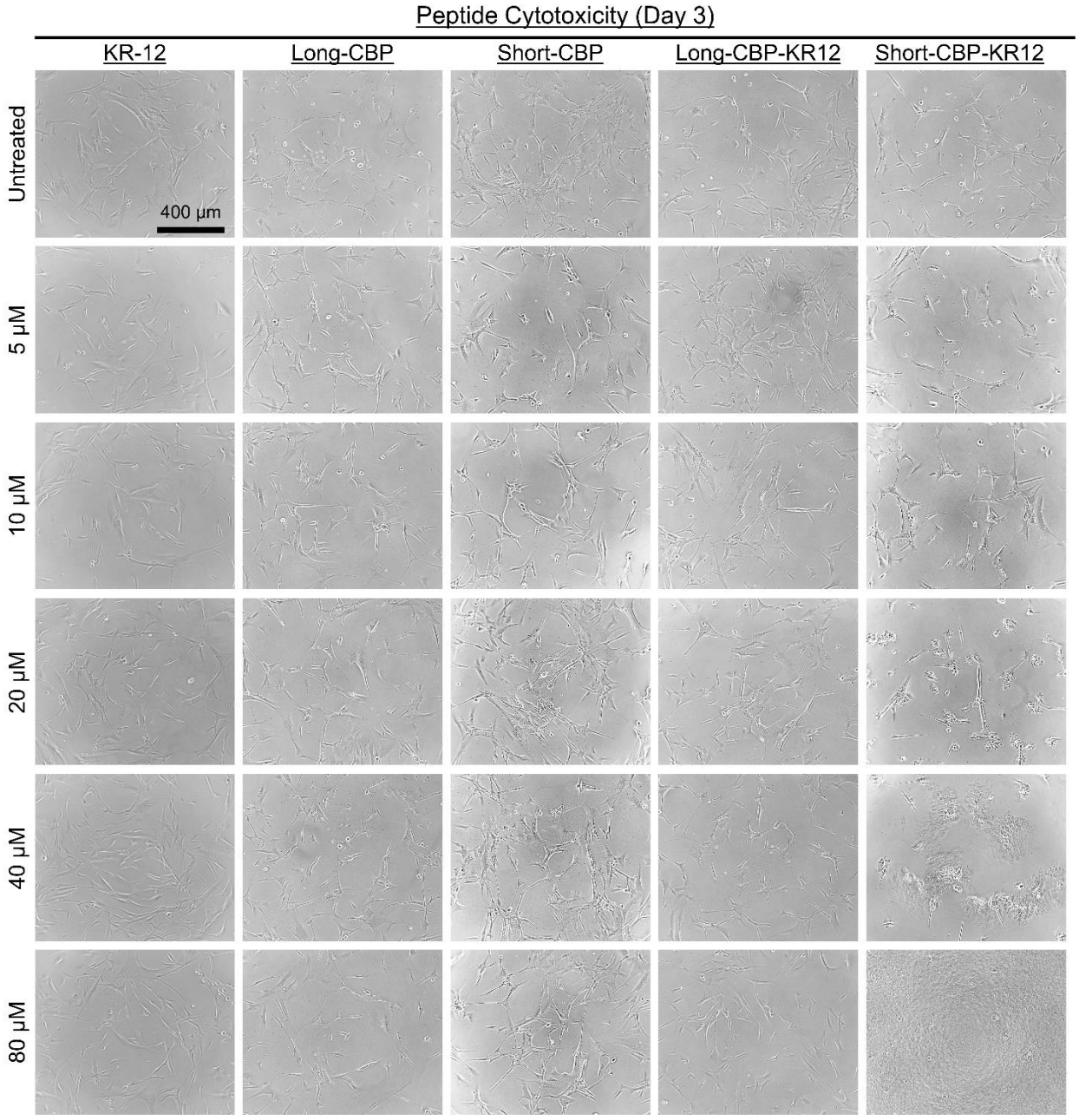

Figure 4.10. Representative images of NHDF on Day 3 after treatment with peptide solutions

4.3.3. Peptide minimum inhibitory concentration (MIC)

To assess if antibacterial activity of KR-12 is maintained with the addition of CBPs, the minimum inhibitory concentration (MIC) of each KR-12 containing peptide was determined against gram-positive *S. aureus*, and gram-negative *E. coli* and *P. aeruginosa*. Effective MIC determination for *S.aureus* was not achieved (**Figure 4.11**). In this study KR-12's MIC against *E. coli* was determined to be 2.5 µM, and was

comparable to the range of 2-2.5 μM previously reported [23, 24, 71]. The MIC of KR-12 against *P. aeruginosa* at 10 μM, however, was higher than literature values of 4 μM [23]. Accepted inhibitory values are variable as MIC values are highly dependent on initial inoculum concentrations and MIC determination method. Additionally, the AMPs mechanism of action can be affected by membrane composition differences between sub strains and the reported MIC values can vary. For example, in the studies performed by Jacob et al. KR-12's MIC against *S aureus* was reported as 10 μM, Luo et al. reported it as 8.4 ± 6.3 μM, and Gunasekera et al. reported it as 4 μM [23, 24, 71]. The determined MIC value using KR-12 against *P. aeruginosa* is well within the accepted range in literature. Additionally, *P. aeruginosa* is a bio-film producing strain that would hinder antibacterial activity through AMPs normal mechanism of membrane interaction through electrostatic forces, allowing for increased inhibitory variability [74]. KR-12 is known to have a wide therapeutic index, where the antibacterial concentration is far lower than the concentrations that result in mammalian cytotoxicity. This is confirmed where the highest MIC observed was 10 μM and no mammalian cytotoxicity was observed up to 80 μM.

When assessing the antibacterial activity of both chimeric peptides a decrease in overall activity was observed. Against *E. coli*, both the Long-CBP-KR12 and Short-CBP-KR12 inhibited bacterial growth at 10 μM, a four-fold increase in inhibitory concentration compared to KR-12. The inhibitory concentration for Long-CBP-KR12 against *P. aeruginosa* was determined to be greater than 80 μM, while the Short-CBP-KR12 peptide was able to inhibit growth at exactly 80 μM, an 8 fold increase compared to KR-12. This decrease in bioactivity was not unexpected. When linking collagen binding domains to LL-37, Lozeau et al. observed an almost 4-fold increase in inhibitory concentration against *E. coli* and an 11-fold increase against *P. aeruginosa* [19]. By linking additional bioactive amino acids to the AMP, side interaction can hinder the effectivity of the AMPs. Additionally, a reduction in hydrophobic moment was identified in both the Long-CBP-KR12 and Short-CBP-KR12 in section 4.3.1.. Torres et al. determined AMP's with hydrophobic moments above 0.6 and below 0.8 fall within a "hot spot" for favorable antibacterial activity [75]. The reduction in hydrophobic moment further explains the need for increased peptide concentration

to inhibit bacterial growth. Overall, antibacterial activity of the linked KR-12 in the designed chimeric peptides was maintained, and the Long-CBP-KR12 exhibited a wider therapeutic window than the Short-CBP-KR12.

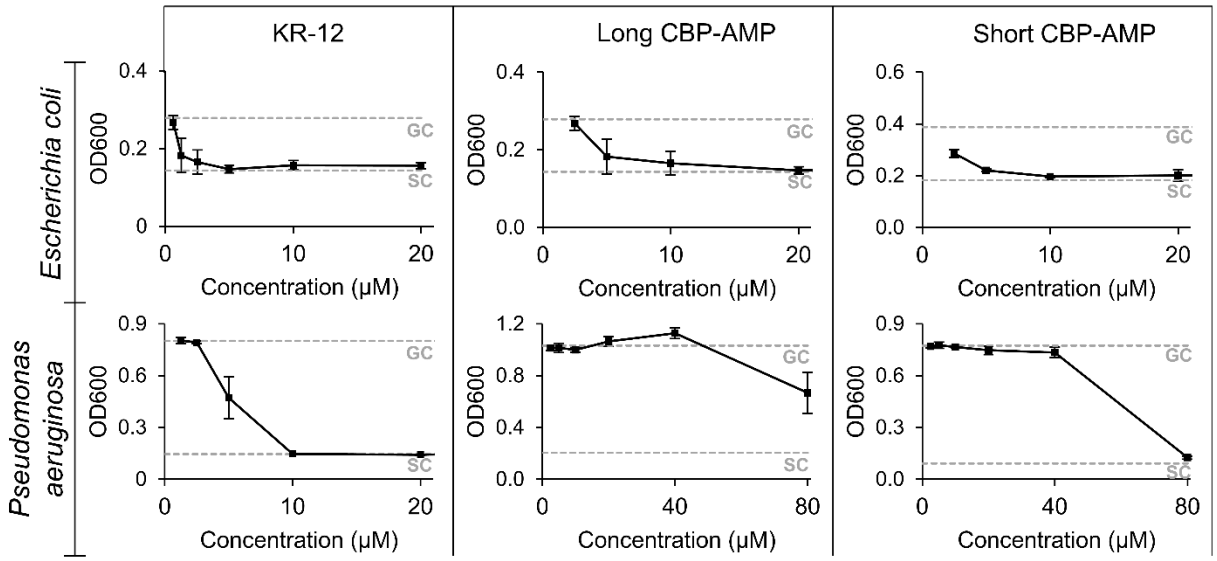

	Minimum Inhibitory Concentration (μM)		
Bacterial Strain	KR-12	Long CBP-AMP	Short CBP-AMP
Escherichia coli	2.5	10	10
Pseudomonas aeruginosa	10	>80	80
Staphylococcus aureus	>80	-	-

Figure 4.11. Minimum inhibitory concentration and MIC values.
E. coli and P. aeruginosa optical density in response to increasing concentrations of KR-12, Long-CBP-KR12 and Short-CBP-KR12 are plotted, with untreated growth control values denoted as GC, and sterile control values denoted as SC. Data are presented as the mean and standard deviation from three independent experiments (n = 3 per experiment). MIC values were determined as the lowest concentration to not be statistical significance compared to the sterile control as determined by an ANOVA followed by a Dunnett HSD test.

4.3.4. Endotoxin binding

LL-37 and KR-12 are able to interact with and mediate the inflammatory pathways stimulated by LPS [23]. LPS, imbedded in the membranes of gram-negative bacteria, is release upon bacterial cell death. Released LPS is known to stimulate toll-like receptor 4 (TLR-4), resulting in activation of downstream pro-inflammatory signaling cascade [23, 72]. To investigate if the antiendotoxin activity in the chimeric peptides was retained, the binding activity of the peptides to LPS was evaluated by chromogenic LAL

assay. The binding efficiency was determined by assessing the peptides ability to inhibit the LPS induced activation of the limulus amebocyte lysate enzyme [23]. Peptide solutions were incubated with 3 EU/mL LPS and LAL enzyme activation was normalized to control wells treated with water that would not neutralize LPS [76] (**Figure 4.13A**). In this setup relative absorbance values close to 1 indicate no LPS binding, while values below 1 indicate binding. The Long-CBP and Short-CBP, with no known LPS binding capacity, exhibited no statistical changes in LPS detection with relative absorption values of 0.88 ± 0.04 and 0.98 ± 0.04, respectively. Interestingly, the Long-CBP-KR12 indicated an increase in detectable LPS resulting in an absorption value of 1.22 ± 0.1. Control wells with each peptide sequence were set up without LPS stimulation to assess if any LPS content was found in the synthetically synthesized peptides and could explain this increase in LPS detection. For all peptides tested no latent LPS was detected, indicating that this increase in LAL enzyme activation is only present when Long-CBP-KR12 is interacting with the spiked in LPS. This interaction between LPS and Long-CBP-KR12 is unknown and warrants further structural investigation. Both the Short-CBP-KR12 and KR-12 peptides exhibited statistically significant decrease in LPS detection with absorption values of 0.08 ± 0.01 and 0.82 ± 0.05, respectively.

Relative absorbance values were converted to endotoxin bound percentage (**Figure 4.12B**). KR-12 was shown to bind to 18% ± 5% of LPS in solution. Though previously published LPS binding capacity for KR-12 have not been reported above 10 μM, assuming increase in peptide concentration would result in increased binding this value is comparable to the previously reported 10% binding capacity at 10 μM [23]. Interestingly, though not statistically significant compared to the untreated control, the Long-CBP peptide was able to non-specifically bind to 12% ± 4% LPS. This is interesting as the CBP is neutrally charged and peptide-LPS interactions are believed to be predominantly driven by electrostatic interactions between positively charged peptides and negatively charged LPS. This non-specific interaction can be attributed to hydrophobic interactions between the hydrophobic residues in the Long CBP sequence and the lipid A domain of LPS. Effectively producing peptide-LPS clusters that may prevent full LAL enzyme activation and detection [77, 78]. This proposed “blocking” effect is different from the AMP interaction with LPS,

which is described to induce a structural change of LPS, preventing detection and activation of the LAL enzyme [79, 80]. Additionally, Rosenfeld et al. proposed that the ratio between hydrophobicity and charge is a strong determinant of LPS interactions [81]. Though the Short CBP has a high hydrophobicity (**Table 4.3**), this same level of hydrophobic interaction is not observed, most likely owing to its smaller size [40]. When linked to KR-12 the Short-CBP-KR12 peptide reported exceptionally high LPS binding capacity at 92% ± 1%. As the KR-12 containing-peptide with the highest calculated hydrophobicity, this high LPS binding capacity is due to a combination of AMP-LPS electrostatic and CBP-LPS hydrophobic interactions. Overall resulting in a chimeric peptide sequence that surpassed the LPS binding capabilities of KR-12 alone.

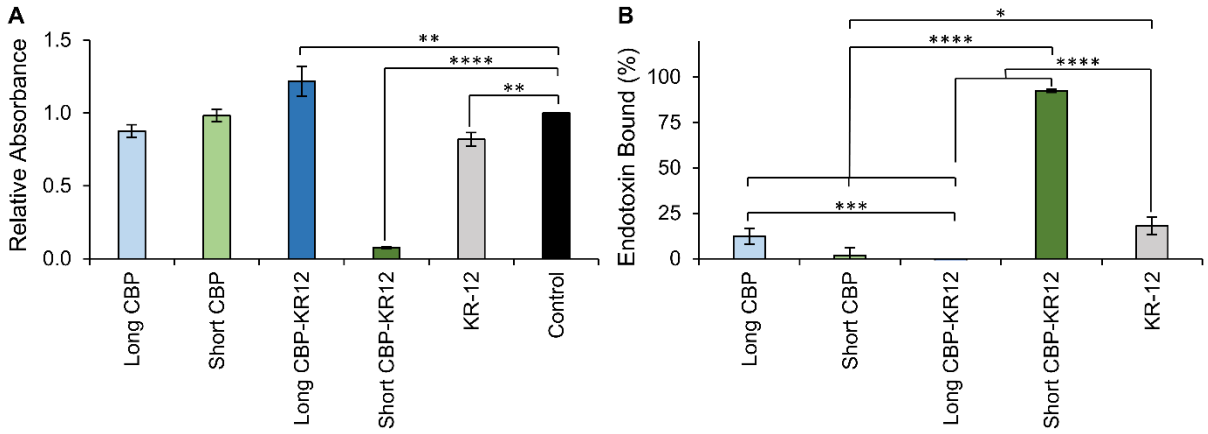

Figure 4.12. Endotoxin binding activity of KR-12 and KR-12 containing chimeric peptides. **(A)** Endotoxin binding capacity normalized to the untreated control. Values below 1.0 indicate endotoxin binding and neutralization. Statistical differences determined by an ANOVA followed by a Dunnett HSD test (** $p < 0.005$, *** $p < 0.0001$). **(B)** Normalized endotoxin binding converted to percent endotoxin bound. Statistical differences determined by an ANOVA followed by a Tukey's HSD test. Data are presented as the mean and standard deviation from three independent experiments (n = 3 per experiment).

4.3.5. Cellulose binding capacity of the CBPs and chimeric peptides

Cellulose binding capacity of Short-CBP, Long-CBP, and both chimeric peptides were assessed to determine the effects of linking KR-12 to the bioactive CBP sequences. BC samples were prepared as previously described to produce opaque (0% arabitol) and transparent (85% arabitol) BC material [33]. Binding was assessed through UV-vis analysis of fluorescently tagged peptides in binding supernatant and reported as peptide concentration bound to individual BC pellicles (**Figure 4.13**). Due to the presence of

residual proteins in the BC material and lack of tyrosine and tryptophan residues in the unaltered KR-12 peptide sequence, protein quantification through BCA assay or 280 nm absorbance could not be performed. Quantification through fluorescent labeling or epitope tagging is well established in the field [19, 34]. Binding assessment was performed on both opaque and transparent BC, with known differences in cellulose fiber microstructure, where transparent BC had an average median fiber width of 32 nm and opaque BC a median fiber width of 39 nm [33]. Previous use of the Short-CBP indicated increased binding selectivity to materials with fiber width in the µm range rather than the nm range [34]. Though not statistically significant, a marginal increase in binding capacity was observed for opaque BC as compared to transparent BC for all peptides tested.

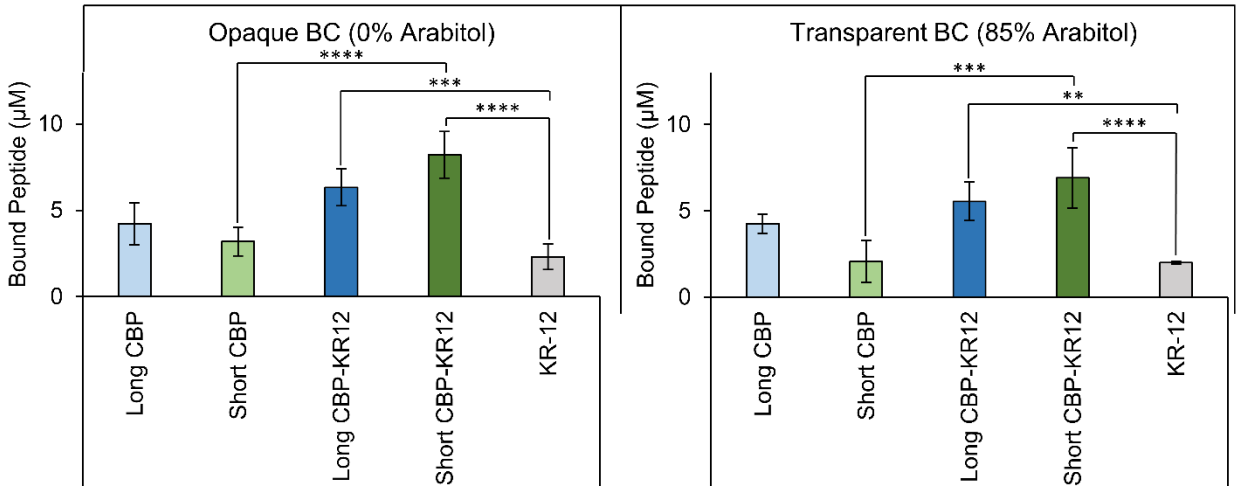

Figure 4.13. Cellulose binding capacity of CBPs and CBP-AMP-KR12.
CBP binding to both transparent and opaque BC. Data are presented as the mean and standard deviation from three independent experiments (n = 3 per experiment). Statistical differences determined by an ANOVA followed by a Tukey's HSD test (** $p < 0.005$, *** $p < 0.001$, **** $p < 0.0001$).

KR-12, with no specific cellulose binding capacity, was used as a binding control. Non-specific adsorption of KR-12 was observed on both the opaque and transparent BC at 2.3 µM and 2.0 µM, respectively. The surface of BC is believed to be slightly negative, allowing for electrostatic interaction between the positively charged AMP and cellulose material. However, this interaction is not stable as fluorescence signal of KR-12 modified BC decayed over a 7 day period (**Figure 4.14, Figure 4.15**). It should be noted that initial fluorescence intensities should not be compared as a measure of binding in the fluorescence images provided. The FAM-tagged peptide solutions all showed varying fluorescence

intensities at the same peptide concentrations, more likely due to hydrophobic interactions between the fluorescent tag and the more hydrophobic peptides [82]. For this reason, fluorescence images only provide a measure of binding longevity and not binding concentration. Control images were taken of opaque and transparent BC, and no autofluorescence was observed. All peptides containing a CBP sequence exhibited

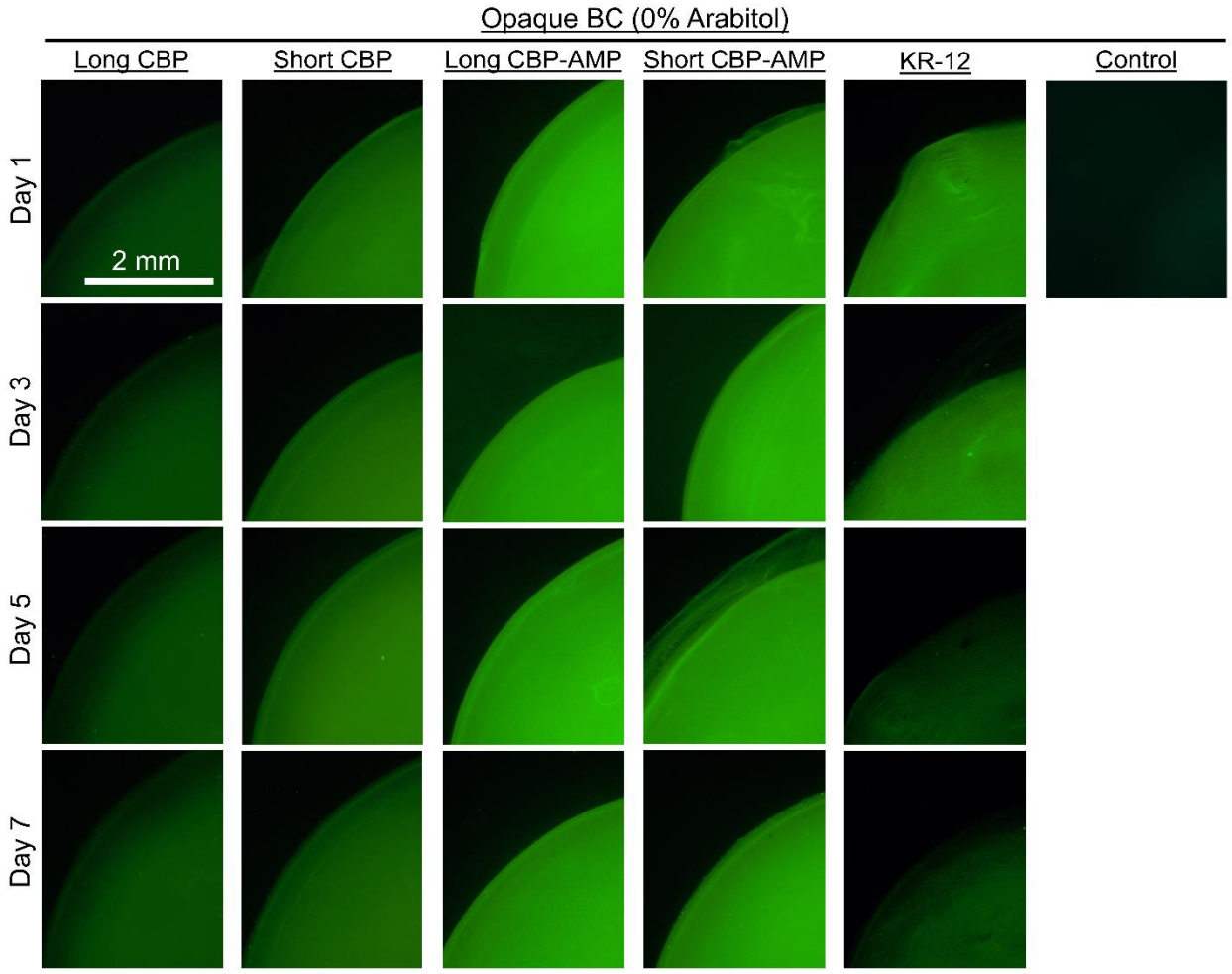

Figure 4.14. Qualitative indicators of binding and stability on 0% arabitol BC over 7 days. Qualitative images of FAM-tagged peptide present on the surface of opaque 0% arabitol BC. Control samples refers to images taken of BC without the presence of fluorescent labeled peptides. Images were taken on days 1, 3, 5, 7 after initial rinsing and gain and exposure time settings were kept constant for all images.

consistent fluorescent signal over a 7 day period on both opaque and transparent BC. This indicated stable immobilization of the peptide using either the Long CBP or Short CBP binding peptides. This prolonged binding was consistent with findings by Weishaupt et al. where the Short CBP effectively immobilized active antimicrobial ligands for up to 21 days [34].

Increased binding was observed for both chimeric peptides compared to their CBP only counterparts, although this difference was only statistically significant for the Short-CBP-KR12 peptide. The Short-CBP-KR12 peptide allowed for 8 µM and 7 µM binding to opaque and transparent BC respectively, while the Short CBP only indicated 3 µM and 2 µM binding. Guo et al. determined that as a short peptide with no tertiary structure the Short CBP has reduced binding affinity to cellulose, but with the addition of larger peptide groups binding affinity increases [40]. This similarity explains the Long CBP's trend of higher binding capacity compared to the Short-CBP, with its more defined cyclized tertiary structure. The Short-CBP-KR12 indicated a tendency for increased binding capacity compared to the Long-CBP-KR12. Khazanov et al., when designing the Long CBP, identified five main residues participating in hydrogen binding and hydrophobic interactions with the cellulose material [35]. The Short CBP, however, is believed to have two main residues responsible for cellulose interactions [40]. It is possible that the smaller size and reduced cellulose interacting residues of the CBP in the Short-CBP-KR12 peptide allows for increased peptide per surface area coverage compared to the Long CBP and resultant Long-CBP-KR12.

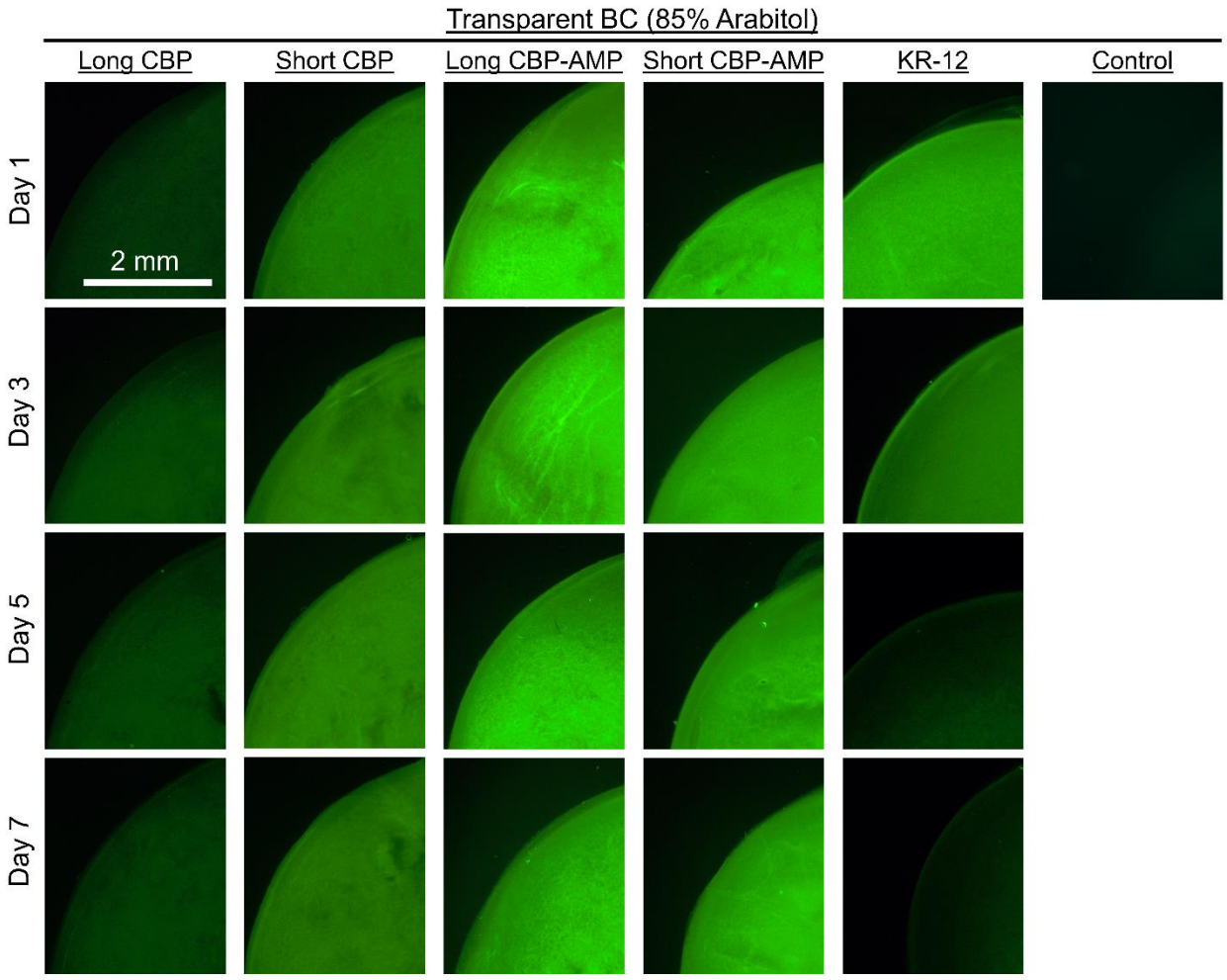

Figure 4.15. Qualitative indicators of binding and stability on 85% arabitol BC over 7 days. Qualitative images of FAM-tagged peptide present on the surface of transparent 85% arabitol BC. Control samples refers to images taken of BC without the presence of fluorescent labeled peptides. Images were taken on days 1, 3, 5, 7 after initial rinsing and gain and exposure time settings were kept constant for all images.

4.3.6. Effect of peptide-functionalized BC on *in vitro* cytotoxicity

Cell proliferation and re-epithelialization of wounds is of great importance in wound care. Previously, BC's biocompatibility and lack of effect on metabolic activity was shown for both transparent and opaque materials [33]. To assess cytotoxicity of Long-CBP-KR12 and Short-CBP-KR12 functionalized opaque and transparent BC, metabolic activity assays were performed. Metabolic activity was assessed in both NHDF and HaCaT cells as the predominant proliferative cells present in the wound bed (**Figure 4.16**) [26, 42]. Unfunctionalized opaque or transparent BC was used as a control. Considering the cytotoxic effects of the Short-CBP-KR12 observed in section 4.3.2, the lack of cytotoxic response here further

indicated effective peptide immobilization to the cellulose material. Consistent with previous findings, tethered KR-12 exhibited no cytotoxic effect across both cell lines and all time points. With the HaCaT cells, a slight increasing trend in metabolic activity was observed in cells exposed to KR-12 functionalized BC. Though not as pronounced, this trend was consistent with prior findings by Song et al. and Liu et al. for HaCaT cells response to KR-12 covalently conjugated to silk and eggshell membrane materials [26, 42]. The lower trend observed here can be attributed to the different methods of cell seeding. Both Song et al. and Liu at al. seeded on top of their functionalized material, allowing for more direct contact and interaction between KR-12 functionalized surfaces and cells. KR-12, like LL-37, is believed to activate the MAPK/ERK signaling pathway via transactivation of EGRF. This increases cell migration, proliferation and differentiation and explains the increase in metabolic activity [26, 83, 84]. Overall, this indicates that BC functionalized with Long-CBP-KR12 and Short-CBP-KR12 not only had no negative effects on metabolic activity but may promote proliferation and re-epithelization of the wound site. Additional representative images of cells for each condition and time point are captured in Appendix 6.1.

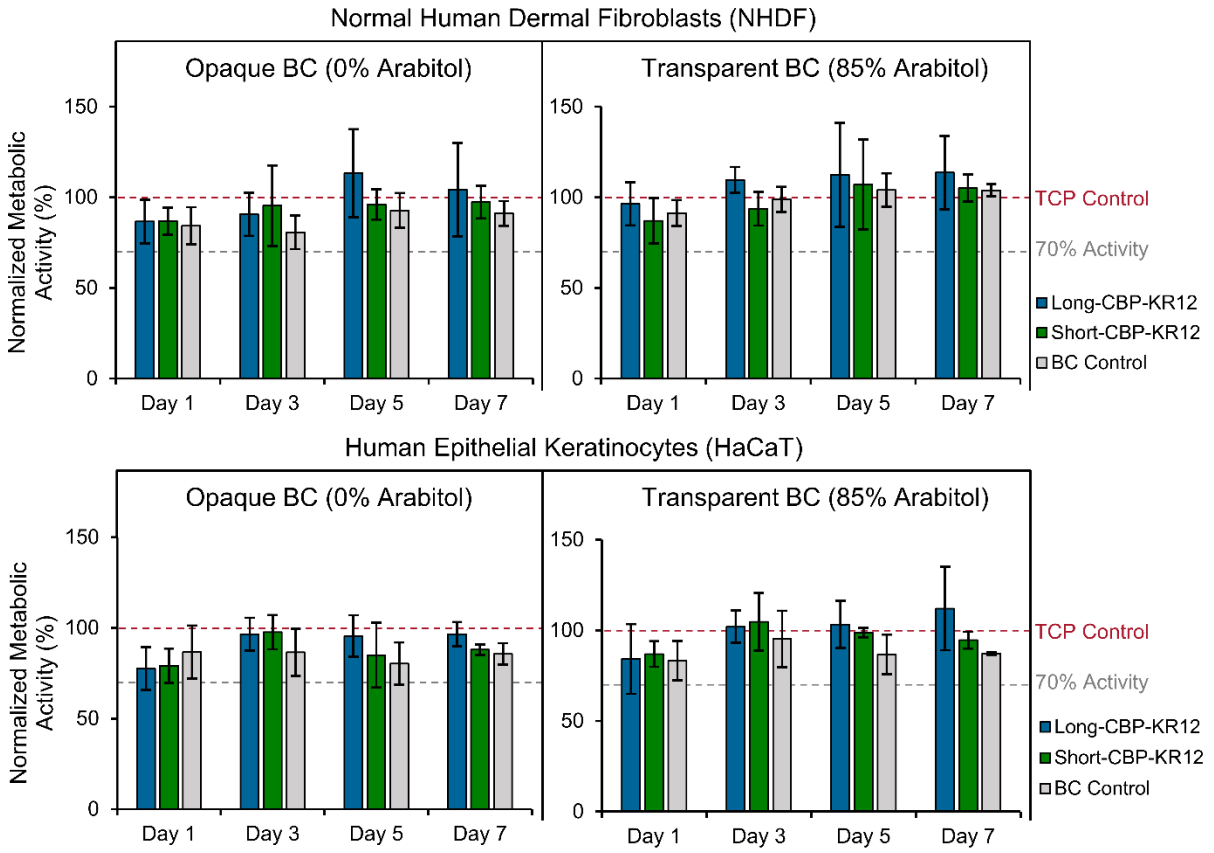

Figure 4.16. Functionalized BC effects on NHDF and HaCaT cell lines.
Metabolic activity values of unfunctionalized BC and BC functionalize with Long-CBP-KR12 and Short-CBP-KR12 normalized to untreated wells. Metabolic effects are depicted for both NHDF and HaCaT cell lines. All data are normalized to the metabolic activity of untreated control wells indicated by the red dashed line, and 70% activity is indicated by the grey dashed line. Data are presented as the mean and standard deviation from three independent experiments (n = 3 per experiment). No statistical differences determined by an ANOVA followed by a Tukey's HSD test.

4.3.7. Surface functionalized BC antibacterial activity

To evaluate the antibacterial activity of functionalized BC, bacterial growth of *E. coli* and *P. aeruginosa* after 1 h exposure to Long-CBP-KR12 and Short-CBP-KR12 functionalized BC were assessed. Functionalized BC samples were then rinsed, allowed to incubate in fresh medium for 12h, and bacterial growth were assessed via absorbance readings at 600 nm. Antibacterial activity of functionalized opaque and transparent BC surface were assessed. Additionally, unfunctionalized BC and a commercially available hydrogel-based wound dressing with no known antibacterial activity were included as negative controls. BC loaded with unbound KR-12 was included as a positive control assessing antibacterial activity of the unaltered, untethered AMP in this set up (**Figure 4.17**).

Though not statistically significant, a decreasing trend in *E. coli* growth was observed when comparing opaque functionalized and unfunctionalized BC. This trend, however, was not observed for the transparent BC against *E. coli*. The Short-CBP-KR12 functionalized opaque BC resulted in a 29% reduction of *E. coli* growth compared to the unfunctionalized BC control Compared to the hydrogel based commercial wound dressing material, opaque BC functionalized with Long-CBP-KR12 and Short-CBP-KR12 both reduced *E. coli* growth by 33% and 36%, respectively. Similar trends were observed for functionalized transparent BC, where tethered Long-CBP-KR12 reduced *E coli* growth by 33% and tethered Short-CBP-KR12 reduced growth by 31%. For both the opaque and transparent BC, adsorbed KR-12 reduced *E. coli* growth by at least 46% compared to the commercially available wound dressing, and upwards of 31% compared to unfunctionalized BC. With the MIC of KR-12 in solution being lower than either of the chimeric peptides, it is expected that the release of untethered KR-12 would result in bactericidal activity. However, KR-12 in solution is unstable in protease rich environments, resulting in almost full degradation in 3 minutes and reduced longevity of the antibacterial activity [71]. Lozeau et al. reported similar finding for peptide driven immobilization of LL-37, where free LL-37 reduced *E.coli* growth by ~65% while immobilized LL-37 reduced bacterial growth by either ~30% or ~60% depending on the respective immobilization method [19]. No statistical difference in bacterial growth was observed across all functionalized and unfunctionalized materials tested against *P. aeruginosa*. This lack of antibacterial activity aligns with the higher minimum inhibitory concentration of the chimeric peptides against *P. aeruginosa* combined with the activity hinderance effects of immobilization [27].

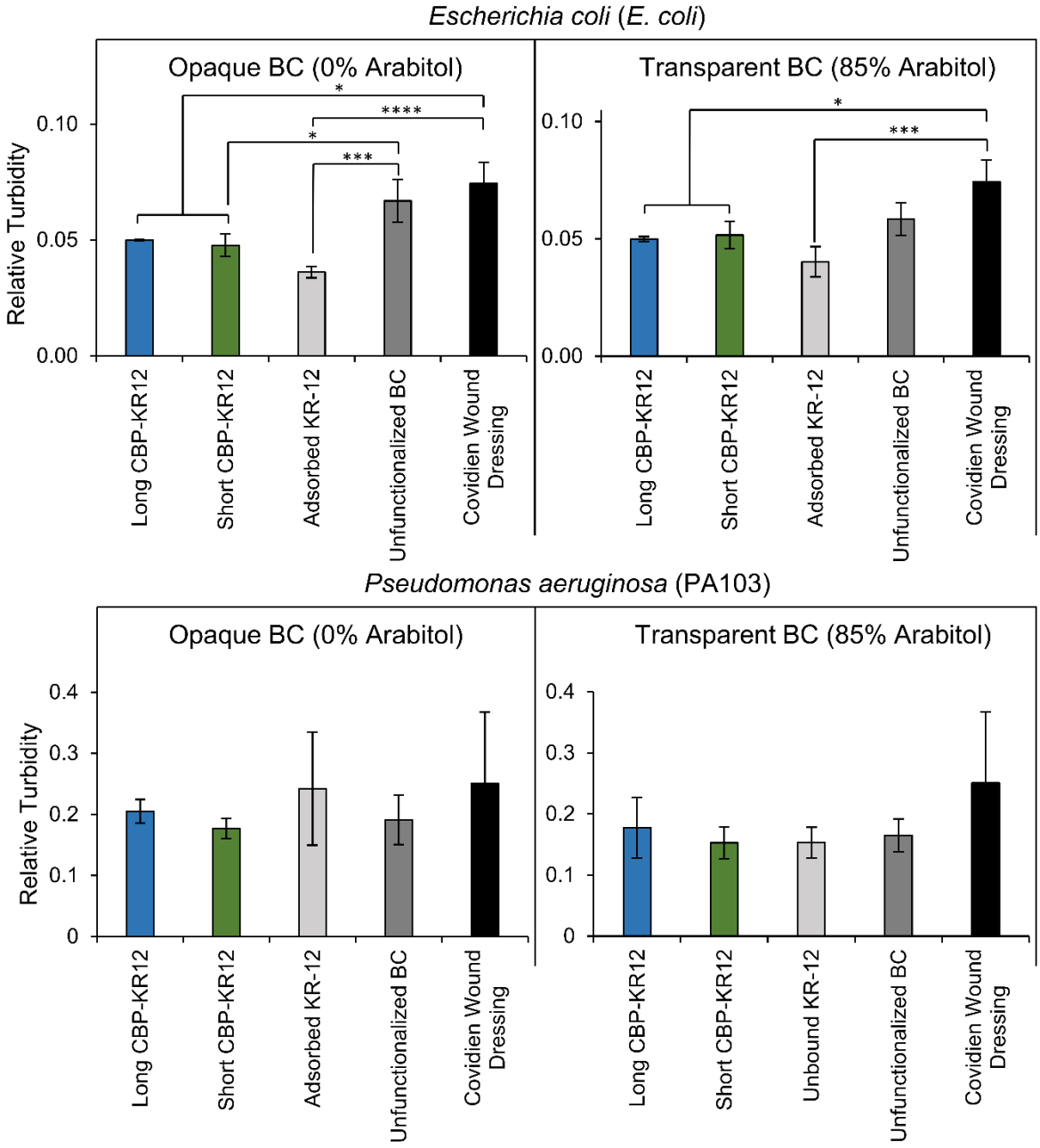

Figure 4.17. Relative turbidity of E. coli and P. aeruginosa incubated with functionalized BC. Relative turbidity after functionalized BC exposure to each respective bacterial strain for 12 hours. Statistical differences determined by an ANOVA followed by a Tukey's HSD test (* $p < 0.05$, ** $p < 0.005$, *** $p < 0.0005$, **** $p < 0.0001$).

Though the MIC of the free peptide determined in section 4.3.3 provided a baseline prediction for the antibacterial activity of BC functionalized with each chimeric peptide, it is very difficult to compare the effectiveness of free versus immobilized AMPs. This is due to a variety of factors that cannot be directly compared, such as surface density versus concentration in solution, and conformational freedom versus

steric hindrance between free and immobilized AMPs [19, 26]. Additional factors such as lack of precise quantification of immobilized AMPs further hinder direct comparisons [85]. In general, direct comparisons of free and immobilized AMPs are rarely described. Of the cases reported, immobilized AMPs resulted in increased MIC values between 8- and 64-fold higher than soluble AMPs [85-87]. Additionally, accurate assessments of reported immobilization effects on AMP activity are confounded specifically by immobilization method and resulted steric hinderance [88]. Steric hinderance of the immobilized AMP poses a great hinderance to peptide bioactivity. For example, LL-37 directly conjugated to titanium fully restricted any bactericidal activity, but when immobilization through a PEG spacer/linker Gabriel et al. demonstrated that antibacterial activity was retained [89]. Further, Bagheri et al. demonstrated that immobilized AMP activity directly correlates to linker length and flexibility [90]. Similar to the work by Weishaupt et al., we utilized a flexible glycine-rich linker to reduce steric hinderance of the immobilized AMP [34, 43]. Additional confounding factors present in literature comparison is the underreported immobilization of the C or N-terminal of the AMP. Previous findings for immobilized LL-37 reported immobilize through C-terminal modifications [16, 19, 20]. Similarly, Mishra et al. reported increased retention of antibacterial activity of C-terminal immobilized LL-37 fragments which had similar structure to KR-12 [91]. More recently, KR-12 immobilization through N-terminal covalent surface conjugation has been explored and heavily advocated for. Both Song et al. and Blasi-Romero et al. argue that due to the high density of hydrophobic residues found at KR-12's C-terminal, covalent immobilization needs to occur at the N-terminal for retained antibacterial activity [26, 27]. However, Bagheri et al. argues that AMP N- or C-terminal immobilization orientation is less relevant with the use of a flexible linker [90, 92]. In the work reported here, KR-12 was immobilized via linker and CBP modification of the C-terminal. Particularly in the case of KR-12 where antibacterial activity is driven by many factors such as secondary structure, hydrophobic moment, and hydrophobicity of the peptide [85]. Overall, we observed a decreasing trend in bacterial growth of *E. coli* through KR-12 immobilization to opaque BC via CBP driven cellulose surface interactions.

4.4. Conclusion

In this study, we designed chimeric peptides to non-covalently modify the surface of BC by linking bioactive CBPs with KR-12 and assessed the overall bioactivity of the chimeric peptides. As the secondary structure of AMPs are believed to be essential for bioactivity, conservation of the helical structure of KR-12 was initial predicted *in silico* and then confirmed experimentally through CD analysis of both the Long-CBP-KR12 and Short-CBP-KR12 sequences. Chimeric peptides and their individual components were assessed for cytotoxicity, where only higher concentrations of Short-CBP-KR12 studied and later timepoints of Short-CBP exhibited negative effects on metabolic activity, which was attributed to solubility issues. Additionally, trends of increasing metabolic activity in response to increasing KR-12 and Long-CBP-KR12 concentrations were observed. All KR-12 containing peptides exhibited antibacterial activity in solution against *E. coli* and *P. aeruginosa*, though higher inhibition concentrations were required for both chimeric peptides likely due to the fact that the chimeric peptides were predicted to exhibit changes of antibacterial activity mediating properties such as hydrophobic moment and hydrophobicity. The Short-CBP-KR12 peptide exhibited enhanced LPS binding capabilities compared to both the KR-12 control and Long-CBP-KR12. Both Long and Short CBP binding mechanisms allowed for effective binding and stabile immobilization of Short-CBP-KR12 and Long-CBP-KR12 over a 7-day period. Reduced antibacterial activity of immobilized Short-CBP-KR12 and Long-CBP-KR12 was observed, which is consistent with previous findings. Additionally, all functionalized materials exhibited no adverse effects on metabolic activity of both NHDF and HaCaT epithelial cells. Results from this study support the effectiveness of CBP-driven immobilization of AMPs and warrant further investigation into the wound healing capabilities of non-covalently immobilized KR-12.

4.5. Acknowledgements

We thank Katelyn Mistretta and Melissa Wojnowski for assisting in the mammalian cell viability assays, and Dhespina (Ina) Zhidro for assisting with the CBP and CBP-AMP functionalized BC fluorescence imaging.

4.6. References

[1] R.G. Frykberg, J. Banks, Challenges in the treatment of chronic wounds, Advances in wound care 4(9) (2015) 560-582.
[2] S.R. Nussbaum, M.J. Carter, C.E. Fife, J. DaVanzo, R. Haught, M. Nusgart, D. Cartwright, An economic evaluation of the impact, cost, and medicare policy implications of chronic nonhealing wounds, Value in Health 21(1) (2018) 27-32.
[3] S.a. Guo, L.A. DiPietro, Factors affecting wound healing, Journal of dental research 89(3) (2010) 219-229.
[4] R. Zeng, C. Lin, Z. Lin, H. Chen, W. Lu, C. Lin, H. Li, Approaches to cutaneous wound healing: basics and future directions, Cell and tissue research 374(2) (2018) 217-232.
[5] M. Walker, D. Metcalf, D. Parsons, P. Bowler, A real-life clinical evaluation of a next-generation antimicrobial dressing on acute and chronic wounds, Journal of wound care 24(1) (2015) 11-22.
[6] S.W. Jere, H. Abrahamse, N.N. Houreld, The JAK/STAT signaling pathway and photobiomodulation in chronic wound healing, Cytokine & growth factor reviews 38 (2017) 73-79.
[7] A.A. Tandara, T.A. Mustoe, Oxygen in wound healing—more than a nutrient, World journal of surgery 28(3) (2004) 294-300.
[8] P.G. Rodriguez, F.N. Felix, D.T. Woodley, E.K. Shim, The role of oxygen in wound healing: a review of the literature, Dermatologic surgery 34(9) (2008) 1159-1169.
[9] S. Dhall, D. Do, M. Garcia, D.S. Wijesinghe, A. Brandon, J. Kim, A. Sanchez, J. Lyubovitsky, S. Gallagher, E.A. Nothnagel, A novel model of chronic wounds: importance of redox imbalance and biofilm-forming bacteria for establishment of chronicity, PLoS One 9(10) (2014) e109848.
[10] P. Basu, J.H. Kim, S. Saeed, M. Martins-Green, Using systems biology approaches to identify signalling pathways activated during chronic wound initiation, Wound Repair and Regeneration 29(6) (2021) 881-898.
[11] H. Ullah, H.A. Santos, T. Khan, Applications of bacterial cellulose in food, cosmetics and drug delivery, Cellulose 23(4) (2016) 2291-2314.
[12] G.W. Thomas, L.T. Rael, R. Bar-Or, R. Shimonkevitz, C.W. Mains, D.S. Slone, M.L. Craun, D. Bar-Or, Mechanisms of delayed wound healing by commonly used antiseptics, Journal of Trauma and Acute Care Surgery 66(1) (2009) 82-91.
[13] S.E. Brooks, M.A. Walczak, R. Hameed, P. Coonan, Chlorhexidine resistance in antibiotic-resistant bacteria isolated from the surfaces of dispensers of soap containing chlorhexidine, Infection Control & Hospital Epidemiology 23(11) (2002) 692-695.
[14] S. Koljalg, P. Naaber, M. Mikelsaar, Antibiotic resistance as an indicator of bacterial chlorhexidine susceptibility, Journal of Hospital Infection 51(2) (2002) 106-113.
[15] I. George Broughton, J.E. Janis, C.E. Attinger, The basic science of wound healing, Plastic and reconstructive surgery 117(7S) (2006) 12S-34S.
[16] L.D. Lozeau, J. Grosha, I.M. Smith, E.J. Stewart, T.A. Camesano, M.W. Rolle, Alginate Affects Bioactivity of Chimeric Collagen Binding LL37 Antimicrobial Peptides Adsorbed to Collagen-Alginate Wound Dressings, ACS Biomater. Sci. Eng. (2020).
[17] R.E. Hancock, H.-G. Sahl, Antimicrobial and host-defense peptides as new anti-infective therapeutic strategies, Nature biotechnology 24(12) (2006) 1551-1557.

[18] J. Kang, M.J. Dietz, B. Li, Antimicrobial peptide LL-37 is bactericidal against Staphylococcus aureus biofilms, PLoS One 14(6) (2019).
[19] L.D. Lozeau, J. Grosha, D. Kole, F. Prifti, T. Dominko, T.A. Camesano, M.W. Rolle, Collagen tethering of synthetic human antimicrobial peptides cathelicidin LL37 and its effects on antimicrobial activity and cytotoxicity, Acta biomaterialia 52 (2017) 9-20.
[20] L.D. Lozeau, S. Youssefian, N. Rahbar, T.A. Camesano, M.W. Rolle, Concentration-Dependent, Membrane-Selective Activity of Human LL37 Peptides Modified with Collagen Binding Domain Sequences, Biomacromolecules 19(12) (2018) 4513-4523.
[21] Ø. Samuelsen, H.H. Haukland, B.C. Kahl, C. von Eiff, R.A. Proctor, H. Ulvatne, K. Sandvik, L.H. Vorland, Staphylococcus aureus small colony variants are resistant to the antimicrobial peptide lactoferricin B, Journal of Antimicrobial Chemotherapy 56(6) (2005) 1126-1129.
[22] D. Ciumac, H. Gong, X. Hu, J.R. Lu, Membrane targeting cationic antimicrobial peptides, Journal of colloid and interface science 537 (2019) 163-185.
[23] B. Jacob, I.S. Park, J.K. Bang, S.Y. Shin, Short KR-12 analogs designed from human cathelicidin LL-37 possessing both antimicrobial and antiendotoxic activities without mammalian cell toxicity, Journal of Peptide Science 19(11) (2013) 700-707.
[24] Y. Luo, D.T. McLean, G.J. Linden, D.F. McAuley, R. McMullan, F.T. Lundy, The naturally occurring host defense peptide, LL-37, and its truncated mimetics KE-18 and KR-12 have selected biocidal and antibiofilm activities against Candida albicans, Staphylococcus aureus, and Escherichia coli in vitro, Frontiers in microbiology 8 (2017) 544.
[25] P. Saporito, M. Vang Mouritzen, A. Løbner-Olesen, H. Jenssen, LL-37 fragments have antimicrobial activity against Staphylococcus epidermidis biofilms and wound healing potential in HaCaT cell line, Journal of Peptide Science 24(7) (2018) e3080.
[26] D.W. Song, S.H. Kim, H.H. Kim, K.H. Lee, C.S. Ki, Y.H. Park, Multi-biofunction of antimicrobial peptide-immobilized silk fibroin nanofiber membrane: Implications for wound healing, Acta biomaterialia 39 (2016) 146-155.
[27] A. Blasi-Romero, M. Ångström, A. Franconetti, T. Muhammad, J. Jiménez-Barbero, U. Göransson, C. Palo-Nieto, N. Ferraz, KR-12 Derivatives Endow Nanocellulose with Antibacterial and Anti-Inflammatory Properties: Role of Conjugation Chemistry, ACS Applied Materials & Interfaces (2023).
[28] N. Mookherjee, K.L. Brown, D.M. Bowdish, S. Doria, R. Falsafi, K. Hokamp, F.M. Roche, R. Mu, G.H. Doho, J. Pistolic, Modulation of the TLR-mediated inflammatory response by the endogenous human host defense peptide LL-37, The Journal of Immunology 176(4) (2006) 2455-2464.
[29] E.J. Jervis, C.A. Haynes, D.G. Kilburn, Surface diffusion of cellulases and their isolated binding domains on cellulose, Journal of Biological Chemistry 272(38) (1997) 24016-24023.
[30] A. Khalid, R. Khan, M. Ul-Islam, T. Khan, F. Wahid, Bacterial cellulose-zinc oxide nanocomposites as a novel dressing system for burn wounds, Carbohyd. Polym. 164 (2017) 214-221.
[31] P. Muangman, S. Opasanon, S. Suwanchot, O. Thangthed, Efficiency of microbial cellulose dressing in partial-thickness burn wounds, The Journal of the American College of Certified Wound Specialists 3(1) (2011) 16-19.
[32] E.M. van Zyl, J.M. Coburn, Hierarchical structure of bacterial-derived cellulose and its impact on biomedical applications, Curr. Opin. Chem. Eng. 24 (2019) 122-130.

[33] E.M. van Zyl, M.A. Kennedy, W. Nason, S.J. Fenlon, E.M. Young, L.J. Smith, S.R. Bhatia, J.M. Coburn, Structural properties of optically clear bacterial cellulose produced by Komagataeibacter hansenii using arabitol, Biomaterials Advances 148 (2023) 213345.
[34] R. Weishaupt, J.N. Zünd, L. Heuberger, F. Zuber, G. Faccio, F. Robotti, A. Ferrari, G. Fortunato, Q. Ren, K. Maniura-Weber, Antibacterial, Cytocompatible, Sustainably Sourced: Cellulose Membranes with Bifunctional Peptides for Advanced Wound Dressings, Advanced Healthcare Materials (2020) 1901850.
[35] N. Khazanov, T. Iline-Vul, E. Noy, G. Goobes, H. Senderowitz, Design of compact biomimetic cellulose binding peptides as carriers for cellulose catalytic degradation, The Journal of Physical Chemistry B 120(2) (2016) 309-319.
[36] E.Y. Kim, G. Rajasekaran, S.Y. Shin, LL-37-derived short antimicrobial peptide KR-12-a5 and its d-amino acid substituted analogs with cell selectivity, anti-biofilm activity, synergistic effect with conventional antibiotics, and anti-inflammatory activity, European journal of medicinal chemistry 136 (2017) 428-441.
[37] M. Gullo, S. La China, P.M. Falcone, P. Giudici, Biotechnological production of cellulose by acetic acid bacteria: current state and perspectives, Appl. Microbiol. Biot. 102 (2018) 6885-6898.
[38] K.V.S. Hodel, L.M.d.S. Fonseca, I.M.d.S. Santos, J.C. Cerqueira, R.E.d. Santos-Júnior, S.B. Nunes, J.D.V. Barbosa, B.A.S. Machado, Evaluation of Different Methods for Cultivating Gluconacetobacter hansenii for Bacterial Cellulose and Montmorillonite Biocomposite Production: Wound-Dressing Applications, Polym. 12(2) (2020) 267.
[39] M. Barbosa, H. Simões, S.N. Pinto, A.S. Macedo, P. Fonte, D.M.F. Prazeres, Fusions of a carbohydrate binding module with the small cationic hexapeptide RWRWRW confer antimicrobial properties to cellulose-based materials, Acta Biomaterialia 143 (2022) 216-232.
[40] J. Guo, J.M. Catchmark, M.N.A. Mohamed, A.J. Benesi, M. Tien, T.-h. Kao, H.D. Watts, J.D. Kubicki, Identification and characterization of a cellulose binding heptapeptide revealed by phage display, Biomacromolecules 14(6) (2013) 1795-1805.
[41] J. Diosa, F. Guzman, C. Bernal, M. Mesa, Formation mechanisms of chitosan-silica hybrid materials and its performance as solid support for KR-12 peptide adsorption: Impact on KR-12 antimicrobial activity and proteolytic stability, Journal of Materials Research and Technology 9(1) (2020) 890-901.
[42] M. Liu, T. Liu, X. Zhang, Z. Jian, H. Xia, J. Yang, X. Hu, M. Xing, G. Luo, J. Wu, Fabrication of KR-12 peptide-containing hyaluronic acid immobilized fibrous eggshell membrane effectively kills multi-drug-resistant bacteria, promotes angiogenesis and accelerates re-epithelialization, International journal of nanomedicine 14 (2019) 3345.
[43] V.P. Reddy Chichili, V. Kumar, J. Sivaraman, Linkers in the structural biology of protein–protein interactions, Protein science 22(2) (2013) 153-167.
[44] H. Nagase, Substrate specificity of MMPs, Matrix metalloproteinase inhibitors in cancer therapy, Springer2001, pp. 39-66.
[45] Z.Y. Ong, N. Wiradharma, Y.Y. Yang, Strategies employed in the design and optimization of synthetic antimicrobial peptide amphiphiles with enhanced therapeutic potentials, Advanced drug delivery reviews 78 (2014) 28-45.
[46] I.B. Pinto, L. dos Santos Machado, B.T. Meneguetti, M.L. Nogueira, C.M.E. Carvalho, A.R. Roel, O.L. Franco, Utilization of antimicrobial peptides, analogues and mimics in creating antimicrobial surfaces and bio-materials, Biochemical Engineering Journal 150 (2019) 107237.

[47] X. Zhou, W. Zheng, Y. Li, R. Pearce, C. Zhang, E.W. Bell, G. Zhang, Y. Zhang, I-TASSER-MTD: a deep-learning-based platform for multi-domain protein structure and function prediction, Nature Protocols 17(10) (2022) 2326-2353.
[48] W. Zheng, C. Zhang, Y. Li, R. Pearce, E.W. Bell, Y. Zhang, Folding non-homologous proteins by coupling deep-learning contact maps with I-TASSER assembly simulations, Cell reports methods 1(3) (2021).
[49] J. Yang, Y. Zhang, I-TASSER server: new development for protein structure and function predictions, Nucleic acids research 43(W1) (2015) W174-W181.
[50] R. Gautier, D. Douguet, B. Antonny, G. Drin, HELIQUEST: a web server to screen sequences with specific α-helical properties, Bioinformatics 24(18) (2008) 2101-2102.
[51] A.J. Miles, S.G. Ramalli, B. Wallace, DichroWeb, a website for calculating protein secondary structure from circular dichroism spectroscopic data, Protein Science 31(1) (2022) 37-46.
[52] L. Whitmore, B.A. Wallace, Protein secondary structure analyses from circular dichroism spectroscopy: methods and reference databases, Biopolymers: Original Research on Biomolecules 89(5) (2008) 392-400.
[53] L. Whitmore, B. Wallace, DICHROWEB, an online server for protein secondary structure analyses from circular dichroism spectroscopic data, Nucleic acids research 32(suppl_2) (2004) W668-W673.
[54] L.A. Compton, W.C. Johnson Jr, Analysis of protein circular dichroism spectra for secondary structure using a simple matrix multiplication, Analytical biochemistry 155(1) (1986) 155-167.
[55] N. Sreerama, R.W. Woody, Estimation of protein secondary structure from circular dichroism spectra: comparison of CONTIN, SELCON, and CDSSTR methods with an expanded reference set, Analytical biochemistry 287(2) (2000) 252-260.
[56] J.M. Andrews, Determination of minimum inhibitory concentrations, Journal of antimicrobial Chemotherapy 48(suppl_1) (2001) 5-16.
[57] X. Wang, B. Mishra, T. Lushnikova, J.L. Narayana, G. Wang, Amino acid composition determines peptide activity spectrum and hot-spot-based design of merecidin, Advanced biosystems 2(5) (2018) 1700259.
[58] M. Monné, M. Hermansson, G. von Heijne, A turn propensity scale for transmembrane helices, Journal of molecular biology 288(1) (1999) 141-145.
[59] M. Monné, I. Nilsson, A. Elofsson, G. von Heijne, Turns in transmembrane helices: determination of the minimal length of a “helical hairpin” and derivation of a fine-grained turn propensity scale, Journal of molecular biology 293(4) (1999) 807-814.
[60] C. Ajish, S. Yang, S.D. Kumar, E.Y. Kim, H.J. Min, C.W. Lee, S.-H. Shin, S.Y. Shin, A novel hybrid peptide composed of LfcinB6 and KR-12-a4 with enhanced antimicrobial, anti-inflammatory and anti-biofilm activities, Sci. Rep. 12(1) (2022) 4365.
[61] N. Pathak, R. Salas-Auvert, G. Ruche, M.h. Janna, D. McCarthy, R.G. Harrison, Comparison of the effects of hydrophobicity, amphiphilicity, and α-helicity on the activities of antimicrobial peptides, Proteins: Structure, Function, and Bioinformatics 22(2) (1995) 182-186.
[62] S.P. Piotto, L. Sessa, S. Concilio, P. Iannelli, YADAMP: yet another database of antimicrobial peptides, International journal of antimicrobial agents 39(4) (2012) 346-351.
[63] S. Omardien, J.W. Drijfhout, S.A. Zaat, S. Brul, Cationic amphipathic antimicrobial peptides perturb the inner membrane of germinated spores thus inhibiting their outgrowth, Frontiers in microbiology 9 (2018) 2277.

[64] K. Lohner, S. Blondelle, Molecular mechanisms of membrane perturbation by antimicrobial peptides and the use of biophysical studies in the design of novel peptide antibiotics, Combinatorial chemistry & high throughput screening 8(3) (2005) 241-256.
[65] F. Zsila, G. Kohut, T. Beke-Somfai, Disorder-to-helix conformational conversion of the human immunomodulatory peptide LL-37 induced by antiinflammatory drugs, food dyes and some metabolites, Int. J. Biol. Macromol. 129 (2019) 50-60.
[66] D. Osorio, P. Rondón-Villarreal, R. Torres, Peptides: a package for data mining of antimicrobial peptides, Small 12 (2015) 44-444.
[67] I. Wilson, M. Henry, Q. RD, B. PJ, The pH of varicose ulcer surfaces and its relationship to healing, (1979).
[68] E. Gasteiger, C. Hoogland, A. Gattiker, S.e. Duvaud, M.R. Wilkins, R.D. Appel, A. Bairoch, Protein identification and analysis tools on the ExPASy server, Springer2005.
[69] Q. Zeng, Y. Han, H. Li, J. Chang, Design of a thermosensitive bioglass/agarose–alginate composite hydrogel for chronic wound healing, Journal of Materials Chemistry B 3(45) (2015) 8856-8864.
[70] G. Wang, K.M. Watson, R.W. Buckheit Jr, Anti-human immunodeficiency virus type 1 activities of antimicrobial peptides derived from human and bovine cathelicidins, Antimicrobial agents and chemotherapy 52(9) (2008) 3438-3440.
[71] S. Gunasekera, T. Muhammad, A.A. Strömstedt, K.J. Rosengren, U. Göransson, Alanine and lysine scans of the LL-37-derived peptide fragment KR-12 reveal key residues for antimicrobial activity, ChemBioChem 19(9) (2018) 931-939.
[72] Y. Kai-Larsen, B. Agerberth, The role of the multifunctional peptide LL-37 in host defense, Frontiers in Bioscience-Landmark 13(10) (2008) 3760-3767.
[73] R.F. Wallin, E. Arscott, A practical guide to ISO 10993-5: Cytotoxicity, Medical Device and Diagnostic Industry 20 (1998) 96-98.
[74] J. Fricks-Lima, C. Hendrickson, M. Allgaier, H. Zhuo, J. Wiener-Kronish, S. Lynch, K. Yang, Differences in biofilm formation and antimicrobial resistance of Pseudomonas aeruginosa isolated from airways of mechanically ventilated patients and cystic fibrosis patients, International journal of antimicrobial agents 37(4) (2011) 309-315.
[75] M.D. Torres, C.N. Pedron, Y. Higashikuni, R.M. Kramer, M.H. Cardoso, K.G. Oshiro, O.L. Franco, P.I. Silva Junior, F.D. Silva, V.X. Oliveira Junior, Structure-function-guided exploration of the antimicrobial peptide polybia-CP identifies activity determinants and generates synthetic therapeutic candidates, Communications biology 1(1) (2018) 221.
[76] S. Huo, C. Chen, Z. Lyu, S. Zhang, Y. Wang, B.e. Nie, B. Yue, Overcoming planktonic and intracellular Staphylococcus aureus-associated infection with a cell-penetrating peptide-conjugated antimicrobial peptide, ACS Infectious Diseases 6(12) (2020) 3147-3162.
[77] S. Finger, A. Kerth, M. Dathe, A. Blume, The efficacy of trivalent cyclic hexapeptides to induce lipid clustering in PG/PE membranes correlates with their antimicrobial activity, Biochimica et Biophysica Acta (BBA)-Biomembranes 1848(11) (2015) 2998-3006.
[78] P. Wadhwani, R. Epand, N. Heidenreich, J. Bürck, A. Ulrich, R. Epand, Membrane-active peptides and the clustering of anionic lipids, Biophysical journal 103(2) (2012) 265-274.
[79] S. Bhattacharjya, De novo designed lipopolysaccharide binding peptides: structure based development of antiendotoxic and antimicrobial drugs, Current medicinal chemistry 17(27) (2010) 3080-3093.

[80] Y. Rosenfeld, N. Papo, Y. Shai, Endotoxin (lipopolysaccharide) neutralization by innate immunity host-defense peptides: peptide properties and plausible modes of action, Journal of Biological Chemistry 281(3) (2006) 1636-1643.
[81] Y. Rosenfeld, N. Lev, Y. Shai, Effect of the hydrophobicity to net positive charge ratio on antibacterial and anti-endotoxin activities of structurally similar antimicrobial peptides, Biochemistry 49(5) (2010) 853-861.
[82] T. Lu, Z. Lin, J. Ren, P. Yao, X. Wang, Z. Wang, Q. Zhang, The non-specific binding of fluorescent-labeled MiRNAs on cell surface by hydrophobic interaction, PLoS One 11(3) (2016) e0149751.
[83] G.S. Tjabringa, J. Aarbiou, D.K. Ninaber, J.W. Drijfhout, O.E. Sørensen, N. Borregaard, K.F. Rabe, P.S. Hiemstra, The antimicrobial peptide LL-37 activates innate immunity at the airway epithelial surface by transactivation of the epidermal growth factor receptor, The Journal of Immunology 171(12) (2003) 6690-6696.
[84] W. Zhang, H.T. Liu, MAPK signal pathways in the regulation of cell proliferation in mammalian cells, Cell research 12(1) (2002) 9-18.
[85] F. Costa, I.F. Carvalho, R.C. Montelaro, P. Gomes, M.C.L. Martins, Covalent immobilization of antimicrobial peptides (AMPs) onto biomaterial surfaces, Acta biomaterialia 7(4) (2011) 1431-1440.
[86] S.L. Haynie, G.A. Crum, B.A. Doele, Antimicrobial activities of amphiphilic peptides covalently bonded to a water-insoluble resin, Antimicrobial agents and chemotherapy 39(2) (1995) 301-307.
[87] W.-M. Cho, B.P. Joshi, H. Cho, K.-H. Lee, Design and synthesis of novel antibacterial peptide-resin conjugates, Bioorganic & medicinal chemistry letters 17(21) (2007) 5772-5776.
[88] T. Long, H. Li, X. Wang, B. Yue, A comparative analysis of antibacterial properties and inflammatory responses for the KR-12 peptide on titanium and PEGylated titanium surfaces, RSC advances 7(55) (2017) 34321-34330.
[89] M. Gabriel, K. Nazmi, E.C. Veerman, A.V. Nieuw Amerongen, A. Zentner, Preparation of LL-37-grafted titanium surfaces with bactericidal activity, Bioconjugate chemistry 17(2) (2006) 548-550.
[90] M. Bagheri, M. Beyermann, M. Dathe, Immobilization reduces the activity of surface-bound cationic antimicrobial peptides with no influence upon the activity spectrum, Antimicrobial agents and chemotherapy 53(3) (2009) 1132-1141.
[91] B. Mishra, G. Wang, Titanium surfaces immobilized with the major antimicrobial fragment FK-16 of human cathelicidin LL-37 are potent against multiple antibiotic-resistant bacteria, Biofouling 33(7) (2017) 544-555.
[92] F.M. Costa, S.R. Maia, P.A. Gomes, M.C.L. Martins, Dhvar5 antimicrobial peptide (AMP) chemoselective covalent immobilization results on higher antiadherence effect than simple physical adsorption, Biomaterials 52 (2015) 531-538.

5. Chapter 5: Conclusions and Future Work

5.1. Overview

The work in this thesis describes the development and characterization of antimicrobial peptide functionalized transparent bacterial derived cellulose. Two aims were completed to fully investigate and explore these research areas. The first aimed to develop a method for transparent cellulose production. We determined that the use of arabitol as an in culture carbon source induces the production of transparent BC with altered microstructure and liquid absorption capabilities. The second aimed to design and characterize the bioactivity non-covalently tethered chimeric antimicrobial peptides on the BC surface. The designed chimeric peptides retained optimal secondary structures, antibacterial activity, and cytocompatibility both in solution and immobilized on the cellulose surface. Further demonstrating the capabilities to develop an enhanced transparent BC wound dressing with the potential for surface antibacterial and wound healing capabilities. The primary scientific contribution of this work is the development of transparent native BC materials for use in a broader range of applications than just chronic wound care, such as biosensors and ocular repair. Additionally, the investigation of novel chimeric peptide design provides insights into more advanced means of antibacterial treatment without the use of antibiotic agents.

5.2. Results and Conclusions

The overall objective of this work was to develop a method for making transparent bacterial-derived cellulose (BC), modify BC with chimeric AMPs, and assess the bioactivity.

5.2.1. Specific Aim 1: Develop and characterize optically clear cellulose

Many studies have demonstrated that altered culture conditions result in hierarchical structural changes of bacterial derived cellulose materials. However, few studies have mentioned the potential for transparent cellulose formation and no in depth analysis of these methods or mechanisms have been performed. This study is the first demonstrated use of alternative in culture carbon sources to alter cellulose transparency. Using arabitol, a pentose-derived sugar, we developed a method for producing transparent

BC. This sugar was chosen for its proposed ability to activate an alternative metabolic pathway known to directly correlate with increased production of cyclic-di-GMP, the known activator of the cellulose synthase complex.

Transparent cellulose was synthesized using increasing ratios of arabitol/glucose, resulting in BC formation with optical transparency values comparable to commercially available transparent wound dressing materials. Additionally, the use of arabitol as the primary carbon source was found to have no significant impact on overall bacterial growth kinetics. All BC samples synthesized with a minimum of 10% arabitol exhibited similar cellulose yield, thickness, and handleability properties. Similar liquid absorption capabilities were also observed in both salt and serum based liquid mediums. Transparency was also found to be maintained when submerged in opaque serum based liquid for 24 h. Additional assessment of transparent and opaque BC was performed with fibroblasts, confirming that transparent BC maintained biocompatibility.

To investigate and elucidate the mechanism behind the increased transparency of the synthesized BC, extensive morphological and structural analysis was performed. Via SEM analysis, transparent BC was determined to have smaller fiber diameters compared to more opaque BC materials. WAXS and solid-state NMR analysis indicated no differences in overall material crystallinity, however, the presence of previously unreported aromatic signatures were observed. These findings suggest additional exopolymers may be synthesized by *K. hansenii*. Overall, this work is the first to show that BC composition and transparency can be manipulated by carbon source alone.

5.2.2. Specific Aim 2: Characterize CBP-AMP bioactivity on the BC surface

In this section of the thesis, we utilized opaque and transparent BC developed and characterized in specific aim 1. For the development of a more clinically relevant wound dressing material we aimed to develop methods to achieve antibacterial surface activity. To achieve this, we designed chimeric bifunctional peptides to non-covalently link KR-12, a potent cationic antimicrobial peptide, to the BC

surface. Chimeric peptide functionality was then assessed both in solution and immobilized to the cellulose surface.

To predict if AMP functionality is conserved in the chimeric sequences tested, structural modeling and helix predictions were assessed *in silico*. Once helical structure was confirmed computationally, experimental CD methods were performed. Both chimeric peptides were confirmed to contain helical conformations, but decreased hydrophobic moments were noted. These physiochemical differences suggested chimeric peptides have altered electrostatic interaction capabilities.

The chimeric peptides were then assessed in solution for cytocompatibility and retained bioactivity compared to unaltered KR-12. During cytocompatibility assessment with NHDF, only chimeric peptides containing the Short-CBP exhibited negative effects on metabolic activity, which was attributed to solubility issues. Additionally, trends of increased metabolic activity in response to KR-12 and Long-CBP-KR12 concentrations were observed. To further assess the retained bioactivity of KR-12 in the chimeric peptide sequences minimum inhibitory concentration analysis was performed. All KR-12 containing peptides exhibited antibacterial activity in solution against *E. coli* and *P. aeruginosa*, though higher inhibition concentrations were required for both chimeric peptides likely since the chimeric peptides were predicted to exhibit changes of antibacterial activity mediating properties such as hydrophobic moment and hydrophobicity as identified earlier. Additional functionality, mainly anti-inflammatory capabilities through LPS binding was assessed. The Short-CBP-KR12 peptide exhibited enhanced LPS binding capabilities compared to both the KR-12 control and Long-CBP-KR12.

Once the retained functionality of KR-12 in the chimeric peptides was confirmed the cellulose binding capacity of both CBPs were assessed. On both transparent and opaque BC Long and Short CBP binding mechanisms allowed for effective binding and stabile immobilization. Additionally, all functionalized BC materials exhibited no adverse effects on metabolic activity of both NHDF and HaCaT epithelial cells. Reduced antibacterial activity of immobilized Short-CBP-KR12 and Long-CBP-KR12 was

observed, owing to steric hinderance and the difficulties of directly comparing antibacterial potential of solution based and immobilized peptides. Overall, results from this work indicate CBP-driven immobilization of KR-12 is effective in retaining peptide activity and stability on the binding substrate.

5.3. Future Work

5.3.1. Evaluation of transparent cellulose composition

The use of alternative carbon sources in culture with cellulose producing bacteria, has previously resulted in hybrid cellulose formation. Yadav et al. described the use of N-acetylglucosamine (GlcNAc) as an in culture carbon source with *K. xylinus*, that resulted in the formation of lysozyme susceptible BC [1]. In this research we assumed the cellulose synthesized by *K. hansenii* was composed of glucose monomers and that the use of arabitol only activates an alternative metabolic pathway [2]. However, if the bacteria can UDPylate the arabitol or a metabolic intermediate of the arabitol, alternative sugars could be incorporated within the synthesized exopolysaccharide. Therefore, the composition of transparent BC could be assessed to determine if hybrid cellulose materials are synthesized. This issue of hydrolyzing cellulose down to its monomer units, however, is not a trivial issue [3]. Methods for effective hydrolysis of the highly crystalline BC materials would need to be developed either through the use of acids such as trifluoroacetic acid, or enzyme cocktails such as cellic Ctec 2 [4]. Once hydrolyzed samples could be dried and dissolved in ammonia. Samples could then be subject to a 1-phenyl-3-methyl-5-pyrazole derivatization reaction prior to monosaccharide profiling via High Performance Liquid Chromatography with Diode-Array Detection (HPLC-DAD) or Ultra-High Performance Liquid Chromatography Triple Quadruple Mass Spectrometry (UHPLC/QqQ-MS) [5, 6].

5.3.2. Evaluation of air permeability and water vapor transmission

Air permeability and water vapor transmission rate (WVTR) are important characteristics for wound healing as optimal air permeability and water vapor transmission prevents wound site maceration. With the changed microstructure observed in this work, the air permeability of transparent BC produced

using arabitol could be characterized to ensure the material still falls within optimal parameters for wound dressings. Air permeability of BC samples could be tested and measured using a FX-3300 Air Permeability Tester II (TEXTEST Instruments) [7]. The FX-3300 instrument uses a powerful suction pump to draw air through an interchangeable test head with a circular opening. BC samples could be produced using varying rations of arabitol/glucose as 5 cm^2 sheets. These samples can then be clamped over the test head opening using the clamping lever, which will automatically start the suction pump. After a few seconds the instrument will display the air permeability of the test specimen in the preselected unit of measure [7]. Wound dressings with air permeability properties between 8.6-16.2 $cm^3/cm^2/sec$ have been identified to provide an ideal moist wound environment while preventing maceration [7, 8].

Additionally, the water vapor transmission rate of the BC materials could be determined using the standard method presented in ASTM E96-00 [9]. BC samples produced using varying concentrations of arabitol could be placed in permeation cells containing distilled water. Permeation cells could then be placed in a desiccator containing silica gel with a relative humidity of 0% at 25°C for seven days. The weight of the cells and samples can be recorded every 24 hours. The WVTR could then be calculated using the following equation:

$$WVTR\left(\frac{g}{m^2}day\right) = \frac{\Delta m}{\Delta t} \times A$$

Where Δm is the permeation cell weight change in grams, Δt is the elapsed time in days, and A is permeation area of the samples in mm.

Extremely high WVTR values are known to accelerate the dehydration of the wound bed resulting in dry scabbing. Alternatively low WVTR values result in exudate fluid accumulation resulting in wound edge maceration, impeded healing, and increased risk of bacterial infection [10]. An ideal WVTR for wound dressing materials has been identified as 2500-3000 g/m^2 day [11].

5.3.3. Effective protein and endotoxin purification of BC

BC's use as an effective would dressing material relies heavily on its ability to be effectively purified. As BC is synthesized by gram-negative bacteria latent endotoxins in the material is of concern. The main methods for purifying BC is through incubation with alkaline solutions, such as NaOH, and it is widely used for endotoxin removal [12]. Though the purification method used in this work (4 h incubation in 0.1 M NaOH solution at 60°C) is well-established, little research has been done comparing purification parameters with final endotoxin levels [13, 14]. To accurately assess BC's effects *in vitro*, the purification process and resultant endotoxin content should be established prior to working with LPS sensitive cell lines such as macrophages. Purification parameters such as incubation time, incubation temperature, NaOH molarity, and number of incubation bath changes could all have effects on the overall endotoxin content [15]. With the high number of possible variables that could influence endotoxin content a design of experiments (DOE) could be established to better narrow down parameters of interest bast on preliminary results. Endotoxin levels could be assessed using the FDA testing methods for bacterial endotoxins [16]. Briefly, the purified BC material could be immersed in endotoxin free water for at least 1 h on an orbital shaker and then endotoxin levels could be determined by LAL assay. Additionally, retained endotoxin content could be indirectly assessed by determining the materials ability to induce oxidative stress in macrophages. Specifically reactive oxygen species could be measured using a CellROX Green dye, that binds to DNA in the presence of free radicals, emitting intense green fluorescence [15].

The use of sodium dodecyl sulfate (SDS) has also been widely used to purify BC [17]. The effective elimination of SDS post purification, however, poses additional concerns as cytotoxicity towards fibroblasts and keratinocytes is well documented [18, 19]. For this reason, investigation into alternative surfactant is warranted. Alternative purification methods using surfactants such as: Triton-X-100, sodium cocoyl isethionate (SCI), CHAPS, decyl glucoside, and cocamidopropyl betaine could be assessed. For latent protein content, post purified BC samples could be subjected to guanidine hydrochloride digestion and analyzed via BCA assay. For DNA content, post purified BC samples could be processed via papain digest

and analyzed via Picogreen Assay. Additionally, FT-IR could be used to determine and identify the presence of contaminants such as whole cells, nucleic acids, lipids, and proteins [20].

5.3.4. Alternative chimeric peptide design for increased bioactivity

The overall chimeric peptide can be iterated off based on key factors identified in this work. Suggested methods to improve the overall bioactivity of the tether peptide system could be done by screening alternative AMPs, linkers, and immobilization directionality. With the understanding that antibacterial activity and LPS binding are predominantly driven through net charge and hydrophobic interactions various changes and substitutions of the original KR-12 peptide sequence have yielded additional KR-12 analogues with improved bioactivity. Thus, to improve the overall antibacterial activity of surface functionalized BC alternative KR-12 analogs or conformations dimerized KR12 could be explored [21, 22]. The specific KR-12 analogues could be chosen based on the specific bioactivity sought. For example the designed analogue KR-12-a5 (KRIV**KL**I**LKW**LR-NH_2) has a +5 charge and a hydrophobicity three times higher than the original KR-12 peptide resulting in comparable antibacterial activity but enhance LPS binding capabilities [21]. KR-12-a2 (KRIVQRIK**KW**LR-NH_2) and KR-12-a4 (KRIV**KL**IK**KW**LR-NH_2) both have a charge of +7 and exhibit a minimum inhibitory concentration of 2 µM against *S. aureus* [21]. Additionally, recent developments of cyclic dimers of KR-12 also offer a potential AMP alternative for improved bioactivity. Crosslinked KR-12 dimers exhibit minimum inhibitory concentration of 0.625 µM against *S. aureus* [22]. Additionally, the KR-12 dimers are synthesized with a disulfide bridge, providing further proteolytic protect of the peptide [22].

Linker length and composition could also be screened to determine steric hinderance and optimize AMP mobility. In this work we used a Gly-rich linker, however PEG based spacers have also been extensively studied and may provide increased flexibility as described in section 4.3.7 [23]. Further assessment and comparison of KR-12 immobilization via the C or N-terminal could also provide better insight into potential steric hinderance. To prevent confounding factors of CBP directionality, this experiment could be carried out using the Long-CBP as the cellulose binding motif. This is because the

Long-CBP is cyclized and thus is not affected by the addition of linked AMPs on either terminal. To assess the impacts on immobilization conformation of KR-12 peptide sequences could be designed as described in **Table 5.1**, and AMP bioactivity could be assessed [24-28]. Additionally, this setup could be used to also screen the use of a PEG linker compared to the gly-rich linker currently used.

Table 5.1. Proposed alternative peptide designs to assess steric hinderance.

Immobilized Terminal	Linker	Peptide Sequence
C-Terminal	GSGSGGS	KRIVQRIKDFLR-GSGSGGS-**C**QVLNPWYSQTTPGWGQ**C**-NH2
N-Terminal	GSGSGGS	**C**QVLNPWYSQTTPGWGQ**C**-GSGSGGS-KRIVQRIKDFLR-NH2
C-Terminal	PEG linker	KRIVQRIKDFLR-(AEEEAc)-**C**QVLNPWYSQTTPGWGQ**C**-NH2
N-Terminal	PEG linker	**C**QVLNPWYSQTTPGWGQ**C**-(AEEEAc)-KRIVQRIKDFLR-NH2

5.3.5. BC immobilized KR-12 release kinetics

Though our results in section 0, indicated prolonged binding over a 7-day period, additional release kinetics experiments are warranted. Release kinetics could be determined through fluorescence analysis of the release supernatant. BC samples could be functionalized with fluorescent tagged Long-CBP-KR12 or Short-CBP-KR12, rinsed, and placed in either phosphate buffered saline (PBS), or PBS supplemented with 1% w/v BSA. Samples could be kept at 37°C and release medium could be removed and replaced with fresh medium at regular intervals. Release concentrations could be determined by spectrophotometric quantification based on the fluorescence intensity of the release medium [29]. This method would establish the baseline release kinetics in a non-proteolytic sink condition.

Although widely accepted for quantitation purposed in the peptide field, there are limitations to purely fluorescence based approaches. Fluorescent tags are generally large and increase the Mw of smaller peptide sequences dramatically. Their large size also has the ability to hinder bioactivity of the tagged peptide. Additionally, for the purpose of this study, it is assumed that increased fluorescence in the release medium is due to full CBP-AMP release, however fluorophore cleavage or peptide cleavage between the substrate and FAM-tag would also result in increased fluorescence. For these reasons alternative release

quantitation methods could also be investigated. The addition of a fusion peptide that acts as an epitope tag such as FLAG (DYKDDDDK), could be included allowing for release quantitation via ELISA [29, 30]. Alternatively release of unlabeled peptides could be assessed by LC-MS using a C_{18} column [31].

5.3.6. Protease stability of KR-12 containing peptides

Proteolytic stability and susceptibility are of great importance to the prolonged effectiveness of KR-12. Though not widely characterized, it has been found that less than 10% intact KR-12 is detectable after 10 mins in dilute human serum [32]. Additionally it has been suggested that surface immobilized AMPs acquire proteolytic protection due to steric hinderance [31]. For this reason, additional experiments on the proteolytic stability of chimeric CBP-AMPs should be assessed both in solution and immobilized onto the cellulose surface. For soluble peptide stability, peptides could be hydrated in dilute human serum (serum/phosphate buffered saline (PBS) 1:4, v/v) to better mimic the composition of wound exudate. Aliquots at regular intervals could be taken and peptide analysis could be conducted using an LC-MS/MS system. Non-degraded peptide percentage could then be compared to determine the proteolytic serum stability of the free chimeric peptides [32]. Additionally, this would allow for understanding of any enzymatically cleavable amino acid sites for the design of more stable peptides.

Though immobilization of KR-12 is suggested to provide proteolytic protection, altered structural conformation during immobilization may also lead to higher exposure of cleavage sites [33]. Thus, stability of immobilized chimeric peptides against proteases could be performed using α-chymotrypsin as a model proteolytic enzyme. Though not a protease found in wound exudate, this serine protease exhibits structural similarities to those found in the wound site and is a well-established model protease [31, 34]. Stability could be assessed by subjecting chimeric peptide functionalized BC to α-chymotrypsin in a 1:10 (w/w) enzyme to substrate ratio for 30 mins. After digestion, remaining supernatant could be assessed by LC-MS using a C_{18} column to detect KR-12 fragments [31].

5.3.7. MMP cleavable linker for controlled release of AMPs

As bacteria not near the surface of the cellulose materials are unlikely to be significantly affected by immobilized KR-12, controlled release may provide additional wound dressing functionalities. This modality would be of specific interest to address the high incidence of biofilm formation in the wound bed. Previously we have observed that untethered KR-12 is able to diffuse out of the BC materials and produce prominent zones of inhibition against *E. coli* (**Figure 5.1**). To further investigate this and provide more controlled release specifically engineered MMP cleavable linkers may be of interest [35].

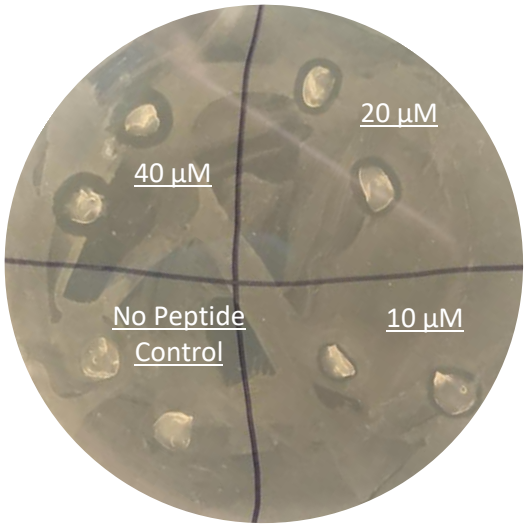

Figure 5.1. Zone if inhibition observed for KR-12 loaded BC
BC samples loaded with varying concentrations of KR-12 exhibited diffusion and growth inhibition capabilities against E.coli on MHB agar plates.

MMP cleavable domains such as GPQG↓IWGQ could be used to replace the glycine-rich linker used in this work and subsequent release and antibacterial activity could be assessed [36]. Specifically, release of immobilized KR-12 from BC materials could be assessed in collagenase containing release medium and quantified via spectrophotometric analysis. Similarly, antibacterial assessment of releasable KR-12 could be assessed using methods described in section 4.2.11, but with the inclusion of collagenase in the bacterial growth medium to promote release. This system for longer range antibacterial activity may overcome limitation seen in this thesis regarding biofilm forming bacterial strains.

5.3.8. Anti-inflammatory assessment of immobilized KR-12

In this work, we showed the LPS binding capabilities of KR-12 and the Short-CBP-KR12 sequences, however, the residual endotoxin content in the BC material may prevent adequate assessment of the anti-inflammatory activity of immobilized KR-12. By utilizing methods for removing endotoxins from BC materials (potential methods described in section 5.3.3), the anti-inflammatory activity of each chimeric peptide immobilized on the BC surface could be assessed with LPS stimulated RAW264.7 mouse macrophages [26]. The use of RAW264.7 murine macrophages is the engineering standard for LPS stimulation studies and it is well established that LPS is a ligand for toll-like macrophage receptors that leads to activation and expression of an M1, or pro-inflammatory phenotype [26]. BC samples functionalized with either Short-CBP-KR12 or Long-CBP-KR12 could be placed in culture with LPS stimulated RAW264.7 cells. After 24 h of culture, media supernatant could be collected and pro-inflammatory cytokine (TNF-α, IL-6, and MCP-1) secretion could be assessed via a mouse ELISA kit. Reductions in pro-inflammatory cytokines could be attributed to the KR-12-LPS interaction and subsequent blocking of TLR-4 receptor stimulation [21, 37]. Additional inflammatory markers such as nitric oxide (NO) could also be assessed via a Griess reagent reaction [37]. After successful assay completion with murine macrophages, these studies could be repeated with differentiated THP-1 human macrophages to develop a more clinically relevant model of LPS stimulation.

5.3.9. *In vivo* wound healing and antibacterial analysis of functionalized cellulose

To determine *in vivo* antimicrobial activity and accelerated wound healing capabilities, *in vivo* assessment could be performed using methods developed by Gurjala et al. [38]. Wound healing and antibacterial analysis experiments could be performed using young New Zealand white rabbits (3-6 months old). Six full thickness dermal wounds (6 mm diameter) can be created in the perichondrium on the ventral surface of the ear, wounds can be dressed with Tegaderm®, a semi occlusive transparent film, for 3 days. On day 3, wounds can be inoculated with $1X10^6$ CFU of *S. aureus* and *P. aeruginosa*. Control wounds can be redressed on days 3, 5, 7, 9, and 10. Inoculated wounds could be dressed with either an active control dressing (a moist foam dressing impregnated with polyhexamethylene biguanide), inactive vehicle

(unfunctionalized BC), or the experimental dressing (BC functionalized with either Long CBP-KR12 or Short-CBP-KR12). Dressings could be checked and changed as needed throughout the 12 day period. Animals can either be designated to the unfunctionalized BC versus control, or functionalized versus control groups, with each ear designated to control or experimental groups. Animals could then be euthanized on days 4, 8, and 12, and wounds could be harvested for analysis.

For viable bacterial counts, wound beds could be biopsied and excised. Samples could be collected into separate MagNA Lyser Green Beads tubes with PBS. Samples could be homogenized and sonicated to break up the bacterial aggregates present in the wound. The resulting solutions can then be serially diluted and plated on Blood Agar (Hardy Diagnostics) and Lipovitellin Salt Mannitol Agar (selective medium for *S. aureus*, Hardy Diagnostics) and allowed to incubate overnight at 37°C. Colonies could then be counted on each plate to determine the overall bacterial concentration as colony forming unit (CFU)/mL [38, 39]. Additional wounds at each time point could be excised and bisected at their largest diameter. Samples could then be fixed in formalin, embedded in paraffin, cut into sections, and stained with hematoxylin & eosin (H&E). Total granulation area, and epithelial gaps could be analyzed, quantified, and compared between groups [38, 39]. This method wound allow for a quantitative assessment of *in vivo* antibacterial activity and reepithelization of the would site.

5.3.10. Manufacturability, FDA clearance, and clinical use

Additional considerations for further translation of the surface functionalized BC material are the manufacturability of the material at large scales. As the production of BC with larger surface areas is only limited by the surface area of the culture container, the production of BC is not a limiting factor in upscaling the BC synthesis process. The chimeric peptides, however, pose more of a challenge due to their cost and difficulty to manufacture. In recent years however, recombinant protein expression of LL-37 and KR-12 analogues have been achieved providing a possible method for peptide production with reduced costs [40, 41].

For FDA regulatory purposes the combinatory nature of BC's hydrogel-like wound dressing material and the surface functionalization using a biological agent would result in a Class II medical device designation. This BC material alone would be classified as a hydrogel wound dressing material that is intended to cover a wound, absorb wound exudate, and protect from abrasion and contamination. Though an AMP-functionalized BC wound dressing has not been FDA approved before, individually BC materials (Xylos X-Cell™ Wound Dressing) and AMPs have (gramicidin, daptomycin, oritavancin, telavancin, and colistin) [42, 43]. These components with similar activity and composition could pave the way for FDA approval of the material developed in this work. Like the X-Cell™ wound dressing, the functionalized material developed in this work could be used for applications other than chronic wounds. For example, the functionalized BC material could be used for the management of partial to full thickness wounds (arterial, venous, pressure, and diabetic ulcers), first and second degree burns, post operative surgical wounds, donor sites, and other dermal lesions. Depending on the nature of the wound, the dressing could be left in place for a prolonged period of time such as 7-9 days. For low exudative dermal lesions that do not require a secondary dressing, the BC dressing could be left in place until normal epithelialization of the wound site causes the dressing to naturally fall off. For highly exudative wounds, secondary dressings may be required to keep the BC dressing in place and to absorb exudate wicked out of the wound bed by the BC material. This would result in increased dressing changes of the secondary dressing, while allowing the BC dressing to be kept in place.

5.4. References

[1] V. Yadav, L. Sun, B. Panilaitis, D.L. Kaplan, In vitro chondrogenesis with lysozyme susceptible bacterial cellulose as a scaffold, J. Tissue Eng. Regen. M. 9(12) (2015) E276-E288.
[2] E.M. van Zyl, M.A. Kennedy, W. Nason, S.J. Fenlon, E.M. Young, L.J. Smith, S.R. Bhatia, J.M. Coburn, Structural properties of optically clear bacterial cellulose produced by Komagataeibacter hansenii using arabitol, Biomaterials Advances 148 (2023) 213345.
[3] L.-t. Fan, M.M. Gharpuray, Y.-H. Lee, Cellulose hydrolysis, Springer Science & Business Media2012.
[4] M.M. Vieira, E. Kadoguchi, F. Segato, S.S. da Silva, A.K. Chandel, Production of cellulases by Aureobasidium pullulans LB83: optimization, characterization, and hydrolytic potential for the production of cellulosic sugars, Preparative Biochemistry & Biotechnology 51(2) (2021) 153-163.
[5] G. Xu, M.J. Amicucci, Z. Cheng, A.G. Galermo, C.B. Lebrilla, Revisiting monosaccharide analysis–quantitation of a comprehensive set of monosaccharides using dynamic multiple reaction monitoring, Analyst 143(1) (2018) 200-207.
[6] P.L. Tang, S.Y. Chew, X. Hou, J. Deng, K. Badri, Novel use of sugarcane leaf polysaccharide in κ-carrageenan blend hydrogel, Biomass Conversion and Biorefinery (2022) 1-15.
[7] B. Gupta, A. Arora, S. Saxena, M.S. Alam, Preparation of chitosan–polyethylene glycol coated cotton membranes for wound dressings: preparation and characterization, Polymers for Advanced Technologies 20(1) (2009) 58-65.
[8] R. Nawalakhe, Q. Shi, N. Vitchuli, M.A. Bourham, X. Zhang, M.G. McCord, Novel Atmospheric Plasma Enhanced Silk Fibroin Nanofiber/Gauze Composite Wound Dressings, Journal of Fiber Bioengineering and Informatics 5(3) (2012) 227-242.
[9] K.V.S. Hodel, B.A.S. Machado, G.d.C. Sacramento, C.A.d.O. Maciel, G.S. Oliveira-Junior, B.N. Matos, G.M. Gelfuso, S.B. Nunes, J.D.V. Barbosa, A.L.P.C. Godoy, Active Potential of Bacterial Cellulose-Based Wound Dressing: Analysis of Its Potential for Dermal Lesion Treatment, Pharmaceutics 14(6) (2022) 1222.
[10] R. Portela, C.R. Leal, P.L. Almeida, R.G. Sobral, Bacterial cellulose: a versatile biopolymer for wound dressing applications, Microbial biotechnology 12(4) (2019) 586-610.
[11] W. Paul, C.P. Sharma, Chitosan and alginate wound dressings: a short review, Trends Biomater Artif Organs 18(1) (2004) 18-23.
[12] I. de Vries, S. Schreiber, D. Boßmann, Z. Hellmann, J. Kopatz, H. Neumann, S. Beutel, Single-use membrane adsorbers for endotoxin removal and purification of endogenous polysialic acid from Escherichia coli K1, Biotechnology reports 17 (2018) 110-116.
[13] V. Yadav, B.J. Paniliatis, H. Shi, K. Lee, P. Cebe, D.L. Kaplan, Novel in vivo-degradable cellulose-chitin copolymer from metabolically engineered Gluconacetobacter xylinus, Appl. Environ. Microb. 76(18) (2010) 6257-6265.
[14] Y. Wan, J. Wang, M. Gama, R. Guo, Q. Zhang, P. Zhang, F. Yao, H. Luo, Biofabrication of a novel bacteria/bacterial cellulose composite for improved adsorption capacity, Composites Part A: Applied Science and Manufacturing 125 (2019) 105560.
[15] A. Junka, K. Fijałkowski, A. Ząbek, K. Mikołajewicz, G. Chodaczek, P. Szymczyk, D. Smutnicka, A. Żywicka, P.P. Sedghizadeh, M. Dziadas, Correlation between type of alkali rinsing, cytotoxicity of bio-nanocellulose and presence of metabolites within cellulose membranes, Carbohyd. Polym. 157 (2017) 371-379.

[16] R. Bech Ørving, B. Carpenter, S. Roth, J. Reich, B.H. Kallipolitis, J. Sonne-Hansen, Bacterial Endotoxin Testing—Fast Endotoxin Masking Kinetics in the Presence of Lauryldimethylamine Oxide, Microorganisms 8(11) (2020) 1728.
[17] M. Roman, A.P. Haring, T.J. Bertucio, The Growing Merits and Dwindling Limitations of Bacterial Cellulose-Based Tissue Engineering Scaffolds, Curr. Opin. Chem. Eng. (2019).
[18] C.S. Newby, R.M. Barr, M.W. Greaves, A.I. Mallet, Cytokine release and cytotoxicity in human keratinocytes and fibroblasts induced by phenols and sodium dodecyl sulfate, Journal of investigative dermatology 115(2) (2000) 292-298.
[19] A. Rusanov, N. Luzgina, A. Lisitsa, Sodium dodecyl sulfate cytotoxicity towards HaCaT keratinocytes: comparative analysis of methods for evaluation of cell viability, Bulletin of Experimental Biology and Medicine 163 (2017) 284-288.
[20] M.E. Fuller, C. Andaya, K. McClay, Evaluation of ATR-FTIR for analysis of bacterial cellulose impurities, Journal of Microbiological Methods 144 (2018) 145-151.
[21] B. Jacob, I.S. Park, J.K. Bang, S.Y. Shin, Short KR-12 analogs designed from human cathelicidin LL-37 possessing both antimicrobial and antiendotoxic activities without mammalian cell toxicity, Journal of Peptide Science 19(11) (2013) 700-707.
[22] T. Muhammad, A.A. Strömstedt, S. Gunasekera, U. Göransson, Transforming cross-linked cyclic dimers of KR-12 into stable and potent antimicrobial drug leads, Biomedicines 11(2) (2023) 504.
[23] G.P. Sakala, M. Reches, Peptide-based approaches to fight biofouling, Advanced Materials Interfaces 5(18) (2018) 1800073.
[24] B. Mishra, G. Wang, Titanium surfaces immobilized with the major antimicrobial fragment FK-16 of human cathelicidin LL-37 are potent against multiple antibiotic-resistant bacteria, Biofouling 33(7) (2017) 544-555.
[25] D.W. Song, S.H. Kim, H.H. Kim, K.H. Lee, C.S. Ki, Y.H. Park, Multi-biofunction of antimicrobial peptide-immobilized silk fibroin nanofiber membrane: Implications for wound healing, Acta biomaterialia 39 (2016) 146-155.
[26] A. Blasi-Romero, M. Ångström, A. Franconetti, T. Muhammad, J. Jiménez-Barbero, U. Göransson, C. Palo-Nieto, N. Ferraz, KR-12 Derivatives Endow Nanocellulose with Antibacterial and Anti-Inflammatory Properties: Role of Conjugation Chemistry, ACS Applied Materials & Interfaces (2023).
[27] M. Bagheri, M. Beyermann, M. Dathe, Immobilization reduces the activity of surface-bound cationic antimicrobial peptides with no influence upon the activity spectrum, Antimicrobial agents and chemotherapy 53(3) (2009) 1132-1141.
[28] F.M. Costa, S.R. Maia, P.A. Gomes, M.C.L. Martins, Dhvar5 antimicrobial peptide (AMP) chemoselective covalent immobilization results on higher antiadherence effect than simple physical adsorption, Biomaterials 52 (2015) 531-538.
[29] L.D. Lozeau, J. Grosha, D. Kole, F. Prifti, T. Dominko, T.A. Camesano, M.W. Rolle, Collagen tethering of synthetic human antimicrobial peptides cathelicidin LL37 and its effects on antimicrobial activity and cytotoxicity, Acta biomaterialia 52 (2017) 9-20.
[30] A. Einhauer, A. Jungbauer, The FLAG™ peptide, a versatile fusion tag for the purification of recombinant proteins, Journal of biochemical and biophysical methods 49(1-3) (2001) 455-465.
[31] J. Diosa, F. Guzman, C. Bernal, M. Mesa, Formation mechanisms of chitosan-silica hybrid materials and its performance as solid support for KR-12 peptide adsorption: Impact on KR-12

antimicrobial activity and proteolytic stability, Journal of Materials Research and Technology 9(1) (2020) 890-901.
[32] S. Gunasekera, T. Muhammad, A.A. Strömstedt, K.J. Rosengren, U. Göransson, Alanine and lysine scans of the LL-37-derived peptide fragment KR-12 reveal key residues for antimicrobial activity, ChemBioChem 19(9) (2018) 931-939.
[33] K. Chanci, J. Diosa, M.A. Giraldo, M. Mesa, Physical behavior of KR-12 peptide on solid surfaces and Langmuir-Blodgett lipid films: Complementary approaches to its antimicrobial mode against S. aureus, Biochimica et Biophysica Acta (BBA)-Biomembranes 1864(1) (2022) 183779.
[34] I. Arenas, E. Villegas, O. Walls, H. Barrios, R. Rodríguez, G. Corzo, Antimicrobial activity and stability of short and long based arachnid synthetic peptides in the presence of commercial antibiotics, Molecules 21(2) (2016) 225.
[35] R. Weishaupt, J.N. Zünd, L. Heuberger, F. Zuber, G. Faccio, F. Robotti, A. Ferrari, G. Fortunato, Q. Ren, K. Maniura-Weber, Antibacterial, Cytocompatible, Sustainably Sourced: Cellulose Membranes with Bifunctional Peptides for Advanced Wound Dressings, Advanced Healthcare Materials (2020) 1901850.
[36] M.P. Lutolf, J.L. Lauer-Fields, H.G. Schmoekel, A.T. Metters, F.E. Weber, G.B. Fields, J.A. Hubbell, Synthetic matrix metalloproteinase-sensitive hydrogels for the conduction of tissue regeneration: engineering cell-invasion characteristics, P. Natl. Acad. Sci. USA 100(9) (2003) 5413-5418.
[37] E.Y. Kim, G. Rajasekaran, S.Y. Shin, LL-37-derived short antimicrobial peptide KR-12-a5 and its d-amino acid substituted analogs with cell selectivity, anti-biofilm activity, synergistic effect with conventional antibiotics, and anti-inflammatory activity, European journal of medicinal chemistry 136 (2017) 428-441.
[38] A.N. Gurjala, M.R. Geringer, A.K. Seth, S.J. Hong, M.S. Smeltzer, R.D. Galiano, K.P. Leung, T.A. Mustoe, Development of a novel, highly quantitative in vivo model for the study of biofilm-impaired cutaneous wound healing, Wound repair and regeneration 19(3) (2011) 400-410.
[39] A.K. Seth, A. Zhong, K.T. Nguyen, S.J. Hong, K.P. Leung, R.D. Galiano, T.A. Mustoe, Impact of a novel, antimicrobial dressing on in vivo, P seudomonas aeruginosa wound biofilm: quantitative comparative analysis using a rabbit ear model, Wound Repair and Regeneration 22(6) (2014) 712-719.
[40] K. Afify, Recombinant expression of; a precursor of cyclotide kalata S, a cyclic dimer of the antimicrobial peptide KR-12 and a mushroom-derived peptide, 2020.
[41] G. Wang, Structures of human host defense cathelicidin LL-37 and its smallest antimicrobial peptide KR-12 in lipid micelles, Journal of Biological Chemistry 283(47) (2008) 32637-32643.
[42] O. Alvarez, T. Phillips, J. Menzoian, M. Patel, A. Andriessen, An RCT to compare a bio-cellulose wound dressing with a non-adherent dressing in VLUs, Journal of wound care 21(9) (2012) 448-453.
[43] C.H. Chen, T.K. Lu, Development and challenges of antimicrobial peptides for therapeutic applications, Antibiotics 9(1) (2020) 24.

6. Appendix

6.1. Appendix 1. Functionalized BC cytotoxicity mammalian cell images

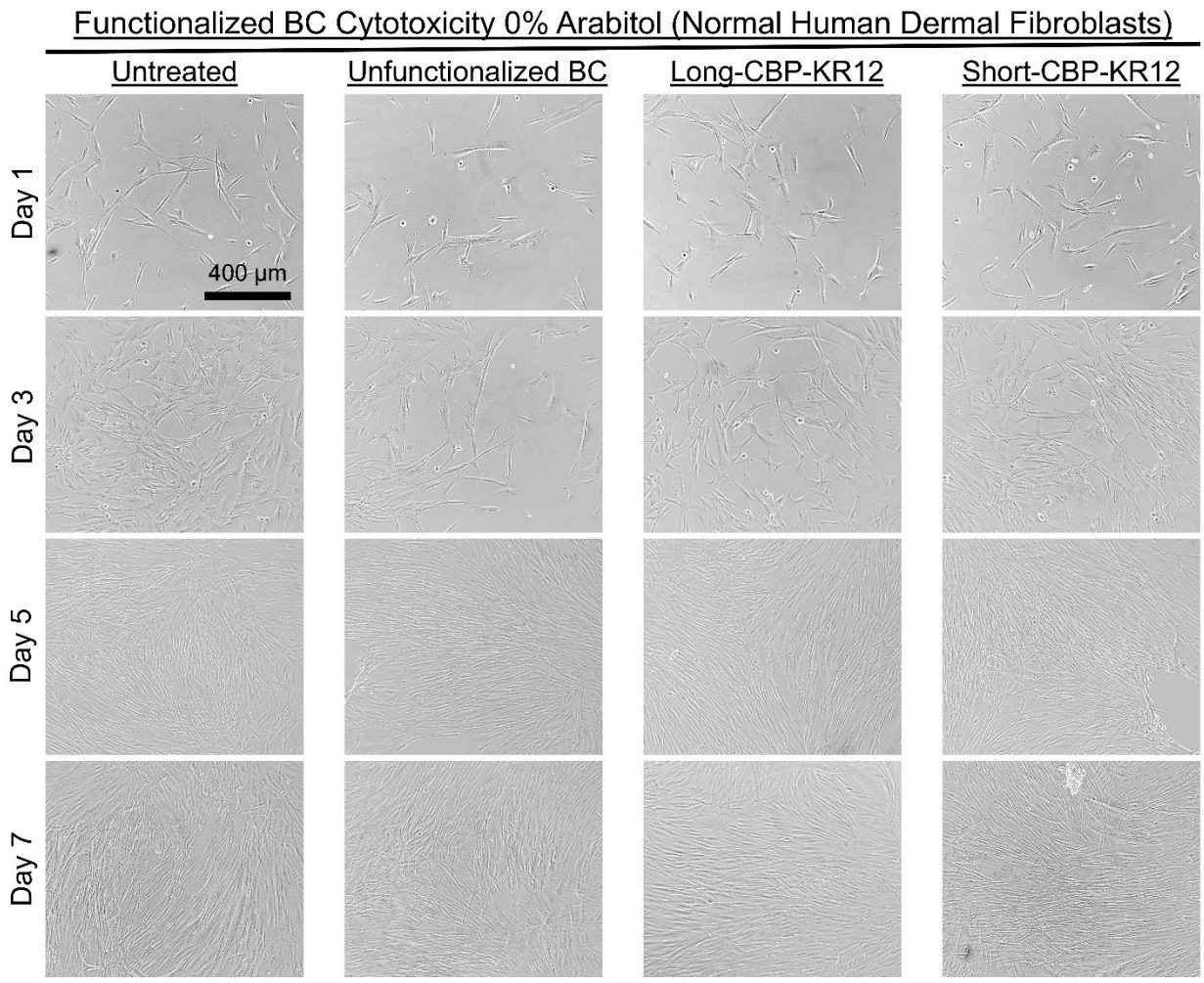

Figure 6.1. Functionalize BC cytotoxicity 0% Arabitol NHDF cells

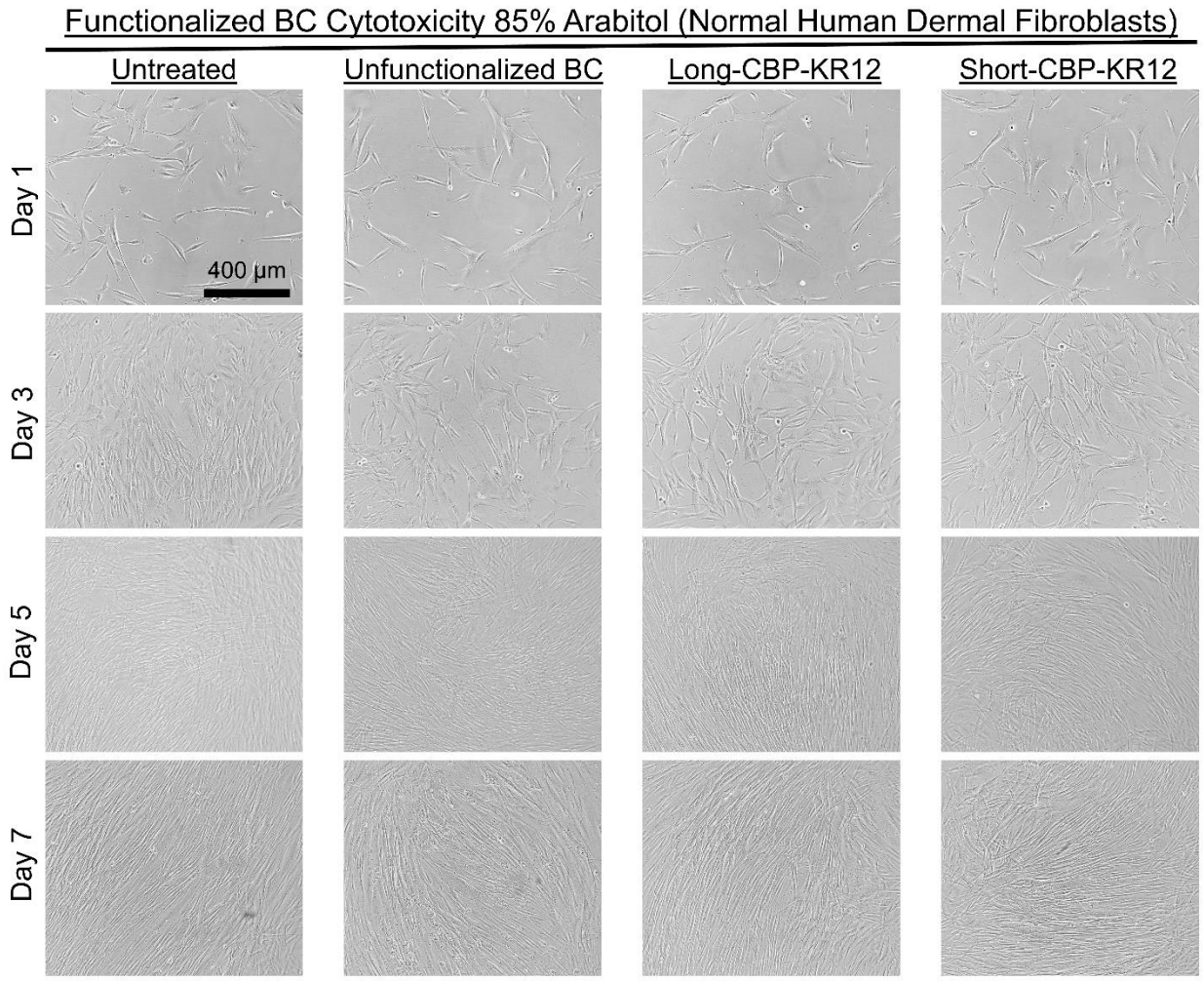

Figure 6.2. Functionalize BC cytotoxicity 85% Arabitol NHDF cells

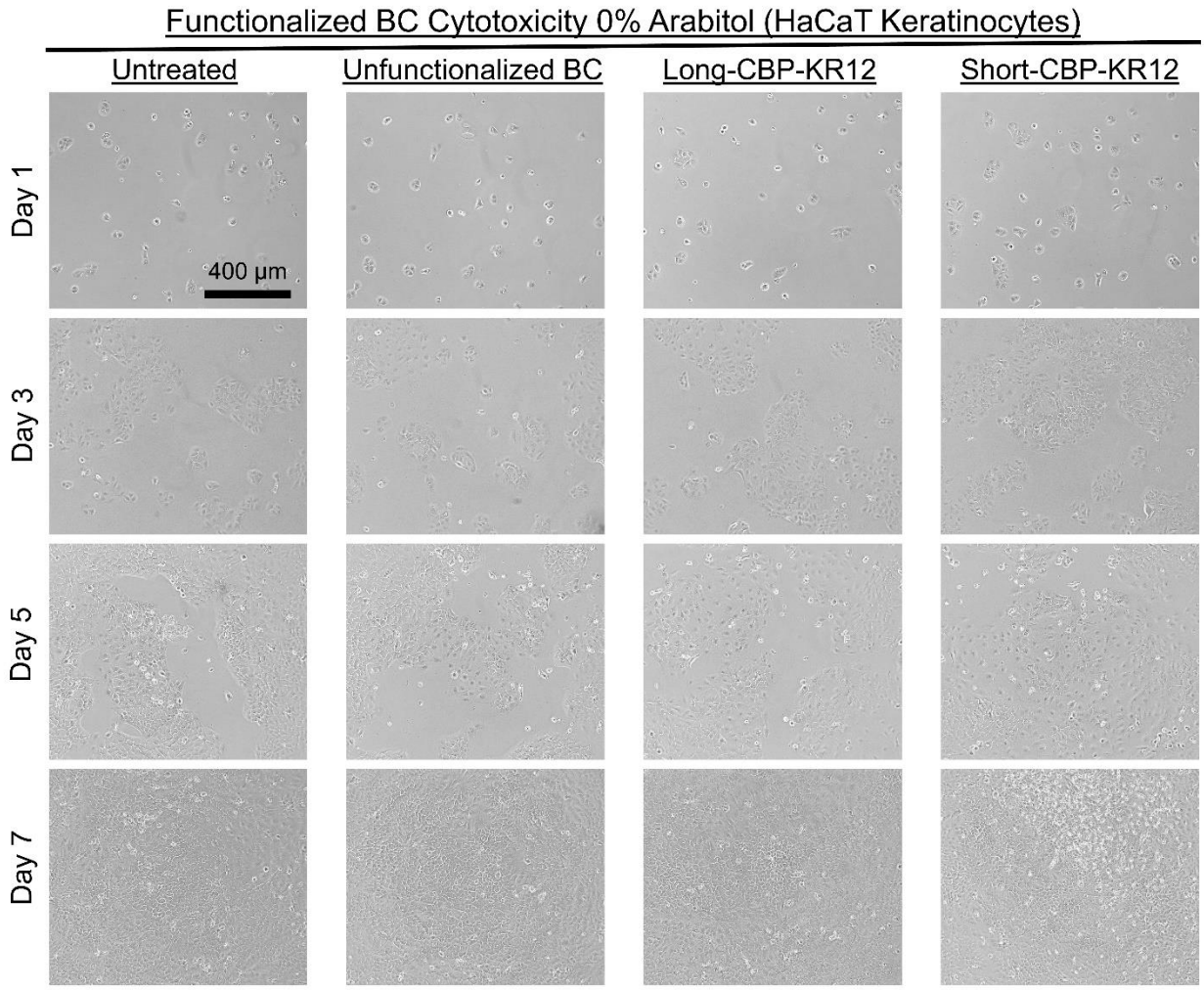

Figure 6.3. Functionalize BC cytotoxicity 0% Arabitol HaCaT cells

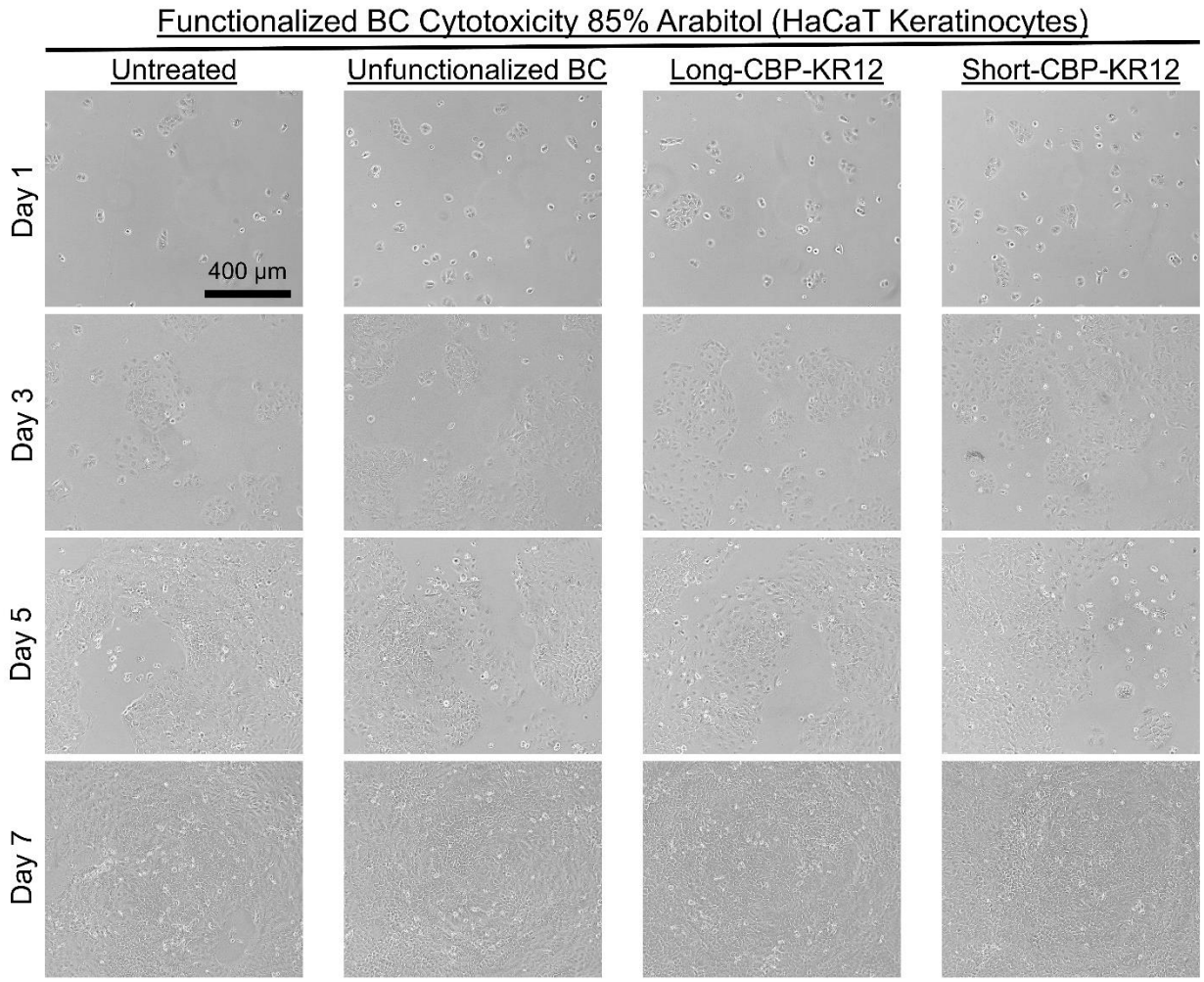

Figure 6.4. Functionalize BC cytotoxicity 85% Arabitol HaCaT cells

6.2. Appendix II. Isolation of DS-12 strain from kombucha culture

6.2.1. Materials and Methods

A home-brewed kombucha pellicle (**Figure 6.5A**), originally sources from Urban Farm (Portland, ME), was streaked onto a black tea agar plate (2 mg/mL steeped black tea was sterile filtered and supplemented with 40 mg/mL sucrose, 10% (v/v) kombucha starter, 15 mg/mL agar, and liquid autoclaved) and allowed to grow at 30°C for 4 d. Cellulose production was observed in specific colonies grown on the black tea agar plate (**Figure 6.5B**). A single cellulose producing colony was picked and re-streaked on a Hestrin-Schramm media (HS) agar plate (20mg/mL glucose, 5 mg/mL peptone, 5 mg/mL yeast extract, 1.15 mg/mL citric acid, 2.7 mg/mL disodium phosphate, 15 mg/mL agar) and allowed to grow at 30°C for an additional 4 d (**Figure 6.5C**). Single colonies from the HS plate were used to inoculate 5 mL of HS medium (20 mg/mL glucose, 5 mg/mL peptone, 5 mg/mL yeast extract, 1.15 mg/mL citric acid, 2.7 mg/mL disodium phosphate) media in a 14 mL Falcon round cell culture tubes and allowed to grow on a rotating drum for 4 d at 30°C (**Figure 6.5D**). Cellulose production ability was confirmed (**Figure 6.5E**), and the isolated strain was labeled DS-12.

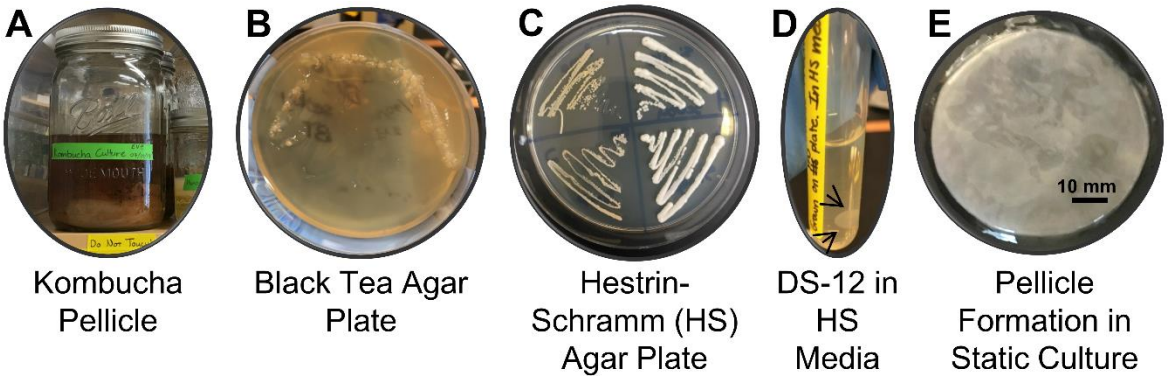

Figure 6.5. Isolation of DS-12.
(A) DS-12 isolated from a kombucha pellicle was **(B)** swab streaked onto black tea agar plate, **(C)** transferred to HS agar plates, and then **(D)** inoculated into HS media **(E)** where cellulose formation was observed.

6.3. Appendix III. Alternative sugar and cellulose producing bacteria screening

The following appendix presents sections from Keating, K. W., van Zyl, Collins, J. H., Nakagawa, C., Weintraub, S. J., Coburn, J. M., and Young, E. M., " Comparative genomics and characterization of Komagataeibacter nataicola DS12 nov. str. and related cellulose-producing bacteria." *In Preparation.*

6.3.1. Materials and Methods

Bacterial strains

DS-12 was isolated using the methods described in Appendix 6.2, while *Komagataeibacter oboediens* NCIB 8034, and *Novacetimonas hansenii* NQ5 cellulose producing strains were purchased from the American Type Culture Collection (ATCC, strains #10245 and 53582, respectively).

Bacterial growth kinetics

Growth kinetic studies were performed for the three bacterial strains. In 96-well plates, inoculated HS media was supplemented with 0.4% (v/v) cellulase from *Trichoderma reesei* (Sigma-Aldrich). The media was supplemented to 1 mM of each carbon source under investigation [glucose, sucrose, fructose, galactose, mannose, mannitol, xylose, arabinose, arabitol, GlcNAc, and GlcN]. Absorbance measurements were taken at 30 min intervals for 7 d at 600 nm under shaken conditions at 30°C (Biotek Synergy H1, Winooski, VT). The maximum growth rate was identified from the linear region of the kinetic curves.

Pellicle production and cellulose yield from alternative carbon sources

Each bacterial strain was streaked onto HS agar plates, and an individual colony picked. The picked colony was inoculated into 5 mL of Hestrin Schramm (HS) medium and incubated for 4 days on a shaker at 30°C. HS medium was supplemented with 1 mM of glucose for *K. nataicola* and *N. hansenii*, or mannitol for *K. oboediens*. Agitated cultures were then expanded in static cultures using 10% (v/v) inoculum in fresh HS medium.

Previously described methods for cellulose production and yield were used [1]. In brief, fresh HS media was inoculated with 0.1% (v/v) static cultured bacteria and supplemented to 1 mM of each carbon source under investigation [glucose, sucrose, fructose, galactose, mannose, mannitol, xylose, arabinose, arabitol, GlcNAc, and GlcN]. To allow for pellicle formation each bacteria carbon source mixture was cultured in 12-well plates under static conditions at 30°C for 7 d. Pellicles were then harvested, washed in 0.1 M NaOH, rinsed with DI H_2O, and then lyophilized using a shelf lyophilizer (Labconco, Kansas City, MO). Lyophilized pellicles were weighed, and cellulose yield was calculated relative to weight of carbon source initially supplemented into the culture using the following equation:

$$\textbf{Equation 1}: \%\ yield = \frac{cellulose\ dry\ mass}{carbon\ source\ mass} \times 100$$

Cellulose Light Transmission Spectroscopy Measurements

BC pellicles were measured for overall light transmission in the visible light region using a UV-Vis spectrophotometer (Thermo Scientific Evolution 300 UV-Visible Spectrophotometer, Waltham, MA) for pellicles produced by all three bacterial strains. Transmission spectral readings were performed between

wavelengths of 300-800 nm with a step size of 2 nm and the visible light transmission (400 – 700 nm range) is reported here.

6.3.2. Results

Strain selection and isolation

We selected the emerging production host NQ5 (ATCC #53582) and the previously engineered NCIB 8034 (NRC 6018, ATCC #10245) because they represent different branches of Acetobacteraceae and were isolated from different sources. NQ5 was isolated from a sugar mill in North Queensland, Australia. Though two genomes for NQ5 are currently available on the NCBI genome database (accessions GCF_001645815.1 and GCF_003416815.1), both assemblies are highly fragmented draft genomes due to short read-only sequencing. NCIB 8034 is of unknown provenance and there is no genome available. To obtain a representative strain from cultured products, strain DS12 was isolated from kombucha. In brief, cellulose producing colonies sourced from a home-brewed kombucha pellicle were selected from agar plates for subculture in Hestrin-Schramm media (HS) and screened for retention of cellulose production after serial subculture. The resulting isolated strain was named DS12. The NQ5 strain has been used in the laboratory and available in culture collection since at least 1987 [2], and the NCIB 8034 strain was available in a culture collection as cited in a patent in 1966 [3], compared to the isolation of DS12 in 2018. Together, these three strains represent different lineages and sources, providing diverse backgrounds to investigate the similarities and differences in Acetobacteraceae.

Phenotypic characterization - Growth

First, we phenotypically characterized the three strains for their carbon source utilization profile, BNC yield, and BNC transparency. To obtain a carbon source profile, we modified the defined Hestrin and Schramm media by substituting 10 carbon sources besides glucose – sucrose, fructose, galactose, mannose, mannitol, N-acetyl-D-glucosamine (GlcNAc), and glucosamine (GlcN), xylose, arabinose, and arabitol. The hexoses, pentoses, disaccharides, and sugar alcohols glucose, galactose, mannose, fructose, mannitol, and sucrose are common carbon sources for cellulose production [4-10]. GlcNAc and glucosamine represent sugar monomers with chemically functional side groups for incorporation and subsequent chemical modification [11-13]. These carbon sources consist of common hexose and pentose growth substrates, as well as sugar alcohols and EPS monomers commonly used in biomaterials. Then, we grew each strain on this modified HS medium and measured the optical density (OD600) over time. Maximum growth rate (μmax) values (**Figure 6.6**, **Table 6.1**) were calculated using the maximum slope from the optical density measurements. Growth was observed on every carbon source except GlcN, consistent with its known toxicity [14]. Both NQ5 and NCIB 8034 exhibited maximum growth rates of 0.005 or more on all carbon sources, save NQ5 on mannose, which none of the strains grew well on. However, DS12 only achieved growth faster than 0.005 on fructose, glucose, and mannitol. The fast growth on glucose and fructose, and limited growth on sucrose, may be an adaptation to kombucha culture. It has been shown in the kombucha symbiotic culture of yeast and bacteria (SCOBY) that yeasts with extracellular invertase activity catabolize sucrose into fructose and glucose [15]. Thus, microbes would have access to abundant glucose and fructose and have no pressure to retain sucrose metabolism. This also may explain the relatively poor growth on all other carbon sources for DS12 in general. The fast growth of all strains on mannitol versus mannose is interesting to note since they are catabolized through different pathways. A complete PEP system in *Komagataeibacter* has not been clearly established, but mannitol has been reported to be

transported into *K. nataicola* RZS01 via the phosphotransferase system, being phosphorylated into mannitol-1-phosphate in the process [16]. It is then isomerized into fructose-6-phosphate and likely is catabolized similarly to fructose, perhaps explaining the similar growth rates.

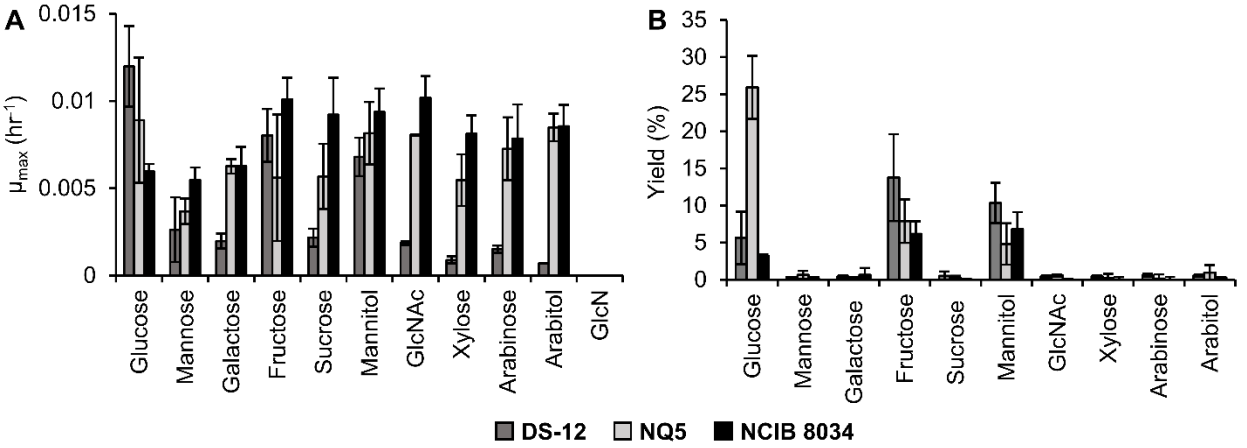

Figure 6.6. Maximum growth rates and cellulose yield on various carbon sources
(A) and cellulose yield (B) of DS12, NCIB 8034, and NQ5 grown on various carbon sources.

Table 6.1. Maximum growth rates of bacteria with various carbon sources

	DS-12	***G. hansenii***	***G. xylinus***
	μmax (h^{-1})	μmax (h^{-1})	μmax (h^{-1})
Glucose	0.0120 ± 0.0023	0.0089 ± 0.0036	0.0060 ± 0.0004
Mannose	0.0026 ± 0.0019	0.0037 ± 0.0007	0.0055 ± 0.0007
Galactose	0.0020 ± 0.0004	0.0063 ± 0.0004	0.0063 ± 0.0011
Fructose	0.0080 ± 0.0015	0.0056 ± 0.0036	0.0101 ± 0.0013
Sucrose	0.0022 ± 0.0005	0.0057 ± 0.0019	0.0092 ± 0.0021
Mannitol	0.0068 ± 0.0011	0.0082 ± 0.0018	0.0094 ± 0.0013
GlcNAc	0.0018 ± 0.0001	0.0080 ± 4.23E-05	0.0102 ± 0.0012
Xylose	0.0009 ± 0.0002	0.0055 ± 0.0015	0.0081 ± 0.0011
Arabinose	0.0015 ± 0.0002	0.0073 ± 0.0018	0.0078 ± 0.0020
Arabitol	0.0007 ± 8.0E-06	0.0085 ± 0.0008	0.0086 ± 0.0012
GlcN	-	-	-

Phenotypic characterization – BNC yield, transparency, and absorption

We then measured BNC production on all carbon sources. There was observable BNC production for most carbon sources. Using **Equation 1** (**Methods**), cellulose yield was determined relative to carbon source mass (**Figure 6.6**, **Table 6.2**). Consistent with literature, DS12, NQ5, and NCIB 8034 were found to support high cellulose yield formation when grown with fructose, mannitol, and glucose as a carbon source [1]. NQ5 produced the highest cellulose yield of 25.9% when glucose was used as a carbon source. NCIB 8034 known to prefer mannitol over glucose as the primary carbon source [17, 18], which is consistent with our findings where 3.2% BC yield was observed using glucose, while 6.8% BC yield was

observed using mannitol. NCIB 8034 also consistently exhibited higher cellulose yield production when using fructose as a carbon source (6.2%). The carbon sources that resulted in highest BC yield by DS12 were fructose and mannitol, with a yield of 13.8% and 10.3%, respectively. Yet, significant BNC yields were only observed for fructose, glucose, and mannitol. BNC biosynthesis depends on UDP-glucose, and in turn glucose. Therefore, the results appear to show that gluconeogenesis is not robust in these bacteria, as they are able to grow but not produce much BNC on carbon sources that do not have a metabolic path through glucose. Of the five carbon feeds, the highest yield was on arabitol, although the productivity was much less.

Table 6.2. Cellulose yield of bacteria with various carbon sources

	DS-12	***K.* hansenii**	***K.* xylinus**
	Yield (%)	Yield (%)	Yield (%)
Glucose	5.65 ± 3.55	25.93 ± 4.24	3.18 ± 0.22
Mannose	0.34 ± 0.03	0.64 ± 0.57	0.05 ± 0.31
Galactose	0.42 ± 0.16	0.05 ± 0.30	0.65 ± 0.92
Fructose	13.76 ± 5.84	7.90 ± 2.93	6.18 ± 1.70
Sucrose	0.51 ± 0.58	0.20 ± 0.31	0.05 ± 0.09
Mannitol	10.33 ± 2.72	4.81 ± 2.79	6.80 ± 2.31
GlcNAc	0.42 ± 0.18	0.56 ± 0.15	0.003 ± 0.08
Xylose	0.45 ± 0.11	0.21 ± 0.55	0.02 ± 0.33
Arabinose	0.60 ± 0.16	0.14 ± 0.57	0.01 ± 0.38
Arabitol	0.54 ± 0.17	0.96 ± 1.00	0.29 ± 0.07
GlcN	-	-	-

The transparency of the BNC products on all sugars was evaluated by overall light transmission in the visible light region using a UV-Vis spectrophotometer. All strains could synthesize transparent BNC, but arabitol particularly resulted in transparent BNC (**Figure 6.7**). The impact of arabitol and glucose cofeeding on BNC material properties for NQ5 is discussed in more detail in our recent report [1]. These results demonstrate that optically clear properties can be achieved across the Acetobacteraceae, indicating that culture conditions and perhaps synthesis rate are the key factors in transparent cellulose synthesis [19].

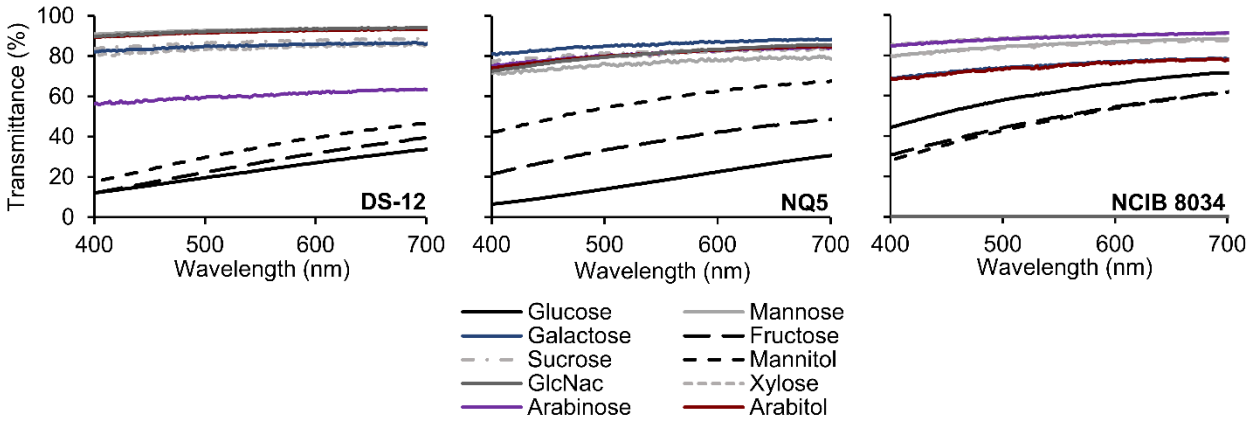

Figure 6.7. Transparency of the bacterial cellulose produced.
Cellulose produced by D2-12, NQ5, and NCIB 8034 when grown on various carbon sources.

6.3.3. References

[1] E.M. van Zyl, M.A. Kennedy, W. Nason, S.J. Fenlon, E.M. Young, L.J. Smith, S.R. Bhatia, J.M. Coburn, Structural properties of optically clear bacterial cellulose produced by Komagataeibacter hansenii using arabitol, Biomaterials Advances 148 (2023) 213345.
[2] T.E. Bureau, R.M. Brown Jr, In vitro synthesis of cellulose II from a cytoplasmic membrane fraction of Acetobacter xylinum, P. Natl. Acad. Sci. USA 84(20) (1987) 6985-6989.
[3] K. Toshihiko, O. Hisayoshi, Y. Hiroshi, N. Kiyoshi, I. Masao, N. Itaru, Method for producing 2-keto-lgulonic acid, Google Patents, 1966.
[4] C. Molina-Ramírez, M. Castro, M. Osorio, M. Torres-Taborda, B. Gómez, R. Zuluaga, C. Gómez, P. Gañán, O. Rojas, C. Castro, Effect of different carbon sources on bacterial nanocellulose production and structure using the low pH resistant strain Komagataeibacter medellinensis, Materials 10(6) (2017) 639.
[5] N. Tyagi, S. Suresh, Production of cellulose from sugarcane molasses using Gluconacetobacter intermedius SNT-1: optimization & characterization, J. Clean. Prod. 112 (2016) 71-80.
[6] S.-P. Lin, Y.-H. Huang, K.-D. Hsu, Y.-J. Lai, Y.-K. Chen, K.-C. Cheng, Isolation and identification of cellulose-producing strain Komagataeibacter intermedius from fermented fruit juice, Carbohyd. Polym. 151 (2016) 827-833.
[7] F. Mohammadkazemi, M. Azin, A. Ashori, Production of bacterial cellulose using different carbon sources and culture media, Carbohyd. Polym. 117 (2015) 518-523.
[8] E. Trovatti, L.S. Serafim, C.S. Freire, A.J. Silvestre, C.P. Neto, Gluconacetobacter sacchari: an efficient bacterial cellulose cell-factory, Carbohyd. Polym. 86(3) (2011) 1417-1420.
[9] H.J. Son, M.S. Heo, Y.G. Kim, S.J. Lee, Optimization of fermentation conditions for the production of bacterial cellulose by a newly isolated Acetobacter, Biotechnology and applied biochemistry 33(1) (2001) 1-5.
[10] M. Schramm, Z. Gromet, S. Hestrin, Synthesis of cellulose by Acetobacter xylinum. 3. Substrates and inhibitors, Biochemical Journal 67(4) (1957) 669.
[11] L. Fang, J.M. Catchmark, Characterization of cellulose and other exopolysaccharides produced from Gluconacetobacter strains, Carbohyd. Polym. 115 (2015) 663-669.

[12] V. Yadav, B.J. Paniliatis, H. Shi, K. Lee, P. Cebe, D.L. Kaplan, Novel in vivo-degradable cellulose-chitin copolymer from metabolically engineered Gluconacetobacter xylinus, Appl. Environ. Microb. 76(18) (2010) 6257-6265.
[13] J.W. Lee, F. Deng, W.G. Yeomans, A.L. Allen, R.A. Gross, D.L. Kaplan, Direct Incorporation of Glucosamine andN-Acetylglucosamine into Exopolymers byGluconacetobacter xylinus (= Acetobacter xylinum) ATCC 10245: Production of Chitosan-Cellulose and Chitin-Cellulose Exopolymers, Appl. Environ. Microb. 67(9) (2001) 3970-3975.
[14] S. Malik, M. Singh, A. Mathur, Antimicrobial activity of food grade glucosamine, Int. J. Biotechnol. Bioeng. Res 4(4) (2013) 307-312.
[15] H. Antolak, D. Piechota, A. Kucharska, Kombucha tea—A double power of bioactive compounds from tea and symbiotic culture of bacteria and yeasts (SCOBY), Antioxidants 10(10) (2021) 1541.
[16] H. Zhang, C. Ye, N. Xu, C. Chen, X. Chen, F. Yuan, Y. Xu, J. Yang, D. Sun, Reconstruction of a genome-scale metabolic network of Komagataeibacter nataicola RZS01 for cellulose production, Sci. Rep. 7(1) (2017) 7911.
[17] M. Gullo, S. La China, G. Petroni, S. Di Gregorio, P. Giudici, Exploring K2G30 genome: a high bacterial cellulose producing strain in glucose and mannitol based media, Frontiers in microbiology 10 (2019) 58.
[18] S. La China, A. Bezzecchi, F. Moya, G. Petroni, S. Di Gregorio, M. Gullo, Genome sequencing and phylogenetic analysis of K1G4: a new Komagataeibacter strain producing bacterial cellulose from different carbon sources, Biotechnology letters 42 (2020) 807-818.
[19] J.M. Coburn, E.M. Van Zyl, E.M. Young, Transparent Cellulose-Based Materials and Methods of Making the Same, Google Patents, 2021.

6.4. Appendix IV. Cell culture components and methods for mammalian cell lines

6.4.1. Normal Human Dermal Fibroblasts American Type Culture Collection CRL-2565

Work under aseptic conditions for everything

Media Components:
450 mL Iscove's Modified Dulbecco's Medium (IMDM) with HEPES and L-glutamine
50 mL fetal bovine serum
5mL 100x penicillin/streptomycin, P/S
5mL 100x L-glutamine
0.01 mL EGF aliquot
0.01 mL FGF aliquot

EGF aliquots
100 μg animal-free EGF, Peprotech#AF-100-15-100UG (comes sterile)
0.2 mL 0.2% BSA in PBS (sterile!) [2mg/ml BSA in PBS]

- Add 0.2 mL sterile PBS to the EGF vial, gently pipette up and down to dissolve and mix well. Stock concentration is 500 μg/mL
- Aliquot into 10 μL (Eppendorf tubes)

FGF2/bFGF aliquots
100 μg animal-free EGF, Peprotech#0621AFC05 (comes sterile)
0.4 mL 0.2% BSA in PBS (sterile!)

- Add 0.4 mL sterile PBS to the EGF vial, gently pipette up and down to dissolve and mix well. Stock concentration is 250 μg/mL
- Aliquot into 10 μL (Eppendorf tubes)

Passaging:
Normal trypsin based passaging can be performed using 0.25% trypsin-EDTA.
Cells above passage number 10 exhibit reduced growth rates and abnormal extracellular cell morphology.

Cell Freezing:
Cells can be frozen down in complete media as described above and 5% DMSO.

6.4.2. Human Keratinocytes (HaCaTs)

Work under aseptic conditions for everything

Media Components:
450 mL Dulbecco's Modified Eagle Medium (DMEM) high glucose
50 mL fetal bovine serum
5 mL 100x penicillin/streptomycin
1 mL 100x L-glutamine

Passaging:
Normal trypsin based passaging can be performed using 0.25% trypsin-EDTA for 5-8 mins. Cells can then be scraped to fully remove them from the tissue culture plastic.

Cell Freezing:
Cells can be frozen down in complete with 20% FBS and 5% DMSO.

6.4.3. Mouse Macrophages (RAW264.7)

Work under aseptic conditions for everything

Media Components:
450 mL Dulbecco's Modified Eagle Medium (DMEM) high glucose
50 mL fetal bovine serum
5 mL 100x penicillin/streptomycin
5 mL 100x L-glutamine

Passaging:
Cells should only be scraped to fully remove them from the tissue culture plastic.

Cell Freezing:
Cells can be frozen down in complete media as described above and 10% DMSO.

6.5. Appendix V. Alternative BC cleaning methods and assessment methods thereof

6.5.1. BC cleaning methods

Bacterial Cellulose Wash Steps and Lyophilization

- BC pellicles were submerged in 10 mL of either Milli-Q, Triton X-100, Sodium Cocoyl isethionate (SCI), CHAPS, Sodium Dodecyl Sulfate (SDS), Decyl Glucoside (DG), and Cocamidopropyl Betaine (CB) at 2% w/v concentrations. Control samples were submerged in 0.1M NaOH pr 0.1M NaOH+2% w/v SDS. All solution groups were placed in the 60°C oven for 3 h. After the initial incubation the samples were rinsed, and surfactant solutions were replaced with fresh solution for an additional 3 h of incubation.
    - Variation of the method has been done where the surfactant is used during the first incubation, and then the second solution consists of only 0.1 M NaOH.
- The BC samples were then removed from the solution and washed with MilliQ water for 15 min increments 5 times.
- Washed BC samples were then placed in individual wells in a 48 well plate and 0.5 mL of MilliQ water was added. Plates were then frozen and lyophilized for 48 hours at -25 °C.

6.5.2. BC purification assessment methods

Papain Digest and PicoGreen Assay for DNA Content

Papain Digest Protocol:

- 10mL of Phosphate buffered EDTA
    - 100mM Na2HPO4 (7.1g/500mL Di:H2O)
    - 10mM EDTA (1.86/500mL Di:H2O)
    - pH 6.5
- 17.5 mg of L-cysteine
- 0.05 mL Papain (use a syringe)

(Protect papain digest solution from light)

Need 0.5 mL of papain digest solution per tube. Calculate total papain digest solution required.

1. Add 0.5 mL of Papain digest to each microcentrifuge tube with 1 96-well plate sized BC pellicle. Let it incubate in the oven at 60°C overnight (15-16 hours).
2. After incubation freeze/thaw samples before performing Pico-green

Picogreen Assay:

- Quanti-iT Picogreen dsDNA Reagent and Kit
    - 20X Tris EDTA Buffer
    - Lambda DNA Standard
    - PicoGreen dsDNA reagent
- Black Plate (brand new)

1. Use phosphate buffered EDTA buffer. Left over buffer can be stored in the fridge 4C.

2. Dilute all the papain digest sample supernatant as described with 1X Phosphate EDTA buffer (10µL sample in 90 µL phosphate EDTA buffer) using labeled new tubes, so that the final concentration of Papain is 0.1%
3. Prepare DNA standard (found in kit in fridge). In 1x phosphate EDTA + 0.1% papain.

Standard	How to Prep
S1 -2 ug	5 µL DNA standard & 245 µL 1X phosphate EDTA
S2- 0.667 ug	75 µL S1 & 150 µL of 1X phosphate EDTA
S3-0.222 ug	75 µL S2 & 150 µL of 1X phosphate EDTA
S4-0.074 ug	75 µL S3 & 150 µL of 1X phosphate EDTA
S5-0.025 ug	75 µL S4 & 150 µL of 1X phosphate EDTA
S6-0.008 ug	75 µL S5 & 150 µL of 1X phosphate EDTA
S7-0.0027 ug	75 µL S6 & 150 µL of 1X phosphate EDTA
S8 Blank	200 µL of 1X phosphate EDTA

4. Prepare pico green reagent diluting 15 µl + 3 mL 1X phosphate EDTA Buffer.
5. Turn off the lights in work area.
6. Grab a black plate and to unused wells, add 50 µL of PicoGreen to each well and then add 50 µL of sample to the respective wells. Mix thoroughly. Plate duplicates of standard.
7. Let incubate in a drawer for 5 minutes.
8. Read on plate reader (excitation: 480 nm, emission: 520 nm)
9. Vacuum out liquid from plate. Tape over wells used to prevent accidental re-use of those wells. Discard of PicoGreen reagent and samples.

<u>BCA Assay for Protein Content</u>

- A 6M guanidine hydrochloride solution was made with Milli-Q water to extract the residual protein from each lyophilized BC sample. In microcentrifuge tubes 250 µL of guanidine hydrochloride was added to individual 96 well plate sized BC pellicles. Solutions were incubated for 15-16 hours at room temperature.
- After the incubation, 250 µL of water was added to each microcentrifuge tube and samples were centrifuged for 6 minutes at 14000 rpm.
- BSA standards were prepared according to the BC protocol, using phosphate buffered EDTA as the diluent.
- 25 µL of each experimental group was pipetted in triplicate into a clear 96-well plate. Standards were pipetted in duplicate.
    - Samples taken from the pellicles were taken from the top of the supernatant in the microcentrifuge tube.
- A working reagent using the Pierce BCA Protein Assay Kit where a 50:1 mixture of Reagent A was mixed with Reagent B is made and 200 µL of the resulting solution is pipetted into each well.
- Plates were then incubated at 37C for 30 minutes, after which absorbance readings at 562 nm are taken.

<u>FTIR Assessment for Material Impurities</u>

- Lyophilized BC pellicles were analyzed using the Bruker Vertex 70 FTIR instrument with a golden gate accessory.

- The background and sample scans were set to 128 scans per sample.
- Wavenumbers for the data were collected between 4000 and 550 cm^{-1} for each sample and repeated three times between different wash pellicles.

6.6. Appendix VI. Characterization of peptides with fluorescent tag

Many of peptide characterization experiments performed in Chapter 4, were repeated using fluorescently tagged peptides. Differences in the overall activity of the FAM tagged versus non-FAM-tagged peptides were observed. The fluorescently tagged peptide data are contained in this appendix section.

6.6.1. Fluorescently tagged peptide CD Spec analysis

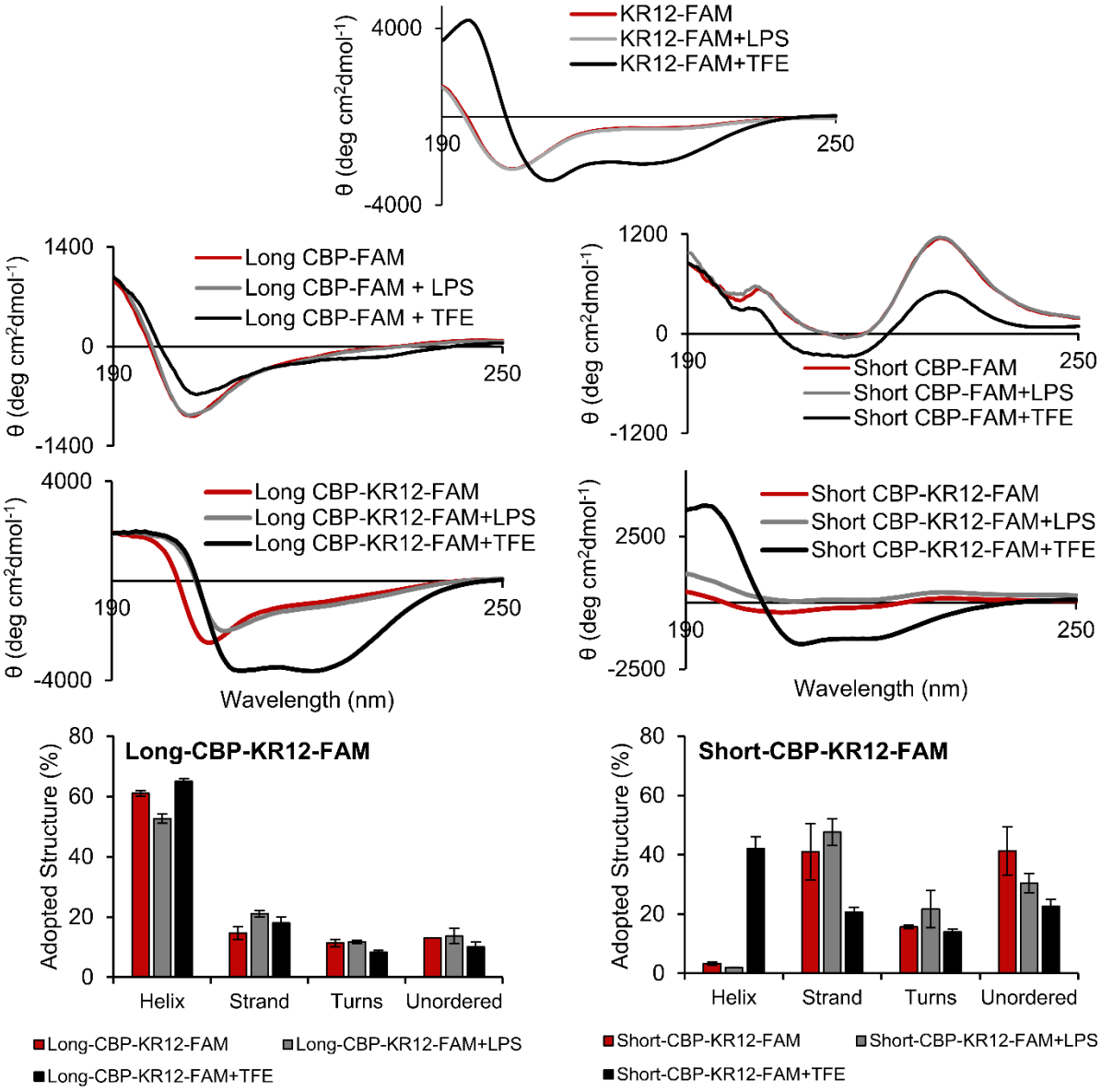

Figure 6.8. Circular dichroism spectra of fluorescently tagged peptides

CD spectra of each peptide in Phosphate buffer (red), buffer with 0.2% LPS (grey), and buffer with 50% TFE (black). Data are presented as the mean spectra from three independent readings (N = 3). Adopted structure were obtained from each independent reading and presented as the mean and standard deviation.

6.6.2. Fluorescently tagged peptide cytotoxicity

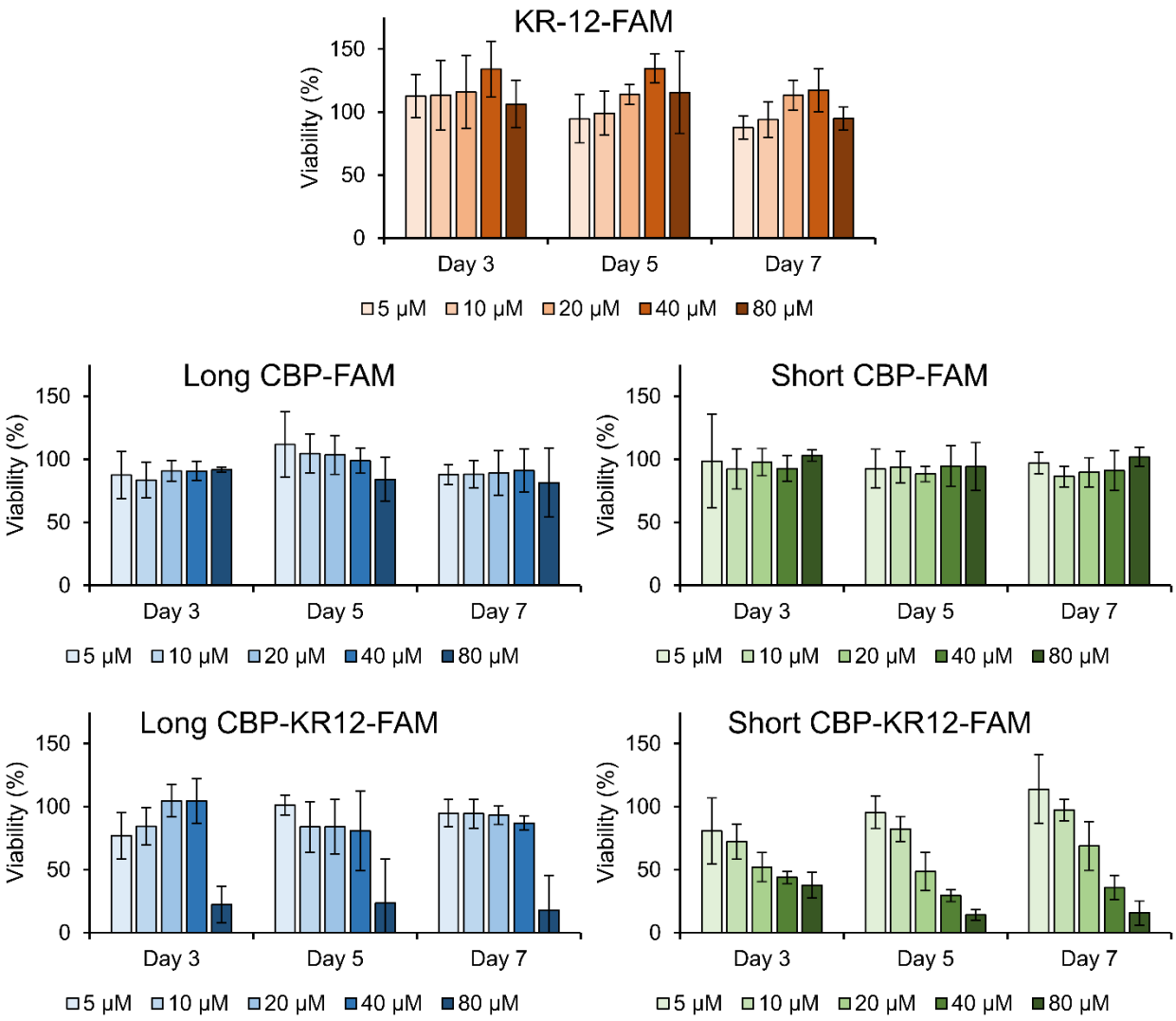

Figure 6.9. Fluorescently tagged peptide effect on fibroblast metabolic activity

Effects of increasing fluorescently tagged peptide concentration on the metabolic activity of NHDF. All data are normalized to the metabolic activity of untreated control wells (100% viability). Data are presented as the mean and standard deviation from three independent experiments (n = 3 per experiment).

6.6.3. Fluorescently tagged peptide minimum inhibitory concentration

Table 6.3. Minimum inhibitory concentration of fluorescently tagged peptides

	Concentration (µM)		
Bacterial Strain	KR-12-FAM	Long CBP-KR12-FAM	Short CBP-KR12-FAM
Escherichia coli	20	>80	40
Pseudomonas aeruginosa	>80	>80	>80
Staphylococcus aureus	>80	-	-

6.6.4. Fluorescently tagged peptide endotoxin binding capacity

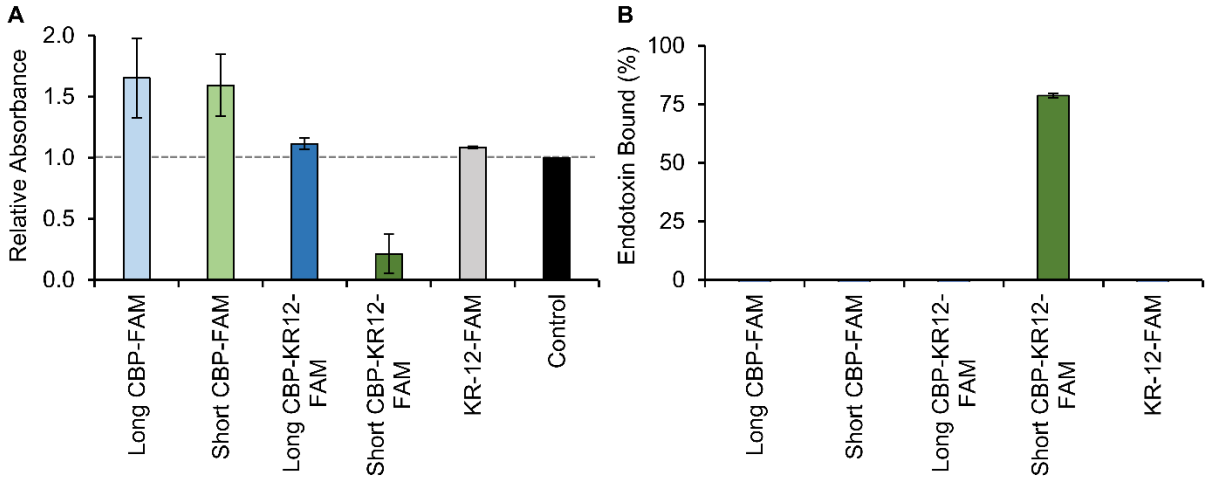

Figure 6.10. Endotoxin binding activity of fluorescently tagged peptides.
(A) Endotoxin binding capacity normalized to the untreated control. Values below 1.0 indicate endotoxin binding and neutralization. **(B)** Normalized endotoxin binding converted to percent endotoxin bound.

6.6.5. Fluorescently tagged peptide functionalized BC cytotoxicity

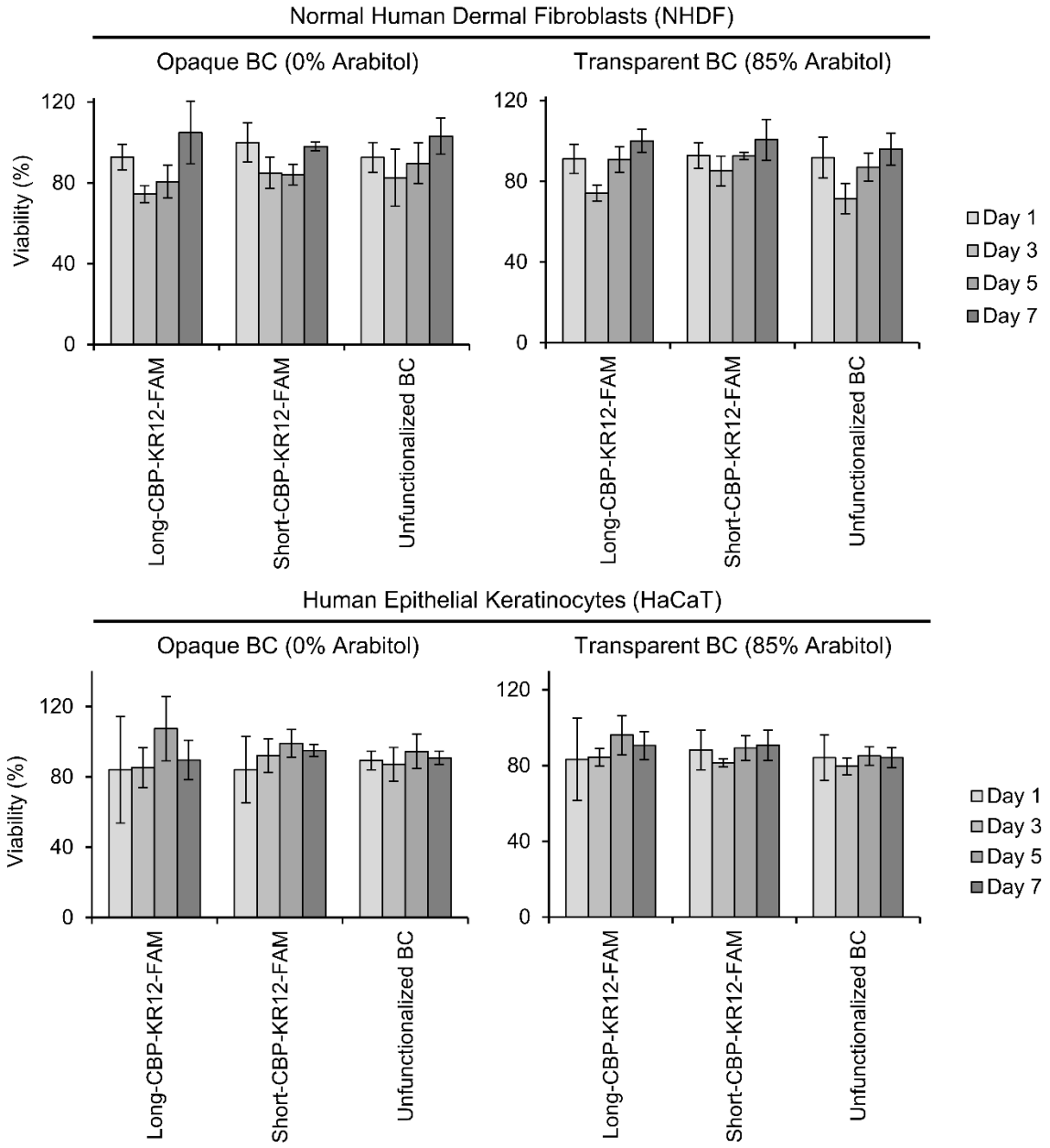

Figure 6.11. Fluorescently tagged peptide functionalized BC effects on NHDF and HaCaT cell lines. Metabolic activity values of unfunctionalized BC and BC functionalize with Long-CBP-KR12-FAM and Short-CBP-KR12-FAM normalized to untreated wells. Metabolic effects are depicted for both NHDF and HaCaT cell lines. All data are normalized to the metabolic activity of untreated control wells. Data are presented as the mean and standard deviation from three independent experiments (n = 3 per experiment).